

The Metamorphic and Structural
Evolution of the Alpujarride Complex -
Internal Zone, Betic Cordillera
(S Spain)

Louise Marie Hollick

University College London

Supervisor: Prof. J P Platt

Submitted for the degree of PhD

July 2001

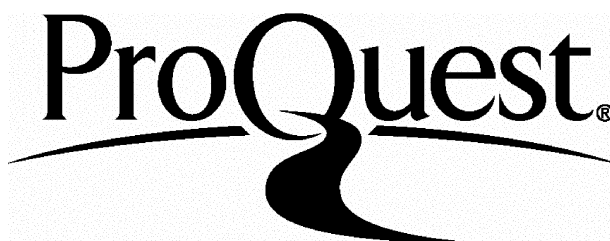
ProQuest Number: 10042802

All rights reserved

INFORMATION TO ALL USERS

The quality of this reproduction is dependent upon the quality of the copy submitted.

In the unlikely event that the author did not send a complete manuscript and there are missing pages, these will be noted. Also, if material had to be removed, a note will indicate the deletion.



ProQuest 10042802

Published by ProQuest LLC(2016). Copyright of the Dissertation is held by the Author.

All rights reserved.

This work is protected against unauthorized copying under Title 17, United States Code.
Microform Edition © ProQuest LLC.

ProQuest LLC
789 East Eisenhower Parkway
P.O. Box 1346
Ann Arbor, MI 48106-1346

ABSTRACT

The Metamorphic and Structural Evolution of the Alpujarride Complex - Internal Zone - Betic Cordillera (S Spain)

Metamorphosed pelitic schists within the Alpujarride Complex - a component of the Internal Zones of the Betic Cordillera, southern Spain – have experienced a complex metamorphic/structural evolution, most recently during an Alpine-age orogenic event. Preservation of disequilibrium textures permits an insight into the metamorphic conditions during the formation of structural fabrics. Metamorphic grade in the area varies from sillimanite grade to chlorite grade.

Rocks in the area (50 km south of Granada) have been affected by at least three phases of ductile deformation. The two most recent fabrics, S_s and S_t , are both crenulation cleavages; widespread examples occur which demonstrate the superposition of S_t on to S_s . Ductile/brittle normal faults developed during and after both phases of ductile deformation.

The D_t phase of deformation generates kilometre-scale folds, the inverted limbs of which overturn the metamorphic sequence related to the D_s deformation and fault contacts that developed during and after the D_s deformation, but prior to D_t . High grade rocks are apparently structurally above low grade rocks in the overturned limbs of D_t folds.

Trajectories in P-T space for rocks of different metamorphic grades, constrained from mineral relations with the regional foliations S_s and S_t and the application of thermobarometric techniques to appropriate assemblages, show that the S_s and S_t foliations developed during decompression, accompanied by heating. Peak metamorphic temperature occurred after the end of the D_s deformation event, and temperatures of above 550°C persisted to low pressure (3-4 kbar) conditions.

Results from geochronology techniques – U-Pb, Ar-Ar on muscovite and biotite, and apatite fission track – yield ages that are within error of each other, indicating that the Alpujarride Complex experienced rapid cooling during decompression from around 19.2 Ma.

ACKNOWLEDGEMENTS

Many thanks to my principal supervisor, Prof. John Platt, for excellent supervision during this thesis, both at UCL and in the field (often in the rain!). Our discussions have contributed enormously to my understanding and enjoyment of concepts and techniques covered in this project. I would also like to thank the other two members of my supervisory panel – Dr Wendy Kirk and Dr Hilary Downes – for the time they have given in providing encouragement and support.

Numerous other people at the Research School of UCL and Birkbeck College and at other institutions have contributed to this research in a multitude of ways. Dr Andy Beard provided technical support on the electron microprobe; advice on computer-related issues has been gratefully received from Maz Iqbal and Steve Hiron. The preparation of thin sections was undertaken by Sean Houlding and Arthur Beer, and my understanding of the fission track technique has been greatly improved as a result of discussion with Dr Andy Carter. I have benefited from discussion with Jose-Miguel Azañon and Antonio Garcia-Casco at the University of Granada, Spain and periods in the field with Miguel Orozco and Juan Soto. Dr Tom Argles, Dr Simon Kelley and Dr Sarah Sherlock at the Open University have also contributed their time and expertise to discussions related to this research.

Fellow post-graduate students – including Room 11 occupants past and present – have made my time here at UCL an enjoyable, memorable experience. A particular ‘thank-you’ to Dave ‘Spain’ Hodgson for use of the Russian Rock Carrier for transporting my samples back from the Betics!

I would like to also thank my parents, Mark, and friends outside of UCL for providing a background of ‘positivity’ to this study and continual encouragement: they have all learnt more about the geology of the Betics than they could have hoped!

CONTENTS

CHAPTER 1	THE CONTEXT OF THE STUDY	PAGE 19
1.1	Introduction	
1.1.2	Introduction to the Internal Zone	
1.1.3	Introduction to the External Zone	
1.2	The Internal Zones of the Betic Cordillera	
1.2.1	Introduction	
1.2.2	The Nevado-Filabride Complex	
1.2.3	The Alpujarride Complex	
1.2.4	The Malaguide Complex	
1.3	The Alpujarride Complex - unravelling Internal Zone P-T-t history	
1.3.1	Introduction	
1.3.2	The principal foliation in the Alpujarride Complex - timing and metamorphic relations	
1.3.3	Sub-divisions within the Alpujarride Complex	
1.3.4	Ductile structures in the Alpujarride Complex of the Central Betics	
1.3.5	Late metamorphic extension in the Alpujarride Complex	
1.3.6	Disequilibrium textures in the Alpujarride Complex	
1.3.7	Constraining the Alpujarride P-T-t path: thermobarometry and geochronology	
1.4	Late stage evolution of the Betic Cordillera	
1.5	Competing hypotheses for the cause of extension	
1.6	Aims of the project	

- 2.1 Introduction
- 2.2 Deformation events and related fabrics
 - 2.2.1 Introduction
 - 2.2.2 Nomenclature of ductile deformation events
 - 2.2.3 Three dimensional description of the ductile fabrics
- 2.3 Rock-types
 - 2.3.1 Introduction
 - 2.3.2 Graphitic schist and quartzite sequence
 - 2.3.3 Non-graphitic schist and quartzite sequence
 - 2.3.4 Phyllite and quartzite sequence
 - 2.3.5 Carbonate rocks
- 2.4 Metamorphic grades
 - 2.4.1 Introduction
 - 2.4.2 Kyanite-sillimanite grade
 - 2.4.3 Kyanite-sillimanite-andalusite grade
 - 2.4.4 Sillimanite-andalusite grade
 - 2.4.5 Garnet and/or staurolite–andalusite grade
 - 2.4.6 Muscovite-biotite grade rocks
 - 2.4.7 Muscovite-chlorite grade
- 2.5 Types of contact
 - 2.5.1 Introduction
 - 2.5.2 Stratigraphic contacts
 - 2.5.3 Pre-metamorphic tectonic contacts
 - 2.5.4 Ductile and/or brittle contacts formed during or after metamorphism

- 3.1 Introduction
- 3.2 Fabrics relating to the D_s deformation
 - 3.2.1 D_s folds and the S_s foliation
 - 3.2.2 Linear features relating to D_s
- 3.3 Fabrics relating to the D_t deformation
 - 3.3.1 D_t folds and the S_t foliation
 - 3.3.2 D_t fold axes (F_t) and the L_{st} lineation
 - 3.3.3 Large-scale D_t folds
- 3.4 Stratigraphic boundaries and contacts that pre-date the D_t event
 - 3.4.1 Introduction
 - 3.4.2 Original stratigraphic contacts
 - 3.4.3 Early tectonic contacts
 - 3.4.3.1 Rio Verde Contact
 - 3.4.3.2 El Tumbo Contact
 - 3.4.3.3 Molvizar Contact
 - 3.4.3.4 Las Palomas Contact
- 3.5 Brittle – ductile contacts formed between D_s and D_t events
 - 3.5.1. Introduction
 - 3.5.2 Comparison of rocks at either side of a D_s/D_t contact
 - 3.5.3 Mineral – fabric relations indicating D_s/D_t structures
- 3.6 Ductile – brittle structures developed after the D_t event
 - 3.6.1 Introduction
 - 3.6.2 Torre Miel fault zone
 - 3.6.3 Cerro Caleta fault zone
 - 3.6.4 Velilla fault zone
 - 3.6.5 Late brittle-ductile faults in the Los Guajares area
 - 3.6.5.1 Pinos Valle fault
 - 3.6.5.2 Guajare Alto faul
 - 3.6.6 Cerro Escalate fault zone
 - 3.6.6.1 Shear fabrics and lineations
 - 3.6.6.2 The Cerro Escalate fault zone
 - 3.6.6.3 Map relations and regional context

3.6.7 Shear fabrics in the phyllite-quartzite sequence

3.7 Deformation after the end of metamorphism

CHAPTER 4 MINERALOGY AND MICROSTRUCTURE PAGE 111

4.1 Introduction

4.2 Kyanite – sillimanite grade rocks

4.2.1 Introduction

4.2.2 Mineral assemblages prior to D_t

4.2.3 Mineral assemblages during and after D_t

4.3 Kyanite-sillimanite-andalusite grade rocks

4.3.1 Introduction

4.3.2 Mineral assemblages prior to D_t

4.3.3 Mineral assemblages during and after D_t

4.4 Sillimanite-andalusite (no kyanite) grade rocks

4.4.1 Introduction

4.4.2 Mineral assemblages prior to D_t

4.4.3 Mineral assemblages during and after D_t

4.5 Garnet/staurolite – andalusite grade rocks

4.5.1 Introduction

4.5.2 Mineral assemblages prior to D_t

4.5.3 Mineral assemblages during and after D_t

4.6 Muscovite–biotite and Muscovite–chlorite grade rocks

4.6.1 Introduction

4.6.2 Locations of Andalusite porphyroblasts

4.7 Case studies from the area

4.7.1 Variation of mineral-foliation relationships with
metamorphic grade: Lower Jete Road / Cotobro and
middle Jete Road

4.7.2 Contrasts and similarities between two areas of equal
metamorphic grade: near to Guajare Faraguit and near
to Salobreña

**CHAPTER 5 CONSTRaining THE P-T PATH –
QUANTITATIVE METHODS**

PART 1 THERMOBAROMETRY

PAGE 159

- 5.1 Introduction and methods
 - 5.1.1 Theoretical basis of thermobarometric techniques
 - 5.1.2 Exchange reactions
 - 5.1.3 Net Transfer reactions
 - 5.1.4 General problems in the application of thermobarometers
 - 5.1.4.1 Inaccurate thermodynamic models of solids
 - 5.1.4.2 Errors in normalising mineral formulae
 - 5.1.4.3 Effect of cation disorder in minerals /
synthetic phases
 - 5.1.5 Special considerations of rocks showing disequilibrium textures
 - 5.1.6 Estimating / minimising errors in pressure-temperature estimates
- 5.2 Manipulation of probe data
 - 5.2.1 Introduction
 - 5.2.2 Cation number calculation
 - 5.2.3 Spinel number selection
 - 5.2.4 Fe³⁺ estimation - garnet and mica
- 5.3 Modelling the activity of garnet
- 5.4 Choice of calibrations for barometers and thermometers
 - 5.4.1 Introduction
 - 5.4.2 Garnet-Biotite - thermometer
 - 5.4.3 Garnet-Hornblende - thermometer
 - 5.4.4 GASP (Garnet-plagioclase-Al₂SiO₅-quartz) barometer
 - 5.4.5 GRAIL (Garnet-ilmenite-rutile-Al₂SiO₅-quartz) barometer
- 5.5 Results from thermobarometry
 - 5.5.1 Introduction
 - 5.5.2 Sillimanite-bearing assemblages

- 5.5.2.1 Garnet zoning profiles
- 5.5.2.2 Pressure estimates - introduction
- 5.5.2.3. Application of the GASP barometer
- 5.5.2.4 Temperature estimation – Introduction
- 5.5.2.5. Application of the GARB thermometer
- 5.5.3 Garnet/staurolite-andalusite assemblages
 - 5.5.3.1 Garnet zoning profiles
 - 5.5.3.2 Pressure estimates - Introduction
 - 5.5.3.3 Application of the GASP barometer
 - 5.5.3.4. Application of the GRAIL barometer
 - 5.5.3.5. Temperature estimates - Introduction
 - 5.5.3.6. Application of the GARB thermometer
 - 5.5.3.7 Application of the Garnet-amphibole thermometer
- 5.5.4 Summary

PART 2

DATING TECHNIQUES

PAGE 184

- 5.6 Introduction
- 5.7 U-Pb technique
 - 5.7.1 Introduction to the technique
 - 5.7.2 Analytical procedure
 - 5.7.3 Description of the sample
 - 5.7.4 Results
- 5.8 Ar-Ar technique
 - 5.8.1 Introduction to the technique
 - 5.8.2 Apparatus and sample preparation
 - 5.8.3 Results
- 5.9 Apatite Fission track technique
 - 5.9.1 Introduction to the technique
 - 5.9.1.1 Estimating the concentration of fission tracks
 - 5.9.1.2 Estimating the concentration of ^{238}U
 - 5.9.1.3 Fission track length information

5.9.2 Analytical procedure

5.9.3 Results from apatite fission track analysis

CHAPTER 6 - CONCLUSIONS AND DISCUSSION

PAGE 238

6.1 Structural evolution of the Alpujarride complex

6.2 Temperature-time constraints of deformation; thermobarometry and geochronology

6.3 Metamorphic and structural evolution of the Alpujarride Complex in the context of the Betic Cordillera

6.4 Further work

APPENDIX ONE MINERAL ABBREVIATIONS AND MINERAL ASSEMBLAGES

PAGE 249

APPENDIX TWO PROBE DATA

PAGE 258

APPENDIX THREE GEOCHRONOLOGY DATA

PAGE 268

REFERENCES

PAGE 275

BACK POCKET

MAP ONE Structure of the area around Almuñecar, Salobreña and Guajare Faraguit

CROSS SECTIONS Figures 3.2 Rio Miel
Figure 3.3 North of Cerro Gordo
Figure 3.4 Cantalobos
Figure 3.5 Cazulas
Figure 3.6 Jete Road
Figure 3.7 West of Itrabo
Figure 3.8 North of Salobreña
Figure 3.9 Cerrajon
Figure 3.10 Escalate

LIST OF FIGURES

Figure	Abbreviated caption	Page
CHAPTER 1		
1.1	Map of the Betic-Rif orogenic belt, with major tectonic boundaries marked	34
1.2	Detailed map of the Betic Cordillera showing the location of Internal Zone components	35
1.3	Location map of volcanic rocks in SE Spain. Source: Turner et al (1999).	36
1.4	Summary of the lithologies in Internal Zone Complexes. Rock type and age information.	37
1.5	Map of the major allochthonous units (ATUs) in the central Betics. Source: Azañon et al (1994)	38
1.6	Geological map of the Alpujarride Complex SSW of Sierra Nevada showing location of Alpujarride Units and metamorphic / lithological sequence of these Units. Source: Azañon & Crespo-Blanc (2000).	39
1.7	Structure in the area to the north of Salobreña and Motril. Source: Simancas & Campos (1993)	40
1.8	Detailed tectonic map of the eastern Alpujarras, showing axial traces of main recumbent folds. Source: Orozco et al (1998)	41
1.9	P-T path for the high grade schist in the Alboran Basin. Source: Soto & Platt (1999)	42
1.10	Timing of the main events in the tectonic evolution of the Alboran Basin. Source: Comas et al, 1999.	43
CHAPTER 2		
2.1	Outcrop distribution of the Alpujarride Complex and the location of the field area	55
2.2	Micro-photograph of the S_s foliation	56
2.3	Field relations between the S_s and S_t foliations in an overturned limb of a D_t fold.	57
2.4	Stress ellipse with axes of principle stress indicated	58

2.5	Map of rock types and locations of stratigraphic boundaries in the field area.	59
2.6	Variation of S_t foliation intensity in schistose and quartzite layers	60
2.7	Map of metamorphic grade distribution in the field area.	61
2.8	Detailed view of the El Cerallo stratigraphic-type contact at VF 43500731	62
2.9	Cross section and map view of a pre-metamorphic contact	63
CHAPTER 3		
3.1	Summary map of ductile and brittle structural features in the area around Almuñecar	80
3.2	Rio de la Miel Cross section – along easting 4290	
3.3	North of Cerro Gordo cross-section – along easting 4320	
3.4	Cantalobos cross section – along easting 4350	
3.5	Cazulas cross section – along easting 4380	
3.6	Jete Road cross section – along easting 4390	
3.7	West of Itrabo cross section – along easting 4420	
3.8	North of Salobreña cross section – along easting 4460	
3.9	Cerrajon cross section – along easting 4490	
3.10	Escalate cross section – along easting 4520	
3.11	Field photograph showing thickening of quartzite layer in hinge of D_s fold	81
3.12	Sketch of S_s foliation lying axial planar to a D_s fold hinge	81
3.13	Areas of north and south vergence of the D_s phase folds	82
3.14	Stereonet of fold hinges relating to the D_s phase of deformation	83
3.15	L_s lineation wrapping around D_t fold hinge	84
3.16	S_t foliation axial planar to D_t folds, and folding S_s	85
3.17	S_s / S_t foliation relationships; variation of S_t development with amount of mica in lithological bands	86
3.18	S_t foliation surfaces form the dominant fabric in the phyllite/quartzite sequence	87
3.19	Field sketch showing the nature of the L_{st} lineation	88
3.20	Stereonet plot of fold axes relating to the D_s and D_t phases of deformation	89

3.21	Sketch to illustrate the concept of vergence for the S_s/S_t foliations	90
3.22	Overtuned stratigraphic boundary between phyllite / quartzite sequence and carbonate rocks	91
3.23	S_s/S_t relationships in an overturned limb of a D_t fold, including an en eschlon array of small quartz veins	92
3.24	Field sketches and photographs of the El Tumbo and Molvizar pre-metamorphic contacts	93
3.25	Configuration of the Alpujarride Complex near to Almuñecar after D_s , prior to the development of D_s/D_t faults	94
3.26	Maps to show location of D_s/D_t structures near to Guajare Faraguit and north of Salobreña	95
3.27	Field sketch from area near to Guajare Faraguit showing structural relationships close to D_s/D_t fault contact	96
3.28	Synthesised sketch to show configuration of rock-types / metamorphic grade north of Salobreña after movement along a D_s/D_t contact	97
3.29	Shear fabric viewed in XZ plane in thin section of sample LH194	98
3.30	Shear fabric viewed in YZ plane in thin section of sample LH194	99
3.31	Field data from the Torre Miel fault zone	100
3.32	Field sketch and data from the Cerro Caleta fault zone	101
3.33	Field sketches and photographs of fault-related features near to Punta de la Mona	102
3.34	Field sketch and field data from the Velilla fault zone	103
3.35	Field sketches and data from the faults in the Los Guajares area	104
3.36	Map of structural data to the north of Motril	105
3.37	Shear data from fabrics in the phyllite and quartzite sequence	106
3.38	Compilation of shear data from features in the phyllite and quartzite sequence	107
3.39	Field photographs and data from the Escalate fault zone	108
3.40	Shear fabrics in a discrete contact to the south of Velez Bernadalla	109
3.41	Map to show the locations of late-formed antiforms and synforms	110

CHAPTER 4

4.1	Map of metamorphic grade distribution	127
4.2	Deformation of sillimanite by D_t folds in kyanite-sillimanite grade	128
4.3	S_s foliation included in garnet – kyanite-sillimanite grade	129
4.4	Constraint of P-T conditions during D_s in kyanite-sillimanite grade rocks	130
4.5	Constraint of P-T conditions before D_t in kyanite-sillimanite grade rocks	131
4.6	S_s foliation and mineral phases included in garnet – kyanite-sillimanite-andalusite grade	132
4.7	Constraint of P-T conditions after D_s in kyanite-sillimanite-andalusite grade rocks	133
4.8	Kyanite deformed by D_t in matrix of kyanite-sillimanite-andalusite grade rock	134
4.9	Variation of the spacing between adjacent S_t foliation planes in different rock types	135
4.10	Relic garnet porphyroblast included in plagioclase porphyroblast that also includes the S_s foliation	136
4.11	Constraint of P-T conditions before D_t in kyanite-sillimanite-andalusite grade rocks	137
4.12	Sillimanite in pressure solution seams parallel to the S_t foliation. Kyanite-sillimanite-andalusite grade rocks	138
4.13	Textural and chemical characteristics of a garnet with two stages of growth. Kyanite-sillimanite-andalusite grade rocks	139& 140
4.14	Staurolite porphyroblast preserving open style of D_t folds. Kyanite-sillimanite-andalusite grade rocks	141
4.15	Staurolite and andalusite porphyroblast relationship to the S_t foliation. Kyanite-sillimanite-andalusite grade rocks.	142
4.16	Andalusite porphyroblast with texture indicating growth during D_t . Kyanite-sillimanite-andalusite grade rocks	143
4.17	S_s foliation preserved in quartz-rich lithon of micaceous rock. Sillimanite-andalusite grade	144
4.18	Constraint of P-T conditions before D_t in sillimanite-andalusite grade rocks	145

4.19	Constraint of P-T conditions during D_t in sillimanite-andalusite grade rocks	146
4.20	Garnet porphyroblast extended parallel to the S_s foliation. Garnet/staurolite-andalusite grade.	147
4.21	Garnet porphyroblast including curved trail of inclusions that pass into continuity with S_s in the matrix. Garnet/staurolite-andalusite grade.	148
4.22	Garnet porphyroblast with chloritoid and staurolite inclusions. Garnet/staurolite-andalusite grade.	149
4.23	Constraint of P-T conditions during D_s in garnet/staurolite-andalusite grade rocks	150
4.24	Textures between garnet and staurolite in a garnet/staurolite-andalusite grade rock	151
4.25	Constraint of P-T conditions after D_s in garnet/staurolite-andalusite grade rocks	152
4.26	Textures indicative of staurolite growth during and after the D_t deformation. Garnet/staurolite-andalusite grade.	153
4.27	Andalusite with rotated internal foliation. Garnet/staurolite-andalusite grade rocks	154
4.28	Map to show the location of garnet-absent assemblages that contain andalusite.	155
4.29	Texture of andalusite porphyroblast in muscovite-biotite grade rock	156
4.30	Comparison of P-T conditions for rocks of different metamorphic grades in Los Guajares area	157
4.31	Comparison of P-T conditions during D_t for rocks from near to Salobreña and in Los Guajares	158
CHAPTER 5		
5.1	Location map of samples used for thermobarometry	197
5.2	K_{eq} lines from the GARB thermometer for a variety of calibrations	198
5.3	Summary of P-T conditions in sillimanite-bearing assemblages	199
5.4	Summary of P-T assemblages in garnet/staurolite-andalusite grade rocks	200
5.5	Plot of $X(Fe)$ for garnet. Source: Spear (1993)	201
5.6	Plot of $M(Fe)$ for garnet. Source: Spear (1993)	202

5.7	Composition variation across LH 125 – kyanite-sillimanite grade	203
5.8	Composition variation across LH 28 – kyanite-sillimanite-andalusite grade	204
5.9	GASP plot for sample LH17 – kyanite-sillimanite grade	205
5.10	GASP plot for sample LH 125 – kyanite-sillimanite grade	206
5.11	GASP plot for sample LH 134 – kyanite-sillimanite grade	207
5.12	GASP plot for sample LH 28B – kyanite-sillimanite-andalusite grade	208
5.13	Textures and composition of plagioclase inclusions in garnet from sample LH 134 – kyanite-sillimanite grade	209
5.14	Textures and analysis locations of biotite inclusions in garnet from sample LH 104 – kyanite-sillimanite grade	210
5.15	Composition variation across LH 104 – kyanite-sillimanite grade	211
5.16	Plot of Fe/(Fe+Mg) ratio for biotite included in garnet, and in the matrix of, sample LH104 – kyanite-sillimanite grade	212
5.17	GARB plot for sample LH 104 – kyanite-sillimanite grade	213
5.18a	Composition variation across LH 56 – kyanite-sillimanite-andalusite grade	214
5.18b	GARB plot for sample LH56 - kyanite-sillimanite-andalusite grade	215
5.18c	Fe/(Fe+Mg) ratio in biotite from sample LH56 - kyanite-sillimanite-andalusite grade	215
5.19	Composition variation across garnet porphyroblast from LH 255 – garnet/staurolite-andalusite grade	216
5.20	Contours of garnet and plagioclase composition in P-T space. Source: Spear (1993)	217
5.21	Composition variation across garnet porphyroblast from LH154 – garnet/staurolite-andalusite grade	218
5.22a	Image of garnet porphyroblast from sample LH255, with locations of plagioclase inclusions marked	219
5.22b	Composition of plagioclase crystals from matrix of sample LH255 – garnet/staurolite-andalusite grade	219
5.23	GASP plot for sample LH255 – garnet/staurolite-andalusite grade	220
5.24a	Image of garnet porphyroblast from sample LH 311 – garnet/staurolite-andalusite grade	221

5.24b	Composition variation across garnet porphyroblast from LH311 – garnet/staurolite-andalusite grade	221
5.25	Textures of ilmenite/rutile in garnet porphyroblast from sample LH138 – garnet/staurolite-andalusite grade	222
5.26	Textures of ilmenite/rutile in garnet porphyroblast from sample LH311- garnet/staurolite-andalusite grade	223
5.27a	GRAIL plot for sample LH138 – garnet/staurolite-andalusite grade	224
5.27b	GRAIL plot for sample LH311 – garnet/staurolite-andalusite grade	224
5.28a	GARB plot for Garnet A – sample LH61 – garnet/staurolite-andalusite grade	225
5.28b	GARB plot for Garnet B – sample LH61 – garnet/staurolite-andalusite grade	226
5.29	GARB plot for sample LH349 – garnet/staurolite-andalusite grade	227
5.30	GARB plot of sample LH154 – garnet/staurolite-andalusite grade	228
5.31a	Composition variation across garnet porphyroblast in sample LH255 – garnet/staurolite-andalusite grade	229
5.31b	Composition variation across amphibole porphyroblast in sample LH255 – garnet/staurolite-andalusite grade	229
5.32	Garnet/hornblende thermometer plots for core, intermediate and rim positions of porphyroblasts from sample LH255 - garnet/staurolite-andalusite grade	230
5.33	Summary plot of the P-T conditions prevailing in the kyanite-sillimanite grade rocks after the end of garnet growth	231
5.34	Summary plot of the P-T conditions prevailing in the kyanite-sillimanite-andalusite grade rocks after the end of garnet growth	232
5.35	Summary plot of the P-T conditions prevailing in garnet/staurolite-andalusite grade rocks after the end of garnet growth	233
5.36	Location map for samples used in geochronology	234
5.37	Images of zircon crystals from sample PB342. Source: Platt & Whitehouse (1999)	235
5.38	Concordia plot for results of U-Pb analysis. Source: Platt & Whitehouse (1999)	236
5.39	Radial plot of apatite fission track data for sample LH 166	237

CHAPTER 6		
6.1	Summary P-T plots for kyanite-sillimanite, kyanite-sillimanite-andalusite, kyanite-andalusite and garnet/staurolite-andalusite grade rocks, showing occurrence of D_s and D_t in P-T space	246
6.2	Metamorphic and structural evolution of Alpujarride Complex	247
6.3	Sketch to show dynamics of structural evolution	248

LIST OF TABLES

CHAPTER 4		
4.1	Summary of mineral relations with the S_s and S_t foliations in all metamorphic grades	126
CHAPTER 5		
5.1	Calculation of cation number values from percent oxide values. Source: Ragland (1989)	164
5.2	Summary of results from the Ar-Ar technique applied to white mica	191
5.3	Summary of results from fission track analysis of apatite	195

CHAPTER 1 - THE CONTEXT OF THE STUDY

1.1 Introduction

The tightly arcuate Betic - Rif mountain chain that spans the Straits of Gibraltar is the most western expression of Alpine tectonics in the Mediterranean region (**figure 1.1**). The orogeny developed in response to pre-Miocene (Cretaceous to Paleogene) convergent plate motion between the African and Eurasian plates, resulting in subduction and continental collision (Bakker *et al*, 1989; Tubia & Gil-Ibarguchi, 1991). The area close to the boundary between these two plates has accommodated approximately 200 km of roughly north-south convergence between the mid-Oligocene and late Miocene (Dewey *et al*, 1989).

Early research workers in the Betics (e.g. Egeler & Simon, 1969) established the nomenclature for the Zones and Complexes within the Betic Cordillera that is in use today. The complexes and palaeo-geographic terrains in this area belong to four pre-Neogene crustal domains (**figure 1.1**)

- (1) South-Iberian passive continental palaeomargin, comprising Mesozoic and Tertiary rocks, now incorporated into the External Zones of the Betic Cordillera
- (2) Maghrebian passive continental palaeomargin, also composed of Mesozoic and Tertiary rocks, and classified as the External Zone of the Rif Chain.
- (3) Flysch Trough Units. Nappes of early Cretaceous - early Miocene sediments deposited in a trough over oceanic or thinned continental lithosphere.
- (4) Alboran Crustal Domain. Paleozoic to Miocene rocks, within the Betic-Rif Internal Zones, and comprising a pre-Miocene crustal stack of three nappe units (see section 1.2 below).

The present day configuration of the Betic-Rif orogen is broadly divided into the Internal and External Zones. Characteristics of each of these zones are briefly outlined below.

1.1.2 Introduction to the Internal Zone

This Zone is composed of mainly metamorphic rocks which are of Tertiary age or older and crops out on the southern margin of Spain and in the north of Morocco (**figure 1.1**). Three main Complexes are defined within the Internal Zone. In the Betic Cordillera of Spain, sequentially from the lowest up, these are the **Nevado-Filabride**, **Alpujarride**, and **Malaguide** Complexes (Balanya & Garcia-Duenas, 1987). In the Rif chain in Morocco,

the Alpujarride Complex and Malaguide Complex are referred to as the Sebtide and Ghomaride nappes, respectively (Michard *et al*, 1997). The Alpujarride and Malaguide Complexes are referred to as the Higher Betic Nappes by Platt *et al* (1983).

Peridotite bodies in the Betic-Rif orogen crop out near Ronda (in the west of the Betics) (**figure 1.2**) and at Beni Boussera (within the Sebtide rocks of northern Morocco). Early researchers proposed that the Ronda peridotite bodies were steep-sided diapiric intrusions (Loomis, 1972; Darot, 1974), but subsequent studies in the region using gravity-profiling have revealed that they have a sheet-like geometry (Torne *et al*, 1992). In the Betics, contact relations between the peridotite and adjacent Alpujarride rocks indicate that the peridotite slabs were emplaced in the solid state (Argles *et al*, 1999). Tubia & Cuevas (1986) suggest that the emplacement of these peridotite slices into the Alpujarride Complex occurred during the thrusting event associated with the initial crustal thickening in the region.

A swarm of tholeiitic dykes intrude the Internal Zone to the north of Malaga, and a suite of magmatic rocks, comprising calc-alkaline magmas, cordierite-garnet dacites and alkali basalts are present in the Alboran Sea (**figure 1.3a**) and along the SE coastal margin of the Betics (Turner *et al*, 1999; **figure 1.3b**). Ar/Ar whole rock dating on a suite of Oligocene mafic dykes intruded in the Malaguide allochthon indicates that these dykes were intruded between 30 Ma and 23 Ma. Sr and Nd isotope data imply that this magma was generated as a consequence of partial melting at a shallow level in the asthenosphere (Turner *et al*, 1999). The calc-alkaline and cordierite-garnet dacite rocks in the south eastern Betics were emplaced between 15 to 6 Ma and contain Sr and Nd isotope signatures indicative of increasing amounts of crustal contamination in the melt; the dacites indicate very high Moho temperatures. Alkali basalts and lamproites, emplaced sequentially between 10 - 7 Ma, indicate partial melting of the lower lithosphere and shallow lithospheric mantle, respectively (Turner *et al*, 1999).

1.1.3 Introduction to the External Zone

The External Zone forms an extensive Neogene fold and thrust belt of unmetamorphosed Mesozoic rocks that crop out to the north of the Internal Zones on the Iberian peninsula, and to the south of the Internal Zones (Alboran nappes) in the Rif (**figures 1.1 & 1.2**). On the Iberian Peninsula, the External Zone is sub-divided into the Subbetic and Prebetic Zones. The Prebetic zone is exposed in the northeast of the Betics and is composed of shallow-water sediments deposited on the Iberian platform. The Subbetic is subdivided

into palaeogeographic regions in the north, central and southern parts of the area; sedimentary sequences within these sub-divisions vary, but overall the Subbetic sediments are more basinal than those of the Prebetic (Vissers *et al*, 1995).

In the west of the Betic Cordillera, the Flysch Units overlie the Internal Zone complexes (**figure 1.2**). The present-day exposure of the Flysch Units extends from the Straits of Gibraltar to Kabylies in northern Africa. As mentioned above, these early Cretaceous – early Miocene sediments were deposited in a trough formed on oceanic or very thin continental crust (Comas *et al*, 1999). Balanya & Garcia-Dueñas (1988) suggest that this palaeo-trough may have formed on the thinned crust between the South Iberian and Maghrebian paleomargins.

1.2 The Internal Zones of the Betic Cordillera

1.2.1 Introduction

The rock units that make up the Internal Zone of the Betic Cordillera are shown in **Figure 1.2**.

The Internal-External Zone Boundary (IEZB) separates the metamorphosed Internal Zones of the Betic Cordillera (the Alboran Crustal Domain) from the un-metamorphosed rocks in the External Zones that belong to the South-Iberian and Maghrebian palaeogeographic terrains (Balanya, 1991) (**figure 1.2**). The IEZB is dominantly a thrust contact that places Internal Zone rocks over the External Zones. Movement along this contact began in the early-to-mid Miocene. Thrusting propagated in a dominantly westward direction from the latest Oligocene to the earliest Miocene, generating the arcuate shape of the peripheral thrust belt (the Gibraltar Arc). Variation of thrust direction occurs within the Betic-Rif orogen. On the Iberian Peninsula, thrust directions vary from north-west (in the Betics) to west (near to Gibraltar) (Kirker & Platt, 1998; Lonergan *et al*, 1994), while in the Rif thrust directions towards west-southwest and west are identified (Frizon de Lamotte, 1987; Platzman *et al*, 1993). Kirker & Platt (1998) propose that the large measured vertical axis rotations identified in the thrust sheets occurred by progressive addition of small differential rotations throughout the stack. Shortening and vertical axis rotation was contemporaneous with extension and crustal thinning within the Alboran Crustal Domain.

The event that generated the thickening of the crust in the Alboran Domain is generally accepted to be of Cretaceous to Paleogene in age (e.g. Tubia & Gil-Ibarguchi, 1991). The subsequent tectonic and metamorphic evolution of the rocks in the area is a more

contentious issue. Similarities between the stratigraphy within the Nevado-Filabride, Alpujarride and Malaguide Complexes indicate that the initial episode of crustal thickening proceeded by nappe duplication (Bakker *et al*, 1989). In each Complex, a sequence of Palaeozoic graphitic schists underlies a Permo-Triassic non-graphitic quartzite and schist sequence. The Permo-Triassic lithologies are in turn overlain by middle to upper Triassic carbonates (Martin & Braga, 1987). The Malaguide Complex preserves a sequence of rocks not seen in the other two Complexes (see **section 1.2.4**). Differentiation between the Nevado-Filabride, Alpujarride and Malaguide complexes is principally based on variation of metamorphic grade. The structurally highest Complex, the Malaguide Complex, shows evidence of having experienced only very low-grade metamorphism. The underlying Alpujarride and Nevado-Filabride Complexes contain early high-pressure/low temperature metamorphic assemblages and subsequent assemblages indicating that lower pressure conditions at moderate to locally high temperatures occurred later in the metamorphic history (**figure 1.4**).

In both the Nevado-Filabride and Alpujarride Complexes, prolific disequilibrium assemblages and textures are preserved (Garcia-Casco & Torres-Roldan, 1996). Theoretically, relic mineral assemblages can be employed to help constrain the pressure-temperature conditions that prevailed during the early metamorphic evolution of these rocks. However, the extreme textural and chemical disequilibrium that is prevalent in the rocks (e.g. Garcia-Casco & Torres-Roldan, 1996; **section 1.3.6**) generates challenges in establishing accurate pressure and temperature estimates from the use of thermo-barometric techniques.

1.2.2 The Nevado-Filabride Complex

The Nevado-Filabride Complex crops out an open-style antiform that is seen in the Sierra Nevada, Sierra de los Filabres and elsewhere. This structure developed during the Miocene (Martinez-Martinez & Azañon, 1997). The Complex is divided into three tectonic units: from the structurally lowest to the highest these are the Veleta, Calar-Alto and Bedar-Macael Units. The Calar-Alto and Bedar-Macael units comprise a metamorphic sequence with basic and ultrabasic igneous rocks. The penetrative sub-horizontal schistosity which is present throughout the Complex was formed under greenschist facies in the structurally lower parts of the Complex, and at amphibolite facies in the upper parts of the Complex (Platt & Behrmann, 1986; Garcia-Deñias *et al*, 1988).

Basic and ultra-basic rocks in the upper part of the Nevado-Filabride Complex provide a source of information about the pre-orogenic history of the Betic Cordillera and the early

high-pressure conditions related to crustal thickening as a consequence of continental subduction and collision. Gomez-Pugnaire & Fernandez-Soler (1987) estimate that the equilibrium conditions in an eclogite body within the Nevado-Filabride were 550°C at 12 kbar. Attempts to date the high- pressure metamorphic assemblages in the Nevado-Filabride complex have produced widely varying results; an age of 48 Ma from Ar-Ar dating of barroisitic amphibole has been interpreted as defining the end of the high pressure episode (Monie *et al*, 1991).

1.2.3 The Alpujarride Complex

The Alpujarride Complex overlies the Nevado-Filabride Complex, and is separated from it by the Betic Movement Zone (BMZ). This tectonic contact is a detachment fault developed in a heterogeneous shear regime, with indicators suggesting top-to-the-west sense of shear. Extension along this contact began at around 23Ma and continues to the present day. The rate of extension has varied over time: the rate of exhumation of Alpujarride rocks decreased from 5 to 1 mm a⁻¹ between 25-19 Ma (Sosson *et al*, 1998); an uplift rate of 2 mm a⁻¹ is estimated for the Nevado-Filabride rocks in the period 23-12 Ma (Sosson *et al*, 1998). These data suggest that final movement along the Betic Movement Zone is likely to have occurred at around 12 Ma (Jabaloy *et al*, 1993).

Rocks belonging to the Alpujarride Complex crop out extensively in the western and central portions of the Betics. These rocks have characteristically experienced an early high-pressure metamorphic event and were later affected by local high temperature metamorphism up to granulite facies (Tubia & Gil-Ibarguchi, 1991). Thin continental crust in the Alboran Basin, which transmits high rates of heat flow (Torre & Banda, 1992), has been interpreted as part of the Alpujarride Complex (Platt *et al*, 1996; Comas *et al*, 1999). Samples of high-grade schist, gneiss, migmatic gneiss, marble, calc-silicate rock and granite recovered from Site 976 in the Alboran Sea (Comas *et al*, 1996) have been assigned to the Blanca Group which crops out onshore in the western Betics, near to the Ronda peridotites (Sanchez-Gomez *et al*, 1999).

A ⁴⁰Ar/³⁹Ar date of 24.8±0.4 Ma from phengite in a carpholite-chloritoid-aragonite assemblage in the Alpujarride Complex is interpreted to date the end of the high-pressure evolution (Monie *et al*, 1991). The convergence of ⁴⁰Ar/³⁹Ar dates obtained from amphiboles, muscovite, biotite and potassium feldspars, in a range between 19-20 Ma, indicates that the final cooling of the Alpujarride Complex was rapid (Monie *et al*, 1991, 1994; Zeck *et al*, 1989; 1992). (See also section 1.3.6).

Aldaya *et al* (1979) subdivides the Alpujarride Complex into units bound by thrust-contacts. The distinction between units was based on rock type, metamorphic grade and the relative structural position of the unit within the Alpujarride Complex. This grouping appears on the IGME geological sheets (e.g. Motril sheet - 19-44, 1:50,000, IGME). Subsequent work in the Betics, including Garcia-Duenas *et al* (1988), Platt & Vissers (1989) and Balanya *et al* (1993) has led to the reinterpretation of many boundaries previously considered to be thrusts as extensional structures. The sub-divisions established by Aldaya *et al* (1979) are used by Azañon *et al* (1994) as the basis of a revised classification of rocks within the Alpujarride Complex (see section 1.3.3).

1.2.4 The Malaguide Complex

The Malaguide Complex overlies the Alpujarride Complex; replication of stratigraphy between the two Complexes is evident. The current boundary between these two Complexes, however, is an extensional contact, across which metamorphic grade increases abruptly downwards. The time at which reactivation of the boundary occurred has been dated, using fission-track techniques, to the Early Miocene (Lonergan & Platt, 1995). Fabrics within the faulted contact show evidence of both brittle and ductile structures (Lonergan & Platt, 1995).

The Malaguide Complex is the structurally highest Complex within the Internal Zone. In addition to the Palaeozoic, Permo-Triassic and Tertiary rocks present in the Nevado-Filabride and Alpujarride Complexes, the Malaguide Complex contains a near-complete, unmetamorphosed, sequence of Silurian to Miocene sedimentary rocks. A well-preserved section of Tertiary sediments, ranging from lower Eocene to middle Miocene in age, is present in the Tertiary Sierra Espuña Basin in the eastern Betics and have undergone shortening and imbrication prior to the Miocene (Lonergan, 1993). Provenance studies, structural analysis, petrography and heavy mineral analysis have demonstrated that the Malaguide Complex was progressively exhumed during a period of approximately 10 Ma, ending in the middle Miocene (Lonergan & Mange-Rajetzky, 1994).

1.3 The Alpujarride Complex - unraveling Internal Zone P-T-t history

1.3.1 Introduction

The Alpujarride Complex is exposed across almost the entire east-west extent of the Betic Cordillera. It enjoys particularly good exposure in the west and central parts of the orogenic belt. The latter of these regions is the location for this study.

The stratigraphic sequence within the Alpujarride Complex is similar to that found in the Nevado-Filabride Complex and in parts of the Malaguide Complex, as discussed above (section 1.2.1). The pressure-temperature history of rocks within the Alpujarride Complex of the central Betics varies. A deformed body of heterogeneous gneiss, the precursor of which was a deformed Hercynian granite body, is present near to Torrox (50 km east of Malaga - Garcia-Casco *et al*, 1993); extensive exposure of low grade phyllites are located in the eastern Alpujarras (to the north of Adra – Orozco *et al*, 1998). Rocks assigned to the Alpujarride Complex preserve the highest temperature assemblages found in the Betic Cordillera. It is these assemblages which allow the metamorphic and structural evolution of this Complex to be well constrained.

1.3.2 The principal foliation in the Alpujarride Complex - timing and metamorphic relations

The main fabric within the quartzite and schist sequences of the Alpujarride Complex cropping out in the central Betics is generally accepted to be a syn-metamorphic foliation which developed during evolution from high P-T ratio metamorphic conditions to low P-T ratio metamorphic conditions (Azañon & Crespo-Blanc, 2000; Sanchez-Gomez *et al*, 1999). The main foliation lies parallel to the boundaries of lithological formations and to metamorphic isograds (Balanya *et al*, 1993; Azañon *et al*, 1994).

During the formation of the main foliation, the rocks of the Alpujarride Complex experienced isothermal decompression as a consequence of exhumation and extreme vertical shortening (Monie *et al*, 1994; Garcia-Casco *et al*, 1993). The metamorphic gradient in the field was condensed (i.e. the isograds were brought closer together) throughout the Alpujarride Complex as a consequence of the attenuation of the crust. A clearly defined example occurs near the Ronda peridotite body crops out in the western part of the Betic Cordillera, where variation of grade from greenschist to granulite facies is seen in a section of 4km structural thickness (Argles *et al*, 1999). Other studies in the western

Betics have recorded the rapid decompression and cooling history of these rocks. $^{40}\text{Ar}/^{39}\text{Ar}$ and fission-track data from the Ojen and Los Reales nappes determine that the rate of cooling in the interval between 19 - 16 Ma was at least $100^\circ\text{C} / \text{Ma}$, during which period the rocks cooled from $500\pm 50^\circ\text{C}$ to $90\pm 30^\circ\text{C}$ (Sosson et al, 1998).

Thermobarometric techniques were applied by Azañon et al (1998) to mineral assemblages lying within the main foliation (S2). From this study they deduced that conditions during the formation of the main foliation in sillimanite-bearing schist from the central Betics varied from 13 kbar to 5 kbar at an approximately constant temperature of $\sim 580^\circ\text{C}$.

1.3.3 Sub-divisions within the Alpujarride Complex

A total of five major allochthonous tectonic units (ATUs) were defined by Azañon *et al* (1994) in the central and eastern sectors of the Betic Cordillera (**figure 1.5**). Classification of these units was based largely on the sub-divisions established by Aldaya *et al* (1979) but also incorporated additional metamorphic and structural data, including the crucial reinterpretation of thrust boundaries throughout the Internal Zones as extensional contacts (e.g. Platt & Vissers, 1989). The allochthonous units of Azañon *et al* (1994) are distinguished from one another on the basis of the relict high-pressure assemblages. Rocks in which high-pressure metamorphic assemblages are preserved are assigned to units that are considered to have originated from structurally lower in the initial metamorphic stack than rocks that do not contain relict high-pressure mineral assemblages (Azañon *et al*, 1994). From their study of relict high pressure mineral assemblages and the present-day distribution of the ATUs, Azañon *et al* (1994) suggest that units which exhibit the highest pressure assemblages currently occupy the structurally highest positions in the Alpujarride Complex (see **figure 1.4**).

The conclusions of Azañon *et al* (1994) imply that the allochthonous tectonic units in the Alpujarride Complex must have undergone significant re-organisation since the original high-pressure event. Azañon *et al* (1994), Balanya *et al* (1997) and Azañon & Crespo-Blanc (2000) invoke a post-metamorphic episode of compression in the lower Miocene (Aquitainian), to 'reshuffle' the ATUs into their present-day configuration. Km-scale north-vergent folds and associated north-directed thrusts were generated during this event. Azañon & Crespo-Blanc (2000) present a simplified map which summarizes the location and relationships of the sub-divided units within the Alpujarride of the central Betics, and the rock-types and mineralogy present in each Unit. (**Figure 1.6**). According to this classification, the rocks in the area studied for this thesis lie mainly within the structurally highest (that is, highest pressure and temperature) ATUs, including the Salobreña,

Guajares, Herradura and Adra Units, among others.

Timing of the compression event proposed by Azañon *et al* (1994), Balanya *et al* (1997) and Azañon & Crespo-Blanc (2000) is constrained by this latter set of workers to have occurred during the earliest Miocene (Aquitanian). This implies that this compressive episode occurred after the period of extension during which the main fabric in the Alpujarride Complex was generated (section 1.3.2) and just prior to the extensional opening of the Alboran Sea in the lower Miocene (Platt *et al*, 1996). During the period of extension in the lower Miocene, the thrust contacts generated during the Aquitanian compression were ubiquitously reactivated, destroying the sense of shear indicators of the thrusts (Garcia-Dueñas *et al*, 1988; Crespo-Blanc *et al*, 1994; Balanya *et al*, 1997; Azañon & Crespo-Blanc, 2000).

In his discussion of Balanya *et al*'s (1997) work, Platt (1998) challenges a number of the major assumptions which underpin the concept of dividing the Alpujarride Complex into Allochthonous Tectonic Units (Azañon *et al*, 1994). Platt (1998) indicates that the early high-pressure history of the Alpujarride Units is likely to have been strongly modified by the subsequent high-temperature history (Balanya *et al* 1997; Soto & Platt, 1999). During this period, extensive textural and chemical disequilibrium features were produced (Garcia-Casco & Torres-Roldan, 1996; Garcia-Casco *et al*, 1993). If it is accepted that the high pressure assemblages within the Alpujarride Complex in the central Betics may have been modified during the high-temperature part of their metamorphic history, then the use of the high-pressure assemblages to predict the structural superposition of the ATUs prior to the Aquitanian episode of compression (Balanya *et al*, 1997; Azañon & Crespo-Blanc, 2000) is evidently unsatisfactory. Platt (1998) also notes that the propensity of an individual nappe-sheet to be characterised by a narrow range of pressure conditions has not been reported in other orogenic settings (Heinrich, 1986). The assumption that the pre-Aquitanian structural positions of ATUs within the Alpujarride Complex of the central Betics may be reconstructed from their palaeo high-pressure assemblages forms the cornerstone of the 'structural correlation' achieved by Azañon *et al* (1994) between exposures of dismembered ATUs in the central Betics.

Results from thermobarometry and geochronology on rocks from the Alpujarride Complex do not support an increase in pressure during the early Miocene history of the Internal Zones (e.g. Monie *et al*, 1991, 1994; Soto & Platt, 1999; Platt *et al*, 1998). Evidence from geochronology indicates that exhumation of a thickened crustal section began around 27 Ma and proceeded rapidly (Platt & Whitehouse, 1999). Exhumation rates in the 19-18 Ma interval have been estimated as ranging from 1 - 3 km/Ma in the western Betics (Sossou *et*

al, 1998).

1.3.4 Ductile structures in the Alpujarride Complex of the Central Betics

Various studies of the Alpujarride Complex in the central Betics have described a phase of km-scale folding that cause inversion of the metamorphic sequence and the configuration of rocks existing prior to this deformation (e.g. Simancas & Campos, 1993; Orozco *et al*, 1998; Azañon & Crespo-Blanc, 2000). Disparities exist between the works of various authors in the descriptions of these folds, and in the consideration of their regional importance. For example, Simancas & Campos (1993) infer that 'late metamorphic' km-scale folds verge to the NNW and locally invert extensive tracts of rock in the area around Almuñecar (**figure 1.7**). In a similar structural / metamorphic study in the same area, Azañon & Crespo-Blanc (2000) conclude that folds equivalent to the 'late metamorphic' folds of Simancas & Campos (1993) create only 'infrequent' inversions of the metamorphic sequence and the pre-existing lithology. Using different nomenclatures, both studies describe a crenulation fabric, axial planar to the km-scale folds, that cross cuts the main (syn-metamorphic) foliation in the area.

Both Simancas & Campos (1993) and Azañon & Crespo-Blanc (2000) attribute the generation of the km-scale folding to an episode of contraction in the late stage of the metamorphic evolution of the Alpujarride Complex, during which the formation of N/NNW directed thrust faults accompanied the large-scale folding.

Folds with a similar orientation and amplitude as the D3 structures of Azañon & Crespo-Blanc (2000) and the 'late metamorphic' folds of Simancas & Campos (1993) have been described in the eastern Betics, near to Adra, by Orozco *et al* (1998). In a sequence of phyllites and carbonates metamorphosed at low-grade, the axial traces of km-scale, north-facing recumbent folds are traced for over 50 km. The hinges of the north-facing folds are demonstrated to be closely associated with north-dipping normal faults (Orozco *et al*, 1998). Mineralogical techniques such as illite crystallinity and the measurement of the basal spacing of phengite, paragonite and chlorite are used to identify the variations of metamorphic grade. The polarity of the metamorphic sequence, and original stratigraphic contacts are inverted in the overturned limbs of the km-scale folds (**figure 1.8**). Orozco *et al* (1998) conclude that the association of north-closing fold hinges with north-dipping normal faults is strongly suggestive that these large-scale folds formed in an extensional regime. Folds in the Austro-Alpine nappes of the Alps are considered by Froitzheim (1992) to have formed from the ductile folding of initially non-horizontal layers during orogen-parallel crustal extension, as a result of gravitational spreading.

1.3.5 Late metamorphic extension in the Alpujarride Complex

Normal faults affecting the Alpujarride Complex in the central and western Betics have been classified into two brittle, sub-perpendicular, extensional fault systems that developed sequentially during the Miocene (Garcia-Dueñas *et al*, 1988; Crespo-Blanc *et al*, 1994; Azañon *et al*, 1997, 1998). The Contraviesa fault system shows hanging-wall movement to the N-NW and was active during the upper Burdigalian and Langhian (Crespo-Blanc, 1995). In the Sierra de Baza region, N of Sierra Nevada, a set of normal faults showing movement to the S-SE are considered to be antithetic to the Contraviesa faults. The Filabres fault system shows hanging wall movement to the W-SW and relationships with Middle Miocene deposits in the Sierra de Baza show that the Filabres fault system was active after the upper Langhian (Martin-Perez & Viseras, 1994). Each of these fault systems have accommodated significant amounts of extension: Beta factors of 1.5 and 1.4 are estimated for the Contraviesa and Filabres systems, respectively (Crespo-Blanc *et al*, 1994).

1.3.6 Disequilibrium textures in the Alpujarride Complex

Disequilibrium textures are almost ubiquitous in rocks from the Alpujarride Complex, some of the most prominent textures in rocks from the central Betics having been described by Garcia-Casco *et al* (1993) and Garcia-Casco & Torres-Roldan (1996). The three aluminium silicate minerals, kyanite, sillimanite and andalusite commonly coexist in rocks of the Alpujarride Complex in the central Betics (Garcia-Casco & Torres-Roldan 1993), although textures clearly indicate disequilibrium between the phases. Chemical disequilibrium between mineral phases in a single sample is widespread, including examples of abnormal Fe-Mg partitioning between biotite, staurolite and garnet and wide heterogeneities in the composition of phases within a single sample (Garcia-Casco & Torres-Roldan, 1996). It is apparent that caution must be exercised in selecting mineral pairs from rocks in the Alpujarride Complex for use in thermo-barometric work.

1.3.7 Constraining the Alpujarride P-T-t path: thermobarometry and geochronology

Samples collected from the Ocean Drilling Program Site 976 in the Alboran basin (see **figure 1.1**) have been assigned to the Alpujarride Complex (Platt *et al*, 1996). A study of the petrology and geochronology of these samples has been carried out by Platt *et al* (1998) in which the P-T history of high-grade pelitic schist sample is traced along a path of decompression from 10.5 to 4 kbar, during heating from 500°C to 650°C. These rocks then

experienced cooling through 500°C at 2 kbar or less: peak temperature of the assemblages occurred under low pressure conditions (**figure 1.9**). Rapid decompression is indicated by the prolific occurrence of disequilibrium textures and overstepped metamorphic reactions (Soto & Platt, 1999).

Other combined geochronology and pressure-temperature studies in the Alpujarride Complex provide confirmatory evidence that rapid exhumation occurred during the early Miocene and indicates that this exhumation proceeded as a consequence of extensional faulting (Monie *et al*, 1994; Platt & Whitehouse, 1999; Sosson *et al*, 1998).

1.4 Late stage evolution of the Betic Cordillera

The sedimentary record in the Alboran Basin indicates that the basin was submerged from Aquitanian-Burdigalian times: the early part of the tectonic history in the Alboran Basin is dominated by extension (**figure 1.10**). Normal faults with a top-to-the-south-west direction dominated the Miocene rifting episode, and an unconformity in the late Miocene indicates the end of rifting. Volcanic activity in the east of the Betic and Rif chains, including the eruption of lamproitic lavas and alkaline basalts, occurred from Langhian times onwards, and so was partly contemporaneous with the extensional evolution of the Alboran Basin (Di Battistini *et al*, 1987).

The later tectonic history of the Alboran Basin is dominated by structures that are indicative of a contractional regime (**figure 1.10**). During the late Tortonian, compression was directed northwest-southeast, subsequently changing to north-south from the late Tortonian to the middle Pliocene and then directed along a north-northwest to south-southeast axis later in the Pliocene and in the Pleistocene (Montenat *et al*, 1987; De Larouziere *et al*, 1988). During this period of compression, open-style east-west trending antiforms and synforms, including the east-west anticlinal component of the Sierra Nevada - Sierra de los Filabres tectonic window, were generated (Martinez-Martinez & Azañon, 1997; Sanz de Galdeano & Vera, 1992; Comas *et al*, 1992). Wrench faulting has been active in the Alboran Basin since the early Pliocene (Comas *et al*, 1999). Strike-slip faults, including the Palomares and Carboneras strike-slip shear zones that crop out on the Iberian peninsula, were generated as a consequence of a transtensive and transpressive regime that is still active in the western Alboran Basin (Comas *et al*, 1999). Conjugate fault systems that trend approximately northeast - southwest and west-northwest - east-southeast, generate the distributed seismic activity recorded in this region (Calvert *et al*, 2000).

1.5 Competing hypotheses for the cause of extension

The processes that have contributed to the evolution of the Betic-Rif arc have been debated in various recent papers (e.g. Lonergan & White, 1997; Platt *et al*, 1998; Martinez-Martinez & Azañon, 1997). Recent seismic studies suggest the presence of up-welled asthenosphere (Seber *et al*, 1996) and isolated bodies of lithospheric mantle in the region (Calvert *et al*, 2000; Blanco & Spakman, 1993).

Various mechanisms which may cause a body of lithospheric material to become separated from the base of the lithosphere have been suggested. Proposed mechanisms include removal of the lithospheric mantle by convection, (Platt & Vissers, 1989), slab detachment / de-lamination (de Jong, 1991; Zeck *et al*, 1992) and a combination of these two processes acting together (Seber *et al*, 1996). Lonergan & White (1997) suggest that the Neogene evolution of the Betic-Rif area is the consequence of a westward-retreating subduction zone that generated rapidly extended continental crust as a consequence of its retreat.

The feasibility of geodynamic models proposed to explain the evolution of the Betic-Rif arc have been explored using the results from thermobarometry, geochronology and studies of mineral phase relations. Each model of the lithospheric response to the Africa-Iberian collision will produce a characteristic pattern of thermal evolution in the overlying crustal rocks. Platt *et al* (1998) produced thermal models of different tectonic scenarios by altering the values of variable parameters including thickness and thermal gradient of post-orogenic lithosphere; depth to which lithospheric mantle was removed and rate of extension. Results that produce pressure-temperature conditions comparable to those evidenced by metamorphic assemblages in rocks from the ODP Site 976 are achieved when parameters defining a significant post-contractional pause, prior to removal of the lithosphere to a depth of 62.5 km, are defined. Delayed onset of lithosphere removal is predicted by numerical models of the behaviour of a conductive thermal boundary layer developed in a fluid with a non-linear viscous behaviour (Molnar *et al*, 1998).

The evolution of mineral assemblages deduced from petrological studies of rocks taken from the Alboran Sea core (Site 976) forms the basis of a study by Soto & Platt (1999). These workers concluded that viable models of crustal evolution need to provide an external source of heat (aside from that produced from radiogenic heat production) in order to generate P-T paths similar to those suggested by the petrology of these rocks. This constraint appears to challenge models involving trench rollback in the absence of lithosphere removal, (e.g. Lonergan & White, 1997) as these models do not permit a sufficient amount of heat to pass into the crust. Models in which post-collisional

radiogenic heating was followed by the removal of the lithospheric mantle below the orogen and rapid extension appear to most closely emulate the P-T paths recorded in the rocks (Soto & Platt, 1999).

Turner *et al* (1999) present a study of the geochronology and isotopic signatures of magmatic rocks within the Betic Cordillera (section 1.1.2). The feasibility of competing hypotheses recently proposed to account for the evolution of the Betic Cordillera are tested according to whether they predict the geochemical signatures and geometrical distribution of magmatic rocks discussed in this work. Models that suggest the orogen developed as the consequence of a retreating subduction zone, detached slab of lithospheric mantle or delamination of the lithospheric mantle are discounted; these mechanisms would be expected to generate a progressive, systematically migrating sequence of volcanism, not concordant with the pattern seen in the Betics (Turner *et al*, 1999; **figure 1.3**). Turner *et al* (1999) propose that a model involving convective removal of the lithosphere most readily explains the diffuse spatial distribution and temporal migration of activity directed outwards from the Alboran Sea.

1.6 Aims of the project

As discussed in sections 1.3 – 1.5 above, numerous models have been suggested to explain the present-day configuration of the Betic Cordillera: it is evident from the preceding discussions that ambiguities as to the evolution of the orogen remain.

In the broadest sense, the principal aim of this research is to provide a new set of structural and metamorphic data, collected from the Alpujarride Complex from within the Internal Zone of the orogen, in order to investigate the nature of the deformation that accompanied the decompression and exhumation of the Complex and to explore the relationship between the deformational history and the thermal evolution experienced by the rocks. From this data, it is the intention that the hypothesis that exhumation was followed by large-scale thrusting and regional nappe-formation (i.e. Balanya *et al*, 1997) may be able to be tested. To achieve this, the zone around the towns of Almunecar, Salobrena and LosGuajares has been elected for the following reasons:

- 1 Within this area, it has been recorded by previous workers that high grade metamorphic rocks (e.g. sillimanite and kyanite bearing assemblages) located predominately near to the coast pass structurally upwards into chlorite-bearing assemblages over a horizontal distance of approximately 8 km. As the dip of the main foliation in this area is recorded as being gently dipping, this indicates that the

transition from high grade to low grade rocks in this zone occurs through a reduced vertical thickness of crust. A study of this area will enable the macro-scale structural configuration of the area to be determined, and analysis of the microstructures and metamorphic mineral assemblages present in these rocks should permit the structural and metamorphic history of the rocks to be elucidated.

- 2 In the north of the area (see figure 1.6), near to the town of Los Guajares, exposures of rocks that have experienced high temperatures crop out immediately adjacent to rocks of considerably lower grade (IGME map of Motril (1972); Azanon *et al*, 1994). One common interpretation of the structure in the existing literature is that the juxtaposition of grades in this area is the consequence of a thrust, which places the higher grade rocks structurally above the low grade rocks (Azanon *et al*, 1994; Simancas & Campos, 1989). This area provides a useful 'testing ground', then, for the hypothesis that the Internal Zones of the Betic Cordillera have experienced alternating periods of extension and compression during their evolution (i.e. Balanya *et al*, 1997) or whether they have experienced continual extension (i.e. Argles *et al*, 1999).
- 3 Numerous well-exposed north-south trending transects through this area, predominately within road-cuttings, provide a source of relatively fresh samples for analysis of metamorphic minerals and microstructure, and the possibility that structural trends will be able to be traced through the area, and perhaps correlated between adjacent sections. It is intended that these sources of information will be synthesised in order to generate a model that improves the understanding of the metamorphic and structural evolution of the rocks in this area.

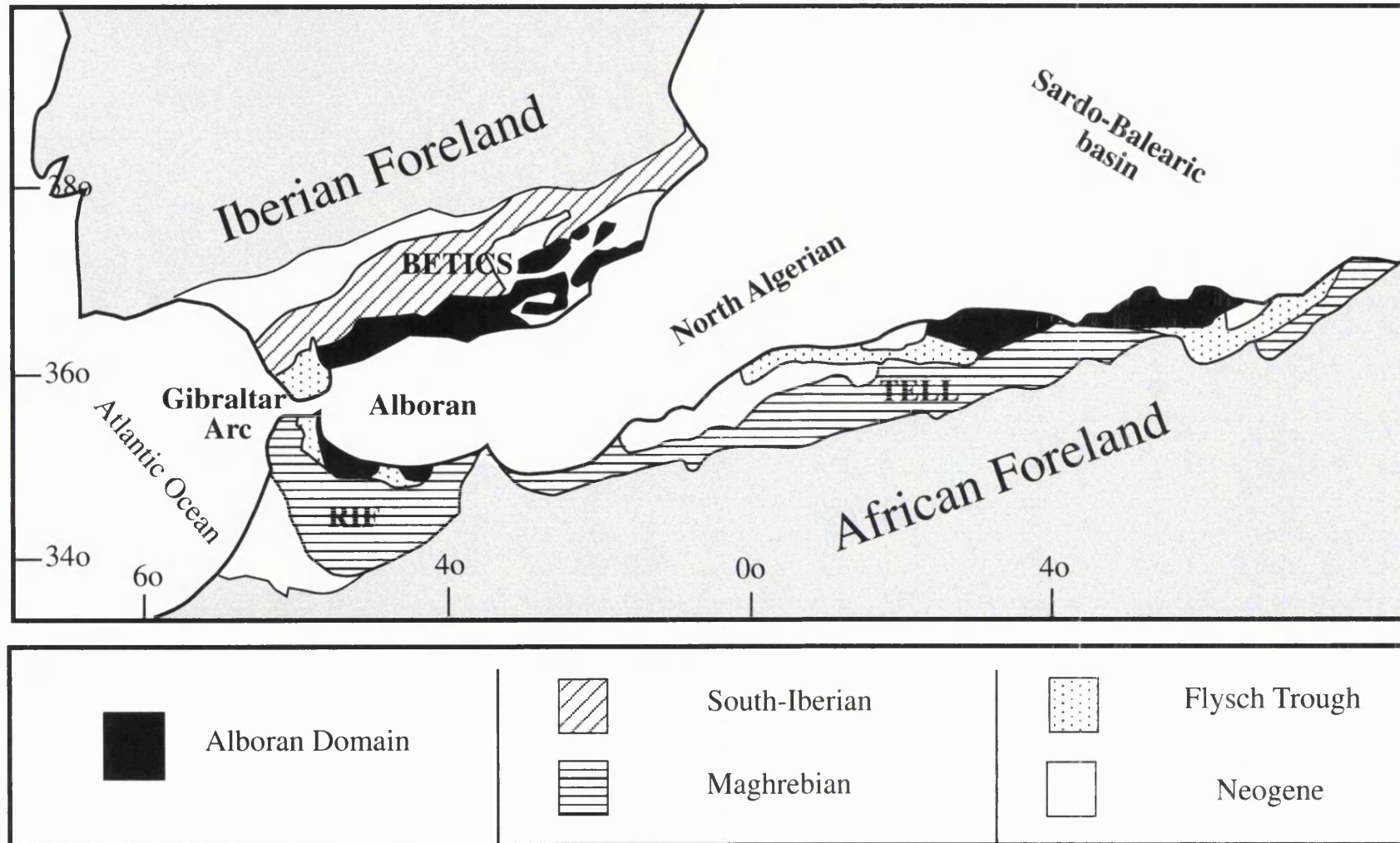


Figure 1.1 Sketch map of the Betic-Rif arc. The locations of the major tectonic domains are marked on an outline of the Iberian and N African present-day margins; the definitions of these domains are those in common use for the Betic Cordillera (i.e. Egler & Simon, 1969).

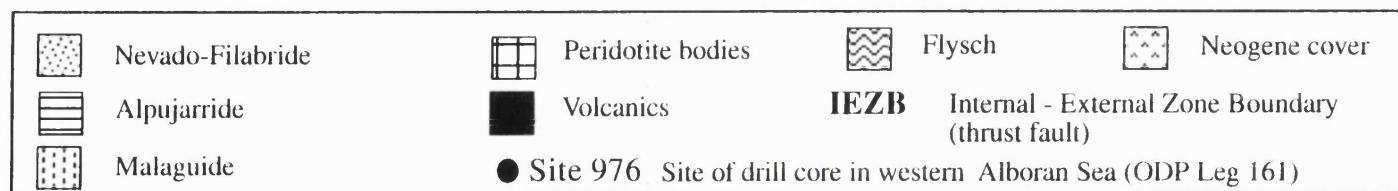
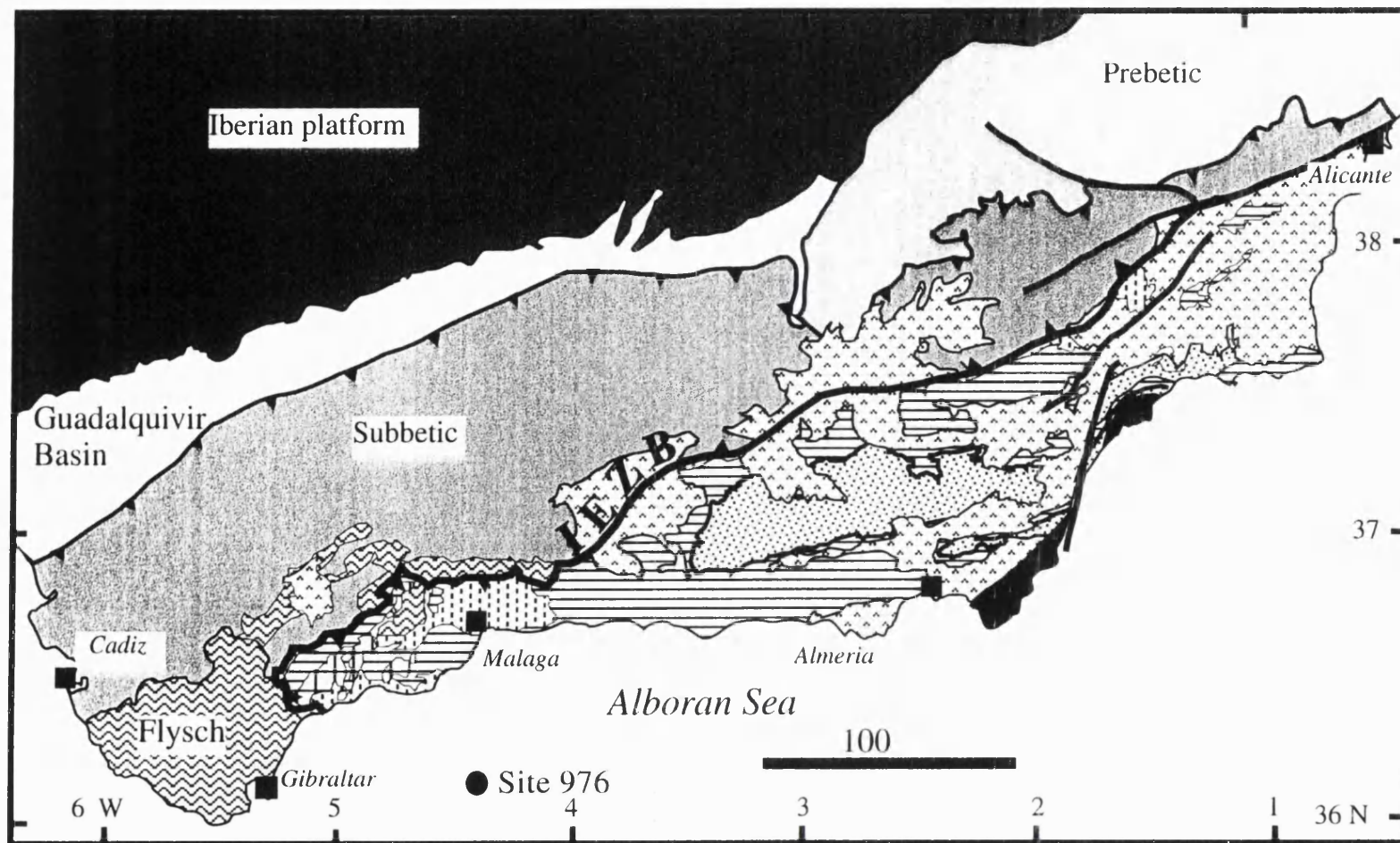


Figure 1.2 Detailed map of the Betic Cordillera, showing the distribution of Internal Zone components and other important features in the orogen.

Figure 1.3a

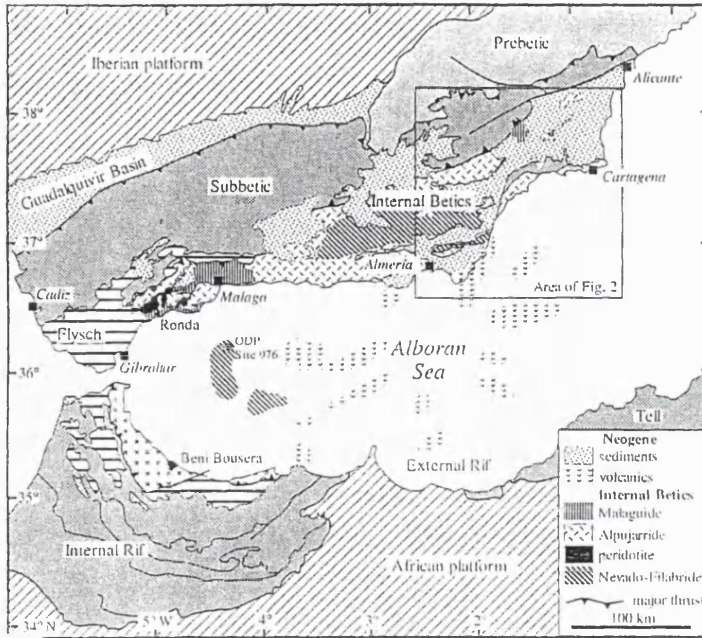


Figure 1.3a Sketch map of the Betic Cordillera showing the location of inset map, seen in figure 1.3b.

From Turner et al (1999).

Figure 1.3b

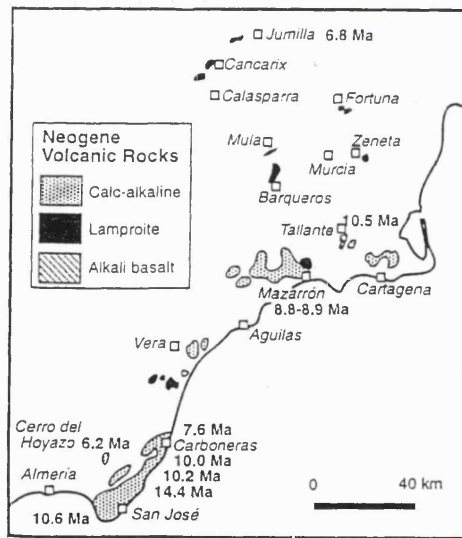


Figure 1.3b Map showing the locations and $^{40}\text{Ar}/^{39}\text{Ar}$ ages for Neogene calc-alkaline and lamproitic magmatic rocks in SE Spain. Lamproites and calc-alkaline volcanics also crop out beneath the Alboran Sea.

Taken from Turner et al (1999).

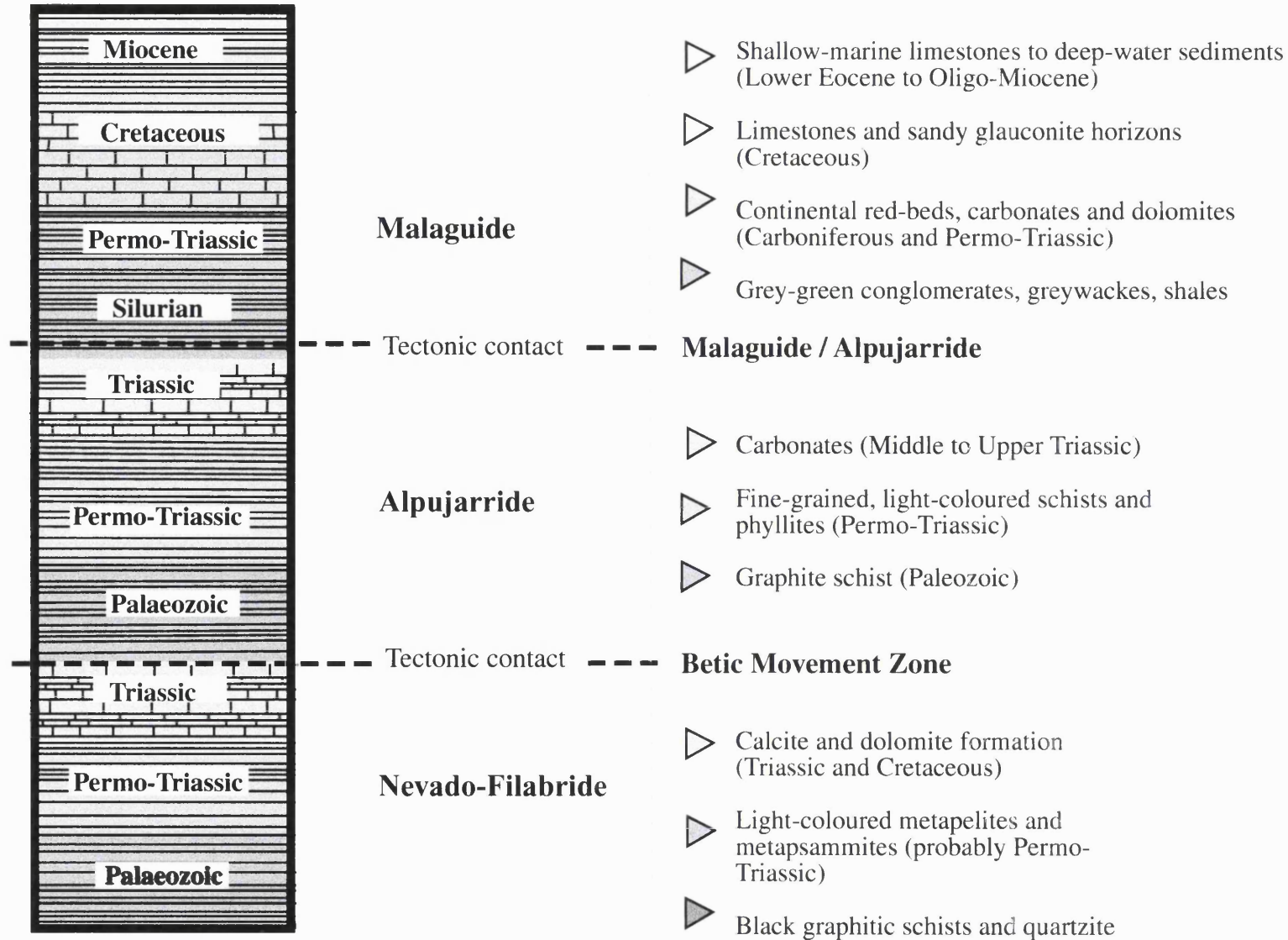


Figure 1.4

Summary of the lithologies within the three Complexes in the Internal Zone of the Betic Cordillera. Detailed stratigraphic data from Martinez-Martinez & Azanon (1997), Lonergan & Mange-Rajetzky (1994) and references therein.

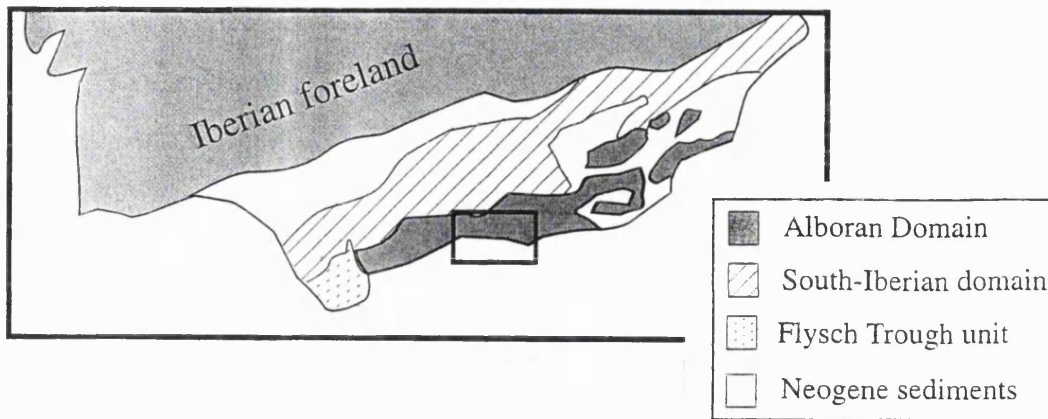


Figure 1.5a Sketch map of the Betic Cordillera to show the location of figure 1.5b.

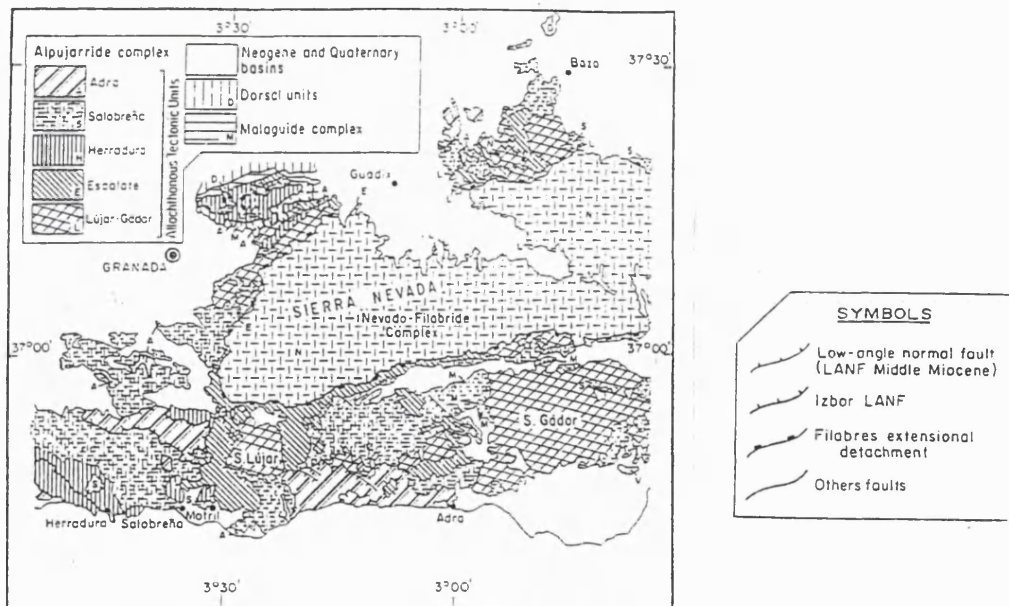


Table HP-LT metamorphic record of the central Betics Alpujarride units (Permo-Triassic rocks), according to Goffé *et al.* (1991), Azañón *et al.*, 1992 and unpublished data of one of the authors (JMA).
 Registre métamorphique des unités Alpujarrides des Betiques centrales (roches permo-triassiques), selon Goffé *et al.* (1991), Azañón *et al.* (1992) et les données non publiées de l'un des auteurs (JMA).

Present Position	Allochthonous Tectonic Units	Mineral Assemblages	HP-LT conditions (kb) (°C)
Top	Adra ATU	Ctd+Ky+Ca (pseudom.)	p > 10, T < 550
	Salobreña ATU	Car+Ctd-Ky	P > 10, T < 500
	Herradura ATU	Gar+Px+Ky	P > 10, T > 550
	Escalate ATU	Car+Ctd+Ar	P > 7, T < 450
Bottom	Luján-Gádar ATU	No carpholite	P < 7, T < 450

Ar: Aragonite; Car: Carpholite; Ctd: Chloritoid; Gar: Garnet; Ky: Kyanite; Px: Pyroxene.

Figure 1.5b Map from Azañón *et al.* (1994) showing the major allochthonous units (ATUs) defined in this work.

Figure 1.6a

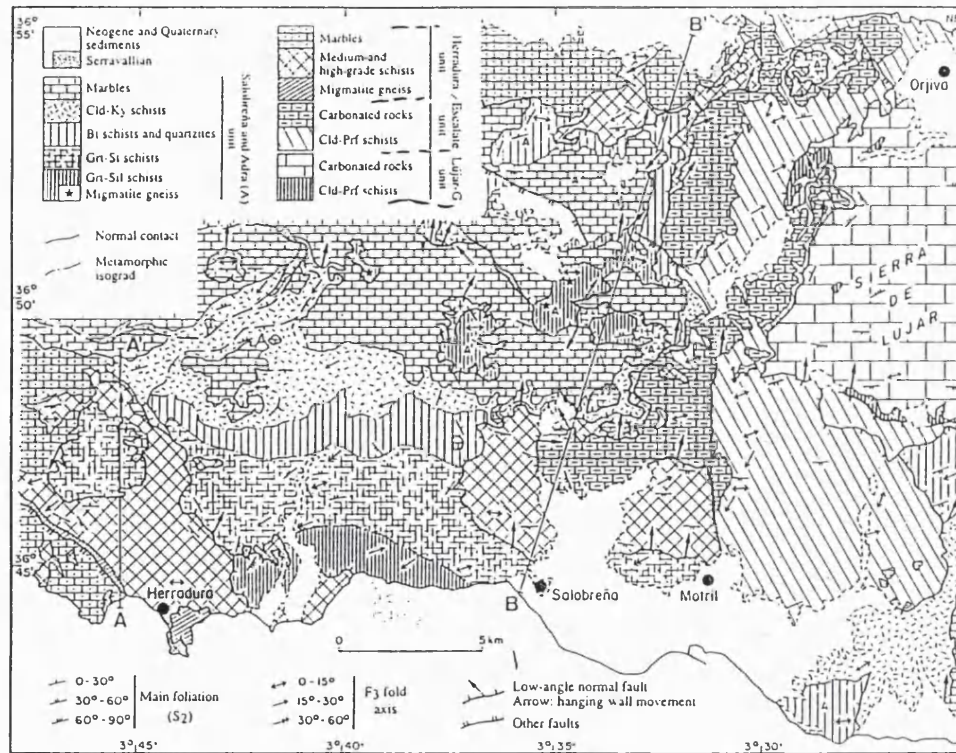


Figure 1.6a

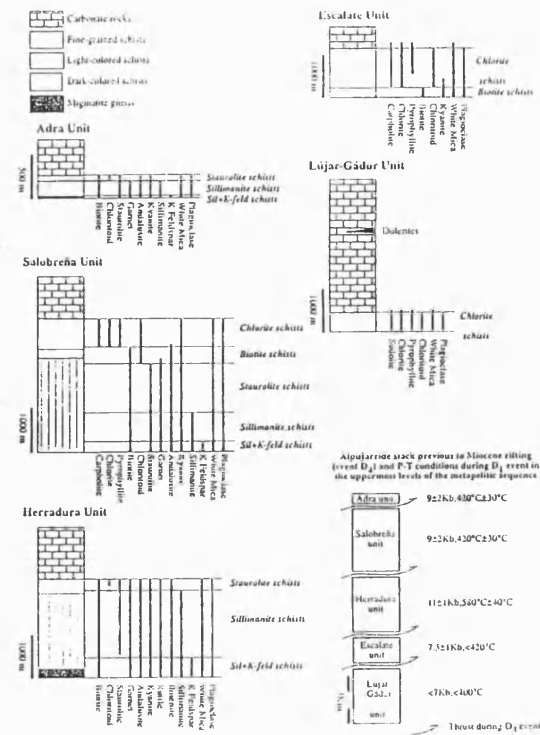
Geological map of the Alpujarride Complex, south-south-west of Sierra Nevada, taken from *Azañon & Crespo-Blanc (2000)*; see references within. Each arrow of F3 fold axes represents average of 3 readings. Each arrow on the hanging-wall movement of a normal fault represents average of 5 readings.

Figure 1.6b

Lithological sequence, metamorphic mineral assemblages and mineral zones of the Alpujarride Units that are shown in figure 1.5a. The thicknesses are calculated perpendicular to the S2 main foliation and represent the maximum value observed in the field. Some Units are strongly thinned by normal faults.

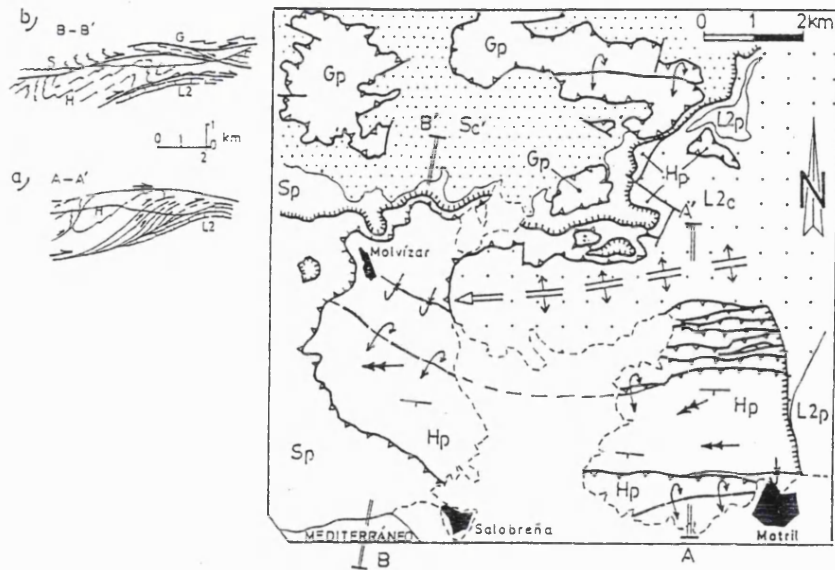
From *Azañon & Crespo-Blanc (2000)*

Figure 1.6b



Alpujarride stack prevails to D1 and P-T conditions during D1 event in the uppermost levels of the metamorphic sequence.

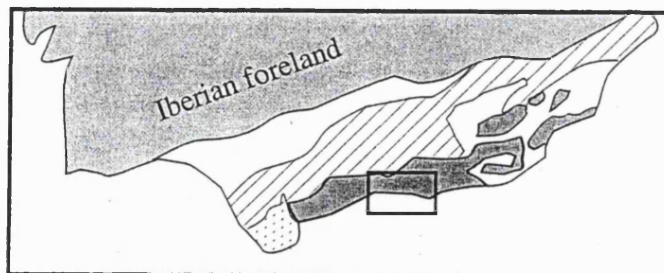
Unit	Metamorphic Conditions
Escalate unit	7.5:1Kb, <420°C
Lujar Gájar unit	<7Kb, <400°C
Salobreña unit	9.2:2Kb, 430°C±30°C
Adra unit	9.2:2Kb, 430°C±30°C



Key to symbols

G_c G_p	Guajares Unit		Low angle normal fault
$L2c$ $L2p$	Intermediate Lujar Unit		Thrust fault
H_c H_p	Herradura Unit		Axial trace
S_c S_p	Salobreña Unit		Late-formed antiform
			Recent sediment cover

	Alboran Domain
	South-Iberian domain
	Flysch Trough unit



Location of map in Figure 1.7

Figure 1.7

Structure in the area to the north of Salobreña and Motril (based on the map by Avidad & Garcia-Dueñas, 1981, with modification).

From *Simancas & Campos, (1993)*.

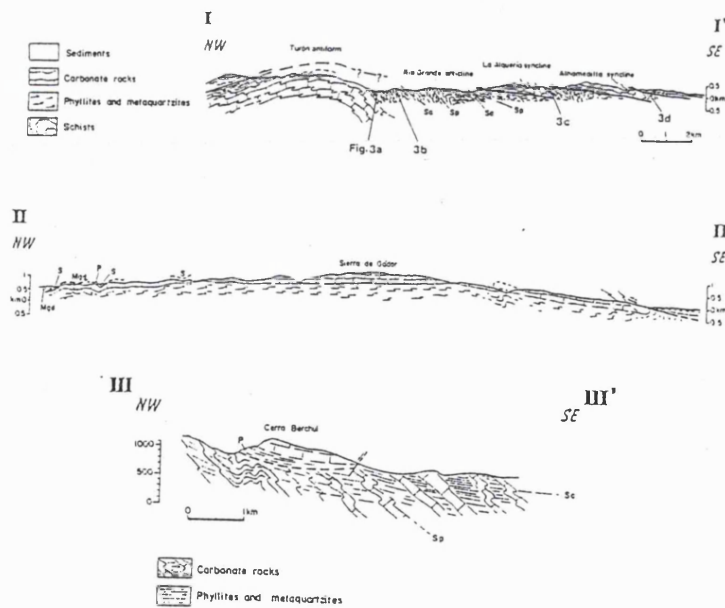
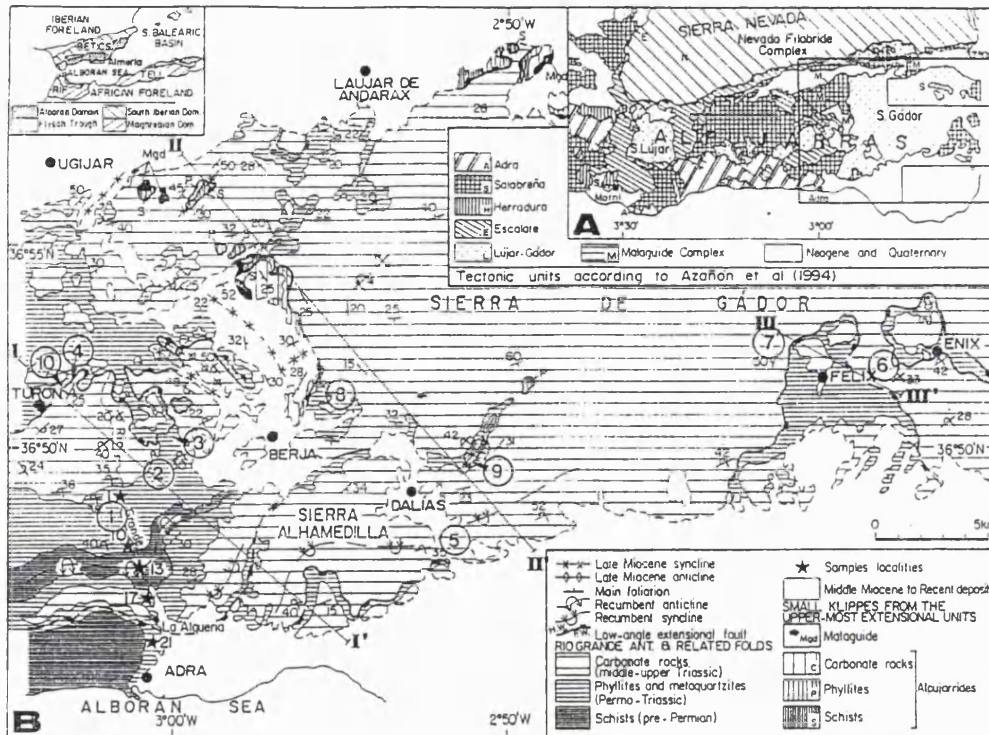


Figure 1.8

Detailed tectonic map of the eastern Alpujarras, showing axial traces of main recumbent folds and low-angle normal faults. Cross-section locations marked. Cross sections shown above, to which the following abbreviations apply:
 Sp = principal metamorphic foliation.
 Sc = axial plane crenulation cleavage

Taken from *Orozco et al (1998)*.

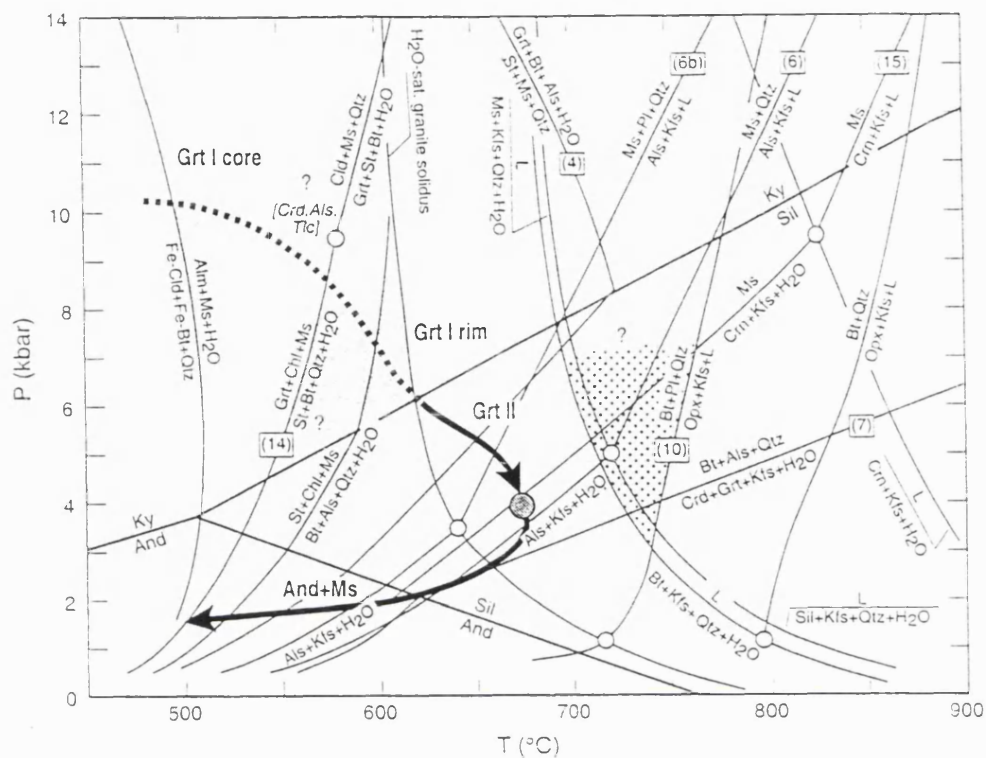


Figure 1.9

P-T path for the high-grade schist of the Alboran Basin basement and approximate melting conditions in the gneiss (stippled area). The cooling P-T path shown is constrained by thermometric data and mineral reactions. The stability fields for the different assemblages discussed in the text are shown in shaded areas: the extent of these fields is constrained by thermobarometric estimates, phase relations and textural considerations.

From *Soto & Platt (1999)*.

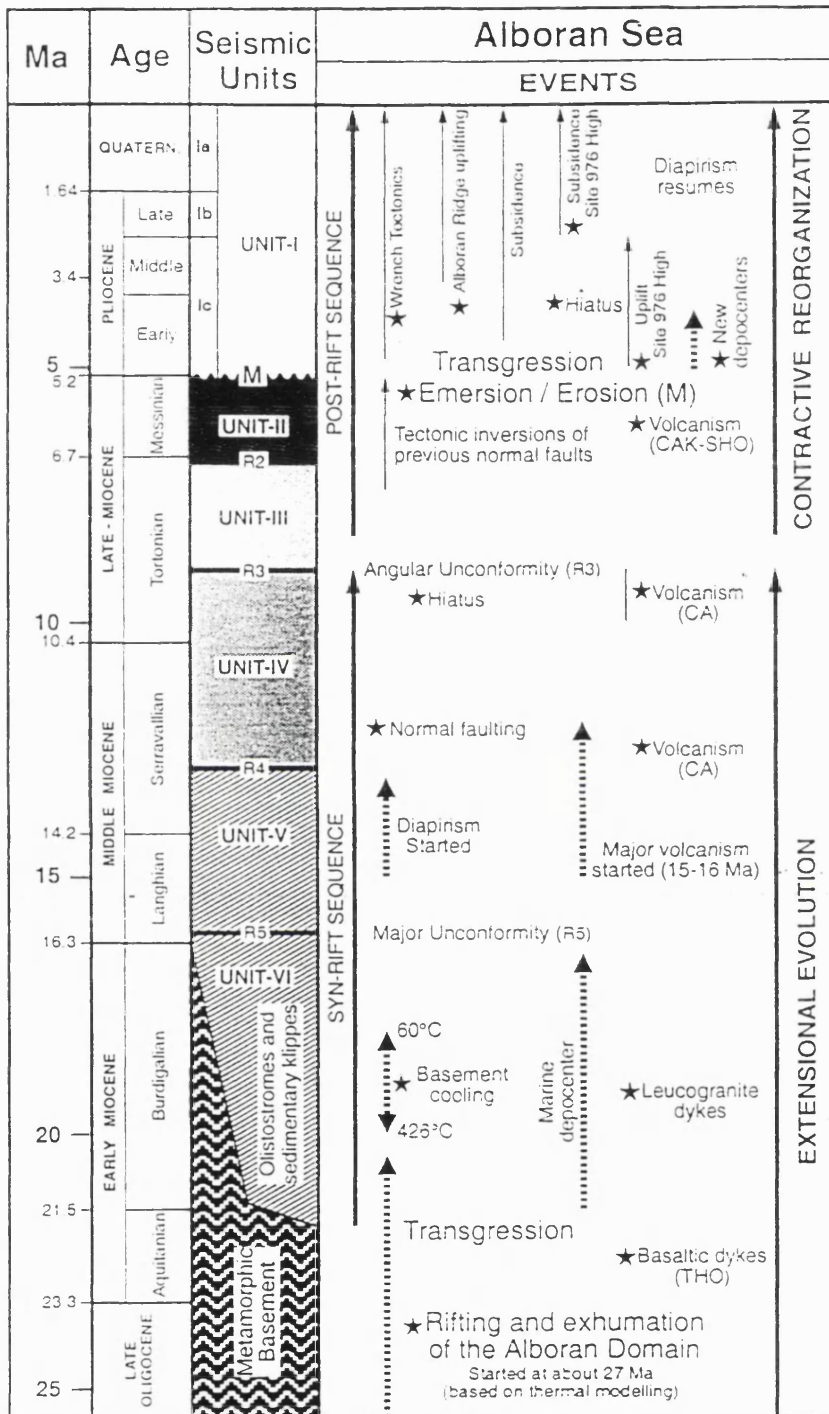


Figure 1.10

Timing of the main events in the tectonic evolution of the Alboran Basin, as constrained by Leg 161 results (marked with stars) and from other sources.

Taken from *Comas et al (1999)*.

CHAPTER 2 INTRODUCTION TO PETROLOGY AND STRUCTURE

2.1 Introduction

The location of the field area is shown in **figure 2.1**.

Prior to the presentation of structural and micro-structural data (Chapters 3 and 4), it is necessary to introduce the rock-types present in the specific area studied, and to provide a broad outline of the metamorphic assemblages in these rocks. This information is presented in the following sections. The UTM co-ordinate grid is used throughout the work.

2.2 Deformation events and related fabrics

2.2.1 Introduction

Rocks within the Alpujarride Complex in the central Betics show evidence of a complex metamorphic and structural history. Evidence of both ductile and brittle deformation is seen and the superposition of fabrics allows the structural development of the rocks to be reconstructed. Two ductile deformation events, which both generated fabrics of regional extent, are used as a 'framework' in which the timing of the brittle structures, of lesser regional extent, are discussed.

2.2.2 Nomenclature of ductile deformation events

Schist and quartzite within this area commonly contain two principal foliations; linear fabrics including fold axes, stretching lineations and intersection lineations are also present. The two foliation surfaces identified in the rocks were produced in two consecutive phases of deformation (abbreviated to 'D'). Sub-scripts of 's' and 't' have been used to distinguish between foliation planes (denoted by 'S'), fold axes (F) or lineations (L) formed during either the first (D_s) or second (D_t) phases of deformation.

The oldest structural fabrics seen at outcrop in the schist and quartzite rocks have been assigned to the D_s ' deformation event. 's' was nominally chosen in preference to 'a', or a

numerical system, to avoid giving the erroneous impression that this fabric represents the first deformation which has affected these rocks, or that the earlier history of these rocks is clearly established. It is likely that sediments of Devonian age and older would have been affected by the Variscan orogeny (Matte, 1991). In thin section, the S_s foliation is seen to be a crenulation cleavage where the S_t foliation is not pervasively developed. A fabric that predates S_s is preserved in some porphyroblast phases (**figure 2.2**). These lines of evidence strongly imply the existence of at least an S_r foliation.

The D_s deformation event occurred during metamorphism and produced isoclinal folds; these folds have an axial planar cleavage that lies parallel to the schist-quartzite layers in the graphitic and non-graphitic schist sequences. Transitional metamorphic grade boundaries are sub-parallel to the S_s foliation. During D_t , that occurred after the main phase of metamorphism but within the ductile regime, km-scale folds deformed the S_s foliation. The axial planar cleavage to these folds (S_t) overprints the S_s foliation (**figure 2.3**).

2.2.3 Three dimensional description of the ductile fabrics

Rocks within the Alpujarride Complex have experienced high values of strain; this is evident from the microstructures that are observed within these rocks, in particular from the pervasive development of a stretching lineation (see Chapter 3). Structures that indicate the operation of ductile and brittle deformation are evidenced; fold axes of ductile structures are dominantly observed to be oriented approximately parallel to the lineations in the rocks.

Depending upon the orientation in which thin sections of rock are cut, different structures will be observed, and different information will be able to be obtained. In sections cut parallel to the stretching lineation and fold axes – XZ sections - fabrics with monoclinic symmetry will typically be observed (**figure 2.4**). These microstructures are able to provide useful information about the direction of shear that has affected the rock; examples include asymmetric pressure shadows of quartz around garnet porphyroblasts, and ‘mica fish’ features. Thin sections cut in an orientation 90° to the lineation / fold axis orientation typically reveal microstructures that have an orthorhombic symmetry, with the exception of samples from locations at which there is a discrepancy between the orientation of fold axes and mineral stretching lineations in which some monoclinic features are observed. In the majority of sections cut at 90° to the lineation / fold axis orientation (YZ sections) a profile

view of the folding developed during D_s and D_t is seen, and from the relationships between the microstructure and the foliation traces it is possible to determine the temporal relationships of the minerals to the two generations of ductile deformation (Chapter 4).

2.3 Rock-types

2.3.1 Introduction

Four distinct rock types are identified within the Alpujarride Complex where it is exposed in the central Betics. These are: (1) graphitic schist and quartzite; (2) non-graphitic schist and quartzite; (3) phyllite and quartzite and (4) carbonate rocks. The distribution of these rock types in the area around Almuñecar and Motril is shown in **figure 2.5**; the basis of classification of contacts as either 'stratigraphic' or 'tectonic' is discussed in section 2.5.

2.3.2 Graphitic schist and quartzite sequence

Graphitic schists and quartzites in the Alpujarride Complex are estimated to be Paleozoic in age (Martinez-Martinez & Azanon, 1997). In the area around Almuñecar, this sequence is well exposed, and the metamorphic grade varies from kyanite-sillimanite grade to muscovite-chlorite (section 2.4). Quartzite bands range in thickness from 1cm to 15cm; schist commonly constitutes over 60% of an outcrop by volume.

Foliation planes and folds, generated by regional deformation events are readily developed in the graphitic quartzite and schist sequence, because of the high proportion of schist and the relatively thin bands of intercalated quartzite. Graphitic schist and quartzite outcrops near to Motril clearly show that the S_t foliation plane, generated during the D_t deformation event (section 2.2) is more pervasively developed in the schistose layers than in bands of quartzite (**figure 2.6**). Garnet and biotite appear to be more prolific in the graphitic schists and quartzites than in non-graphitic schists and quartzites of equivalent grade. This may be a result of the graphitic schist and quartzite sequence having a bulk composition that is more enriched in Fe^{2+} and / or Ca^{2+} than the non-graphitic sequence. The red/orange weathering product of this schist sequence indicates that they do indeed contain a significant proportion

of iron; the quartzite layers in the graphitic schist and quartzite layers are characteristically stained orange.

2.3.3 Non-graphitic schist and quartzite sequence

Rocks belonging to this sequence are also deemed to be of Palaeozoic age; it is proposed that the sedimentary protolith of these rocks was deposited on top of the sediments that now comprise the graphitic schist and quartzite sequence (Martinez-Martinez & Azañon, 1997). This sequence typically consists of quartzite, schist, muscovite-rich quartzite intercalations and amphibole/epidote-rich bands. Schist and quartzite in this sequence are commonly blue-grey in colour, while the amphibole/epidote rich bands tend to weather to a characteristic green colour. The amphibole/epidote layers are likely to represent basic igneous material intruded into the sedimentary pile, or volcanic deposits that were contemporaneous with sedimentation.

Quartzite constitutes up to 70% of a single exposure of the non-graphitic schist and quartzite sequence. The main foliation in these rocks, S_s , is ubiquitously well defined in many outcrops but the S_l foliation that formed later in the metamorphic evolution of the rocks is commonly developed pervasively only where the proportion of schist locally exceeds 50-60%.

The occurrence of the aluminosilicate minerals, staurolite and garnet is restricted to the schistose horizons. More specifically, garnet is commonly present in, or adjacent to, the amphibole/epidote bands. Spear (1993) reports that the nucleation of garnet is enhanced by the presence of calcium, and as the presence of epidote and sodic-calcic amphibole suggests that calcium is prolific in these green-weathering horizons, it is likely that Ca promotes the nucleation of garnet.

2.3.4 Phyllite and quartzite sequence

The phyllite and quartzite sequence is widely exposed in the north and east of the area (**figure 2.5**). This sequence is distinct from the Palaeozoic non-graphitic schist and quartzite sequence in that the amphibole/epidote layers described above are absent and mica-rich layers are more dominant. Layers of phyllite in this sequence have a characteristic soft sheen and a distinctive blue-grey colour.

Phyllites and quartzites in the Alpujarride Complex are generally attributed to the Permo-Triassic (Martinez-Martinez & Azañon, 1997). In a regional context, the phyllite sequence overlies the Paleozoic non-graphitic schists and quartzites; if the Paleozoic sequences were affected by the Variscan orogeny, the contact between the Paleozoic and Permo-Triassic rocks is likely to be unconformable. The pervasive deformation of the Alpujarride rocks during the D_s deformation event (see section 2.2) and the generation of many tectonic contacts before, during and after the Alpine-age orogenic event, are likely to have destroyed many of the original stratigraphic contacts between rock units in the Alpujarride Complex. A gradational boundary between the phyllite / quartzite sequence and the overlying carbonate rocks is locally seen (**figure 3.22** and section 2.5).

2.3.5 Carbonate rocks

Exposures of carbonate rock dominate the geology and scenery of the north part of the studied area: the carbonate rocks form prominent ridges with locally well-developed karst features, in contrast to the poor levels of exposure that characterise the schist/quartzite and phyllite/quartzite sequences. The carbonate is dated as Upper Triassic (Kozur & Simon, 1972). Carbonate rocks are typically grey/blue in colour and are extensively dolomitised. Oxidation of iron generates a red/orange deposit where these rocks are extensively weathered.

2.4 Metamorphic grades

2.4.1 Introduction

The distribution of metamorphic grades in the study area is shown on the map in **figure 2.7**. The mineral assemblages for all the samples from this area are listed in Appendix One with a list of mineral abbreviations (Kretz, 1983).

2.4.2 Kyanite-sillimanite grade

Kyanite-sillimanite grade rocks crop out extensively in the southern part of the mapped area, near to the coast west of Almuñecar (e.g. at VF 43430658); an isolated patch of exposure also occurs to the east of Guajare Faraguit (VF 44900770) (**figure 2.7**).

The eastern edge of the kyanite-sillimanite grade rocks near to Almuñecar is apparently transitional into kyanite-sillimanite-andalusite assemblages. To the north and north-west, this metamorphic division is transitional into garnet/staurolite-andalusite assemblages. Tectonic contacts at the edge of the carbonate exposures at Cerro Gordo (VF 43150660) and Punta de la Mona (VF 43470645) form the southern edge of the area in which this grade is exposed.

Southeast of Guajare Faraguit, (VF 44900770), the exposure of kyanite-sillimanite grade rocks is transitional at its southern extent with rocks of garnet/staurolite-andalusite grade. To the north, the extent of the kyanite-sillimanite grade rocks is bound by a tectonic contact that developed after the end of D_s and prior to the onset of D_t . The eastern and western terminations of the kyanite-sillimanite grade rocks in this area are not seen but are presumed to be tectonic.

- **Common mineral assemblage:** Sil, Ky, Grt, St, Pl, Bt, Ms, Qtz, Ilm
- **Porphyroblast phases:**

Garnet	up to 4mm diameter
Staurolite	up to 3mm diameter
Kyanite	up to 3mm diameter
- **Fabric-defining minerals:** Sil, Bt, Ms

2.4.3 Kyanite-sillimanite-andalusite grade

Rocks containing this assemblage are mainly exposed near to Almuñecar, in the south of the area. Here, the northern and eastern extremes of the kyanite-sillimanite-andalusite grade exposures are transitional into garnet/staurolite-andalusite assemblages. To the west of Almuñecar, this metamorphic grade has a transitional boundary into kyanite-sillimanite grade rocks, while the contact in the east is tectonic.

A small exposure of rocks containing these minerals is present to the south of Guajare Alto (VF 44460789) but this exposure is bound on all sides by tectonic contacts so that the relationships with rocks metamorphosed to other metamorphic grade are not seen.

➤ **Common mineral assemblage:** Sil, Ky, And, Grt, St, Pl, Bt, Ms, Qtz, Ilm

➤ **Porphyroblast phases:**

Garnet	up to 4 mm
Staurolite	up to 3 mm
Kyanite	up to 2 mm
Andalusite	up to 4 mm

➤ **Fabric-defining minerals:** Sil, Bt, Ky, Ms

2.4.4 Sillimanite-andalusite grade

Rocks containing this assemblage constitute only a small proportion of the total area of metamorphic rocks: exposures of sillimanite-andalusite grade rocks are confined to the north of the area, and crop out in the Sierra de Chapparal (VF 44300760) and in Los Guajares (VF 44950765) – **figure 2.7**. At both these localities, the exposures of the sillimanite-andalusite grade rocks are entirely bound by fault contacts, so that the relationship of rocks bearing this assemblage with respect to rocks of other metamorphic grades is not determined.

➤ **Common mineral assemblage:** Bt, Ms, Grt, St, And, Pl, Qtz, Ilm, Mag

➤ **Porphyroblast phases:**

Garnet	up to 3 mm diameter
Staurolite	up to 3 mm diameter
Andalusite	up to 5 mm diameter

➤ **Fabric-defining minerals:** Sil, Bt, Ms

2.4.5 Garnet and/or staurolite–andalusite grade

Rocks containing garnet and/or staurolite and andalusite are widespread in the area.

Staurolite and other aluminium-rich minerals tend to grow only in the schistose layers in the rock, presumably controlled by the availability of aluminium. Garnet is commonly prolific in isolated horizons within the schistose layers and absent, or very sparse, in the remainder of the outcrop. Almandine is the major component of the garnet crystals in this area, with spessartine, grossular and pyrope components typically forming less than 10% of the volume of garnet (sections 5.5.2.1 and 5.5.3.1). The nucleation of almandine-rich garnets is promoted by the presence of calcium (Yardley, 1990) and it is likely that local concentration of this element controls the distribution of garnet.

Where rocks from the graphitic schist and quartzite sequence are metamorphosed to garnet/staurolite-andalusite grade, biotite is commonly very prolific and is an important fabric-defining phase. Up to 40% of biotite in these samples appears to have been formed from the breakdown of garnet. Non-graphitic schist and quartzite rocks, metamorphosed to

an equivalent grade, typically contain less biotite by modal volume, and muscovite is commonly the most important fabric-defining mineral in these samples.

➤ **Common mineral assemblage:** Bt, Ms, Grt, St, Ky, And, Pl, Qtz, Ilm, Mag

(green bands): Amph, Ep, Cal, Qtz

➤ **Porphyroblast phases:** Garnet up to 4 mm diameter

Staurolite up to 3 mm diameter

Andalusite up to 5 mm diameter

Fabric-defining minerals: Bt, Ms, Ilm

2.4.6 Muscovite-biotite grade rocks

The graphitic and non-graphitic schist and quartzite sequences, and the phyllite and quartzite sequence, are all metamorphosed to muscovite-biotite grade where they crop out in the northern and eastern part of the mapped area. The contact of this grade to the south with the garnet and/or staurolite-andalusite grade rocks is transitional, although it is locally affected by late brittle faults (see **figures 3.4, 3.6 & 3.8**). Variation in metamorphic grade from muscovite-biotite to muscovite-chlorite grade appears to be mainly transitional, but late brittle normal faults locally disrupt the contacts.

Phyllites and quartzites compose the majority of the rocks metamorphosed to muscovite-biotite grade. In this sequence, the S_1 foliation is the dominant fabric, and a structural section to the north of Jete (VF 44050727) clearly illustrates the gradual increase of intensity of the S_1 foliation planes with progression from the schist and quartzite sequences into the phyllites and quartzites. (Section 3.3).

Typical assemblage: Ms, Bt, Chl, Chd, Pl, Qtz, Ilm, Mag

Porphyroblast phases: Ilmenite up to 2 mm length

Magnetite up to 2 mm diameter

Fabric defining minerals: Bt, Ms

2.4.7 Muscovite-chlorite grade

Muscovite-chlorite grade rocks crop out to the north of the muscovite-biotite grade exposures, and in the east of the area (**figure 2.7**). The relationship with the muscovite-biotite grade rocks is commonly transitional, but are locally affected by normal faults. In the northern most part of the mapped area, muscovite-chlorite grade rocks from the phyllite and quartzite sequence show a gradational boundary with the carbonate rocks (**figure 3.22**). This indicates that at least some of the carbonate outcrops in the north of the area have experienced only low-grade metamorphism. Elsewhere the boundary between these two lithologies is abrupt, presumably affected by faulting, and the metamorphic grade of the carbonates in these localities cannot be determined.

Typical assemblage:	Ms, Chl, Pl, Qtz, Ilm, Mag
Porphyroblast phases:	Ilmenite up to 2 mm length Magnetite up to 3 mm diameter
Fabric defining minerals:	Bt, Ms

2.5 Types of contact

2.5.1 Introduction

Contacts in the area have been classified into three categories, each of which is described briefly below.

2.5.2 Stratigraphic contacts

An example of this type of contact is seen to the north of Cantalobos (VF 43550690); portion of the cross-section that passes through this area is shown in **figure 2.8**. In the absence of metamorphic grade variation, and where no evidence of tectonic disturbance is seen, it is

assumed that this relationship represents a preserved stratigraphic contact that has been metamorphosed during the Alpine-age orogeny affecting these rocks.

2.5.3 Pre-metamorphic tectonic contacts

Relationships between rock-types that vary from the stratigraphic sequence established in the region may reasonably be assumed to be a consequence of tectonic displacement. In the absence of metamorphic grade variation across such a contact, it is apparent that the juxtaposition of the rock units occurred before the onset of metamorphism (i.e. that the rocks at either side of the contact have shared a metamorphic history). The locations of contacts that fall into this category are marked on **figure 2.5**, and an example is shown detail in **figure 2.9a**. The identification of this type of contact is an important component in understanding the structural evolution of the area.

Non-stratigraphic, pre-metamorphic contacts may only be identified where they juxtapose two different rock-types, as elsewhere (in the absence of metamorphic grade change and variation of rock type) they are effectively 'invisible' (**figure 2.9b**). Variation of the structural thickness of a body of rock between adjacent cross-sections may indicate the location of these pre-metamorphic, non-stratigraphic contacts.

2.5.4 Ductile and/or brittle contacts formed during or after metamorphism

A combined study of the metamorphic minerals and rock-type enable the timing of displacement across ductile/brittle and brittle tectonic contacts to be identified across the area, relative to the metamorphic evolution. All the faults identified exhibit decrease of metamorphic grade upwards across the structures, indicating that a normal sense of displacement has occurred across them.

55

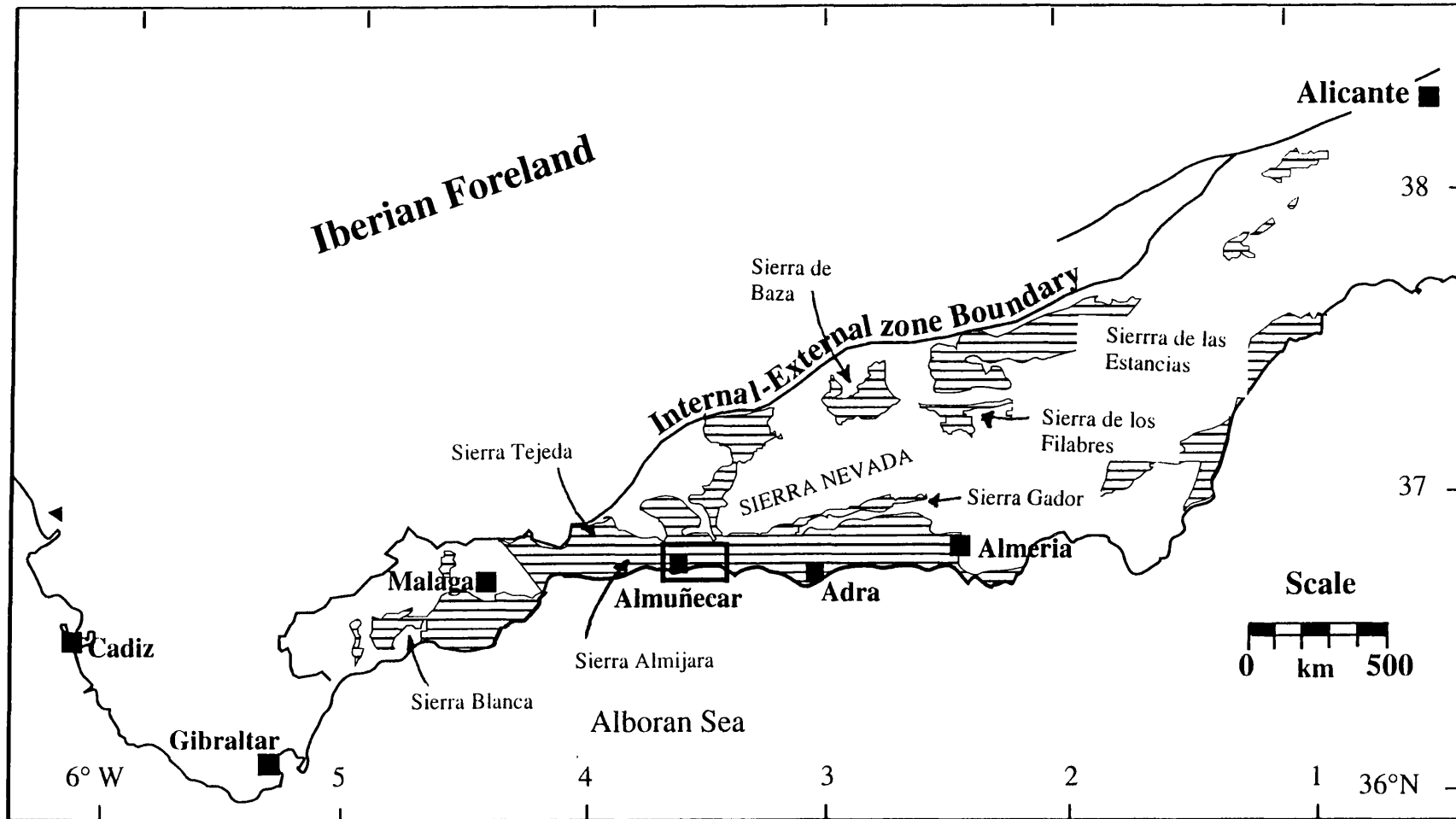


Figure 2.1 Map to show the outcrop distribution of the Alpujarride Complex, and the location of the area

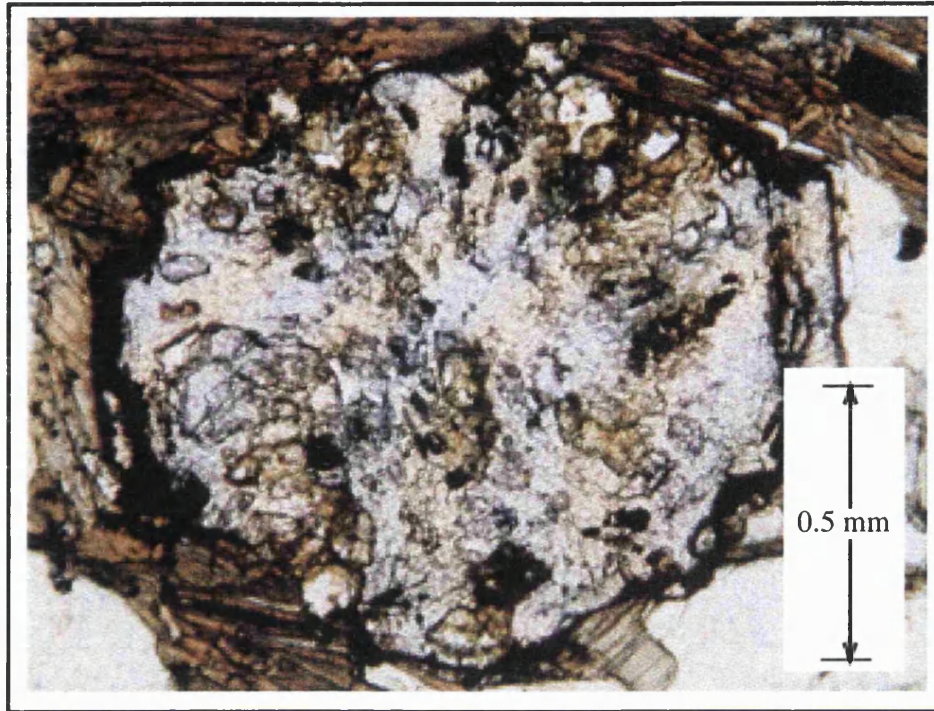
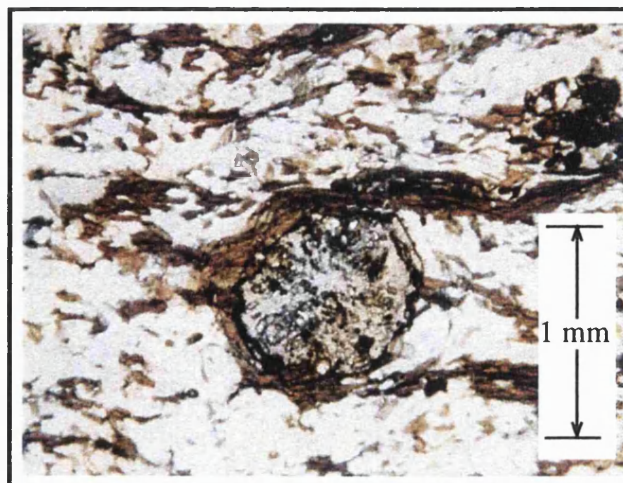


Figure 2.2a Above. Garnet porphyroblast from sample LH 351 (garnet/staurolite-andalusite grade) with irregular inclusion array inside the garnet. This view is in the YZ plane (i.e. at 90° to the lineation) and elsewhere in this section the S_s foliation is dominant (see figure 2.2b below). It is likely that this porphyroblast of garnet grew prior to the D_s deformation. Note heavy resorption at edges of crystal.

Figure 2.2b Below. View of garnet porphyroblast in figure 2.2a, showing the dominance of the S_s foliation in the matrix of the sample.



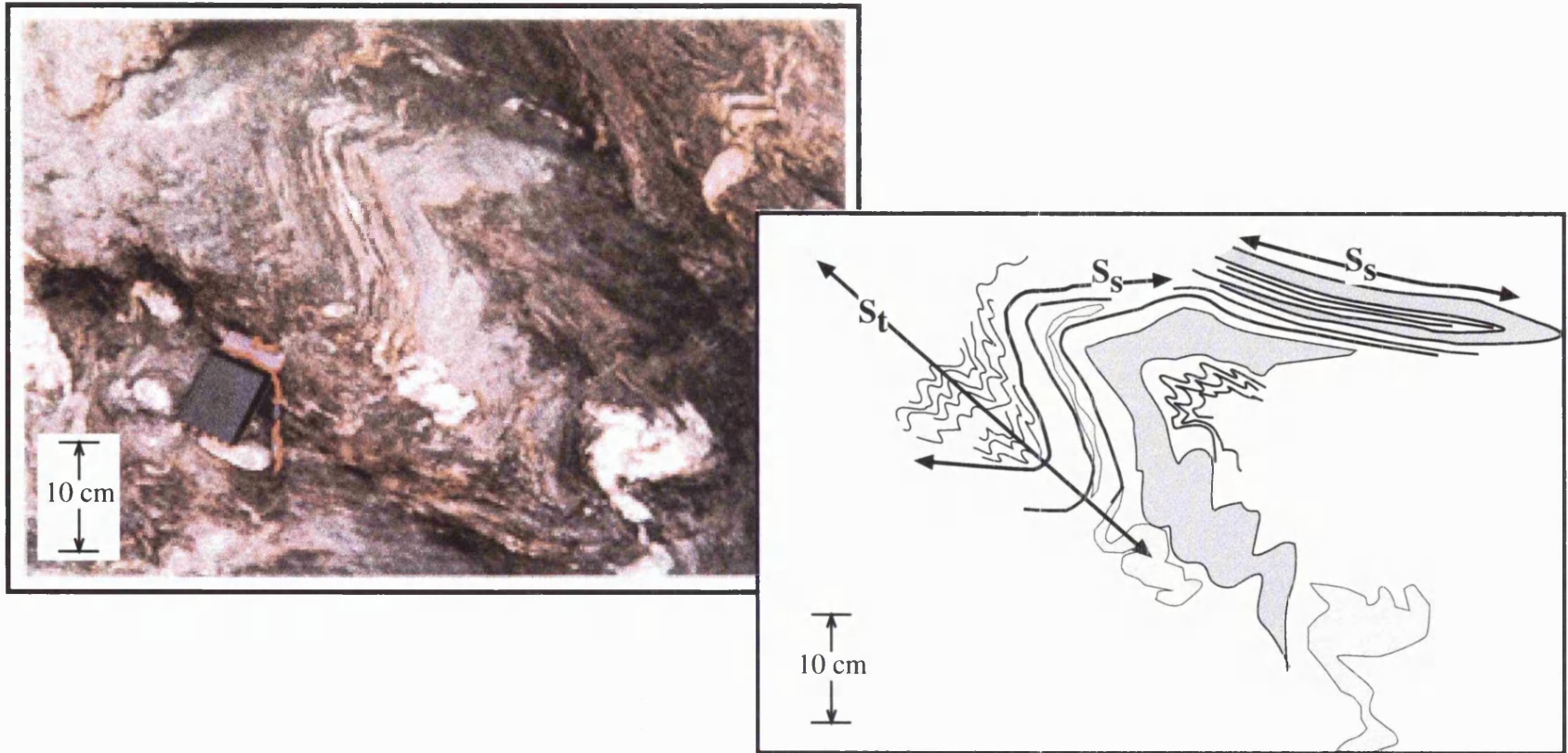


Figure 2.3

A field example of the relationship between the S_s and S_t foliations. The S_s foliation is parallel to the intercalations of quartzite and schist, and is axial planar to tight, isoclinal folds formed during D_s . This is not visible on the photograph, but is shown in the interpretative sketch. The S_t foliation folds the S_s foliation, and is axial planar to the phase of folds generated during D_t . Locality of photo at VF 44230676 in graphitic schist and quartzite sequence, metamorphosed to kyanite-sillimanite-andalusite grade.

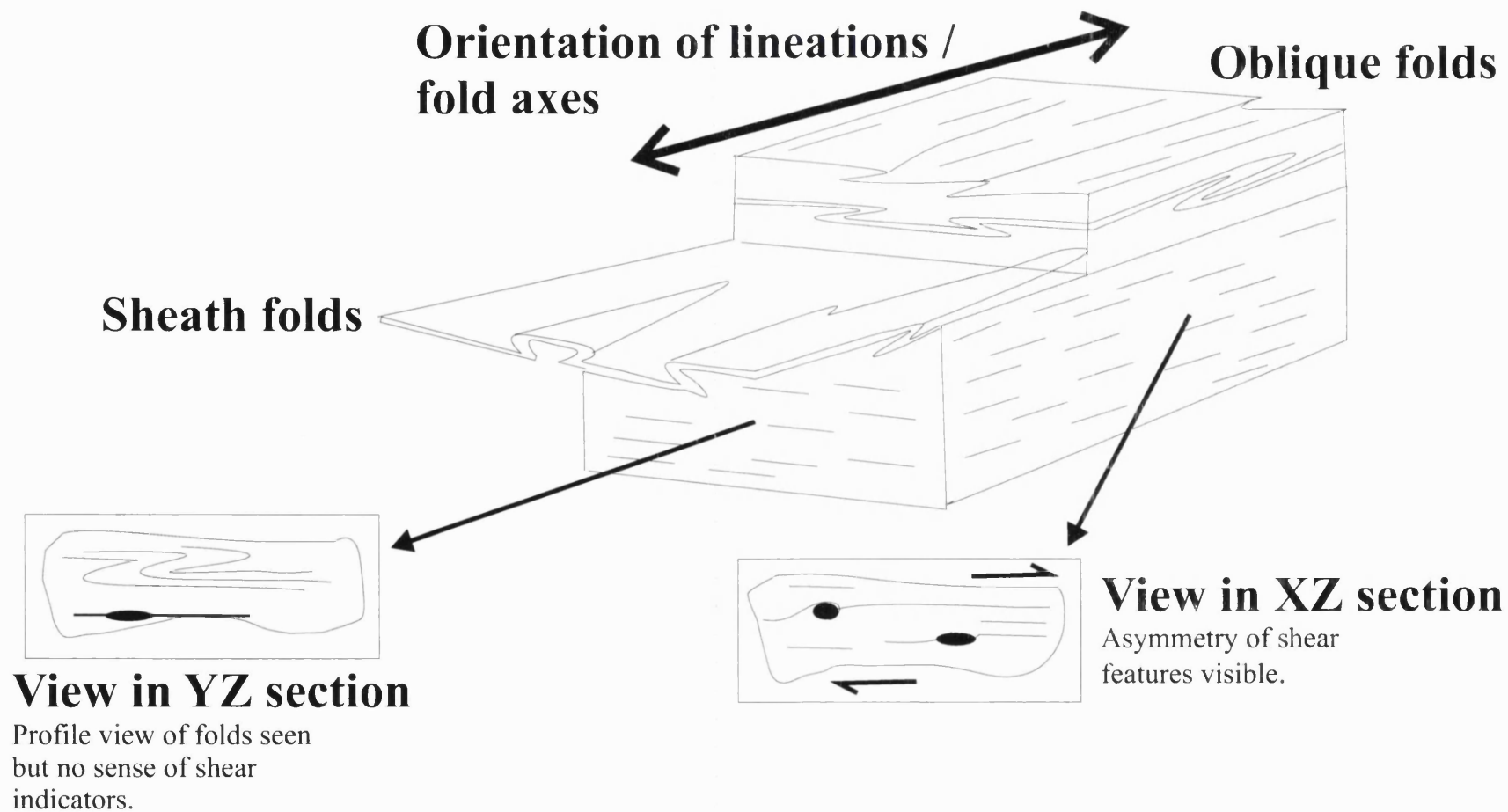


Figure 2.4 Sketch to show the micro-structural features observed in thin sections cut parallel to, and at 90° to the lineation / fold axis orientation. Amended from Passchier & Trouw, 1996.

Figure 2.5 Locations of the early tectonic contacts and stratigraphic boundaries in the field area, as discussed in the text.

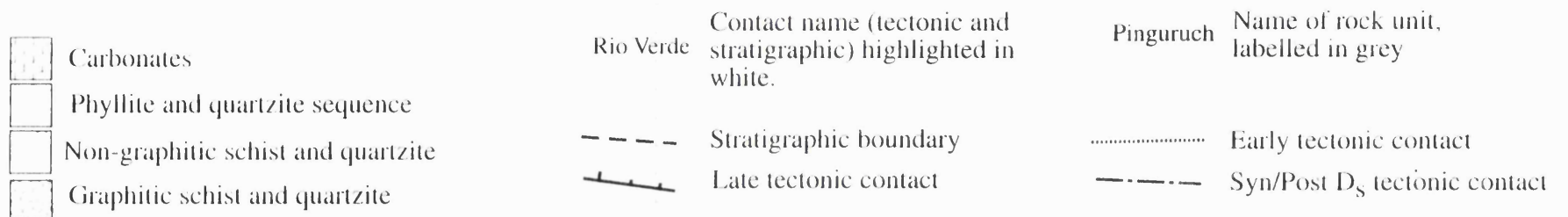
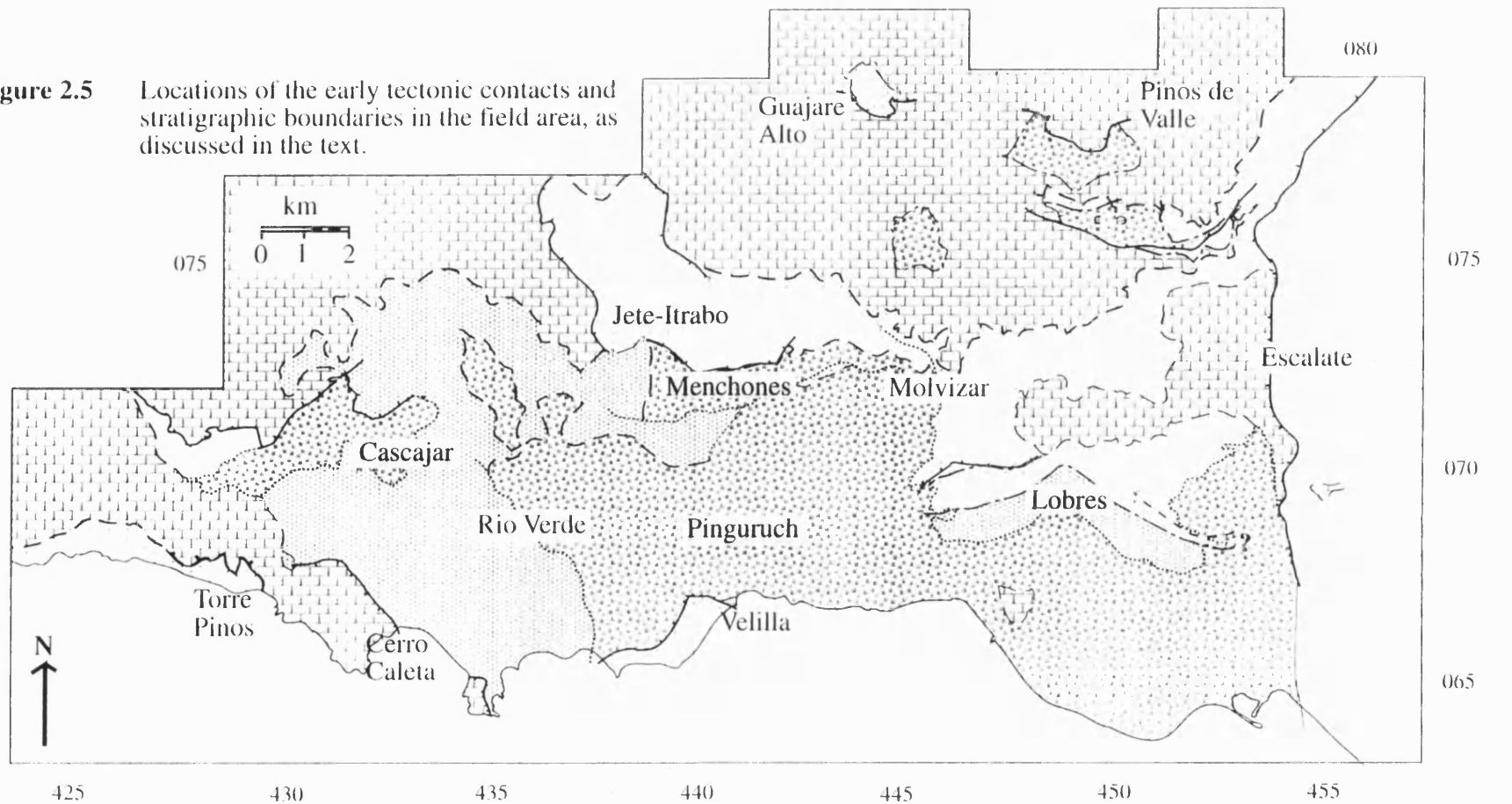
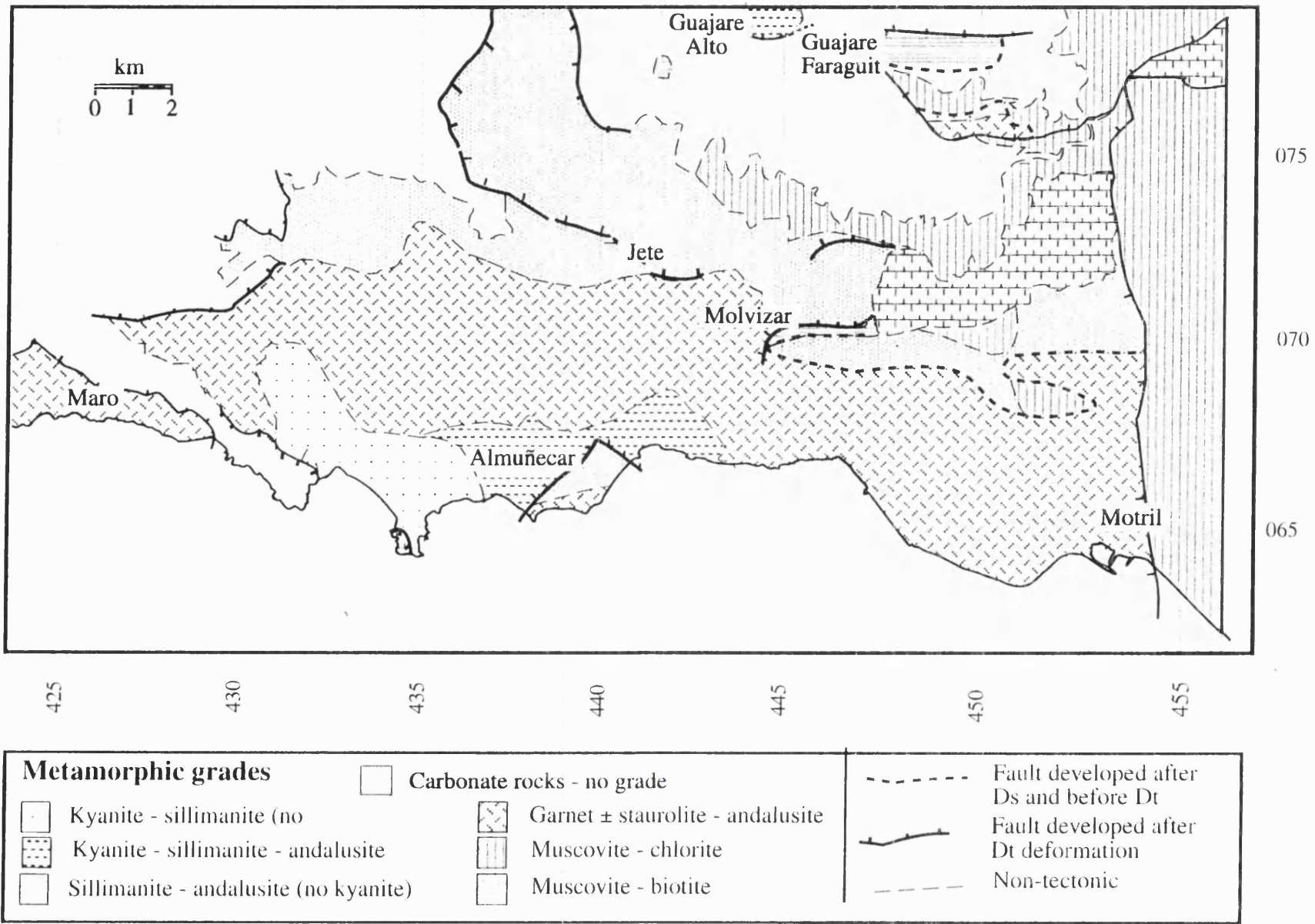




Figure 2.6 S_t foliation plane developed in an outcrop of the graphitic schist and quartzite sequence, near to Motril (VF 45300674). The shaft of the hammer is aligned approximately parallel to the orientation of the incipient S_t foliation. It is evident that the S_s foliation is more tightly folded in the schistose layers (middle of the field of view) than in the pale ~ 5cm wide quartzite bands (at top of field of view). S_t foliation planes are locally visible at close range in the schistose layers but not present in the quartzite layers.

Figure 2.7 Map showing the distribution of the metamorphic grades and tectonic contacts.



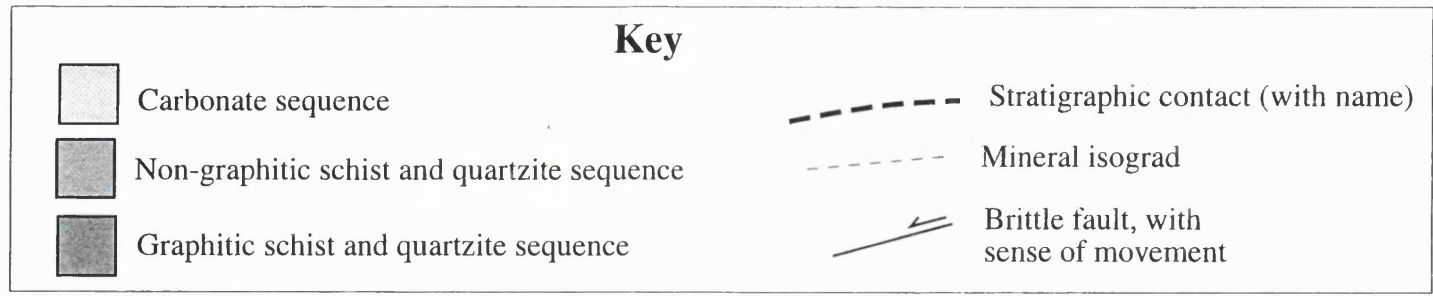
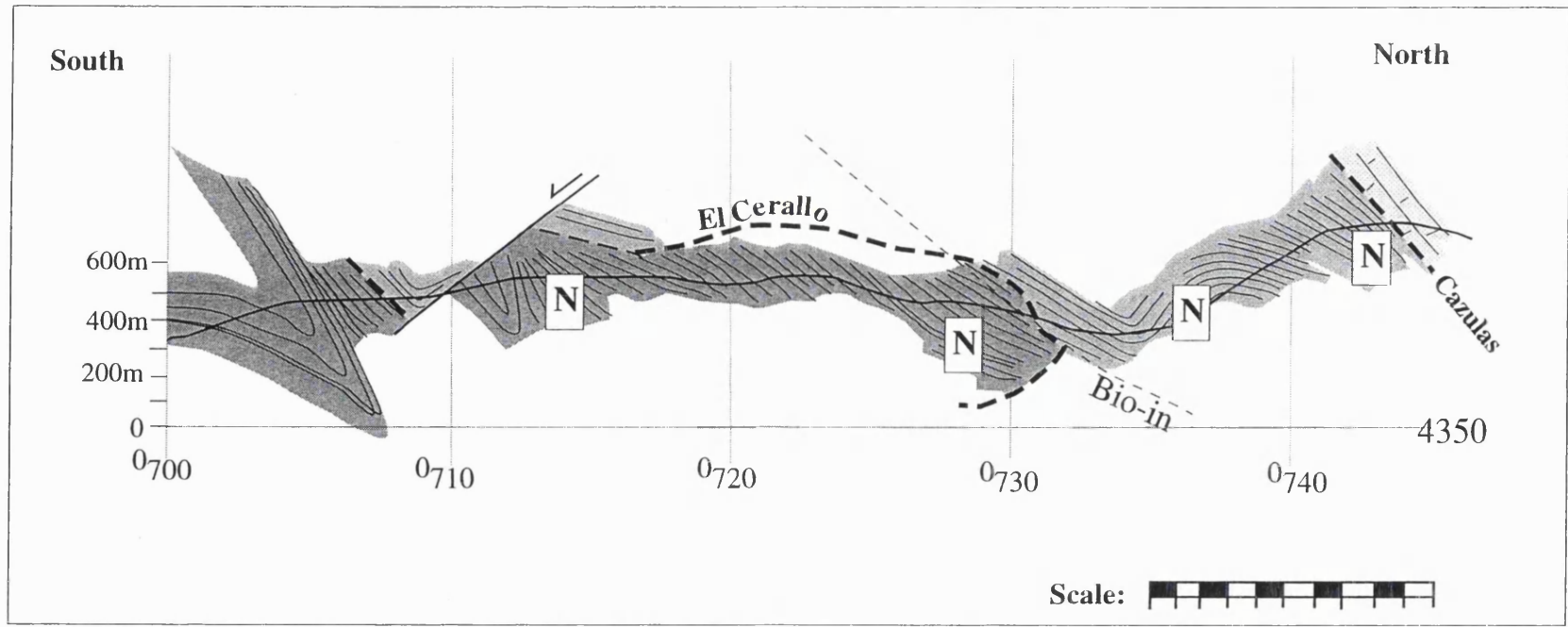
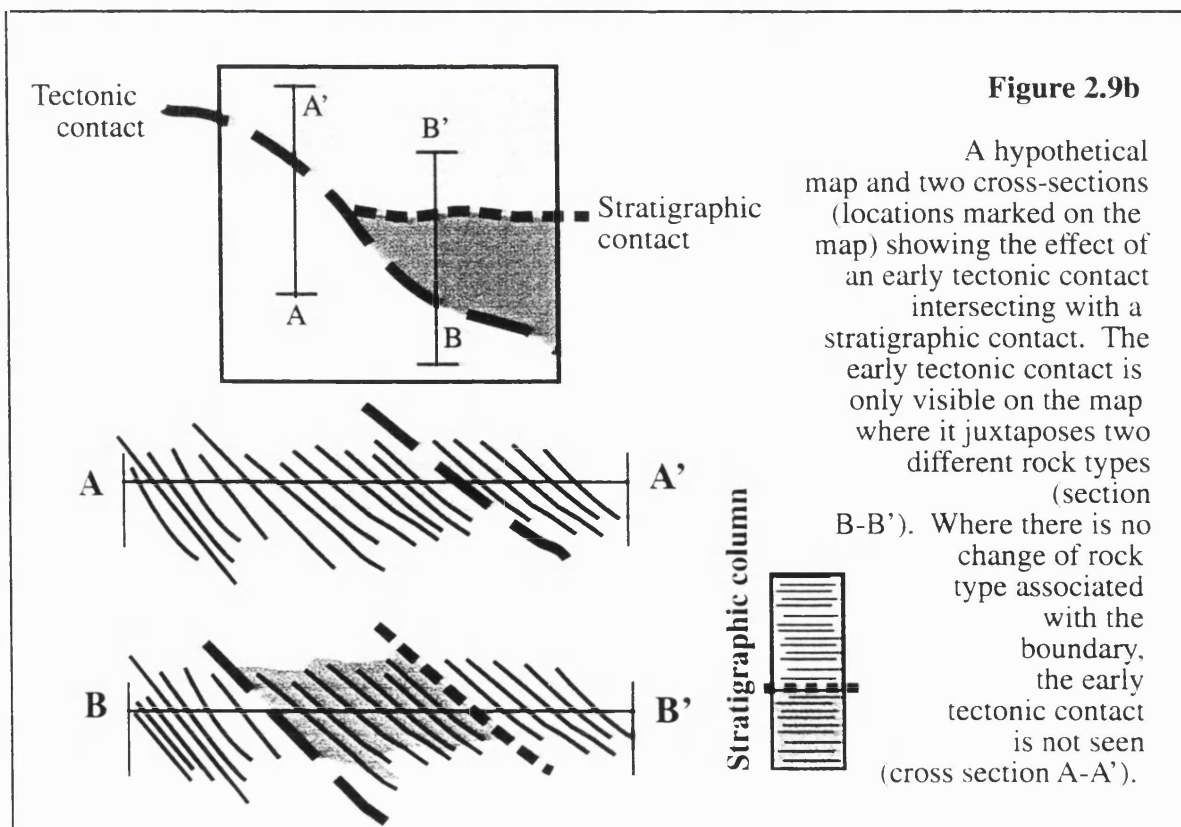
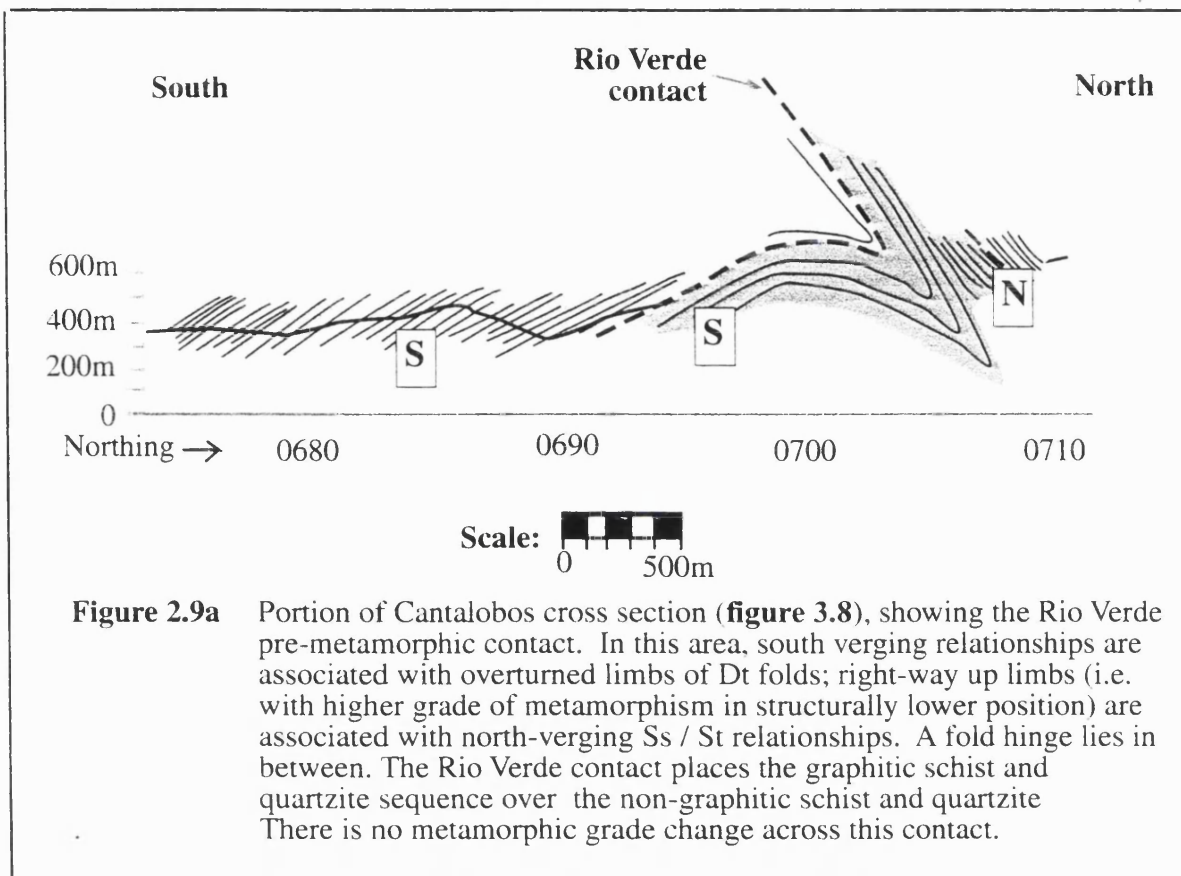


Figure 2.8

Portion of cross section from the north of Cantalobos (figure 3.4) showing the El Cerrallo gradational contact between the graphitic schist and quartzite sequence, and the non-graphitic schist and quartzite sequence. North-verging S_t folds indicate that this sequence is in the right-way-up limb of a D_t fold. The graphitic schist and quartzite sequence clearly underlies the non-graphitic schist and quartzite sequence. To the north, the non-graphitic schist and quartzite sequence underlies the carbonate sequence. The biotite isograd passes close to the contact, perhaps due to the change of bulk composition between the two sequences.



CHAPTER 3 – STRUCTURE

3.1 Introduction

The Alpujarride Complex near to Almuñecar is affected by structures formed in the ductile, ductile-brittle and brittle regimes. The time of formation of the ductile fabrics, S_s (early) and S_l (later), relative to the metamorphic cycle, has been deduced by micro-structural analysis of mineral-fabric relations (see Chapter 4). The variation of metamorphic grade across the ductile-brittle and brittle contacts permits these structures to be analysed also in the context of the metamorphic evolution.

A summary of the features produced by the ductile, ductile-brittle and brittle deformation events that have affected this area is presented in **figure 3.1**: ductile-brittle and brittle contacts developed before, during and after both phases of ductile deformation. The location of cross-sections across this area are indicated on this sketch and on Map One (pocket inside back cover); individual cross-sections are presented in **figures 3.2 – 3.10** (pocket inside back cover).

In this chapter, the fabrics relating to the two generations of ductile deformation, D_s and D_l will be described first. These fabrics are pervasive across the area, and provide a framework in which the development of the ductile-brittle and brittle discontinuities may be discussed.

3.2 Fabrics relating to the D_s deformation

3.2.1 D_s folds and the S_s foliation

The D_s phase of deformation has generated a sequence of asymmetric, isoclinal folds in the quartzite and schist sequences. The geometry of these folds is most easily discerned in the quartzite bands within the quartzite-schist sequences: the D_s fold limbs are elongate, while locally preserved fold hinges exhibit thickening of the quartzite layer up to factor of eight relative to that in the limb (**figure 3.11**). The isoclinal geometry of the folds in the quartzite indicates that the rock has experienced significant bulk strain. The schistosity in the quartzite

and schist sequences define the axial planes to these folds, S_s ; this fabric is parallel to the parting between adjacent quartzite and schist layers, except in the hinges of D_s folds, where the S_s foliation intersects the quartzite and schist layers (**figure 3.12**).

The S_s foliation is the dominant planar fabric in the majority of the exposures of the quartzite and schist sequences. The S_t foliation, formed in a later deformation event, D_t , is dominant in the phyllite and quartzite sequences, and locally in sillimanite-bearing rocks from the graphitic schist and quartzite sequence (section 3.3.).

Folds generated by the D_s deformation event are observed in outcrop with wavelengths varying from 2 cm to 2m. Thin-section studies indicate that D_s folds with amplitudes of less than 2 cm are also developed, and the presence of D_s folds at scales greater than outcrop may be inferred from the compilation of D_s fold vergence data across the area. Zones in which vergence of the D_s folds is uniform (i.e. limbs of the D_s folds) trend approximately east-west (**figure 3.13**): this is concordant with the NE-SW trend of the D_s fold hinges (section 3.2.2). This evidence indicates that a series of folds with similar geometry developed at a variety of scales during the D_s deformation.

3.2.2 Linear features relating to D_s

The fold hinges of the D_s folds, F_s , trend consistently NE-SW at all locations in the area studied (**figure 3.14**). The D_s fold hinges are ubiquitously sub-parallel to an intersection fabric L_{st} that was generated by the imposition of the S_t foliation onto S_s during the D_t deformation (see section 3.3.2). The L_{st} lineation is the dominant linear fabric seen at outcrop.

Evidence of a lineation formed during the D_s deformation event is only seen at localities where the S_t fabric is not pervasive (and hence where L_{st} fabric is weakly developed). A mineral-stretching lineation, L_s , containing sillimanite in the high-grade rocks and muscovite / biotite in lower grade assemblages, lies within the plane of the S_s foliation and is locally seen to wrap obliquely around D_t fold hinges (**figure 3.15**). This relationship indicates that the L_s lineation pre-dates the D_t folds.

3.3 Fabrics relating to the D_t deformation

3.3.1 D_t folds and the S_t foliation

The D_t phase of deformation has deformed the S_s fabric, generating a crenulation cleavage, with foliation surface S_t . The S_t foliation plane is axial planar to D_t folds (**figure 3.16**). D_t folds with asymmetric and symmetric geometry are both seen at outcrop, in the limbs and fold hinges of larger-scale structures, respectively. The inter-limb angle of the D_t folds varies between $50 - 20^\circ$: the folds may be classified as tight or close (according to definition of Fleuty, 1964).

The spacing of adjacent S_t foliation planes depends on the proportion of quartzite and schist, and the thickness of the quartzite-schist intercalations, at a given exposure. S_t planes are most closely spaced in schistose bands, more broadly spaced within quartz-rich schist and commonly absent in quartzite bands of 3 cm width or greater. Well-defined examples of S_t crenulating S_s are developed in sequences of thinly-bedded quartzite and schists (**figure 3.17**). The non-graphitic schist and quartzite sequence tends to contain a higher proportion of quartzite than the graphitic schist sequence; as a consequence, the S_t fabric is commonly less apparent in the former.

Folds at varying scales with similar geometries, were generated during the D_t deformation event. Consequently, the variation of D_t fold vergence at outcrop scale have been used to infer the location of D_t structures at scales greater than a single exposure (section 3.3.3).

Within the phyllite and quartzite sequence (see section 2.3.4), the S_t foliation is pervasively developed and is the most prominent fabric seen in outcrop. The S_s foliation is locally preserved in the vicinity of quartzite layers and quartz veins that pre-date the formation of the D_t deformation event. To the north of Jete the progressive increase of intensity of the S_t fabric, with transition from the schist and quartzite sequence into the phyllite and quartzite unit, is clearly seen (**figure 3.18**).

3.3.2 D_t fold axes (F_t) and the L_{st} lineation

The intersection of the planar S_t foliation with the folded surface of the S_s foliation generates an intersection lineation, L_{st} : this L_{st} lineation is parallel to the fold hinges of the D_t folds (F_t) and lies within the S_s lineation (**figure 3.19**). As mentioned above (section 3.2.2.), L_{st} forms the dominant lineation seen at outcrop.

The orientation of the fold hinges of the D_s and D_t deformations, F_s and F_t , are approximately parallel (**figure 3.20**). Both sets of fold hinges trend approximately NE-SW and plunge at less than 20° : where ductile-brittle or brittle discontinuities affect the area, lineations in adjacent exposures plunge significantly more steeply.

The anisotropy in the rocks prior to the onset of the D_t deformation, as a consequence of the D_s deformation (section 3.2.2), may have influenced the orientation in which the fold hinges of the D_t folds have developed. Alternatively, L_s and F_s may have been rotated into the same orientation as F_t .

3.3.3 Large-scale D_t folds

The relationships between the S_s and S_t foliations seen at outcrop scale are used to elucidate the presence of regional scale D_t folds. The acute angle of intersection between the average orientation of S_s and the S_t foliation will increase with increasing proximity to a hinge zone of a large-scale D_t fold. Limbs on opposite sides of a D_t fold hinge are identified by a change of vergence across the hinge zone (Bell, 1981). As shown above in **figure 3.20**, F_t in this area trends approximately ENE – WSW, so that vergence relations between the S_s and S_t fabrics vary from south to north across hinges of the D_t folds - **figure 3.21** and **figure 3.1**. Along north-south transects, the level of exposure is commonly sufficient to identify D_t phase folds of 500 m limb-length or greater.

The right-way up and inverted limbs of the D_t folds in this area are characterised by north-verging and south-verging S_t/S_s relationships, respectively. Metamorphic grade decreases at progressively higher structural levels in the right-way up limbs, and shows the opposite relationship in the inverted (south-verging) limbs. Other structures that were present prior to the D_t deformation, such as stratigraphic boundaries between units of different rock types

and ductile - brittle contacts, are inverted in the south-verging limb of the D_1 folds - **figure 3.22**. The south-verging (overturned) limbs of the D_1 folds are commonly more deformed than corresponding right-way-up limbs (**figure 3.23**).

3.4 Stratigraphic boundaries and contacts that pre-date the D_1 event

3.4.1 Introduction

Two types of contact that were present prior to the D_1 deformation of the Alpujarride rocks in this area may be identified. Contacts across which an original stratigraphic sequence is apparently preserved (apparent stratigraphic boundaries) are distinguished from contacts across which the stratigraphic succession of rock units has been modified (early tectonic contacts). No variation of metamorphic grade occurs across either of these types of contact: rocks on either side have experienced the same metamorphic history. The distribution of these two types of contact in the area studied is shown in **figure 2.5** and each category of contact is described in turn below.

3.4.2 Apparent stratigraphic contacts

At the contact between the phyllite and quartzite sequence with the overlying carbonates, some intercalations of phyllites in carbonate are seen near to the boundary (see **figure 3.22**). This indicates that locally the original transitional contact between the phyllite and carbonate sequence has been preserved. Elsewhere, the existence of original stratigraphic boundaries between the non-graphitic quartzite and schist sequence and the graphitic quartzite and schist sequences are slightly more ambiguous. A stratigraphic -type boundary is deduced to exist where, in a right-way-up limb of a D_1 fold, the non-graphitic schist and quartzite sequence overlies the graphitic schist sequence. It is possible that these contact relations are the consequence of deformation during the D_5 event, or during an earlier deformation, but the distinction between early contacts that do and do not preserve the stratigraphic sequence (section 3.4.3) is a useful one in determining relations within the area.

Two apparent stratigraphic boundaries are identified from east to west across the mapped area (**figure 2.5**). The El Cerrallo boundary separates the Pinguruch graphitic schists and El Tumbo non-graphitic schists (see **figure 2.5**): the boundary intersects the line of the Jete

Road cross section (**figure 3.6** – at VF 43900708) and the Cantalobos cross section (**figure 3.4** – at VF 43500708 and VF 43500709). On both these sections, the graphitic schist and quartzite sequence underlies the non-graphitic schist and quartzite sequence, where the boundary is seen in the right way up limb of a D_1 phase fold. Similar relationships are evident at the Haza Llano boundary, which trends approximately east-west to the south of Jete (VF 44050727): north-dipping normal faults have caused some offset along this contact, but it is essentially an original stratigraphic boundary between the graphitic and non-graphitic quartzite and schist sequences.

3.4.3 Early tectonic contacts

Early tectonic contacts within the Alpujarride complex can only be identified where the contact has juxtaposed two different rock units: the absence of grade change across these contacts mean that where the early contacts juxtapose two rock bodies of the same lithological unit, the contact is very difficult to trace. (See also Chapter 2 – section 2.5.3).

Of the four early tectonic contacts identified in the area, three of them place the graphitic schist and quartzite sequence above the non-graphitic schist and quartzite sequence (in the right-way-up limbs of the D_1 generation folds). These contacts are described below. The Las Palomas contact in the south of the area juxtaposes carbonate rocks below the non-graphitic schist and quartzite sequence in the right-way-up limb of an S_1 fold.

Regionally, the graphitic schist and quartzite sequence is generally acknowledged to underlie the non-graphitic quartzite and schist sequence, and the carbonates regionally overlie the non-graphitic phyllite and quartzite sequence (Chapter 2). The juxtapositions of the rock types generated by these early contacts suggest that reverse movement occurred along these early structures. These early contacts are likely to have formed during the crustal thickening event in the early compressional part of orogenic evolution (Chapter 1).

3.4.3.1 Rio Verde Contact

The Rio Verde Contact, well exposed in a road section of the CN340 at VF 43710666, is an example of a tectonic boundary that formed prior to or during the D_5 deformation. At this location, in the north-verging (right way up) limb of a D_1 fold, graphitic schists and quartzites

overlie the non-graphitic schist and quartzite sequence. This sequence is clearly non-stratigraphic, and both the graphitic and non-graphitic sequences at this locality are of kyanite-sillimanite-andalusite grade.

The Rio Verde Contact may be traced north from the locality given above, progressively passing into rocks of lower metamorphic grade. The contact cuts the Cantalobos cross-section (**figure 3.4**) at VF 43500694, where it is seen in the inverted (south-verging) limb of a D_1 fold: here, the graphitic schist and quartzite sequence is vertically beneath (yet structurally above) the pale schist and quartzite sequence. The rocks at both side of the Rio Verde Contact at this location are metamorphosed to garnet/staurolite-andalusite grade.

To the north of its exposure on the Cantalobos cross-section, the Rio Verde Contact intersects a stratigraphic contact (the Haza Llano boundary: Chapter 2). As a consequence of this, the trace of the Rio Verde Contact to the west is not evident (**figure 2.9b**).

Graphitic schists and quartzites on Morro del Cascajar (VF 43250705) overlie non-graphitic schists (**figure 3.3**): on the Rio Miel cross section (**figure 3.2**) the Cascajar body of graphitic schist is directly in contact with carbonate rocks (VF 42820697). This contact is clearly not stratigraphic, and may be attributed to the westward continuation of the Rio Verde contact, or another early tectonic contact (**figure 2.5**).

3.4.3.2 El Tumbo Contact

On the Jete Road cross-section (**figure 3.6**), the El Cerallo stratigraphic boundary between the graphitic schist and quartzite sequence and the non-graphitic schist and quartzite sequence is seen at VF 43900706. The thickness of non-graphitic schist seen to the north of this contact is thinned by the El Tumbo Contact (at VF 43900712): at this location, the graphitic schist and quartzite sequence is clearly placed structurally above the non-graphitic schist and quartzite sequence exposed to the south. **Figure 3.24a**.

The El Tumbo Contact may be distinguished further to the east, where similar contact relations to those seen on the Jete Road cross-section (**figure 3.6**) are identified at VF 44330723. At this location, an exposure of the non-graphitic schist and quartzite sequence is seen in the right-way-up limb of a D_1 fold and exposures of the graphitic schist and quartzite sequence lie structurally above and below this exposure (**figure 3.7**). Further east from this

location, no exposures of the non-graphitic schist and quartzite sequence are identified, and the trace of the El Tumbo Contact cannot be discerned as the graphitic schist and quartzite sequence lies on both sides of the contact.

3.4.3.3 Molvizar Contact

Near to Molvizar (VF 44570713), in the right-way-up limb of a D_t fold, the graphitic schist and quartzite sequence is clearly seen to lie structurally above the non-graphitic schist and quartzite sequence (**figure 3.24b**). North of Molvizar, the traceable extent of the contact is limited as it intersects the Haza Llano stratigraphic boundary (e.g. **figure 2.2**): to the north of this intersection, the non-graphitic schist and quartzite sequence lies either side of the Molvizar Contact.

Consistent contact relations may be traced to the south of this location: graphitic schists exposed in the Las Dehasas area (to the north of Salobreña) are topographically higher than the exposures of the non-graphitic quartzite and schist sequence to the east, around Lobres (VF 44950700).

Near to Motril the Molvizar Contact is clearly identified at VF 45830680: to the north of here it is displaced by syn- D_s /pre- D_t age faults (section 3.5).

3.4.3.4 Las Palomas Contact

The Las Palomas Contact is inferred from map relations. The vergence of the D_t folds (see section 3.3.3) indicates that the non-graphitic schist and quartzite sequence exposed to the north and east of the carbonate masses at Cerro Gordo (VF 43150660) and Punta de la Mona (VF 43480645) are in an overturned limb of a D_t phase fold. Late faults that have reactivated this contact clearly dip to the south: these relationships indicate that prior to brittle faulting and the D_t phase of deformation, the carbonate that now forms these two promontories lay below the non-graphitic schist and quartzite sequence. Regional relations (Chapter 2) indicate that this is contrary to the original stratigraphic configuration; consequently the contact is inferred to be due to early tectonic activity.

A reconstruction of the configuration of rocks that existed in this area, immediately after the early high-temperature episode of metamorphism and the D_s deformation event, is presented in **figure 3.25**: the contacts identified on **figure 2.2** are indicated on this figure.

3.5 Brittle – ductile contacts formed between D_s and D_t events

3.5.1. Introduction

The identification of brittle-ductile contacts that formed between the two phases of ductile deformation, D_s and D_t , has been achieved primarily by analysing the mineralogy and microstructure of samples on either side of the tectonic contacts. It may be expected that samples from opposite sides of a contact that formed after D_s and prior to D_t will have different early (high pressure – high temperature) metamorphic histories, but share the late (low pressure, moderate temperature) portion of the P-T evolution.

3.5.2 Comparison of rocks at either side of a D_s/D_t contact

Evidence that indicates the presence of a D_s/D_t contact is found in the east of the studied area: this contact intersects the cross sections to the north of Salobreña, Cerrajon and Escalate (**figures 3.8, 3.9 and 3.10**, respectively). The mineralogy of the rocks on opposite sides of the D_s/D_t structures is summarised in **figure 3.26**. A detailed field sketch, showing the relationship of the lithologies on either side of the D_s/D_t boundary, where it is exposed at VF 44940756 in Los Guajares is shown in **figure 3.27**.

Where the D_s/D_t discontinuity is seen in the right-way-up (north verging) limbs of D_t folds, the spatial and metamorphic grade relations of the rocks suggest that the structure may have originated as a north-dipping normal fault. Movement along the fault would have brought low-grade metamorphic rocks (in the hanging wall of the fault) into contact with high-grade metamorphic rocks (in the foot-wall) **figure 3.28**.

3.5.3 Mineral – fabric relations indicating D_s/D_t structures

Where andalusite is not present in the rocks, shear-fabrics, and the relationship of the minerals to the shear fabrics, may indicate the timing of the ductile-brittle deformation relative to the ductile deformation history. The XZ plane (i.e. parallel to L_{st} and F_t) is the appropriate orientation in which to view shear fabrics: the relationship of these shear surfaces to the D_s and D_t fabrics is seen in the YZ plane (i.e. at 90° to L_{st} and F_t).

Thin sections cut parallel to the main lineation locally reveal the presence of ductile-brittle shear features that disrupt high pressure and high-temperature minerals – **figure 3.29**. In a view at 90° to the lineation (i.e. in the YZ plane), shear surfaces are locally folded by the D_t generation of folds – **figure 3.30**. This relationship indicates that part of the ductile – brittle shearing evident in this area occurred prior to the onset of the D_t event.

A phase of ductile / brittle shearing prior to the generation of the D_t folds is likely to have affected the thickness of the metamorphosed rock stack across the area from west to east (**figures 3.2 – 3.10**). The direction of movement on this set of shears is likely to have been top-to-the-north, as this is the sense of motion deduced for the ductile-brittle discontinuities discussed above (section 3.5.2) and of shear features that post-date the D_t phase of deformation (section 3.6).

3.6 Ductile – brittle structures developed after the D_t event

3.6.1 Introduction

Numerous examples of brittle faulting are seen in the area: all the faults show normal sense of displacement along north or northwest dipping fault planes. Rocks on opposite sides of the post- D_t deformation structures do not share any part of their pressure – temperature history. The amount of displacement along a fault plane is approximately proportional to metamorphic grade across the fault plane: a greater amount of displacement is expressed as a larger variation in metamorphic conditions across a contact.

The character of the post-metamorphic contacts seen varies from ductile – brittle to entirely brittle. This variation is likely to be linked to the rheology of the rocks adjacent to the faults:

brittle faults are more commonly developed where carbonate rocks are adjacent to the fault plane. The ambient temperature at which the faults formed may also influence the style of faulting, with higher temperatures promoting the formation of more ductile fabrics.

A summary of the most regionally important brittle-ductile structures in this area, from east to west, is presented in the following sections. The locations of these faults are shown on **figure 3.1**.

3.6.2 Torre Miel fault zone

This fault is seen only on the 'Rio Miel' cross-section (**figure 3.2**): it forms the contact between non-graphitic schists and quartzites to the south (exposed on the CN340) and the carbonate mass of 'Gibraltarillo' (VF 42720693) and 'Sol' (VF 42900693) to the north (**Figure 3.31a**). A branch of the fault is exposed to the north of Torre de Pinos at VF 42890676: the geometry of the adjacent quartzite-schist layers indicates that this part of the fault dips to the north (**figure 3.31b**).

At VF 42740678, to the west of this location, south-dipping surfaces with lineations are locally exposed on the CN340: these surfaces may represent a conjugate fault surface with the main slip surface seen north of Torre Pinos (**figure 3.31c**).

3.6.3 Cerro Caleta fault zone

The Cerro Caleta fault zone intersects the 'North of Cerro Gordo' cross-section (**figure 3.3**) at VF 43200666. Surfaces within the Cerro Caleta fault zone are well exposed to the north of Cerro Caleta (VF 43010683), where the relationship between the dominant fault surface and the Riedel shear surfaces indicates normal movement along a south dipping fault zone (**figure 3.32a**). To the west (VF 42980677), polished surfaces that dip steeply to the south are developed where the fault zone cuts carbonate rocks. (**figure 3.32b**): lineations on these surfaces lie within the plane of the polished surface and are inclined steeply to the S-SE (**figure 3.32c**).

To the east, the carbonate ridge that is prominent on the Punta de la Mona promontory (VF 43460646) is bounded to the north and east by a series of south-dipping faults. Zones of extensive recrystallization commonly accentuate faults developed within the carbonate

(**figure 3.33a**). Numerous local south-dipping faults are seen in the non-graphitic quartzite and schist sequence to the north, including a south-dipping exposure of pseudotachylite at VF 43490655 (**figure 3.33b**).

It is likely that the contacts which defines the northern boundary of the carbonate exposures at Punta de la Mona (VF 43480645), Cerro Gordo (VF 43150658) and Cerro Caleta (VF 43050670) are formed by a single structure: the Cerro Caleta fault zone. The evidence from Riedel shear relations to the fault zone suggests that the most recent movement along this fault zone has been towards the south i.e. normal movement. Relations with the Rio Miel fault zone to the west, and the extremely re-crystallised character of the carbonate bodies that compose the ridges near the coast suggest that the carbonate bodies near to the coast were positioned below the Cantarrijan non-graphitic schists during the phase of high-temperature metamorphism (**figure 3.25**). As a consequence, it seems likely that the Cerro Caleta fault zone was dipping to the north earlier in its history and experienced normal movement with displacement to the north, prior to rotation to its present-day steep orientation to the south.

3.6.4 Velilla fault zone

The Velilla fault is well-exposed at VF 44050670, to the north of Velilla - **figure 3.34a**. The fault juxtaposes the graphitic schist and quartzite sequence (metamorphosed to kyanite-sillimanite-andalusite grade) to the north with non-graphitic schist and quartzite sequence (at muscovite – biotite grade) to the south. The rocks at either side of the fault contact do not share any part of the metamorphic history with one another. $S_s - S_t$ relations in the graphitic schist sequence verge to the south, indicating that this area is in the inverted limb of a D_t phase fold (**figure 3.1**).

The majority of surfaces measured in the zone of fault gouge seen at VF 44050670 dip moderately steeply towards the north: a second, less prominent, set of surfaces is inclined steeply to the south (**figure 3.34b**). Local north-dipping faults accommodating displacement of between 2 – 10 cm are seen in the non-graphitic schist and quartzite sequence around Velilla (VF 44000665). Overall, the fault is a north / north-east dipping normal fault that has developed within the inverted (south-verging) limb of a D_t phase fold. Sillimanite-bearing graphitic schists in the hanging wall of the fault are brought into contact with the muscovite-biotite grade non-graphitic schists in the footwall as a consequence of movement along the

fault plane after the end of the D_1 deformation event. The width of the fault zone is estimated to be between 30 and 80 m.

To the west of Velilla, local evidence of faulting is seen at VF 43980666 in a road section of the CN340. The dip of the fault plane is apparently to the north-west, with lineations on the surfaces plunging to the north. (**figure 3.34b**). It is likely that this contact is a normal fault, related to the structure seen to the north of Velilla (VF 44050670). The sequence of graphitic schists and quartzites (to the west) lies in the hanging wall of the fault, and the non-graphitic schist and quartzite sequence that crops out in Velilla (to the east) comprise the footwall.

3.6.5 Late faults in the Los Guajares area

3.6.5.1 Pinos Valle fault

This fault is seen at a single location (VF 44990779) to the north east of the town of Guajare Faraguit, where it forms the boundary between exposures of carbonate (to the north) and the graphitic schist and quartzite sequence, metamorphosed to kyanite-sillimanite grade (to the south). The orientation of the main fault plane and associated minor shear planes (Riedel shears) indicate that normal movement has occurred along the fault plane, with displacement of the hanging wall to the north (**figure 3.35a**). It is not possible to determine the lateral extent of the structure (as alluvial deposits obscure its extent to the west) or the amount of displacement that the structure causes. However, the juxtaposition of carbonate with the graphitic schist and quartzite sequence may be traced along the strike of the fault for approximately 3 km.

3.6.5.2 Guajare Alto fault

As with the structure discussed above in section 3.6.5.1, the fault at Guajare Alto is exposed at a single locality (VF 44460789) where it forms the contact between a restricted outcrop of the non-graphitic quartzites and schist sequence (metamorphosed to kyanite-sillimanite-andalusite grade) and carbonate rocks - **figure 3.35b**. The main fault plane dips north at a moderate angle: Riedel structures indicate normal movement along the surface. The extent of this fault is obscured to the east by Quaternary deposits and the amount of displacement experienced along this contact is difficult to assess. The juxtaposition of the

non-graphitic schist and quartzite sequence with carbonate is laterally limited, possibly due to other faulted contacts (not seen) between these two rock types to the west (along Bco del Curato) and east (along Rio de la Toba).

3.6.6 Cerro Escalate fault zone

3.6.6.1 Shear fabrics and lineations

The phyllites and carbonates exposed along the road section to the north of Motril (**figure 3.36**) show mica-fish shear indicators and strain fabrics indicative of high strain ratios in the rocks in this section. All the shear indicators show top-to-the-north movement and locally the stretching lineations here, L_{motril} , are oriented to a more north-south orientation than in the rest of the area (i.e. compare **figure 3.37b** with **figure 3.38b**). Folds seen in quartzite layers verge to the west. The stretching lineation on the foliation surfaces – L_{motril} – has a similar orientation to the fold axes of folds seen in the quartzite layers – **figure 3.37b**.

The L_{motril} lineation and the fold axes are likely to have been formed during the same phase of deformation, with both linear features being rotated into the direction of shear.

3.6.6.2 The Cerro Escalate fault surface

At VF 45380692, a large exposure (approximately 10m along-strike) of fault gouge is developed within carbonate (**figure 3.39a & b**) – numerous surfaces and lineations on surfaces were measured (**figure 4.39c**).

The main fault surface has a moderate dip towards the NW-NNW. A second set of surfaces dip more steeply to the NW – NNW; these may be Reidel shear surfaces. The acute angle between these two main surfaces closes to the north in the hanging wall of the fault, indicating normal movement along the fault plane

A near-vertical fault zone that is exposed approximately 4 km to the north (at VF 45360752) clearly indicates a normal sense of movement with the hanging wall moving to the south –

figure 3.40. The extensive shear features developed along this section (described above) imply that this fault is likely to be associated to the Cerro Escalate fault to the south: this steeply inclined fracture may be a R' shear surface with antithetic movement to that of the parent structure.

3.6.6.3 Map relations and regional context

If the NW-NNW dipping Escalate fault plane is extrapolated to the east, the resistant-weathering carbonate rocks that form a local 'cap' on topographical high-points immediately to the east of the fault zone appear to lie within the Escalate fault plane **figure 3.36**.

Elsewhere in this area, carbonate rocks do not clearly overlie the phyllite/quartzite sequence; this is further evidence that the carbonate present above the phyllite sequence to the east is likely to be incorporated into the Escalate fault zone (**figure 3.36**). The 'finger-like' geometry of the carbonate rock forming Cerro Gordo (VF 45340705) is suggestive that this body of carbonate too may also be incorporated into the fault zone.

The thickness of the Escalate fault zone clearly exceeds 20m, although no maximum thickness can be determined from the limited exposure available. The fault can be traced for approximately 5 km along strike.

Overall, the evidence from the area to the north of Motril suggests that the Cerro Escalate fault zone is a NW-NNW dipping normal fault: the graphitic schist and quartzite sequence exposed to the east of the contact is in the hanging wall of the fault (**figure 3.39b**). The phyllites and carbonates cropping out to the east have been incorporated into the fault zone, and are in the footwall of the structure. The contrasting grade of metamorphism across the Escalate fault indicates that important movement occurred along this structure after the end of metamorphism.

3.6.7 Shear fabrics in the phyllite – quartzite sequence

In the phyllite and quartzite sequence that is exposed to the north of Jete (**figure 3.6** – VF 44050726) and in equivalent rocks metamorphosed to muscovite-biotite grade or lower that crop out to the west and east of this location, evidence of extensive shearing is present - **figure 3.38a**. The dominant fabric seen in these rocks is S_1 (**figure 3.18**). The geometry of the shear fabric in the phyllites indicates consistently top-to-the-north-east movement, and the

lineations on the shear surfaces are consistently oriented NE-SW throughout the extent of the phyllite and quartzite exposures (**figure 3.40**). Shear fabrics with top-to-the-north / north-east movement are also seen where the phyllite and quartzite sequence crops out to the south and north of Loma de Cerrajon (VF 44850715).

3.7 Deformation after the end of metamorphism

The orientations of the S_s and S_t foliations, and the ductile and brittle discontinuities have been deformed by broad (wavelength of 500 m and greater) anticline and syncline structures with axes trending approximately E-W. The traces of 3 antiforms may be identified within the area, two of which extend for a distance greater than 15 km. Two synforms are identified, one of which has a traceable extent of greater than 15 km - **figure 3.41**.

Similar late-formed features have been identified in other locations within the Betic Cordillera (i.e. Orozco *et al*, 1998): the open structures in this area have formed in response to north-south directed compression in the late Miocene (Comas *et al*, 1999).



Figure 3.11 Fold hinge from the D_S phase of folding developed in quartzite layer, showing pronounced thickening in the hinge of the fold. Long edge of compass is aligned to the S_t foliation that has caused subsequent deformation of the D_S fabrics. Graphitic schist and quartzite sequence - exposure at VF 44230676

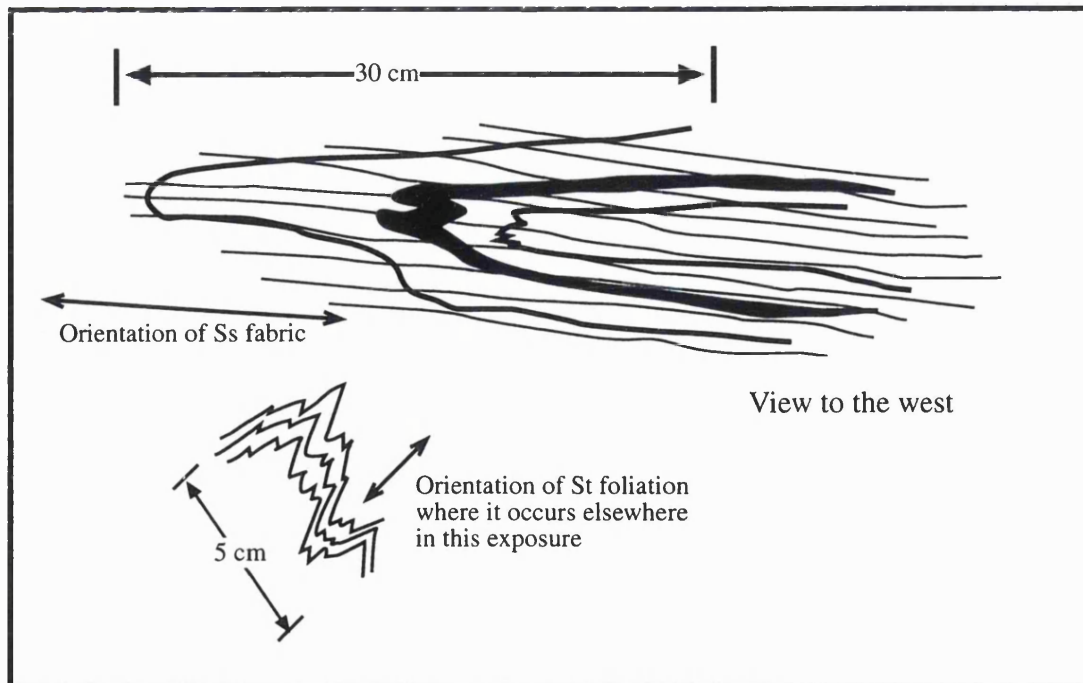


Figure 3.12 Field sketch of D_S fold hinge developed in graphitic schist and quartzite sequence: the S_S fabric is clearly axial planar to the D_S fold hinge. In the D_S fold hinge, the S_S fabric is locally at right angles to the compositional layers in the quartzite-schist sequence: in the limbs of the fold, the compositional layers and the S_S fabric are parallel. Graphitic schist and quartzite sequence - VF 44640672.

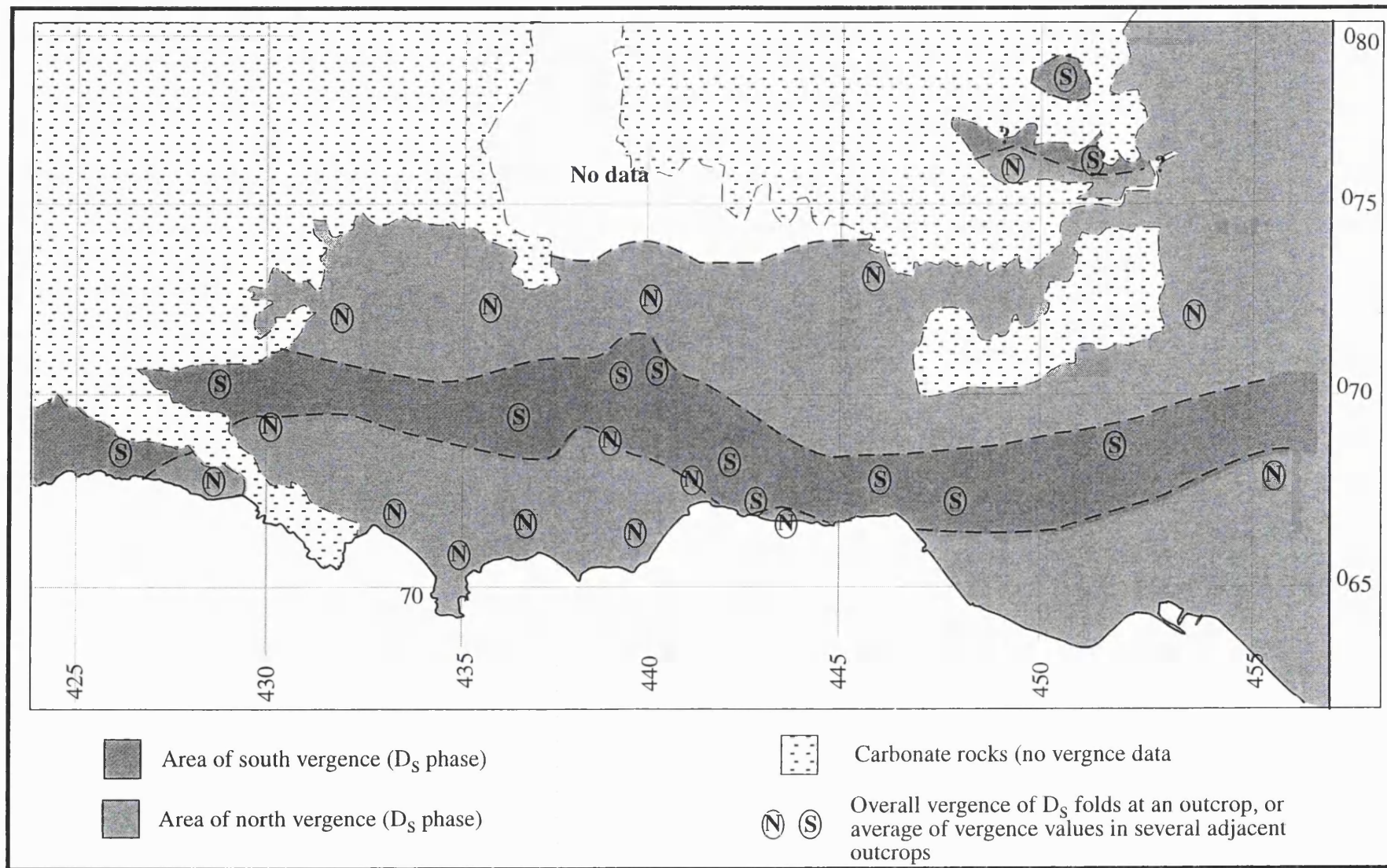


Figure 3.13 Areas of north and south vergence of the D_5 phase folds.

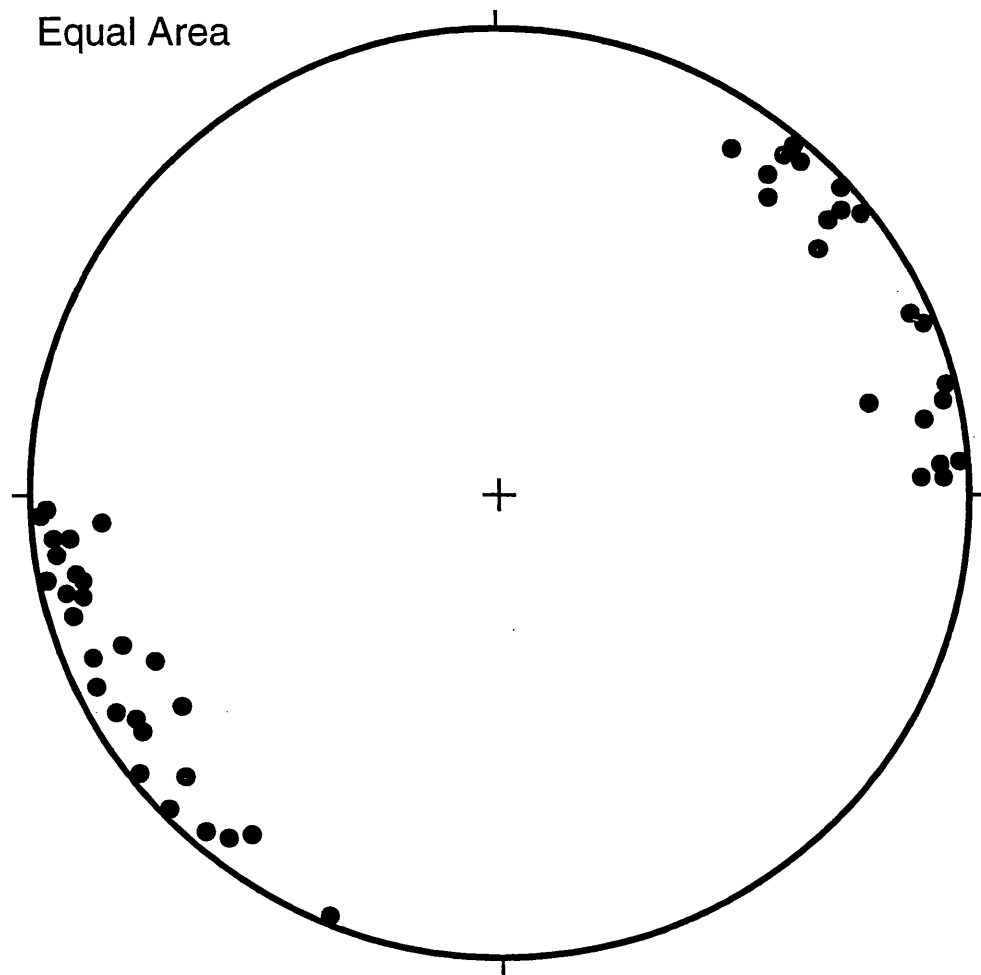


Figure 3.14 Stereonet plot indicating the orientation of some fold hinges related to the D_S phase of deformation. The trend of the data is approximately to 60° : the fold axes have a consistently gentle plunge. The trend of the fold axes relating to the D_S event is also identified by the orientation of the bands of varying vergence of the D_S folds (see **figure 3.13**).

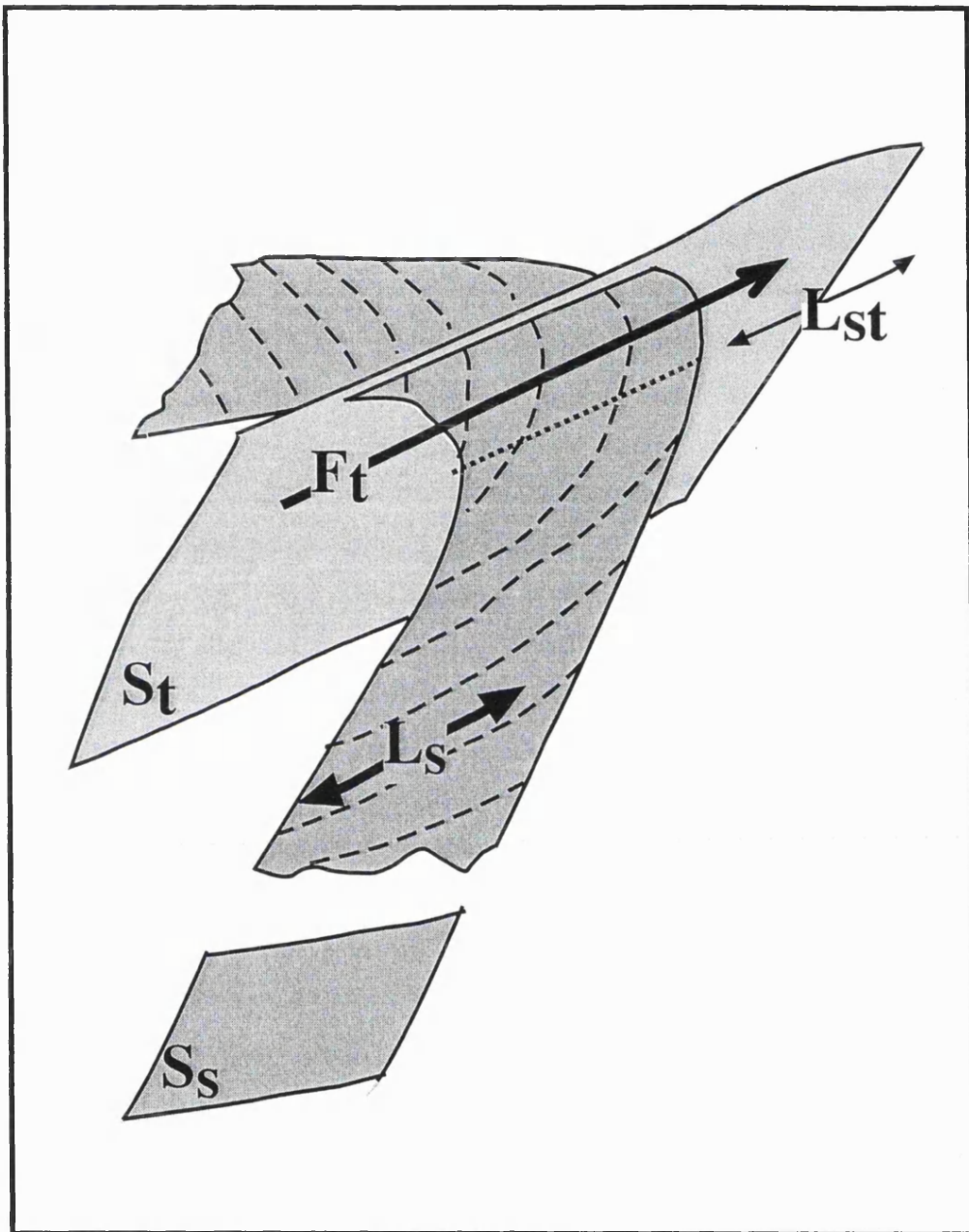
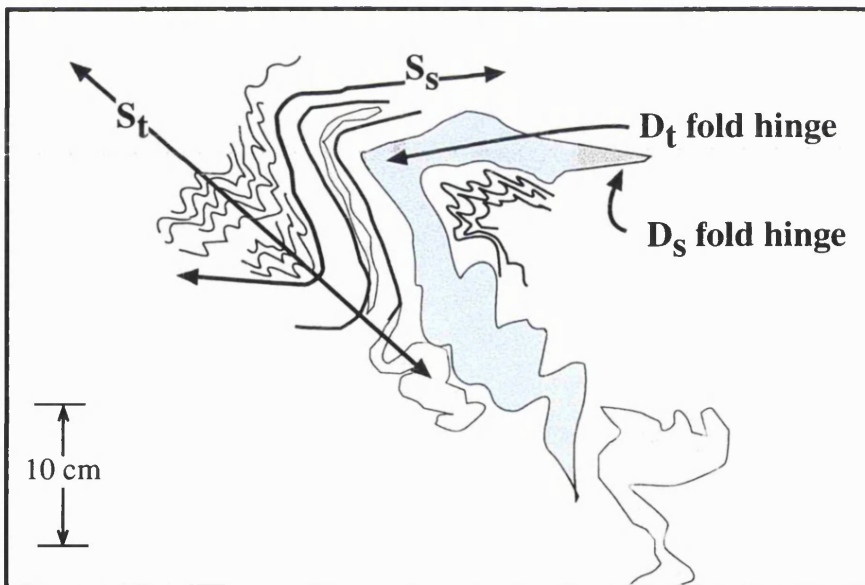


Figure 3.15 Schematic sketch of the relationship between fabric elements generated by the D_s and D_t deformation events. The L_s lineation is not exclusively parallel to the L_{st} lineation (the intersection lineation of S_t on S_s). Where the S_t foliation is not pervasively developed, the L_s lineation wraps around the F_t fold hinge. This relationship clearly indicates that the L_s lineations predate the D_t deformation.



Quartzite



Quartz vein

Figure 3.16 Graphitic schist and quartzite sequence at VF 44240668. Photograph (top) and interpretation (below).

The band of quartzite within the area of exposure shown here has preserved the (now folded) S_s fabric: the S_t foliation is clearly seen to be axial planar to the D_t fold hinge. In the areas of the exposure dominated by schist, the S_t fabric is pervasively developed. Thin quartz veins, apparently aligned to the S_s fabric may show boudinage forms and are deformed by the D_t deformation.



Figure 3.17

Example of the S_1 foliation cross-cutting fabrics from the D_1 deformation. The pale quartzite layers preserve fold hinges of the D_1 folds and the parting between the quartzite and schist layers approximates to S_0 . The long edge of the compass is aligned with the S_1 foliation; spacing of adjacent S_1 planes in the schist layers is very close (2mm) while this separation is greater in the quartzite layers.

Graphitic schist and quartzite sequence at VF 44320669. View looking East.

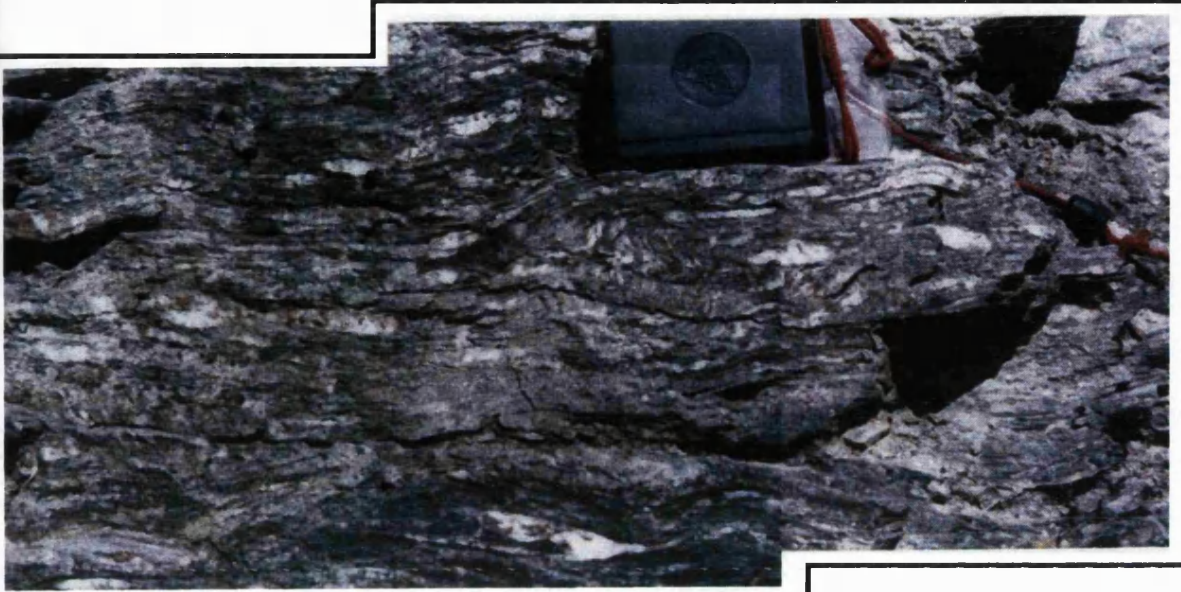


Figure 3.18

3.18a Above

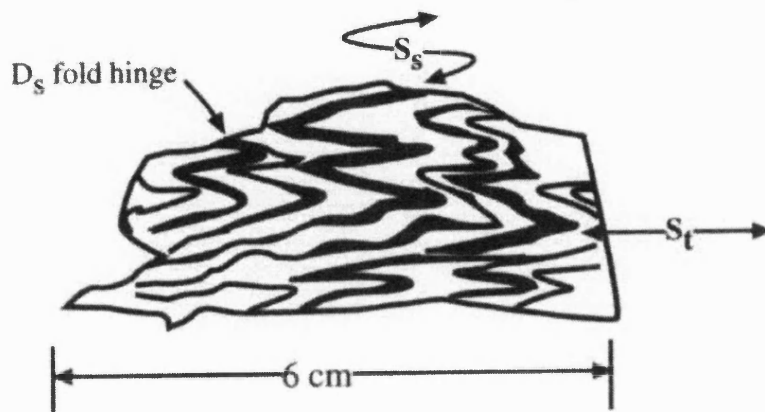
Quartz-rich area within the phyllite and quartzite sequence, in which tight folds in the S_2 foliation are preserved. Away from the more competent quartz-rich area (containing numerous small quartz veins) the main fabric (S_1) is parallel to the axial plane of these small folds.

At VF 44040740 - muscovite-chlorite grade

3.18b Below

Detail of a section through phyllitic band cut at 90° to the lineation. The D_2 fold hinges are apparent, and the S_2 foliation is still visible. The S_1 foliation is locally the most dominant fabric in the section.

At VF 44060731 - muscovite-biotite grade.



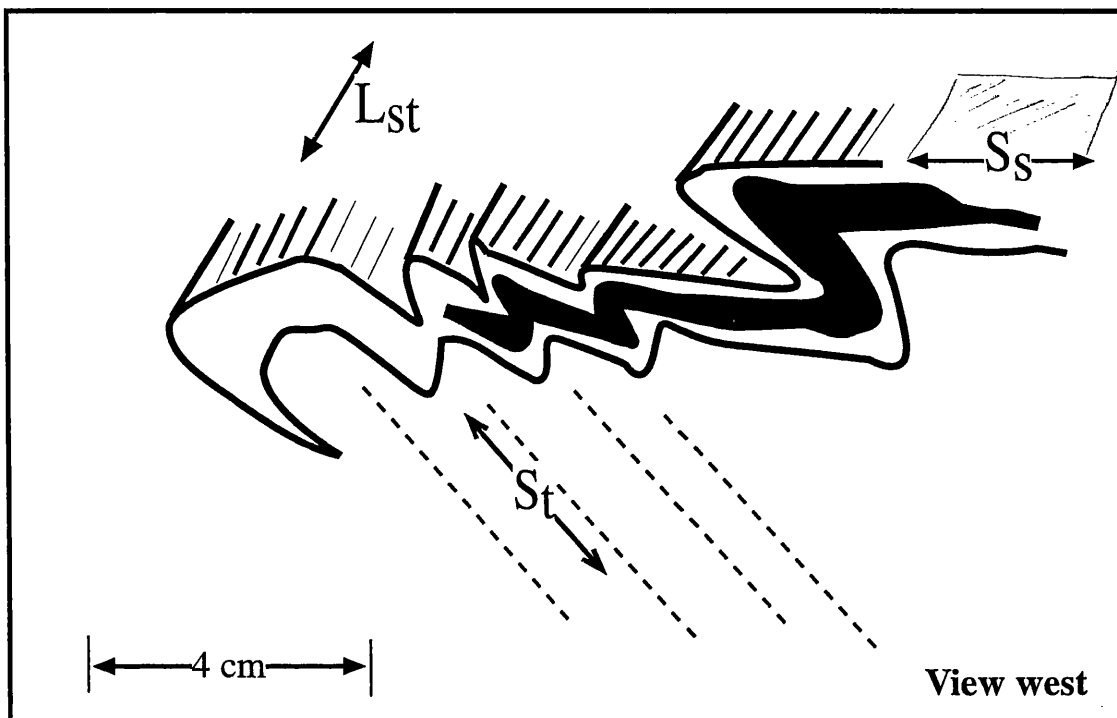
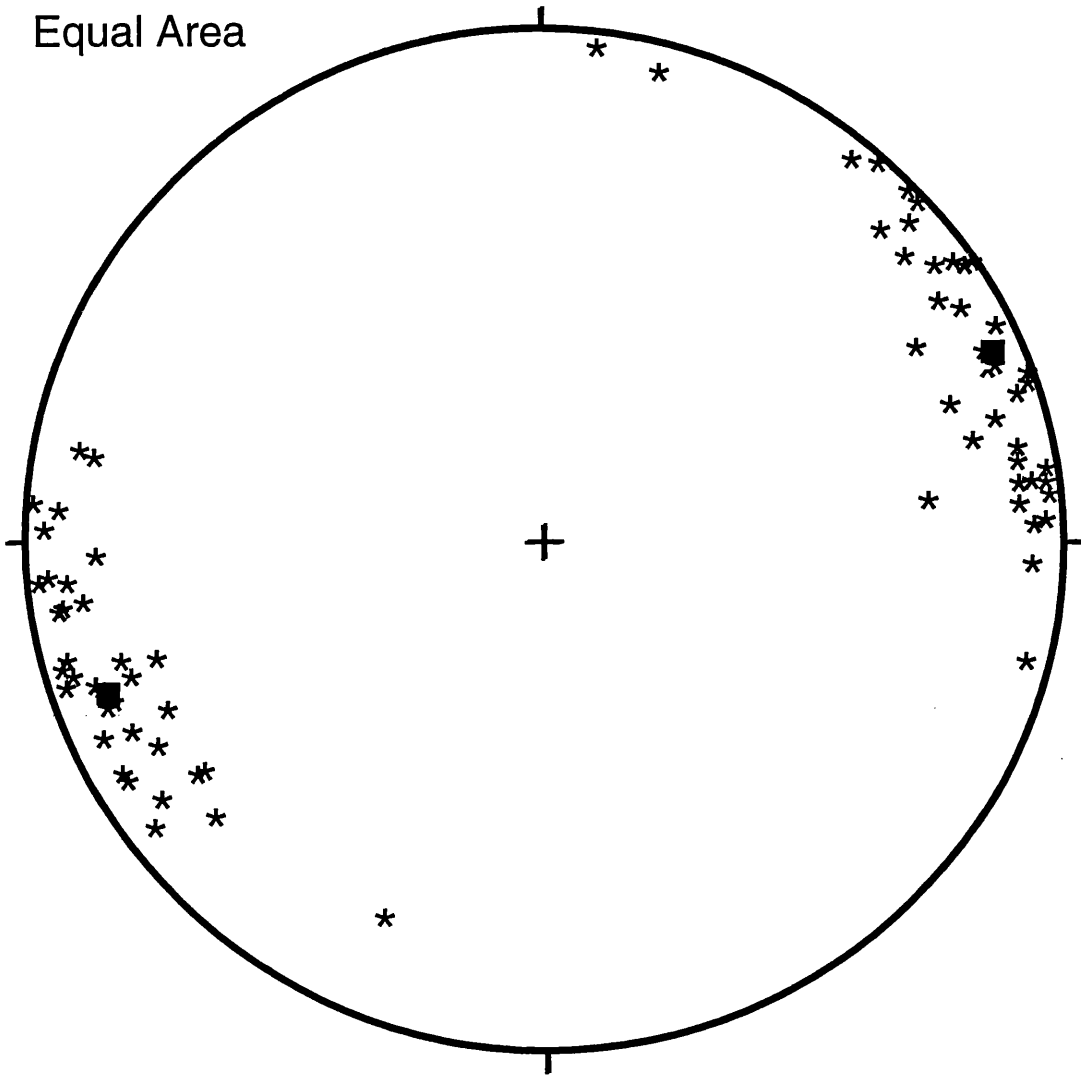


Figure 3.19 Field sketch showing the nature of the lineation L_{st} . The S_s foliation is deformed by the D_t deformation: the intersection of S_t with S_s generates the L_{st} lineation that lies within the S_s foliation plane. Fold axes of the D_t folds are parallel to the L_{st} lineation. Fabrics seen in graphitic schist and quartzite sequence at VF 43900678.

Equal Area



- * Orientations of F_t (axes of the folds generated by the D_t deformation)
- Average orientation of F_s : averages calculated individually for the NE and SW plunging populations of lineations.

Figure 3.20 Stereonet plot of fold axes relating to the D_s and D_t phases of deformation. The fold axes of both sets of lineations trend towards either NE / ENE or SW / WSW. The F_t lineations plunge more steeply than the F_s lineations in some locations.

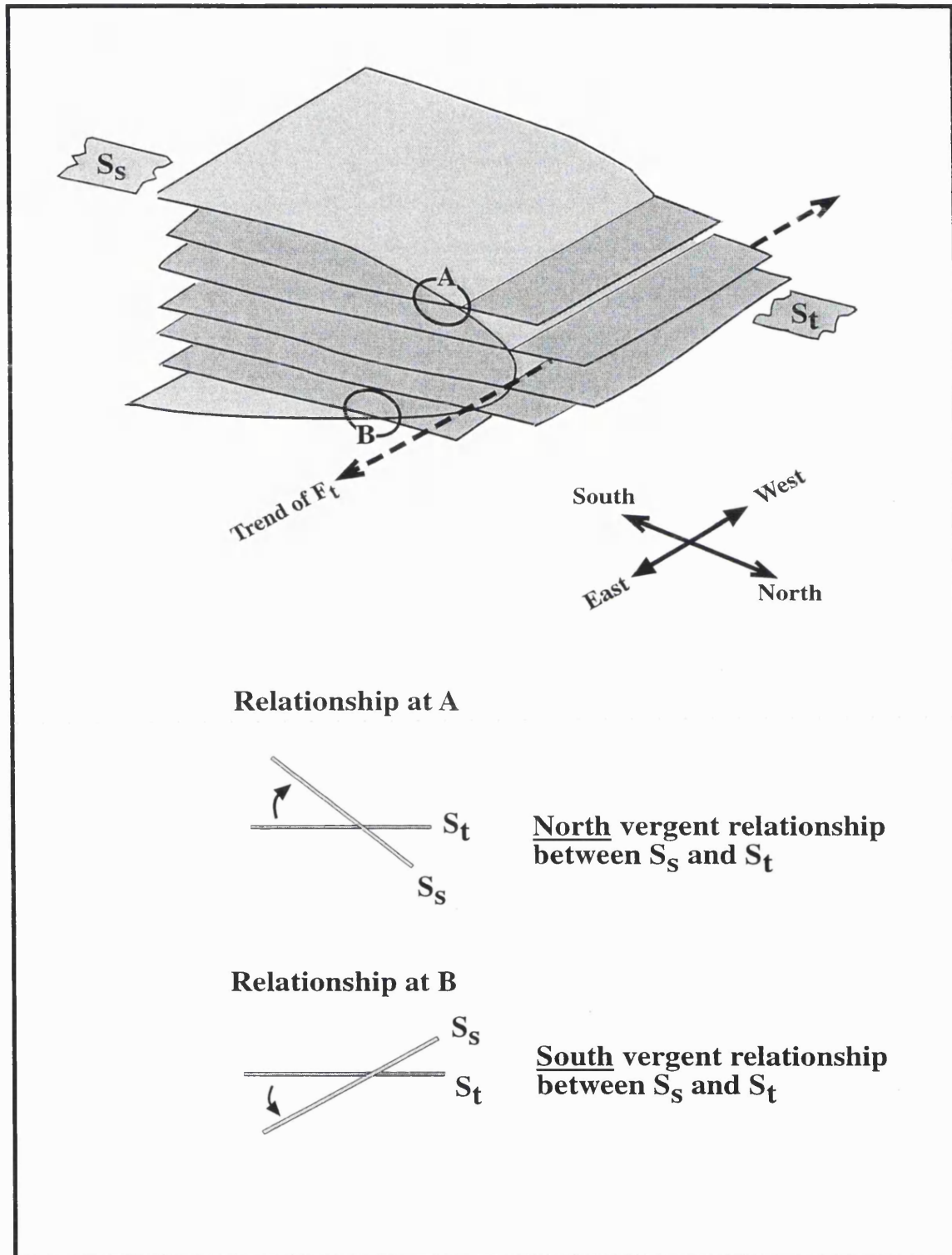


Figure 3.21 Schematic sketch of D_t fold hinge and the relationships of the S_s fabric to the S_t foliation on either side of the D_t hinge. The D_t fold hinge, F_t , trends east-west, so the vergence of the S_s - S_t relationship is either to the north or south. The direction of vergence between the S_s and S_t fabric changes across the fold hinge.

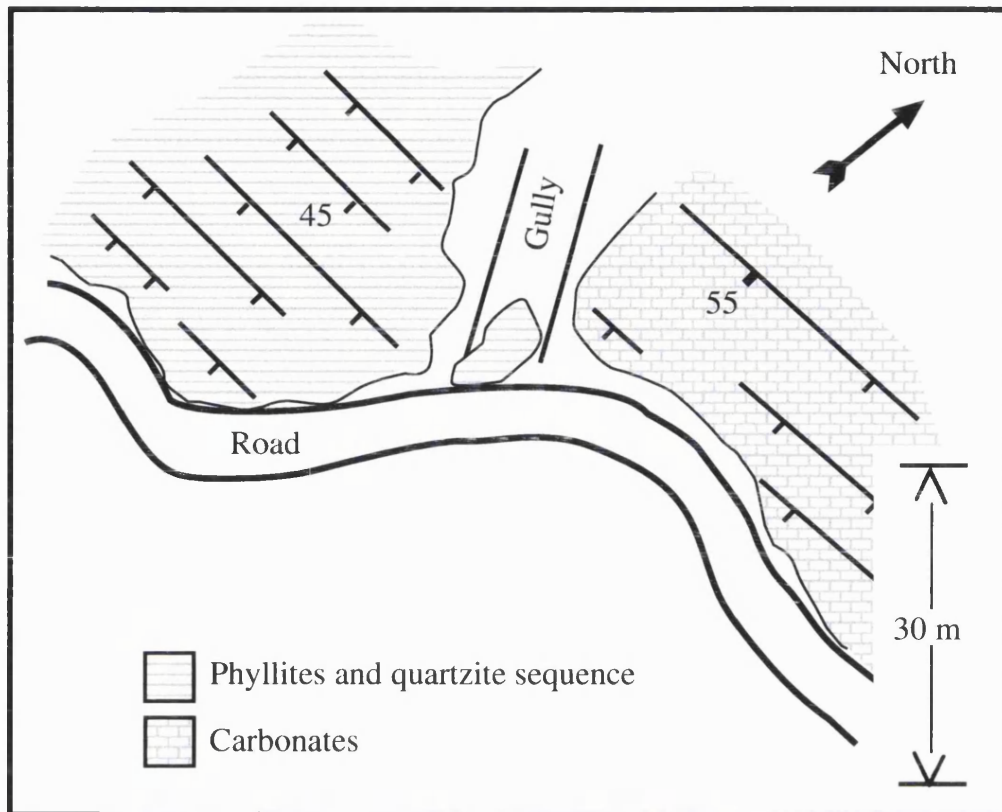
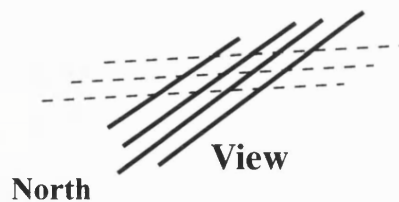
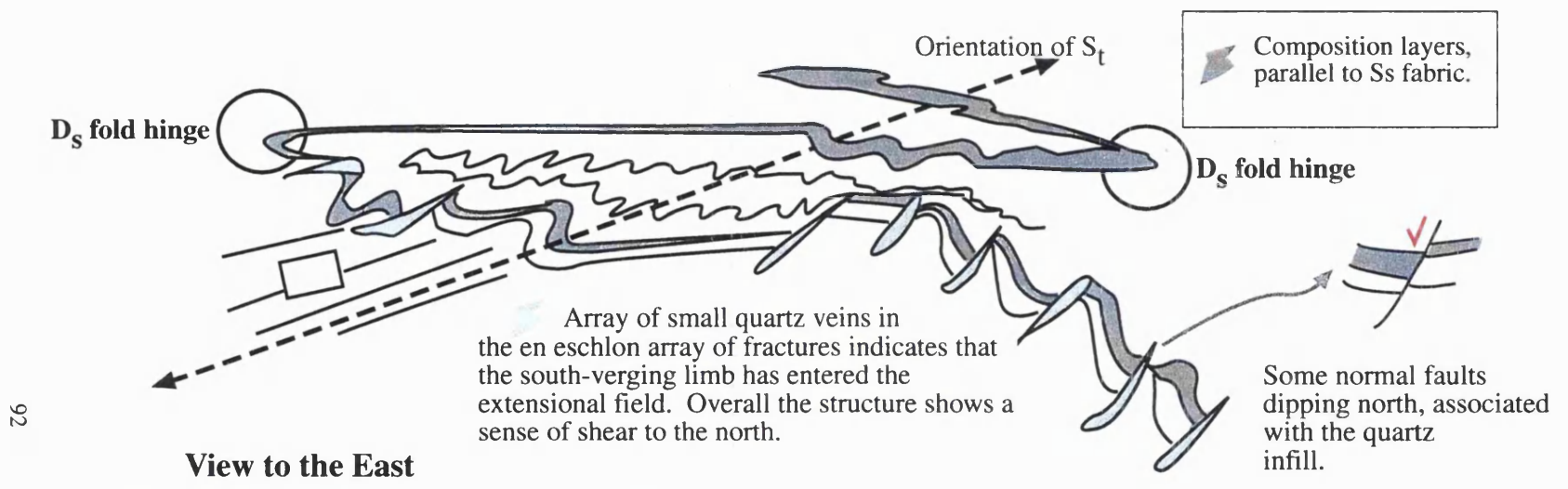


Figure 3.22 above Plan view of inverted contact between phyllite and quartzite sequence and carbonates. Both sequences dip moderately steeply towards the south: the carbonates clearly dip beneath the phyllite and quartzite sequence. Contact seen at VF 43740764.

below Photograph of the inverted phyllite - carbonate boundary: some intercalations of phyllites are locally seen at the base of the carbonate unit, indicating that here the boundary is likely to be an original stratigraphic contact. VF 43770767.

S_s (dark lines)
 S_t (dotted lines)
 Orientation in phyllite and quartzite sequence indicates a south verging relationship.





92



Figure 3.23
 Field sketch and photograph from west of 'Urbanisation Delta' - VF 44230676. The S_t - S_s fabric relations are clearly south vergent. The geometry of the fold limb is more elongate than that seen in the right-way-up (north-verging) limbs of the D_t folds.

El Tumbo Contact

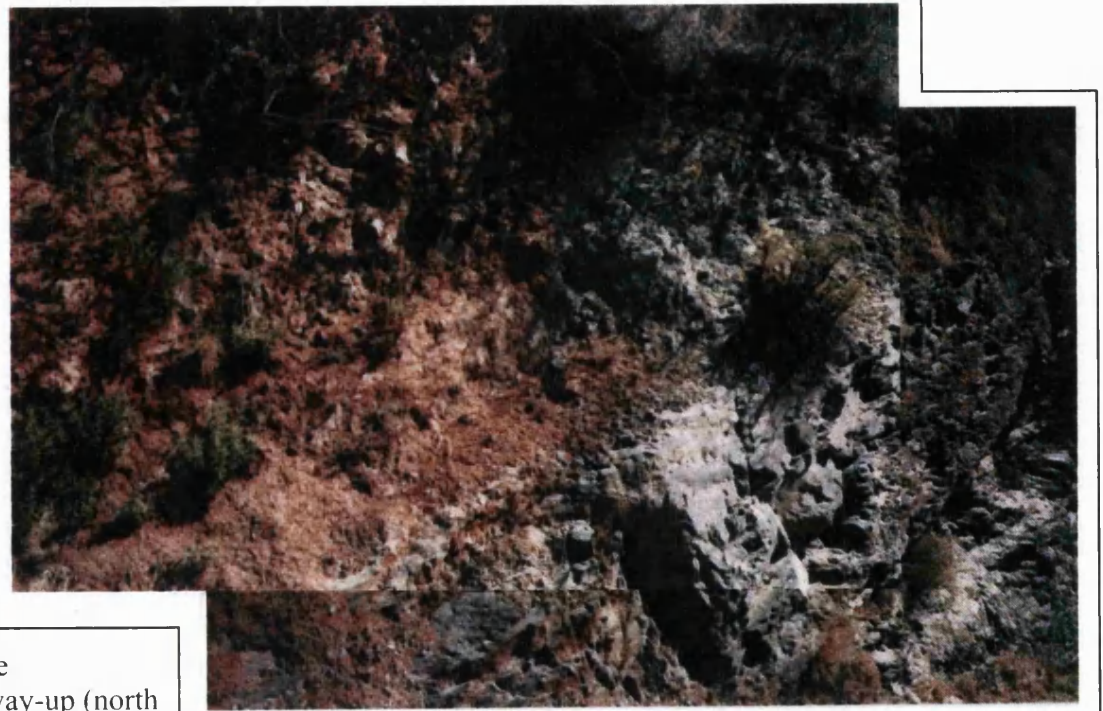
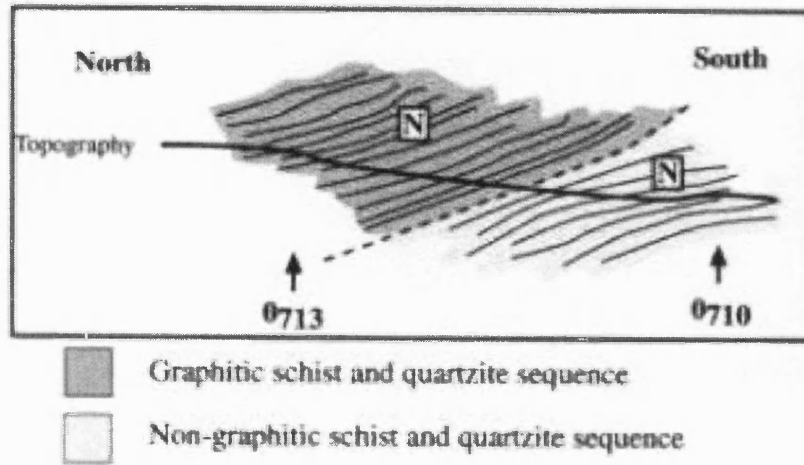


Figure 3.24a above

Field sketch and photograph of El Tumbo contact, seen on Jete Road cross section (figure 3.20) at VF 44020714. In a right-way-up (north verging) limb of a D_1 fold, graphitic schists and quartzites lie structurally above the non-graphitic schist and quartzite sequence. Along 100° .

Figure 3.34b right

Photograph of Molvizar contact at VF 44560714, taken along a bearing of 000° . The graphitic schist and quartzite sequence is seen to the west (on the right), overlying the non-graphitic schist and quartzite sequence to the east (left).

Hammer for scale. Shaft lying parallel to the contact.



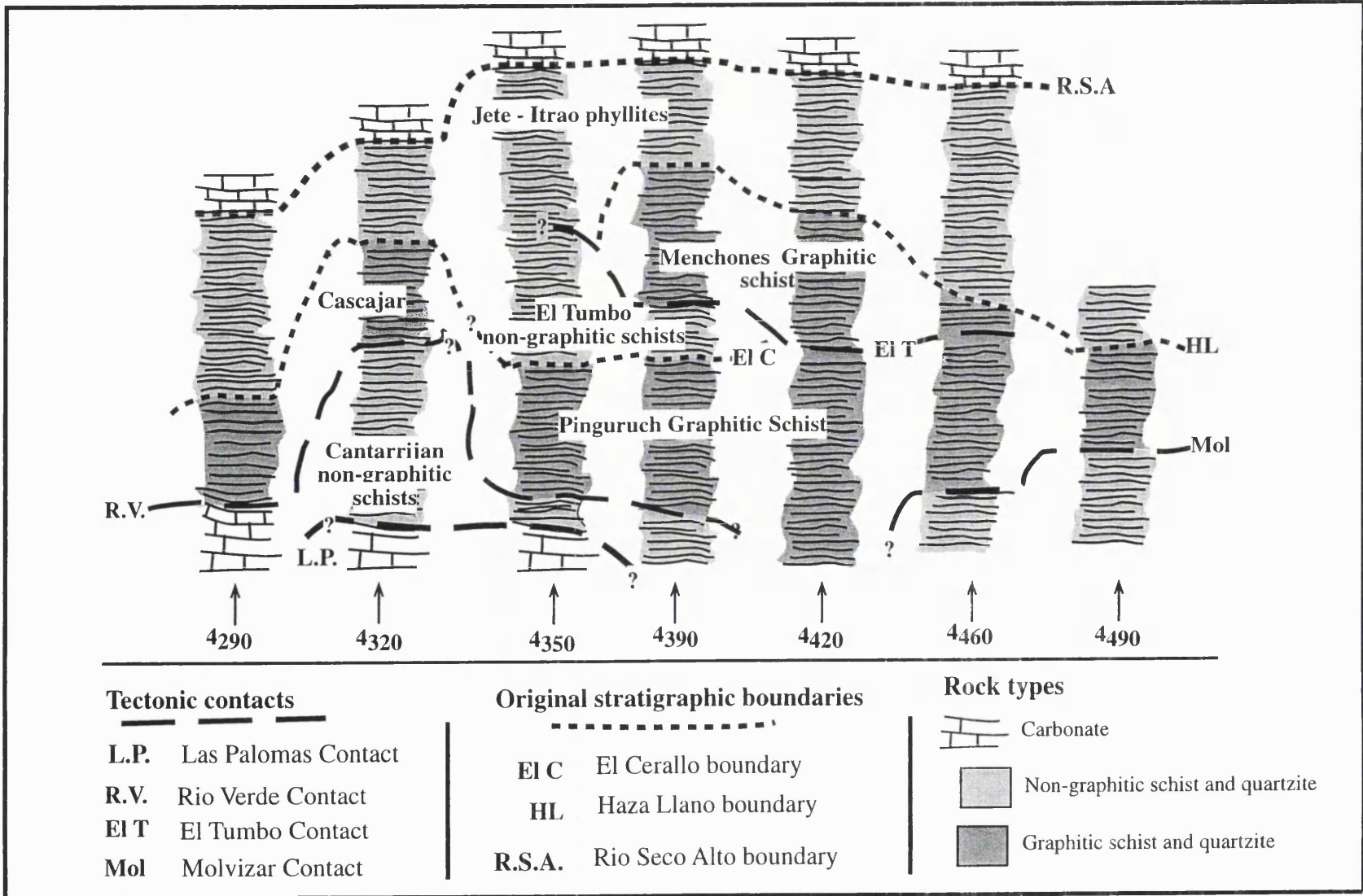


Figure 3.25 Configuration of the Alpujarride Complex in the area near to Almunecar after the D_s deformation, prior to the development of inter- D_s/D_t structures.

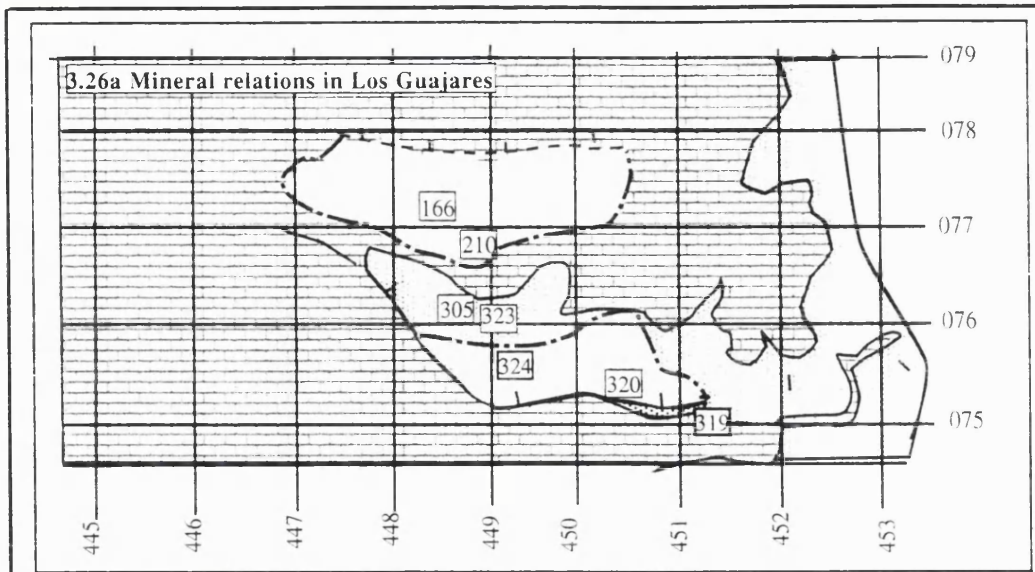


Figure 3.26

Maps to show locations of D_s/D_t contacts. The contacts separate rocks with different early (high T) metamorphic history and similar late (low pressure) history.

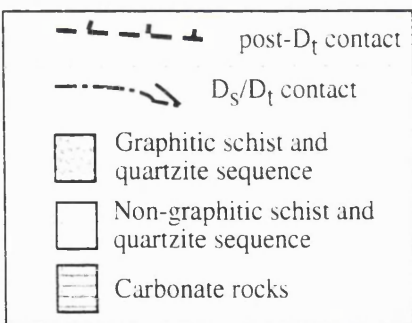
3.26a top Los Guajares area
3.26b bottom South of Cerrajon

High grade rocks

- 320 Ms Sil Grt Bt And Pl Qtz
- 324 ms Sil grt ky bio and qz
- 210 Ms St Grt Bt Pl Qtz Ilm
- 166 Ms Sil And St Grt Bt Qtz

Low grade rocks

- 305 Ms Bt And Chl Pl Qtz
- 319 Ms Chl And Pl Qtz
- 323 Ms Bt And Qtz Mag

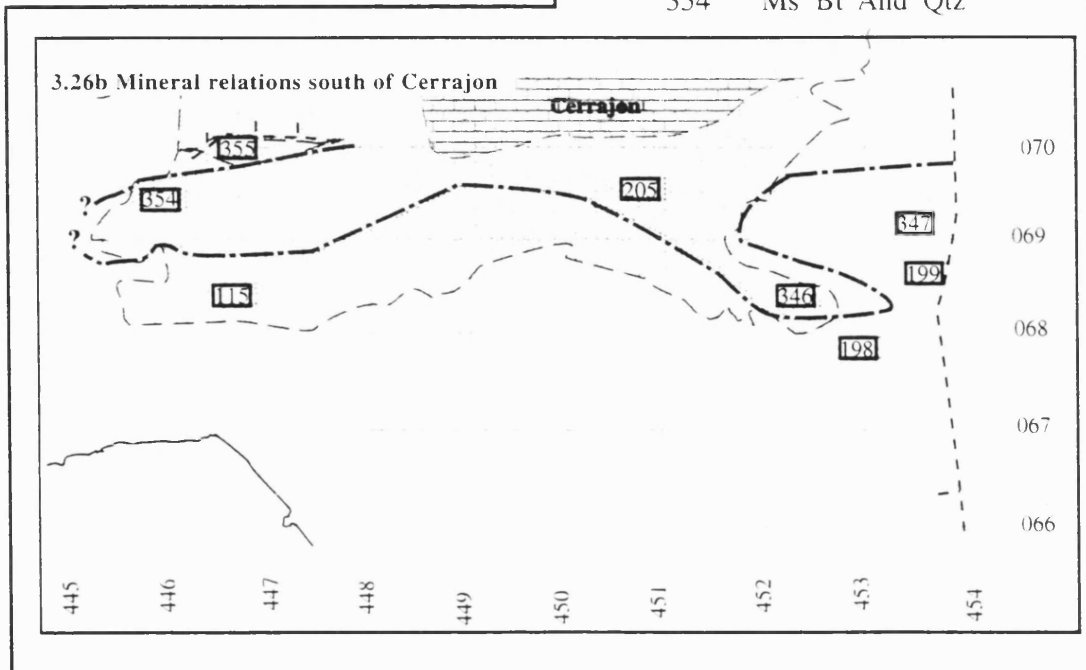


High grade rocks

- 115 Ms Bt St And Pl Qtz
- 198 Ms Bt St And Pl Qtz
- 199 Ms Grt Bt And Pl Qtz
- 347 Ms Grt St Bt And Qtz
- 355 Ms Sil Grt Bt And Qtz

Low grade rocks

- 205 Ms Bt And Pl Qtz
- 346 Ms Chl And Pl Qtz
- 354 Ms Bt And Qtz



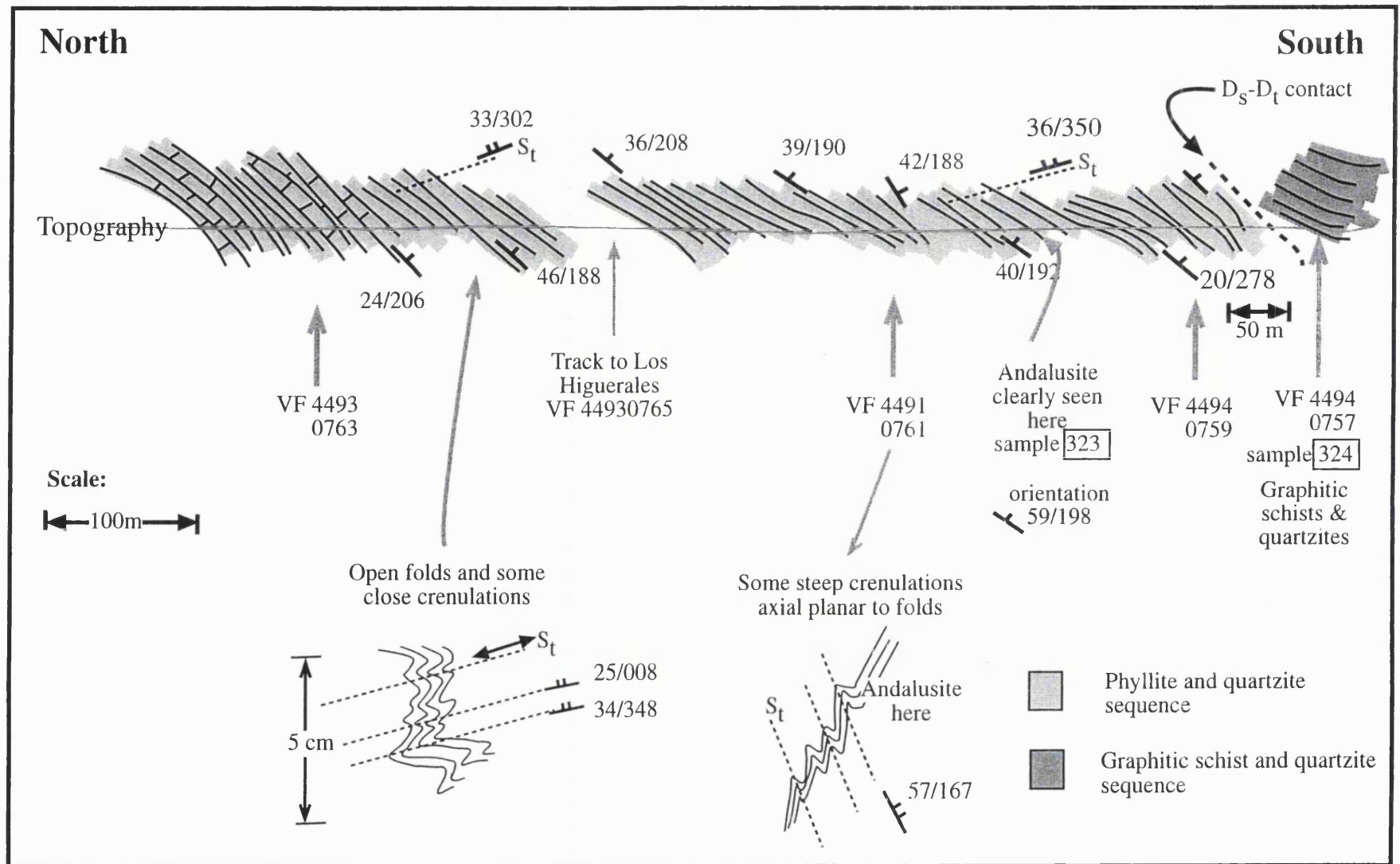
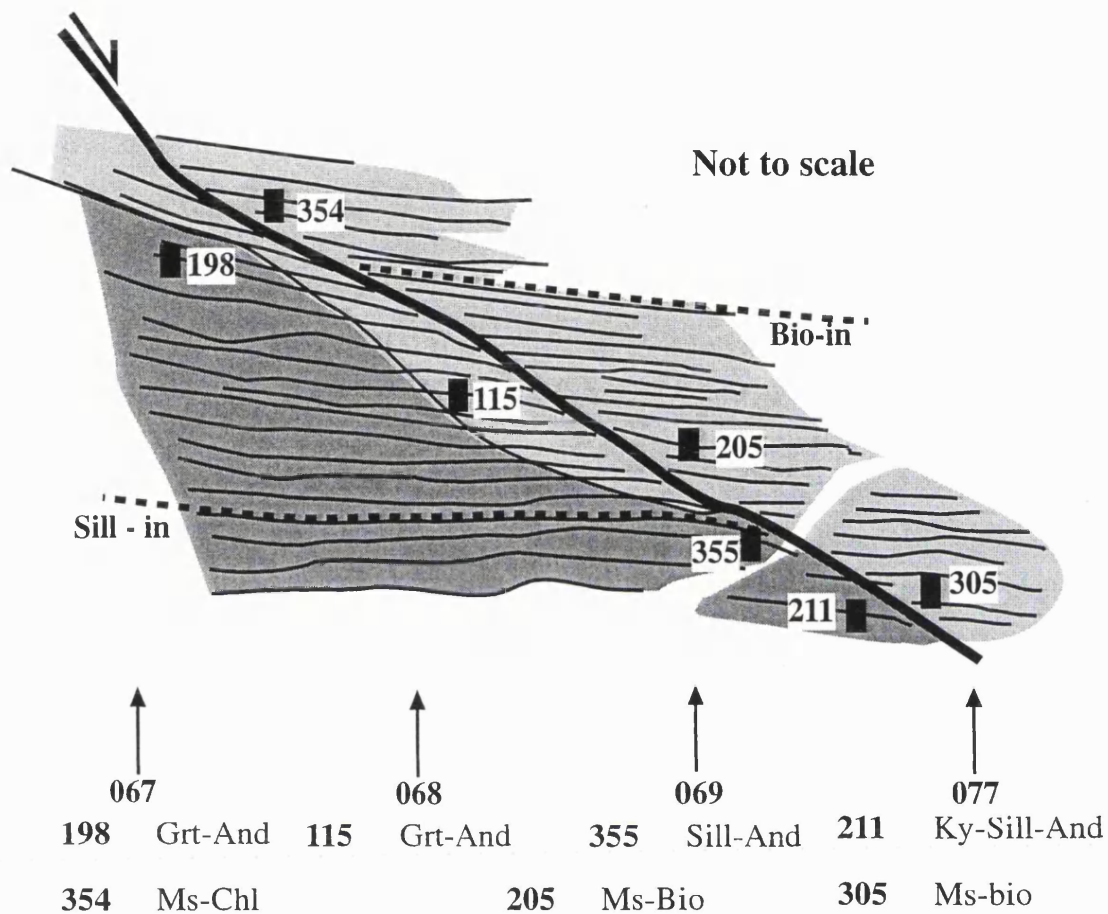


Figure 3.27 Area within Los Guajares, SE of Guajare Fondon. Field sketch from notebook showing relationships of carbonates, phyllites and quartzites and the graphitic schist and quartzite sequence. The phyllites and graphitic schists are separated by an inferred ductile contact that formed after the high temperature phase of metamorphism (during or after the D_S event) but before the low pressure part of the P-T history.



Key

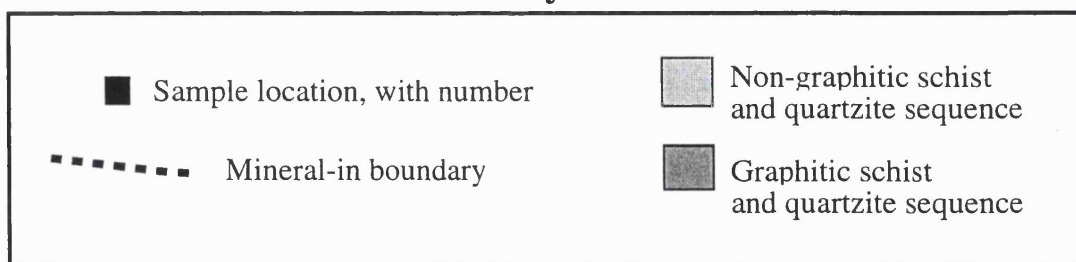


Figure 3.28 Synthesised vertical section across the D_S/D_T structure to the south of Loma de Cerrajon, prior to the D_T deformation. The section shows the relationship of the low and high-grade rocks in this area with the D_S/D_T contact: the northing line along which the samples are located, and the grade of the sample, is shown at the base of the section, and the grade to which each sample has been metamorphosed.

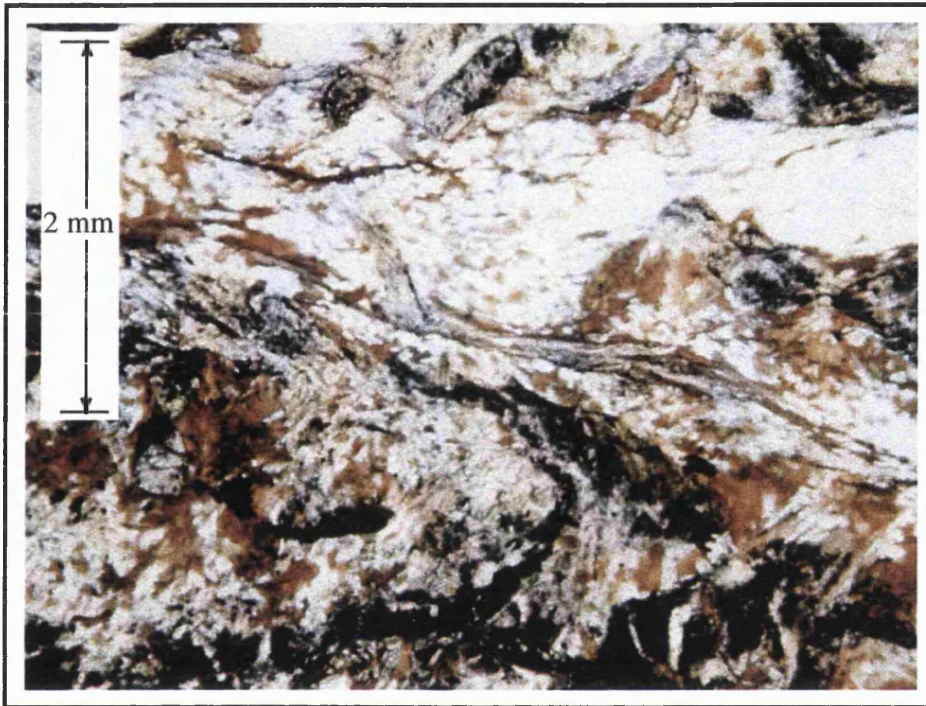


Figure 3.29

View of thin section cut parallel to the L_{st} lineation (XZ plane) of sample LH194 (Garnet/staurolite-andalusite grade). In thin orientation, shear planes that cut across all mineral phases in the samples are identified.

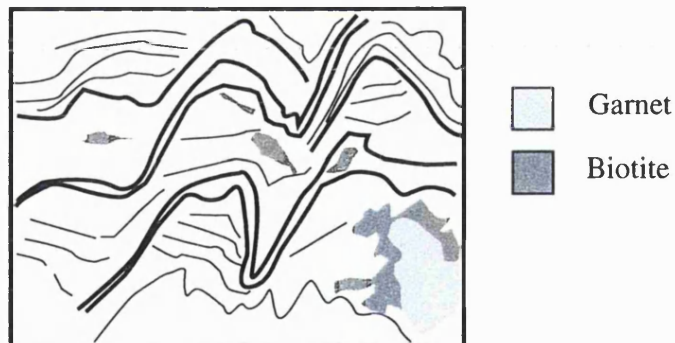


Figure 3.30

View of thin section cut at 90° to the L_{St} lineation (XZ plane) of sample LH194 (Garnet/staurolite-andalusite grade). In thin orientation, alternating layers of quartz-rich and mica-rich rock (S_S) terminate against surfaces containing biotite, folded by the D_t deformation. These surfaces are likely to be the shear surfaces that cut across the fabric seen in sections parallel to the L_{St} lineation (see **figure 3.29**). As the shear surfaces are folded by D_t , it may be deduced that some shearing in this sample occurred between the D_s and D_t deformation events.

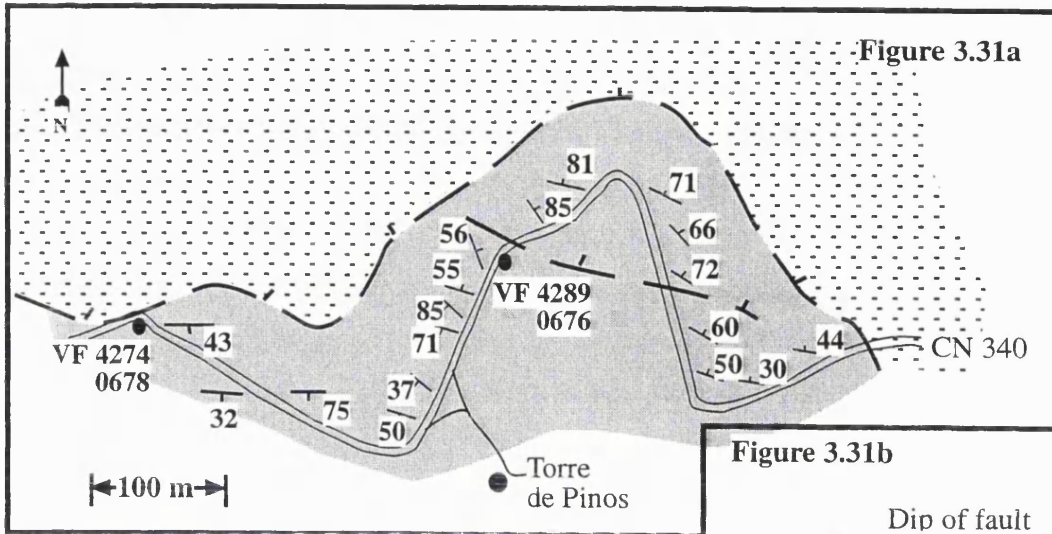


Figure 3.31

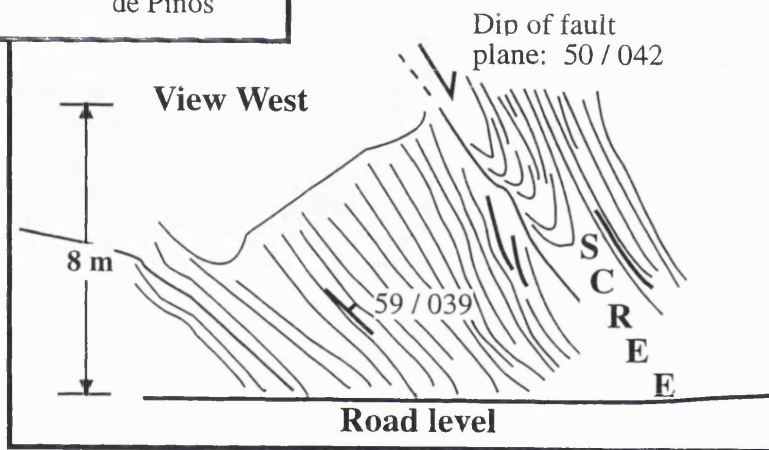
3.31a

Sketch map of part of the Torre Miel fault zone, showing dip of Ss foliation and trace of faulted contacts.

- Non graphitic schist and quartzite
- Carbonate

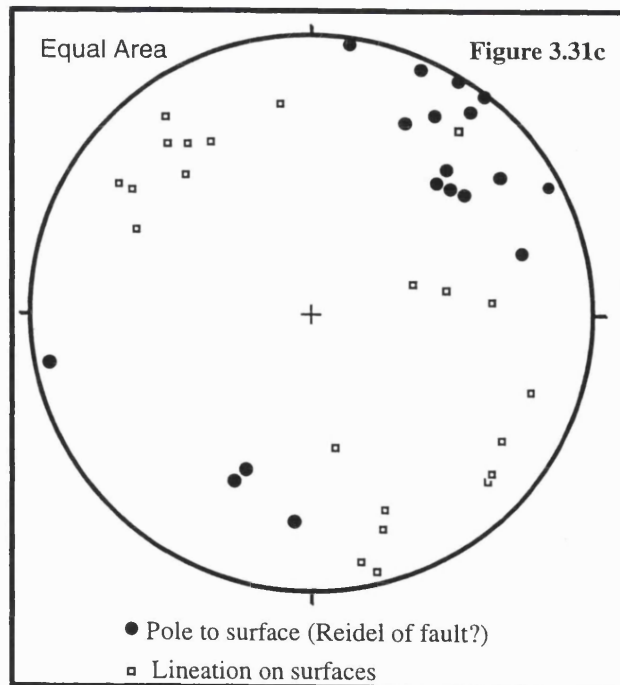
Trace of faulted contact

Figure 3.31b



3.31b Field sketch of the Torre Miel fault at VF 42890676

3.31c Stereonet plot of data from exposure of Torre Miel fault at VF 42740678.



- Pole to surface (Reidel of fault?)
- Lineation on surfaces

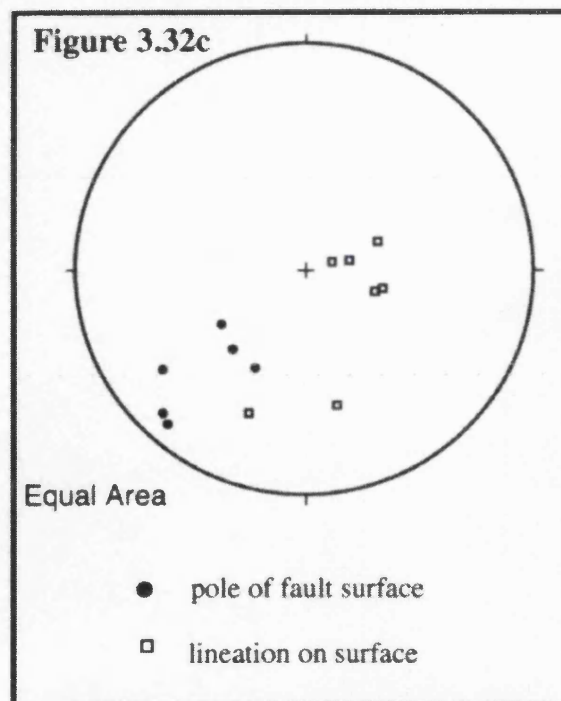
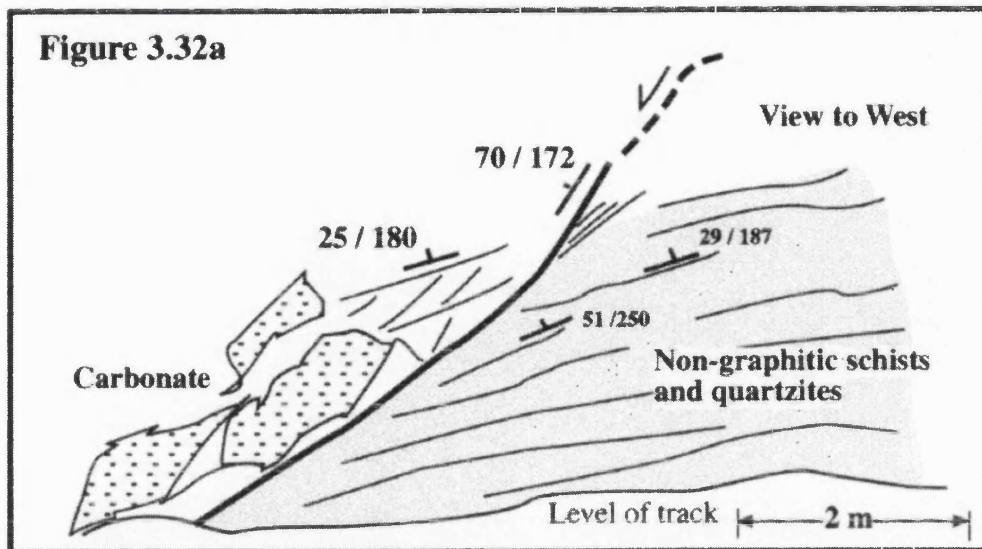


Figure 3.32a
Field sketch of Cerro Caleta fault zone where it is exposed north of Cerro Caleta (VF 43010683). The fault plane dips to the south: carbonates are in the hanging wall and graphitic or non-graphitic schists form the footwall.

Figure 3.32b
Photograph of lineations developed on a surface in carbonate, representative of the Cerro Caleta fault zone. View along bearing of 310° at VF 42980677. Hammer to lower left of surface for scale.

Figure 3.32c
Lineations from the Cerro Caleta fault plane where it is exposed at VF 43010683. Fault plane dips steeply or moderately to the south - lineations on the fault surface dip down the fault plane.

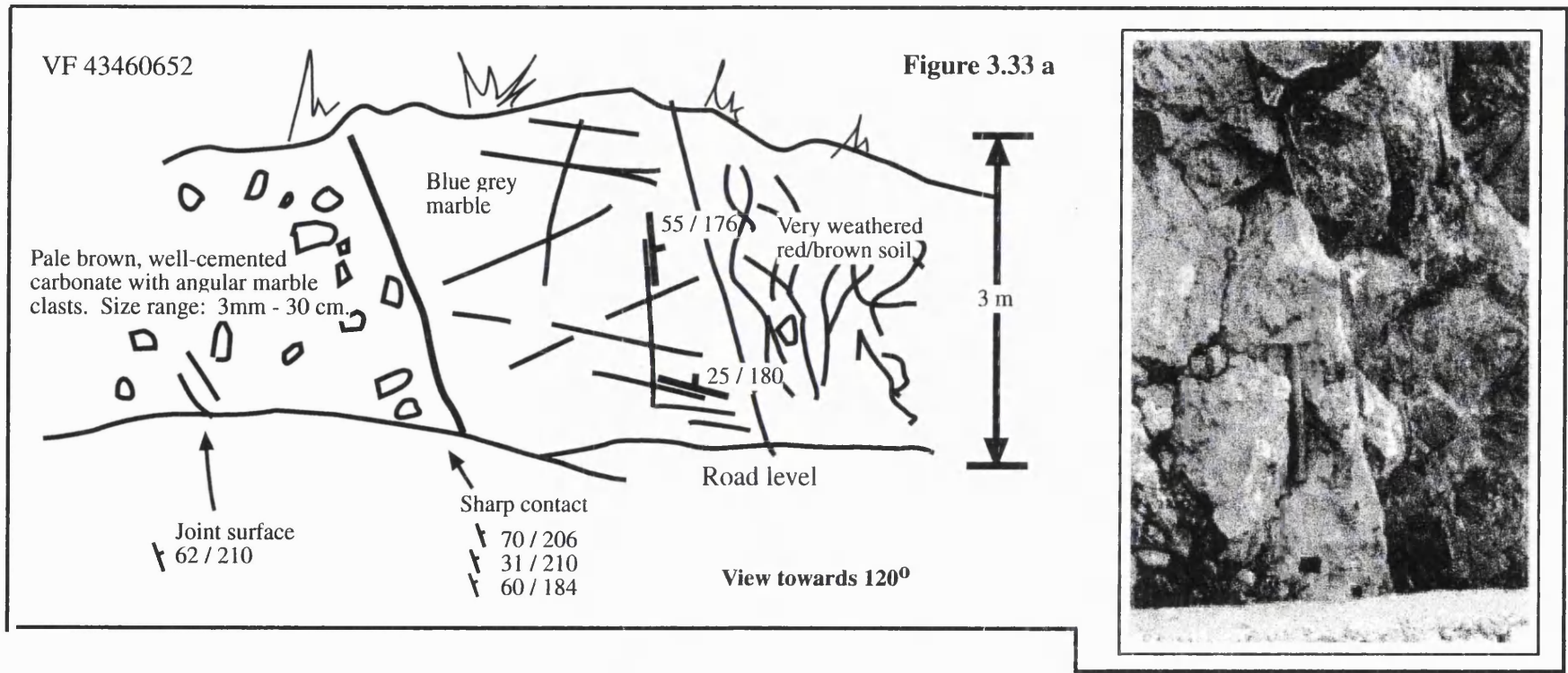
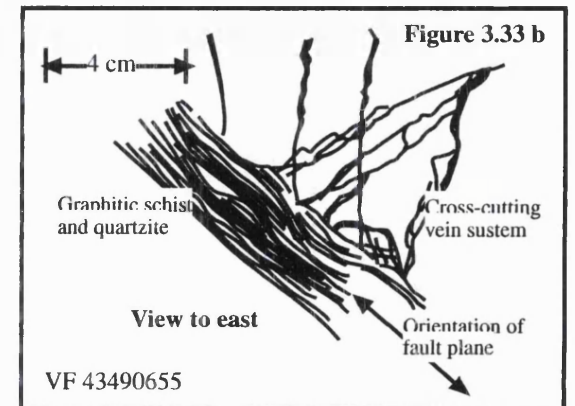


Figure 3.33a Local fault plane, dipping to the south, developed in the carbonate sequence. The fault plane is a sharp contact, close to which extensive recrystallisation of the carbonate, and some brecciation, has occurred as a consequence of movement along the fault plane.

Figure 3.33b South-dipping surface developed within the graphitic schist and quartzite sequence, forming part of the south-dipping Cerro Caleta fault zone at the north edge of the Punta de la Mona carbonate mas. Pseudotactalyte has developed. along the contact shown here.



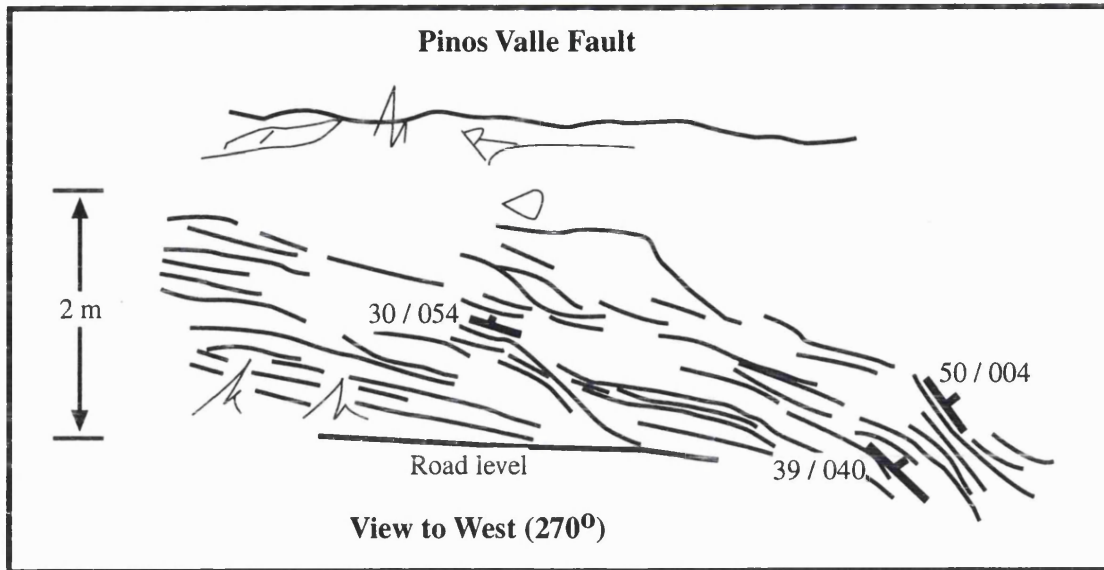


Figure 3.35a (above) Field sketch of the north-dipping normal fault seen at VF 44990779. Carbonates are exposed immediately to the north of this location: to the south, graphitic schist and quartzite sequence is seen.

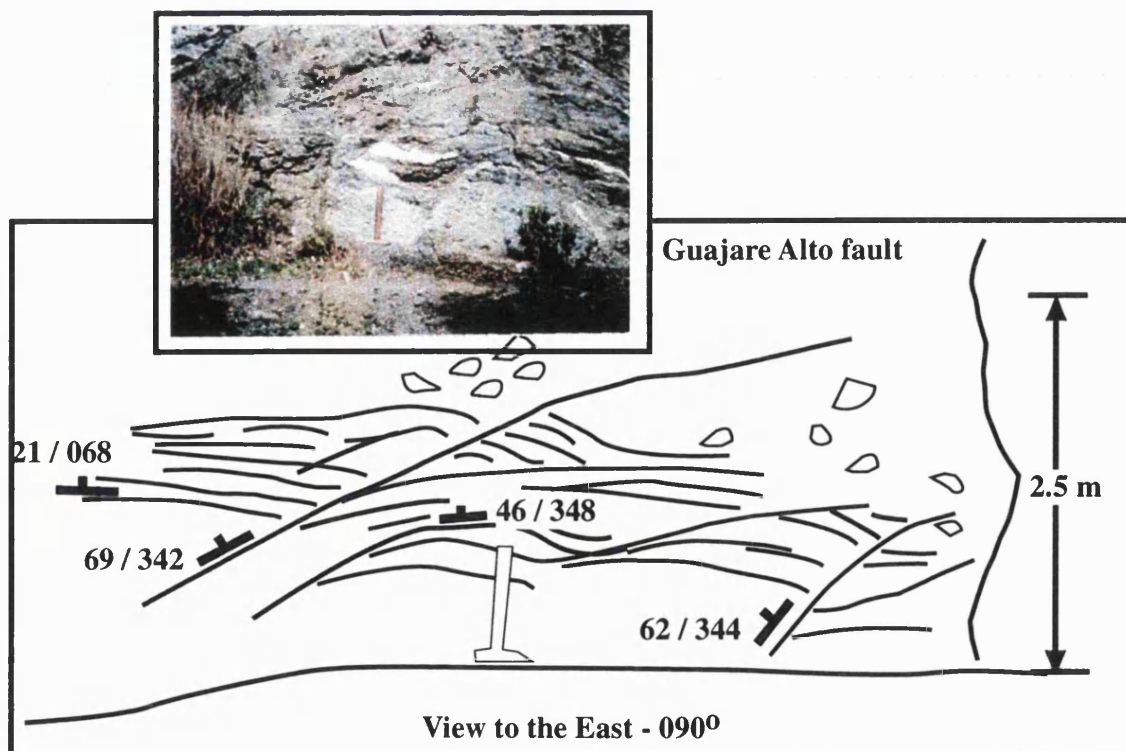
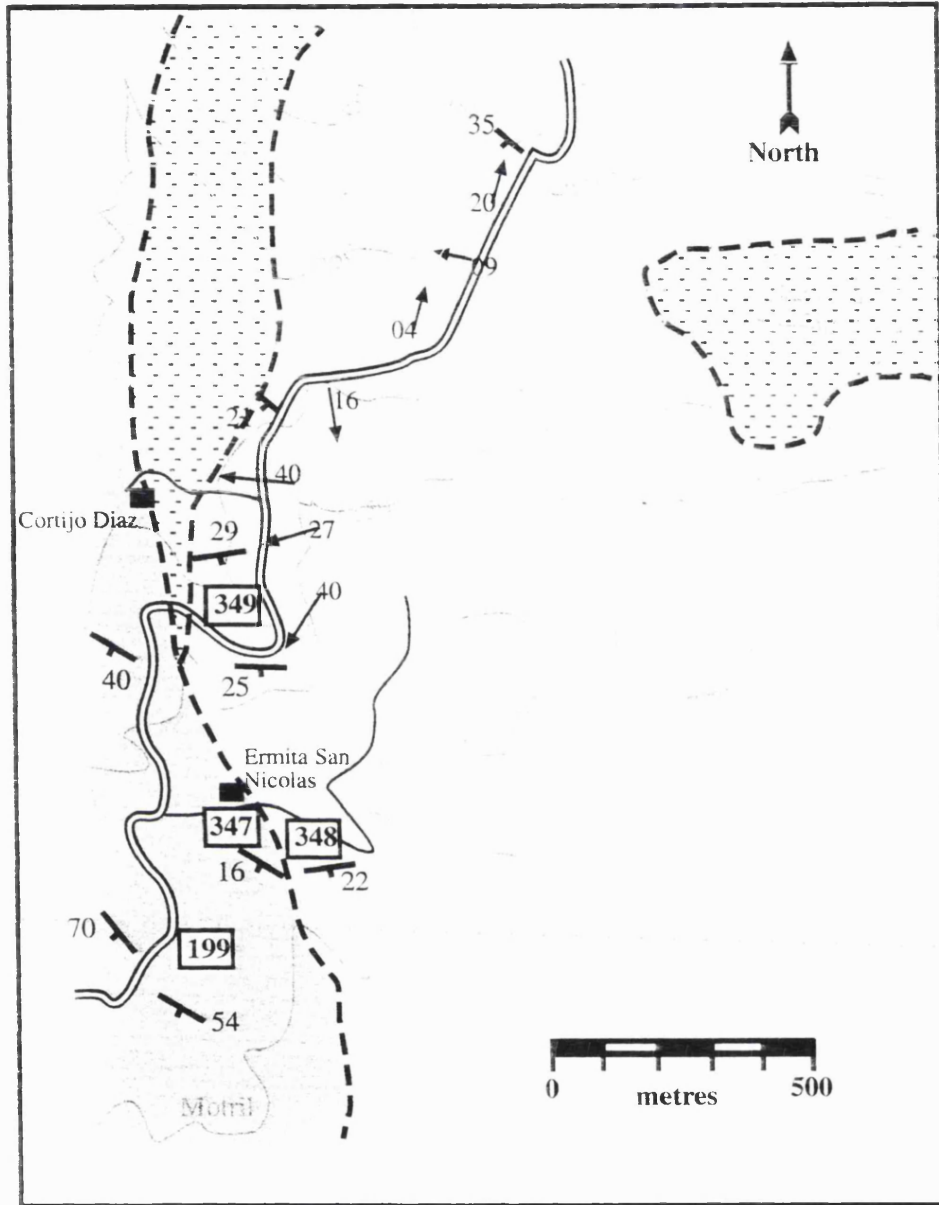


Figure 3.35b (above) Field sketch and photograph (inset) of fault present at VF 44460789. The main fault surfaces dip to the north: the geometry of the Riedel fractures indicates normal movement along the fault. River deposits obscure the amount of displacement.



0700

0690

0680

4540

4550

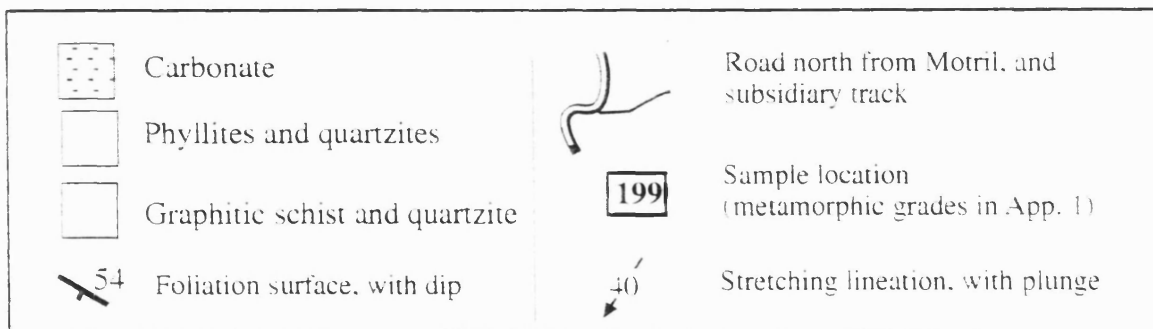


Figure 3.36 Map of the area to the north of Motril showing the contact relations near to the Cerro Escalate fault zone.

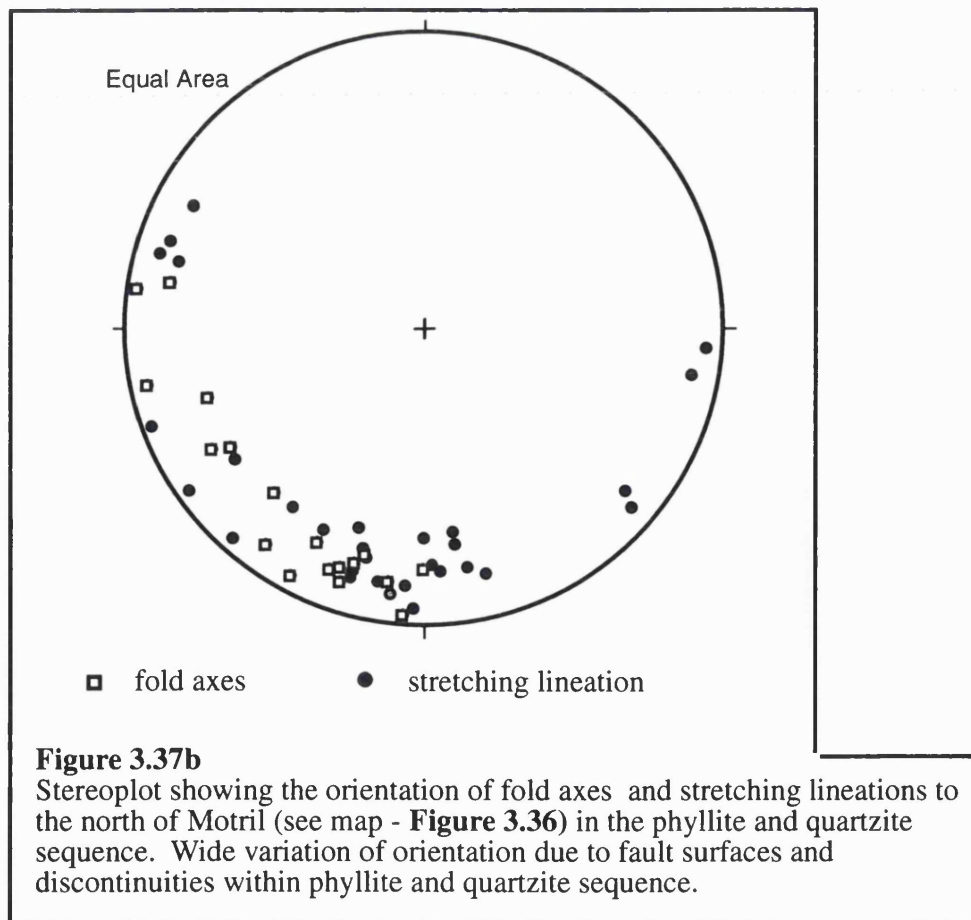
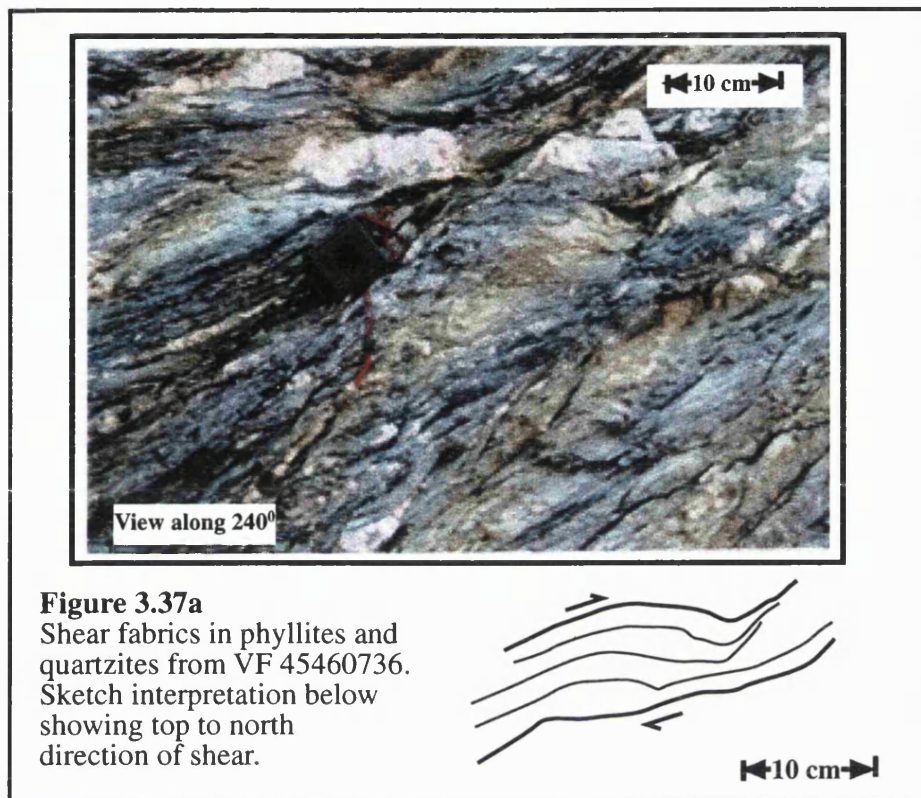




Figure 3.38a Photograph from VF 44060730 - north of Jete. View towards 080° . Thin layers of phyllite develop shear indicators that are inclined gently to the south. Long edge of compass is parallel to main fabric (S_t) in outcrop.

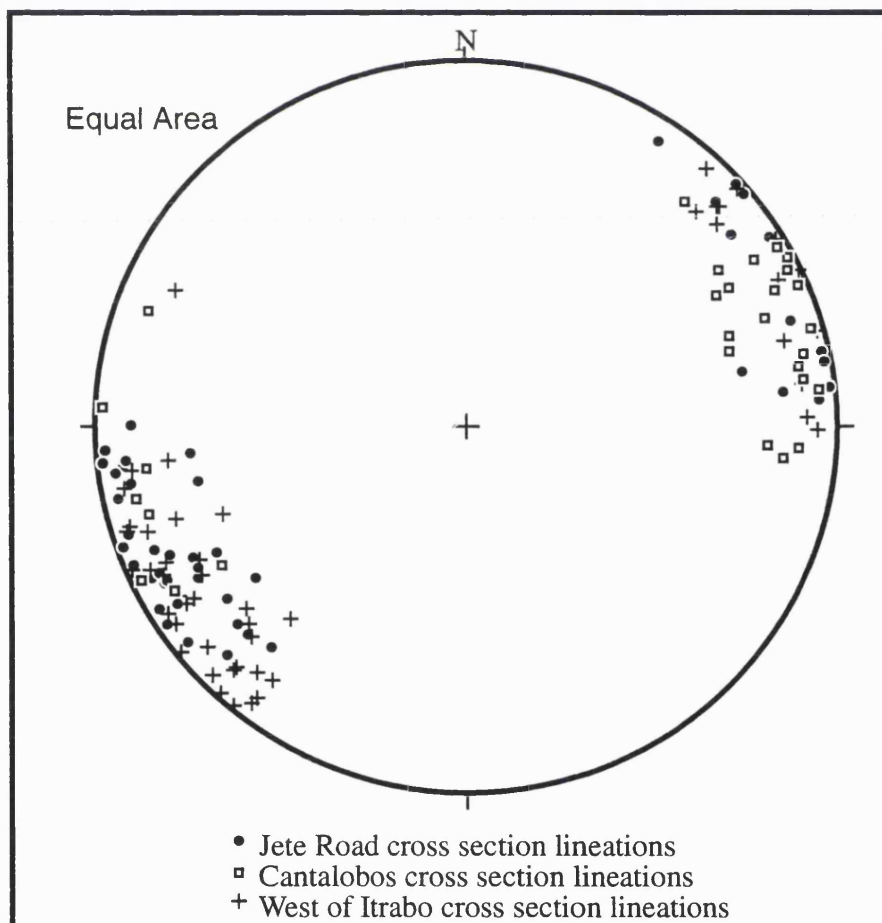


Figure 3.38b L_{st} lineations plotted on a stereonet from three areas in which the phyllite and quartzite sequence is exposed. The orientation of the lineations is very consistent across the area, indicating consistent shear direction in the ductile - brittle regime.



Figure 3.39b Fault gouge developed in carbonate at VF 45390692. View along 020°. Surface inclined at moderate angle to the NNW, defined by edge of intense gouge fabric, may indicate main fault plane. Subsidiary surfaces, dipping more steeply to the north are Reidel fractures. The acute angle between these two surfaces indicates hanging wall moved NW down dip of fault.



Figure 3.39b View along 020° from VF 45380691, approximately along the trend of the Escalante fault. Carbonate peak to the east (right hand side) at VF 45410706, is in footwall of fault; graphitic schist and quartzite to west (left hand side) at VF 45350703 in the hanging wall of the fault.

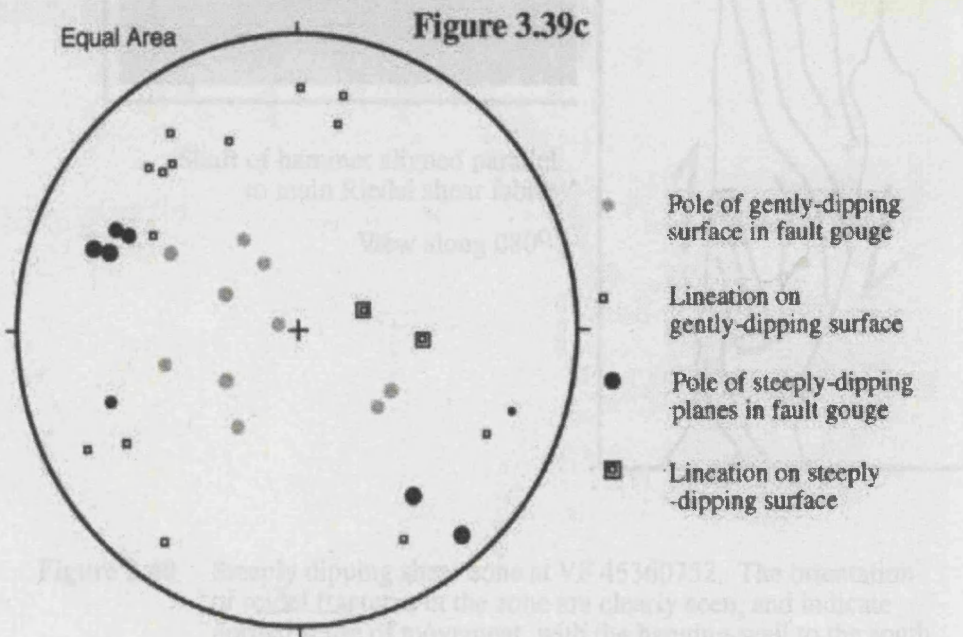


Figure 3.39c Stereoplot of surfaces and lineations measured in exposures of fault gouge in carbonate around VF 45390692.



Shaft of hammer aligned parallel
to main Riedel shear fabric

View along 080°

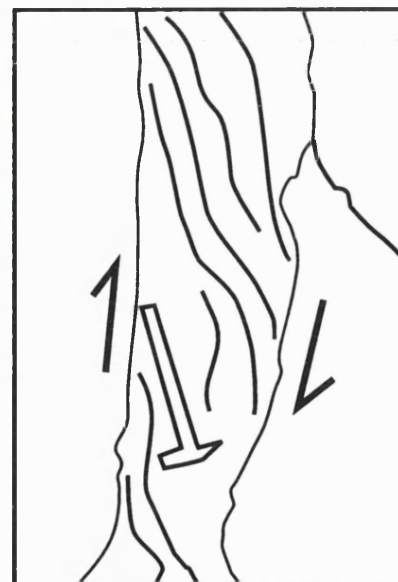


Figure 3.40 Steeply dipping shear zone at VF 45360752. The orientation of reidel fractures in the zone are clearly seen, and indicate normal sense of movement, with the hanging-wall to the south. It is hypothesised that this fracture may represent an R' shear surface of the Cerro Escalate fault zone. R' - type surfaces characteristically have an opposite sense of displacement to that of the main displacement surface.

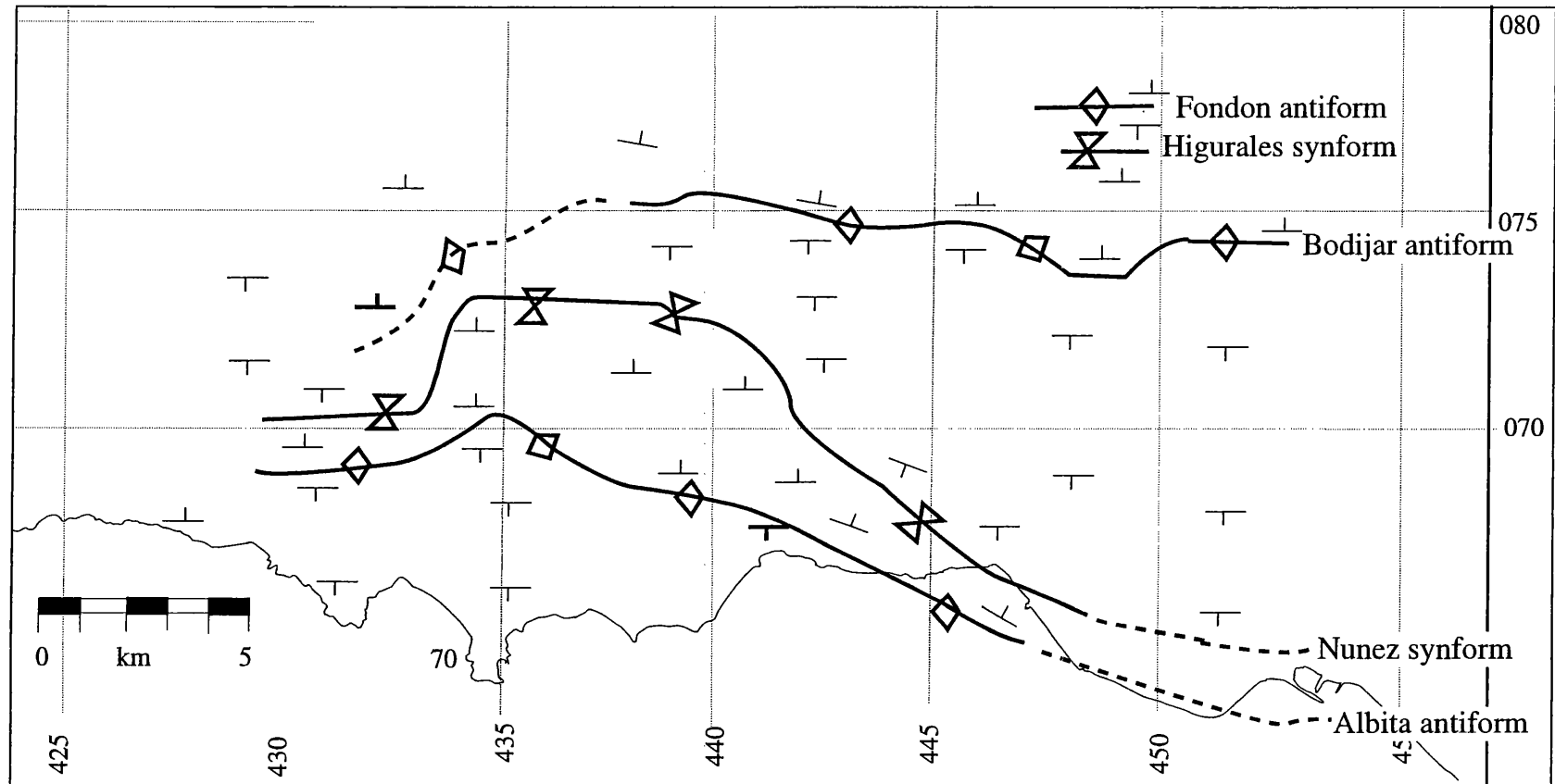


Figure 3.41 Sketch map to show the trace of late-formed (post- D_1) antiforms and synforms in the area.

CHAPTER 4 MINERALOGY AND MICROSTRUCTURE

4.1 Introduction

The preservation of disequilibrium mineral assemblages and textures in the Alpujarride Complex permits an insight into the pre-peak metamorphic history: mineral phases indicative of earlier pressure-temperature conditions persist as relic minerals. The sequential development of mineral phases within a single sample may be deduced from analysis of the way in which the minerals are related to the structural fabrics (**Chapter 3**). Analysis of multiple samples of equal metamorphic grade permits a metamorphic history to be developed within the framework of the structural fabrics in the area. Sections cut at 90° to the $L_{s/t}$ lineation (i.e. in the YZ plane – section 2.2.3) allow the S_s and S_t foliations to be distinguished from each other. Temporal variation of mineral growth relative to a foliation is likely to occur between rocks of different metamorphic grade, and some variation of mineral-fabric textures may occur within a metamorphic zone.

A table summarising the mineral-foliation relationships described in this chapter is presented in **table 4.1**. The distribution of the metamorphic grade divisions represented in table 4.1, and used in the text, is shown in **figure 4.1**.

4.2 Kyanite – sillimanite grade rocks

4.2.1 Introduction

The geographical distribution of the kyanite-sillimanite rocks may be seen on **figure 4.1**. This zone is characterised by mineral assemblages that contain both kyanite and sillimanite but do not contain andalusite.

4.2.2 Mineral assemblages prior to D_t

Sillimanite fibres lie within and define the P-domains of the S_t foliation in many samples of this grade. Where the S_s and S_t foliations are at a high angle to each other (i.e. in the hinges of the S_t folds), sillimanite fibres are clearly affected by the D_t deformation (**figure 4.2**). Sillimanite fibres lying parallel to the S_s foliation (in the P-domains) are tightly folded by D_t . Locally the hinge regions of the D_t folds coalesce and the S_t fabric is locally dominant in the section. These textures indicate that the majority of sillimanite (if not all) grew in the S_s foliation, prior to D_t , and was subsequently deformed.

In samples that contain wide P-domains, or where the angle between S_s and S_t is low, it is often difficult to distinguish between the S_s and S_t foliations: the tendency of sillimanite to preferentially nucleate on a biotite substrate (Kerrick, 1990) further impedes fabric identification.

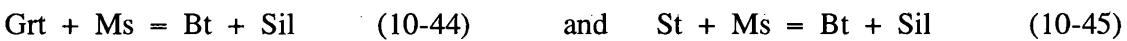
Mineral phases that occur as inclusions in garnet porphyroblasts provide an insight into the earliest mineral assemblages in these rocks: kyanite, staurolite, ilmenite and plagioclase are commonly identified. Kyanite crystals lie both oblique to, and parallel with, the S_s foliation, indicating that kyanite probably grew before and /or during D_s . The inclusions in garnet commonly define a linear trace in thin section, representing a planar foliation in three dimensions. The internal fabric in garnet porphyroblasts does not pass into continuity with the foliation in the matrix (**figure 4.3**). This relationship suggests that the garnet porphyroblasts grew over a pre-existing foliation, postulated to be S_s .

The absence of rutile in this metamorphic zone may indicate that these samples did not experience pressure conditions sufficient to stabilise rutile. However, as rutile is present in assemblages that have not experienced such a high-temperature evolution as this group,

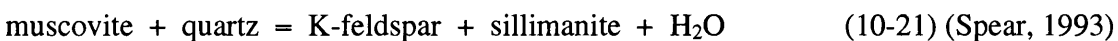
(section 5.5.2.2) a more plausible explanation may be that rutile was present in the early assemblage of these rocks but that it back-reacted to ilmenite prior to the growth of garnet.

The stability fields of the mineral phases preserved as inclusions in the garnet porphyroblasts may be plotted on P-T axes in order to constrain the ambient pressures and temperatures prevailing prior to and during the development of the S_s fabric in the kyanite-sillimanite rocks. A general grid showing the reactions within KFMASH compositional space that are used to constrain P-T conditions are shown in **figure 4.4a**. A summary of P-T conditions for rocks metamorphosed to different grades is presented in Chapter 6. Constraint of P-T conditions pertinent to the kyanite-sillimanite rocks is seen in **figure 4.4b**. This plot suggests that pressure conditions before and during this deformation were likely to have been near to 10.5 kb, and that temperature was in the range 550 – 650°C: further constraint is provided by the application of the GASP barometer to this mineral assemblage (section 5.5.2.3).

Locally, garnet porphyroblasts in the kyanite-sillimanite grade rocks have experienced extensive resorption. Many crystals have an anhedral shape and some porphyroblasts seem to have been entirely replaced by an assemblage of sillimanite, plagioclase, biotite and quartz.



Relict laths of kyanite and staurolite commonly lie parallel to the S_s foliation and are deformed by D_t . Plagioclase porphyroblasts in sample LH 129 (VF 43510656) contain relict staurolite and are deformed by the D_t deformation: this texture implies that some plagioclase was growing after the end of the D_s deformation, but prior to the onset of D_t , and that staurolite was unstable at this time. Muscovite mica in this sample is present in small, anhedral-subhedral crystals (<0.5mm), indicating that the recrystallisation of muscovite has not occurred (i.e. the conditions for the recrystallisation of muscovite have not been exceeded). From these textures, a plot of stable (sillimanite, plagioclase, muscovite?) and unstable (staurolite) mineral phases prior to the onset of the D_t deformation may be constructed and allows the likely area of P-T space which the kyanite-sillimanite rocks occupied at this time to be estimated (**figure 4.5**). The absence of re-crystallised muscovite in this sample indicates that muscovite breakdown, i.e.



has not occurred. These constraints indicate that pressure conditions were below 9.5 kb, and that temperatures were in the range 650 – 750°C.

4.2.3 Mineral assemblages during and after D_t

Biotite is the only mineral phase that over-prints the S_t foliation. The cooling path of these rocks from the P-T area defined for the pre- D_t assemblage (**figure 4.5**) to ambient temperature and pressure may have not intersected the stability field of andalusite, or the rocks may have passed through the andalusite stability field with insufficient energy to nucleate new crystal phases.

4.3 Kyanite-sillimanite-andalusite grade rocks

4.3.1 Introduction

Rocks containing all three of the aluminosilicate polymorphs enjoy a fairly wide distribution in the study area (**figure 4.1**). The boundaries with the kyanite-sillimanite and garnet/staurolite-andalusite grade rocks appear to be gradational.

4.3.2 Mineral assemblages prior to D_t

Garnet porphyroblasts within the kyanite-sillimanite-andalusite zone tend to show less alteration and resorption at the rim of the crystals than those present in the kyanite-sillimanite grade samples: inclusion-suites within garnet porphyroblasts are more commonly preserved. Prolific kyanite, quartz and ilmenite crystals define straight inclusion trails in garnet from samples close to Almuñecar (**figure 4.6a**): a single lath of biotite, is seen in sample LH 56 (VF 43860681) – section 5.5.2.5. Staurolite inclusions in garnet are present in samples from Cotobro (LH 28 – VF 43730665) and Jete Road (LH 339 – VF 43880680): the included fabric in the staurolite crystals passes into continuity with those in the garnet (**figure 4.6b**).

The growth of garnet in these rocks is likely to have occurred as a consequence of the breakdown of chloritoid i.e.



as textures from rocks within this area locally preserve chloritoid inclusions within the garnet porphyroblasts, yet no chloritoid is present in the matrix of the rocks (re: **figure 4.22**). The inclusion suite of garnet porphyroblasts from samples near to Almuñecar help to constrain the ambient pressure and temperature conditions at the time when garnet was growing in these rocks (at the end of D_s) (**figure 4.7**). Textures suggest that garnet grew after the end of the D_s deformation, although some relics of earlier garnet porphyroblasts (before D_s) are seen. This P-T plot indicates that temperature and pressure conditions in the kyanite-sillimanite-andalusite grade rocks after the end of D_s lay in the range 600 – 670°C, 7 – 10 kb. Results from calibrated thermobarometers confirm these estimations (section 5.5.2).

Relict kyanite is present (and prolific) in the matrix of kyanite-sillimanite-andalusite grade samples: the kyanite crystals lie in the S_s foliation and are deformed by the D_t deformation (**figure 4.8**). These relations indicate that kyanite grew in the assemblage before (and possibly during) the D_s deformation.

The extent to which the S_t foliation has developed in the kyanite-sillimanite-andalusite grade rocks varies widely. The S_t foliation is the most dominant fabric at outcrop and in thin section in the graphitic schist and quartzite sequence where they crop out on the southern part of the road to Jete (VF 43900675). Elsewhere, in a quartzite-dominated exposure of the non-graphitic schist and quartzite sequence near to Almuñecar. (LH 312 – VF 43730665), the S_t foliation is barely visible (**figure 4.9**).

Where the S_s and S_t fabrics are clearly identified, sillimanite fibres lie in the P-domains (i.e. phyllite-rich layers) of the S_s foliation and wrap around the garnet and plagioclase porphyroblasts, indicating that sillimanite may have grown after D_s , but was certainly stable prior to the onset of the D_t deformation. Plagioclase porphyroblasts locally contain the S_s foliation, and relict crystals of garnet and staurolite (**figure 4.10**). These textures indicate that garnet and staurolite became unstable before the onset of the D_t deformation event. The absence of re-crystallised muscovite mica indicates that the muscovite breakdown reaction has not been surpassed. Together these textures serve to constrain the maximum temperature to which these samples have been exposed.

A plot of the mineral stability fields on P-T axes is shown in **figure 4.11**, and indicates that prior to the development of the D_t fabric the kyanite-sillimanite-andalusite grade rocks

experienced conditions of 4-8 kbar and 600 – 775 °C. These conditions prevailed later in the metamorphic history than the conditions defined by the plot in **figure 4.7**.

Sillimanite fibres locally define the S_t fabric, in either coalesced P-domains of the S_s foliation (where S_t is pervasively developed), or in pressure-seams in which sillimanite has accumulated (**figure 4.12**). These textures are consistent with the interpretation that sillimanite nucleated and grew before the onset of the D_t deformation, and during at least the early part of the D_t deformation event.

Garnet textures from samples near to Torrecuevas (VF 43800690), from both the kyanite-sillimanite-andalusite and garnet/staurolite-andalusite grade rocks suggest that two phases of garnet growth occurred in this area. Porphyroblasts with ‘core and rim’ structures contain very few inclusions in the ‘core’ of the crystals, while prolific small opaque inclusions in the ‘rim’ portion preserve traces of the S_s foliation (**figure 4.13a**). The planar fabric defined by these inclusion trails does not pass into continuity with the S_s foliation, deformed by D_t , in the matrix; this texture suggests that the rim of the garnets grew after the end of the D_s deformation, but prior to the onset of D_t . A distinct change in the garnet composition is seen at the core-rim boundary; this supports the hypothesis of two phases of garnet growth (**figure 4.13b**), perhaps relating to the ‘pre- D_s ’ and ‘post- D_s ’ stages of garnet growth discussed above.

4.3.3 Mineral assemblages during and after D_t

In the sample discussed above from Torrecuevas that contains garnet porphyroblasts with ‘core and rim’ textures (**figure 4.13**), the S_t fabric is defined by sillimanite fibres and is the dominant foliation in the sample. This texture supports the interpretation that sillimanite was stable during the D_t deformation (see **figure 4.12** and discussion above). Staurolite porphyroblasts include open crenulations that are interpreted to be an early phase of deformation of S_s by the D_t deformation event. The D_t deformation continued to develop after the end of staurolite growth, tightening the crenulations of the S_s foliation in the matrix, while more open style folds were preserved in the staurolite porphyroblasts. The S_t foliation, defined by the orientation of sillimanite fibres, wraps around the porphyroblasts (**figure 4.14**). Examples of euhedral staurolite that incorporate the S_t fabric are also seen (**figure 4.15**), providing evidence that staurolite grew in this area during and after the D_t deformation.

Andalusite and biotite overprint the S_t fabric in the majority of these samples. The S_t fabric may be traced continuously through andalusite and biotite crystals into the matrix. Some crystals of andalusite and biotite include S_t helicically while others include rotated trails of inclusions. These textures indicate that these mineral species grew during and after the D_t deformation event (**figure 4.16**). Where the chiastolite variety of andalusite occurs, the foliations in the matrix cannot be traced through the crystals: chiastolite preferentially incorporates inclusion trails in a characteristic 'X' pattern, when viewed in the (001) section (Kerrick 1990).

4.4 Sillimanite-andalusite (no kyanite) grade rocks

4.4.1 Introduction

Rocks that contain sillimanite and andalusite, but do not preserve any relicts of kyanite from the early part of the metamorphic evolution, are present only in the Los Guajares area (VF 44950768), and in the Sierra Chapparal (VF 44170775) - **figure 4.1**.

4.4.2 Mineral assemblages prior to D_t

In the Sierra Chapparal (i.e. LH335 – VF 44170775) and in Los Guajares (i.e. LH 303 – VF 44860776), S_t commonly forms the dominant fabric: the S_s foliation is preserved only within quartz-rich lithons in the schist horizons (**figure 4.17**- and section 3.3.1). Within these quartz-rich lithons, sillimanite-bearing P-domains and Q-domains define the S_s fabric, indicating that sillimanite was present before the D_t deformation. Plagioclase porphyroblasts in samples from these areas commonly include sillimanite fibres: rotated internal fabrics indicate that plagioclase grew during D_t . Together, these textures imply that sillimanite growth in the Los Guajares and Sierra de Chapparal areas predominately or wholly predated the D_t deformation.

The early part of the metamorphic history of the rocks within this zone is difficult to deduce due to the major modification of the S_s foliation wrought by the D_t deformation. Scant evidence is provided by inclusions from the relict garnet and staurolite porphyroblasts due to extensive alteration (as described in section 4.2.2), but rare examples of garnet and staurolite porphyroblasts that preserve a straight or curved inclusion trail are seen. These internal fabrics are commonly defined by quartz and ilmenite inclusions, and do not pass into

continuity with the dominant foliation in the matrix: this suggests that garnet and staurolite growth occurred during and after the development of the S_s fabric. The mineral assemblage at the end of the D_s deformation, prior to the onset of D_t (i.e. garnet, staurolite, probably sillimanite), provides an approximate constraint on the ambient pressure and temperature at this time (**figure 4.18**). From this plot it is estimated that pressure conditions lay in the range 3 – 6 kbar and the temperature was between 550 – 650°C.

4.4.3 Mineral assemblages during and after D_t

The textural relationships of the andalusite porphyroblasts and euhedral staurolite crystals (which have a length of up to 1 mm) with the S_s and S_t foliations help to constrain the low-pressure portion of P-T history for the sillimanite-andalusite grade rocks. Andalusite crystals contain rotated inclusion trails that pass into continuity with S_t in the matrix, indicating that andalusite grew during the D_t deformation event (as seen in kyanite-sillimanite-andalusite grade rocks – **figure 4.16**). Small euhedral crystals of staurolite that also include rotated inclusion trails that pass into continuity with S_t in the matrix are seen locally in the area of Los Guajares, implying that staurolite was also growing during D_t . Other staurolite crystals helicitically include D_t folds; these crystals grew after D_t .

These mineral textures may be used to constrain an area of P-T space in which the sillimanite-andalusite rocks are likely to have been located during the D_t deformation (**figure 4.19**): temperature appears to have been near to 500°C at pressures of less than 4 kbars.

4.5 Garnet/staurolite–andalusite grade rocks

4.5.1 Introduction

Rocks containing garnet and/or staurolite, with andalusite are well exposed in the studied area (**figure 4.1**). Sillimanite is absent in this zone. Kyanite is locally present: its distribution is likely to be controlled by bulk composition of the schists (Kerrick 1990). The growth of garnet is also controlled by bulk composition: Spear (1993) shows that the amount of calcium in the rock is an important parameter controlling the nucleation of garnet. Horizon-specific distribution of garnet is seen at outcrop and at thin section scale in all schists from this area.

4.5.2 Mineral assemblages prior to D_t

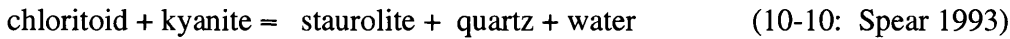
Many garnet porphyroblasts in rocks from this metamorphic grade contain planar internal fabrics defined by quartz and/or ilmenite inclusions that represent a planar foliation included in the garnet in three dimensions. The included foliation is likely to be S_s , and the textural relations suggest that garnet grew after the development of S_s .

The inclusion trails in the garnet porphyroblasts do not pass continuously into the dominant foliation in the matrix, indicating that garnet growth ended prior to the subsequent phase of deformation (D_t). Local examples of garnet porphyroblasts that have developed brittle fractures at 90° to the S_s foliation: this may suggest extension parallel to the S_s foliation occurred after the end of garnet growth (i.e. during the D_t deformation - **figure 4.20**). The edges of the garnet crystals are commonly embayed.

'Core and rim' textures described from garnet porphyroblasts in sillimanite-kyanite-andalusite grade rocks near to Torrecuevas (section 4.3.2 and **figure 4.13**) are also locally present in rocks from the garnet/staurolite-andalusite zone to the north of this location. S_s and S_t foliations are at a high angle to each other in this area as the fold axial trace of the Torrecuevas D_t fold hinge passes close by (**figure 3.1**). Garnet porphyroblasts in this area (and the rims of 'core and rim' crystals) include straight inclusion trails at the rim that pass into continuity with the S_s fabric in the matrix, although the S_s foliation in most of the matrix has been strongly affected by the D_t deformation. These textures support the conclusion discussed above that most garnet grew after the end of the S_s fabric formation but had stopped growing prior to the onset of the D_t deformation. The early stage of garnet growth evidenced in the 'cores' of some crystals is likely to represent a pre- D_s phase of garnet growth (seen also in kyanite-sillimanite-andalusite and kyanite-sillimanite grade rocks).

In the west of the studied area near to Rio de la Miel (VF 42730682) and at a location outside the study area to the east (near to Rubite: VF 46700719), large garnet porphyroblasts with prolific inclusions permit an insight into the early metamorphic history. At both these localities, large garnet porphyroblasts contain curved inclusion trails indicative of garnet growth during the D_s deformational event (Passchier & Trouw, 1996) (**figure 4.21**). Garnet porphyroblasts from samples from near to Rubite include chloritoid in the core of the garnet

porphyroblasts and staurolite at the rims: staurolite is also present in the matrix of the samples (**figure 4.22**). This texture indicates that the 'chloritoid-out' reaction



was surpassed during the growth of the garnet porphyroblasts. This reaction is well constrained on the petrogenetic grid for pelites in the KFMASH system and indicates that the ambient temperature during the growth of garnet was likely to have been 500 – 550°C.

(**figure 4.23**), approximately concordant with the conditions predicted from elsewhere in this zone. The garnet porphyroblasts in which chloritoid and staurolite are preserved may represent an earlier part of the prograde development of garnet than seen elsewhere in the studied area.

The garnet/staurolite-andalusite rocks to the north of Torrecuevas contain local inclusions of staurolite within garnet porphyroblasts. One sample to the NW of Torrecuevas (LH 140 – VF 43560704) contains prolific examples of staurolite crystals in the matrix and staurolite included within garnet porphyroblasts (**figure 4.24**). The mineral relations suggest that garnet and staurolite formed simultaneously, after the D_s deformation event, perhaps as a consequence of the reaction:



Relict kyanite is present in the matrix of many samples in this area. Isoclinal fold hinges locally deform individual kyanite laths: the axial planes of these folds are parallel to the S_s foliation. The isoclinal folds developed during D_s : this texture implies that kyanite grew prior to D_s or during the early part of the D_s deformation in these rocks.

The assemblage in the garnet/staurolite–andalusite rocks prior to the onset of the D_t deformation (i.e. ilmenite, staurolite, garnet, kyanite) allow some constraint to be placed on the P-T conditions prevailing at this stage of the evolution (**figure 4.25**). From this plot, the temperature prior to the development of the S_t foliation is likely to have been 510 – 630 °C: ambient pressure was in excess of 5 kbar.

Refinement of pressure/temperature estimates for these rocks has been achieved from the application of calibrated thermometers and barometers (section 5.5.3).

4.5.3 Mineral assemblages during and after D_t

A late generation of staurolite crystals is developed locally in this zone. The subhedral to euhedral crystals, up to a maximum of 3 mm in length, commonly show strong yellow pleochroism in thin section, and some sector twinning.

At outcrops to the north of Torrecuevas (VF 43800691), north of Salobreña (VF 44760668) and near to Motril (VF 45350675), the staurolite crystals helicitally include the S_t fabric. There is no rotation between the fabric included in the staurolite crystals and that in the matrix, clearly indicating that the staurolite grew after the end of the D_t deformation. This 'late' generation of staurolite indicates that the temperature of the rocks in these areas must have remained elevated to at least 500°C until after the formation of the S_t foliation in these rocks.

To the west of Torrecuevas (VF 43800691), the 'late' (i.e. small, euhedral) staurolite crystals contain curved, spaced inclusion trails. In some cases, these trails do not pass into continuity with the deformed S_s foliation in the matrix (**figure 4.26a**): in other examples there is continuity between the internal and external fabrics (**figure 4.26b**). These relations imply that staurolite at this locality was stable from the early part of the D_t deformation until after the end of the D_t deformation event.

Andalusite porphyroblasts are present in the majority of garnet/staurolite-andalusite grade rocks: the relationship of these porphyroblasts with S_s and S_t shows slight variation over the area in which rocks of this grade crop out. To the north of Torrecuevas (VF 43800691), andalusite crystals grew after the D_t deformation: the andalusite porphyroblasts include the fabric in the matrix without distortion (**figure 4.27**). North of Salobreña (VF 44760668), north of Motril, (VF 45350675) and around Los Guajares (VF 44900768), rotated inclusion trails in andalusite porphyroblasts pass into continuity with the S_t fabric in the matrix, indicating that andalusite grew during the D_t deformation at these locations (as seen in **figure 4.16**). Andalusite porphyroblasts that grew after the development of the S_t fabric, and helicitally include the S_t foliation are also present in rocks from these areas.

4.6 Muscovite – biotite and Muscovite –chlorite grade rocks

4.6.1 Introduction

Rocks in which garnet is not present have been divided into two categories, the assemblages of which are:

Muscovite - biotite	Ms Bt Qtz Pl ± And ± Ky ± Cld ± Chl ± Ilm ± Mag
Muscovite – chlorite	Ms Chl Qtz Pl ± And ± Cld ± Ilm ± Mag

Kyanite occurs locally in the muscovite – biotite schists but is not present in the muscovite – chlorite schists. Andalusite porphyroblasts are present locally in both the muscovite–biotite schist and muscovite-chlorite schist sequences (section 4.6.2).

Only one foliation is commonly seen when these fine-grained, mica-rich sections are viewed in the YZ plane (ie at 90° to the lineation). As both the S_s and S_t foliations are crenulation cleavages (section 2.2.2), it is not possible to name the fabric present in a sample by analysis of an isolated sample. Just north of Jete (VF 44050727), the transition from a garnet-bearing to a garnet-absent assemblage is seen over a short structural distance. From a study of fabrics in this area it is evident that the principal foliation present in the phyllite and quartzite sequence, containing garnet-absent assemblages, is likely to be S_t (section 3.3.1 and **figure 3.18**).

Evidence of post-metamorphic deformation of the S_t foliation e.g. kink-bands, shear fabrics, brittle fractures, are seen in phyllite exposures - section 3.6.7.

4.6.2 Locations of Andalusite porphyroblasts

Samples from these two metamorphic zones locally contain andalusite: the location of these samples is shown on the sketch map in **figure 4.28**.

In the western and central portions of the area, garnet-absent assemblages in which andalusite is identified tend to be close to gradational metamorphic contacts with the garnet/staurolite-andalusite rocks. The andalusite in these samples grew after the end of the D_t deformation event, as they helicitically include the S_t foliation (texture as seen in **figure 4.27**). These textures imply that temperatures after the D_t deformation were sufficiently high at the base of the garnet-absent rocks to permit andalusite to nucleate and grow.

In the east of the area, numerous examples of andalusite in garnet-absent metamorphic assemblages close to rocks containing sillimanite are seen: a summary of the metamorphic grade relationships in this area is presented in **figure 3.28**. From this figure, and from cross-sections in the east of the area (**figures 3.2 – 3.10**) it may be seen that the growth of andalusite porphyroblasts in the east of the area has been attributed to a fault that developed after the D_s deformation and prior to D_t . Movement along this fault, prior to the end of metamorphism, juxtaposed the muscovite-biotite and muscovite-chlorite grade rocks (previously structurally higher in the metamorphic pile) adjacent to sillimanite-bearing assemblages that originated at towards the base of the metamorphic sequence (as shown in **figure 3.28**). As a consequence of movement along the D_s/D_t fault, the muscovite-biotite and muscovite-chlorite grade rocks adjacent to the D_s/D_t contact shared a P-T history of moderate temperature at low-pressures with rocks that had a high temperature early metamorphic history (i.e. garnet/staurolite-andalusite rocks and kyanite-sillimanite-andalusite grade rocks). Andalusite was able to nucleate and grow in these conditions, and incorporate the S_t fabric. Irregular, anhedral areas of andalusite are present at some exposures close to where equant, euhedral andalusite crystals are seen (i.e. near to Guajare Faraguit: VF 44890767), the presence which attest to conditions at the periphery of the andalusite stability field.

Muscovite-chlorite and muscovite-biotite rocks structurally higher in the metamorphic pile (i.e. the phyllite and quartzite sequence near to Otivar (VF 43950748) and north of Itrabo (VF 44300730) were not exposed to sufficiently high temperatures to enable andalusite to nucleate and grow.

4.7 Case studies from the area

4.7.1 Variation of mineral-foliation relationships with metamorphic grade:

Lower Jete Road / Cotobro and middle Jete Road

Kyanite-sillimanite-andalusite grade rocks within Cotobro (VF 43650660) and along the lower portion of the road to Jete (south of Torrecuevas – VF 43850690) contain textures that indicate garnet and staurolite grew during the D_s deformation. Andalusite, biotite and muscovite crystals overprint the S_t foliation in these rocks.

Structurally higher in the section (Jete Road cross-section – **figure 3.6**), garnet / staurolite – andalusite rocks along the road to Jete, and to the west of Torrecuevas, contain textures that indicate garnet and staurolite grew after the cessation of the D_s event are identified. The S_t foliation in these rocks is helicically included by andalusite, staurolite and biotite porphyroblasts. To the west of Torrecuevas, local textures suggest that some staurolite porphyroblasts grew during the D_t deformation (e.g. as seen in **figure 4.26**).

These textures indicate that garnet/staurolite-andalusite grade samples from the west of Torrecuevas and middle Jete Road passed through the stability fields of staurolite and andalusite towards the end of, and after, the D_t deformation event. In contrast, the sillimanite-bearing rocks exposed on the Lower Jete Road (structurally below the garnet grade lithologies – **Figure 3.6**), do not contain equivalent ‘late’ staurolite crystals; this may indicate that these rocks cooled directly from the sillimanite stability field into that of andalusite without nucleating staurolite – **figure 4.29**.

A general trend may be observed across the area: a given mineral phase grows earlier in a high grade rock, relative to the S_s and S_t foliations, in comparison to a rock of lower grade.

An exception to this general trend is encountered near to Guajare Faraguit (VF 44890767). Textures here suggest that garnet grew in both the garnet/staurolite-andalusite and sillimanite-bearing rocks during the D_s deformation. However, some variation of P-T conditions may be identified in these rocks during the D_s event: staurolite grew in the garnet/staurolite-andalusite grade rocks while sillimanite was growing in the higher-grade

lithologies. These mineral-fabric relations have been used to constrain P-T conditions during the formation of the S_s fabric (**figure 4.30**).

4.7.2 Contrasts and similarities between two areas of equal metamorphic grade: near to Guajare Faraguit and north of Salobreña

Near to Guajare Faraguit (VF 44890767), the sillimanite and garnet-bearing assemblages contain andalusite porphyroblasts with textural relations to the S_t foliation that indicate growth during and after the D_t event. Biotite laths overprint the S_t fabric in the sillimanite-bearing schists, while the garnet-bearing schists contain euhedral staurolite porphyroblasts that helicitically include the S_t fabric: the 'late' staurolite porphyroblasts are locally included by andalusite porphyroblasts .

North of Salobreña (VF 44800670) mineral-fabric relations vary to those seen in Los Guajares. Garnet/staurolite-andalusite grade rocks contain andalusite porphyroblasts with textures that imply growth during the D_t deformation event: continuation of the graphitic schists to the east, towards Motril, provides numerous examples of garnet grade rocks with andalusite porphyroblasts growing during and after the D_t deformation. However, sillimanite-bearing rocks from the north of Salobrena (at VF 44600701 - **figure 3.26**) contain andalusite porphyroblasts that include the S_t fabric without rotation. Garnet/staurolite-andalusite grade rocks from near to Salobreña contain euhedral staurolite crystals over-printing the S_t fabric, and locally included in andalusite porphyroblasts, as seen at Los Guajares..

The textures discussed above imply that garnet/staurolite-andalusite grade rocks from both Los Guajares and near to Salobreña were within the andalusite stability field during and after the D_t event, and within the staurolite stability field after D_t . Sillimanite-bearing rocks to the north of Salobreña, however, were outside (above) the stability field of andalusite during D_t , while equivalent grade rocks at Los Guajares were within the stability field (**figure 4.31a & 4.31b**). These results suggest that the sillimanite-bearing schists near to Guajare Faraguit were at lower pressure and/or lower temperature during the D_t deformation event than those from near to Salobreña.


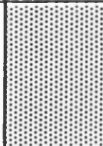


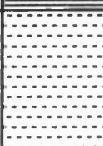

Metamorphic Grade		Deformation event					
		Before D _s	During D _s	After D _s	Before D _t	During D _t	After D _t
Muscovite-Chlorite			?		Ms, Chl		And
Muscovite-Biotite			?		Ms, Bt		An, And
Garnet / Staurolite - Andalusite		Qtz, Ilm, Ky, Rt, Grt, Cld	Ky?, Grt St?	Grt, St		And, Bt, St	And, Bt, St
Sillimanite-Andalusite		Qtz, Ilm	Grt, St	Grt, St	Sil? Sil	St, An, And	Bt, And, St
Kyanite-Sillimanite-Andalusite		Ilm, Ky, Ky? Bt, Chl, St Grt, Cld	Ms, Bt, St	Grt, St	Sil? Sil, Pl, Ms	Sil? St, And	St, And, Bt, Ms
Kyanite-Sillimanite		Ilm, Ky Grt, St, An, Rt?	Sil	Sil, An Grt?	Sil, An, Ms	?	Bt, Ms

Table 4.1 Summary of the mineral assemblages within each metamorphic division, relative to the regional deformation events D_s and D_t.

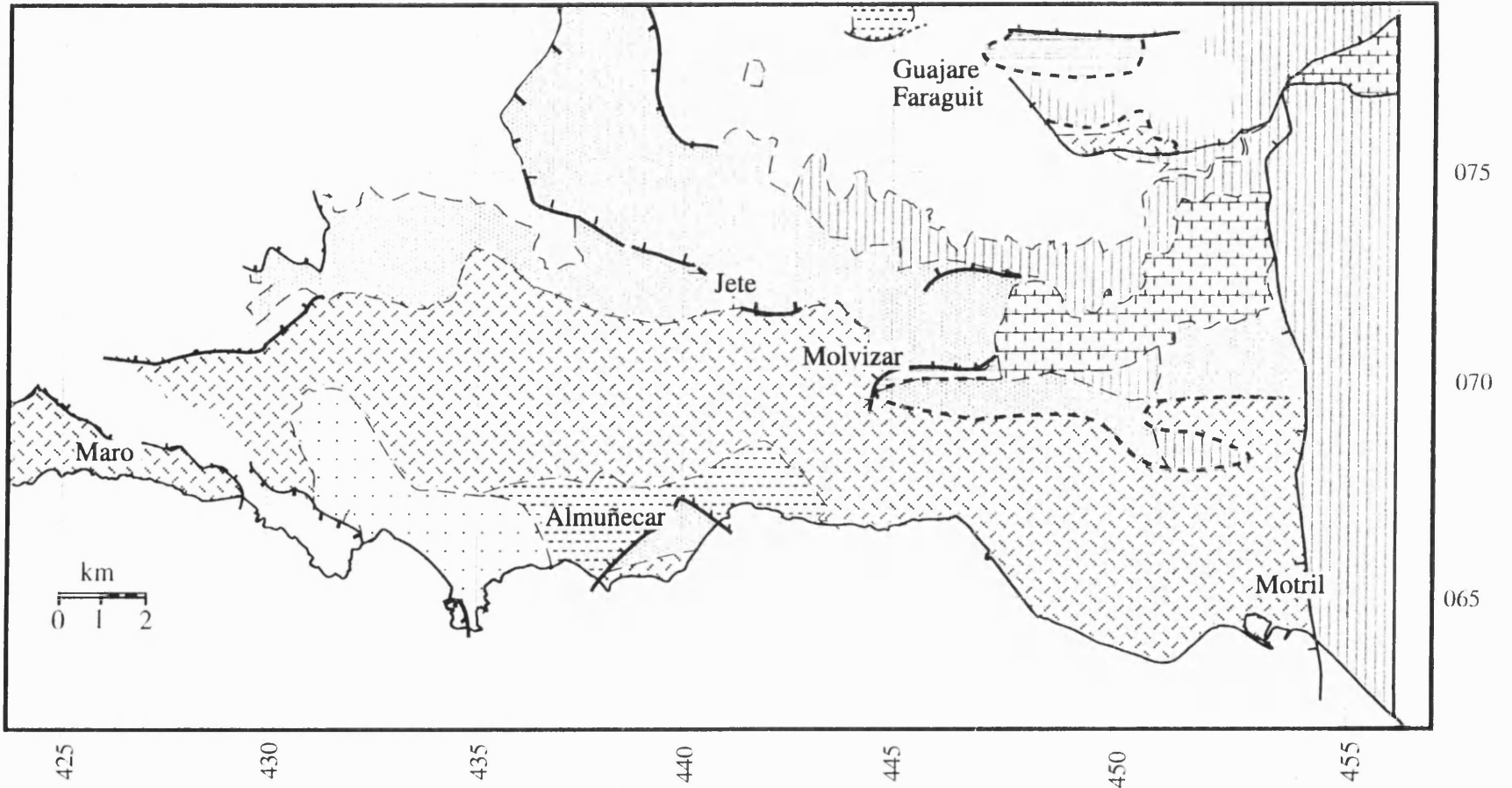
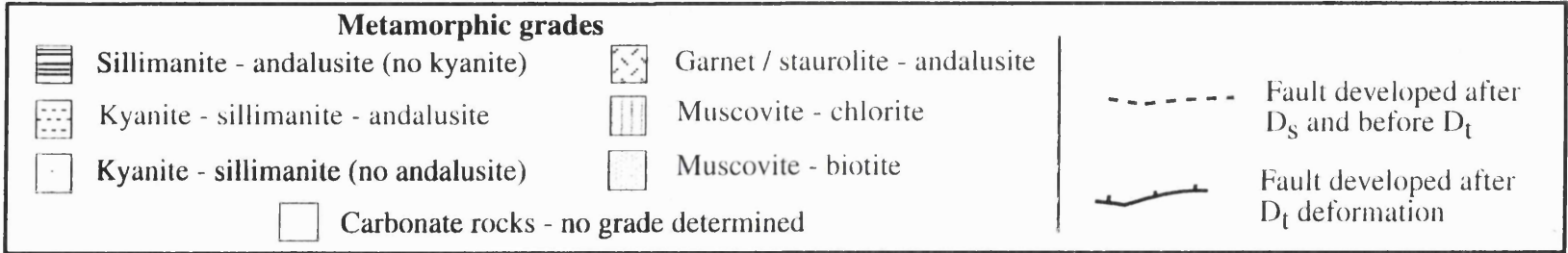


Figure 4.1 Map of the area studied showing the distribution of metamorphic grades



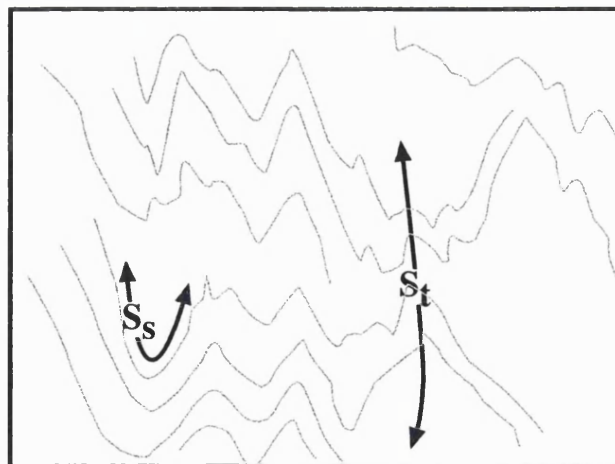


Figure 4.2 Compositional layering between muscovite and sillimanite / biotite layers, defining the S_s foliation, are crenulated by the D_t deformation event. The S_t foliation is incipient here, and orientated top - bottom with respect to this photograph. The crenulation of sillimanite by D_t indicates that it was present at least prior to the onset of this deformation event. Elsewhere in this section, the crenulations are very tightly transposed and S_t forms the main foliation.

Sample LH 131 - kyanite-sillimanite grade

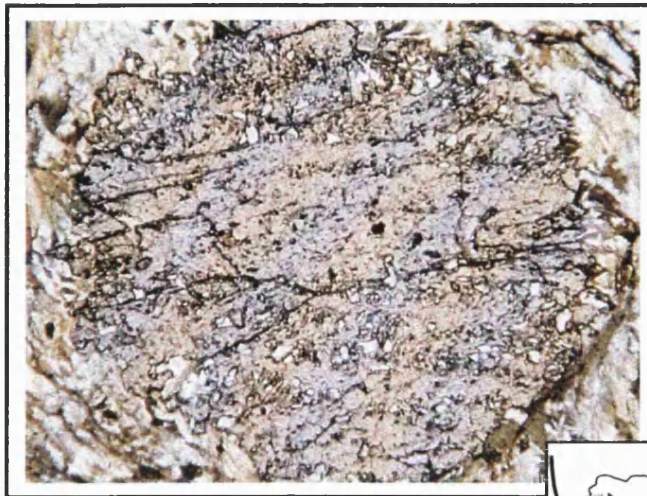


Figure 4.3a (above) Garnet porphyroblast including a linear crenulation fabric: the quartz-rich hinge areas of the S_s foliation are preserved.
Sample LH 134.
Kyanite-sillimanite grade.
Viewed in YZ plane

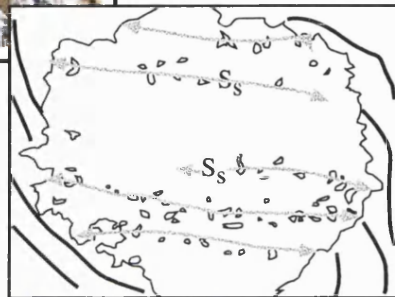
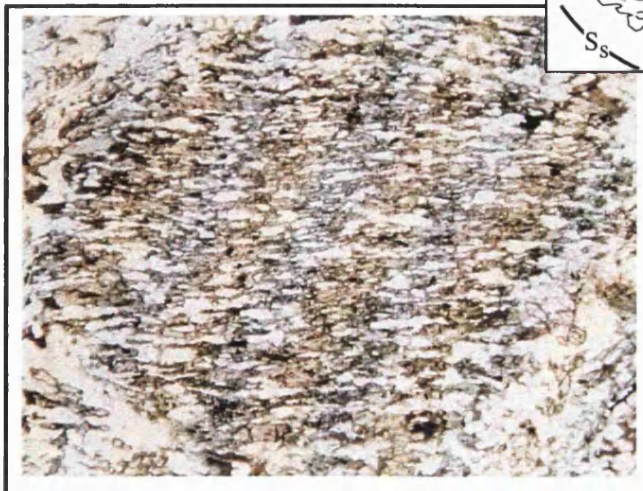
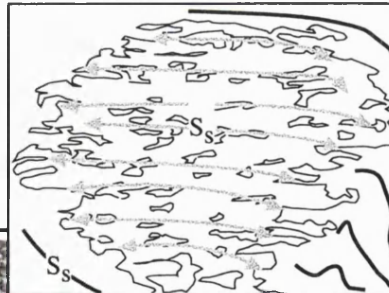


Figure 4.3b (below) Garnet porphyroblast including prolific quartz inclusions, in straight arrays, creating a 'seive' texture. Relict S_c foliation. Perimeter of garnet is embayed.
Sample LH 311.
Kyanite-sillimanite grade.
Viewed in YZ plane.



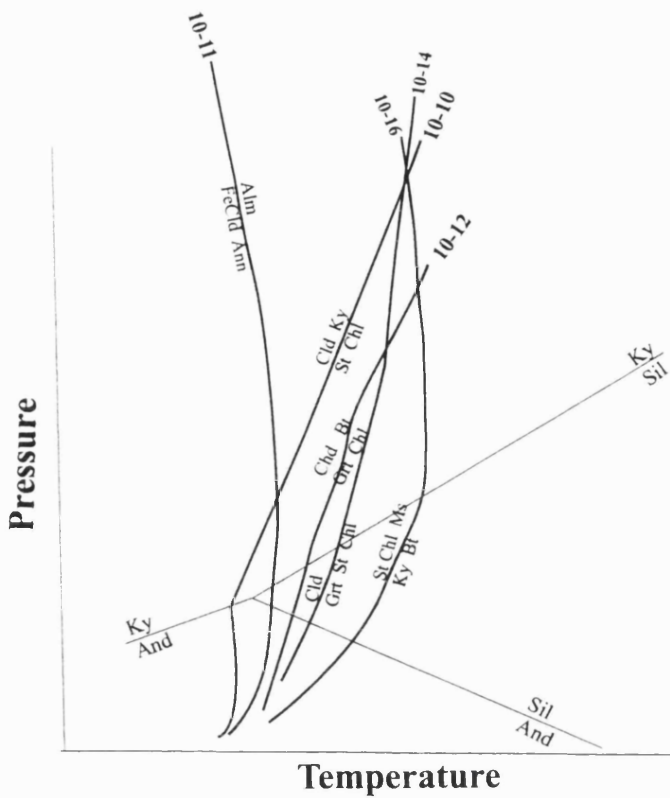
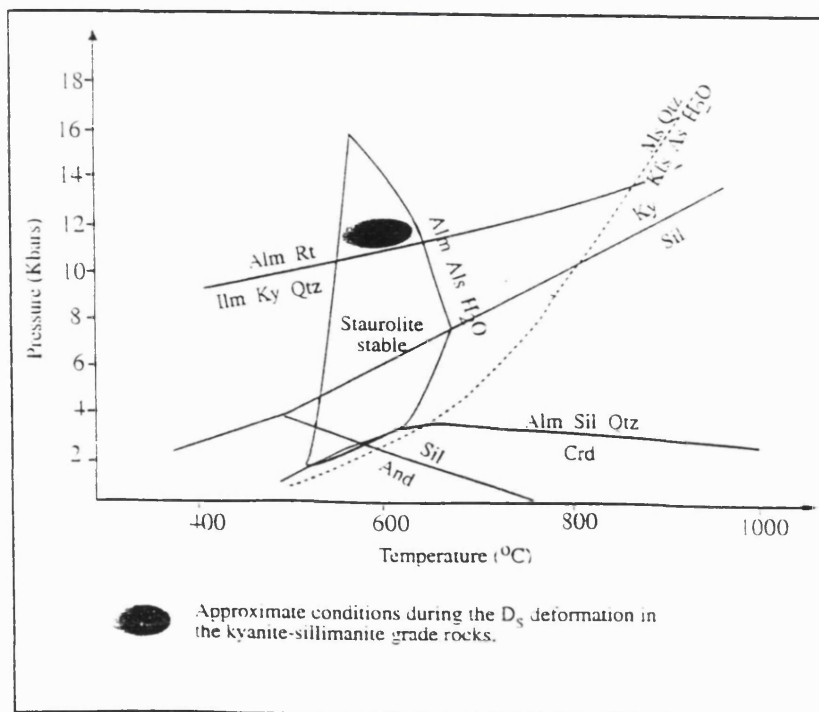


Figure 4.4a above

Plot on Pressure / temperature axes to show the approximate positions of some common reactions mentioned in the text. From Spear (1990).

Figure 4.4b below

P-T plot with shaded area to indicate the proposed conditions experienced by the kyanite-sillimanite grade rocks before / during the D_s deformation. The P-T conditions have been constrained by analysis of multiple samples from the kyanite-sillimanite grade rocks.



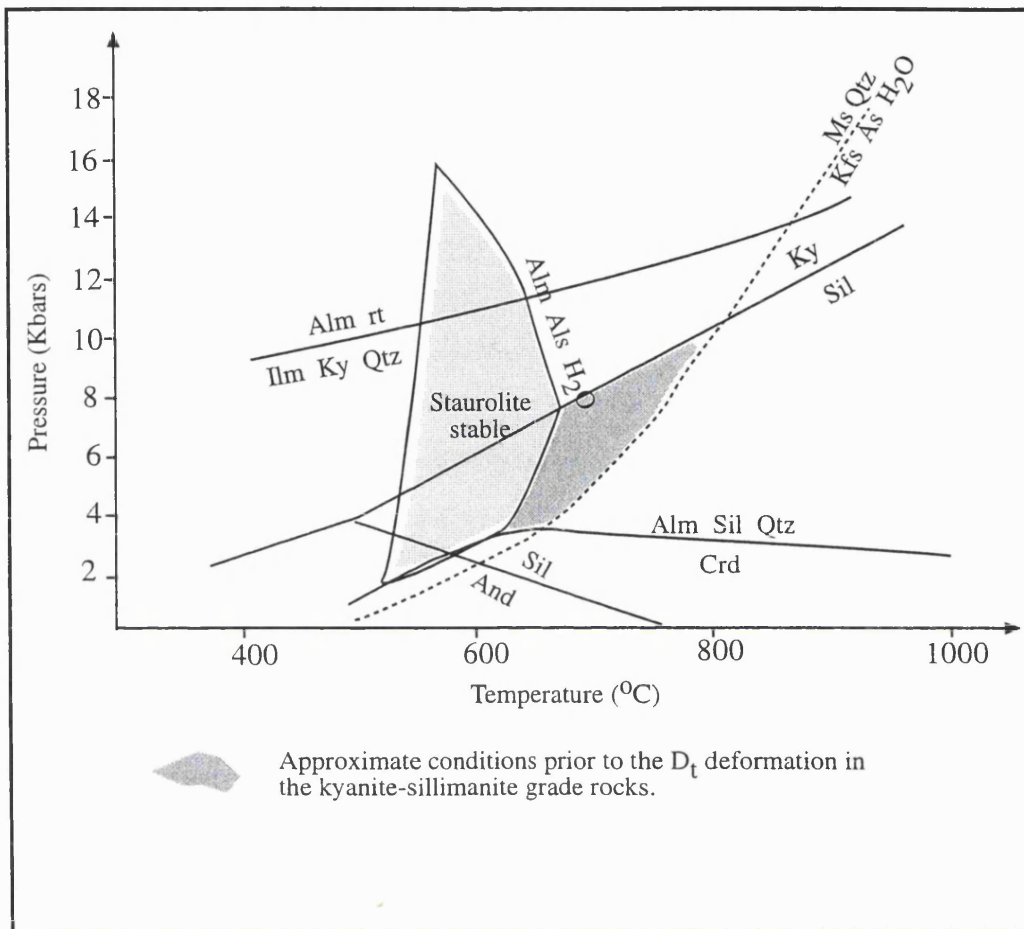


Figure 4.5 P-T plot with shaded area to indicate the likely location in P-T space of the kyanite-sillimanite rocks before the occurrence of the D_t deformation event. The area of P-T space has been constrained by the stability and instability of mineral phases, assessed from the mineral-fabric relations in numerous thin-sections of rocks from the kyanite-sillimanite grade.

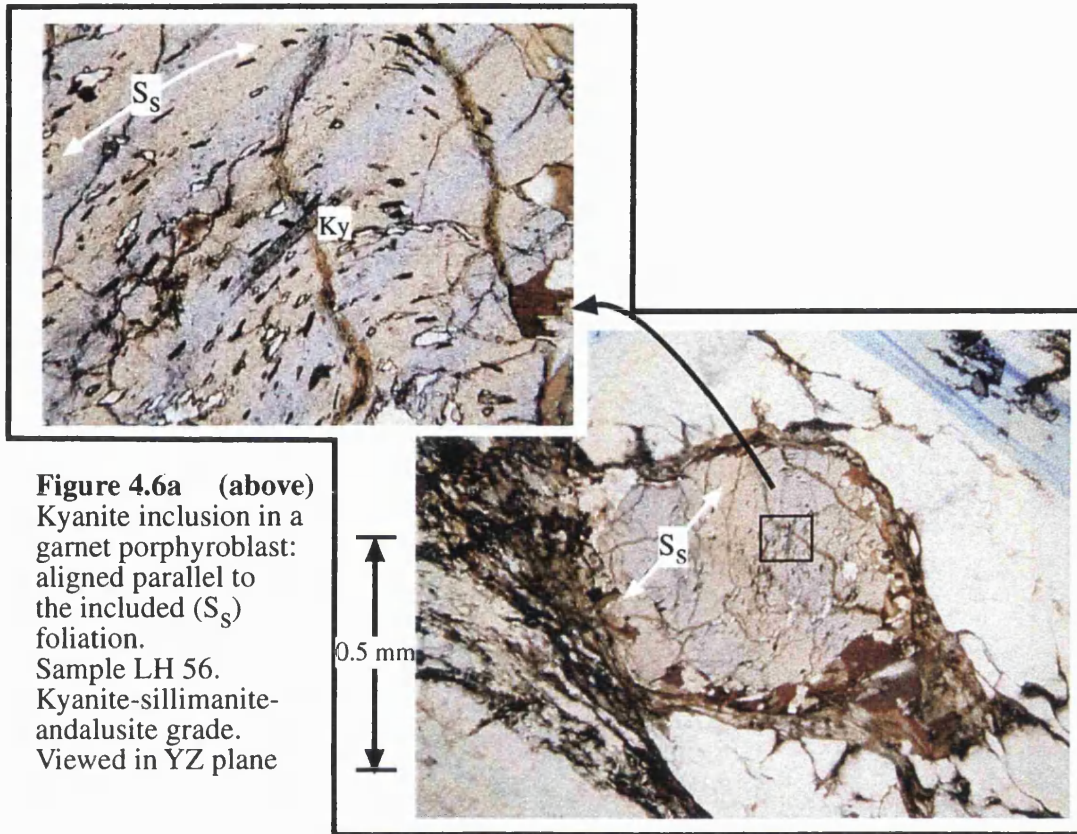
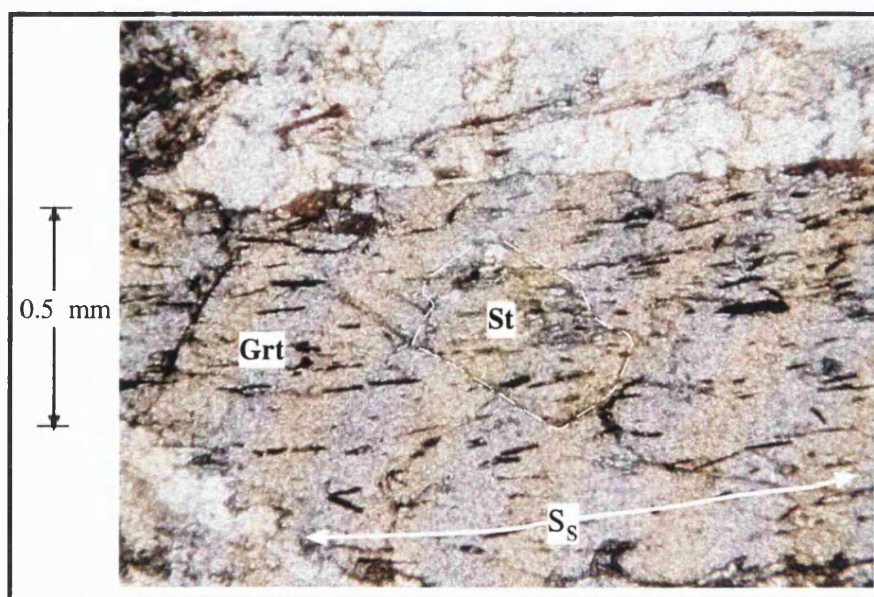


Figure 4.6b (below) Staurolite inclusion in garnet porphyroblast. Inclusions of ilmenite define a linear inclusion trail in the garnet: this is the two dimensional representation of the S_s foliation plane. The inclusion trail passes undeflected through the staurolite inclusion.

Sample 28 - viewed in the YZ plane.
Kyanite-sillimanite-andalusite grade.



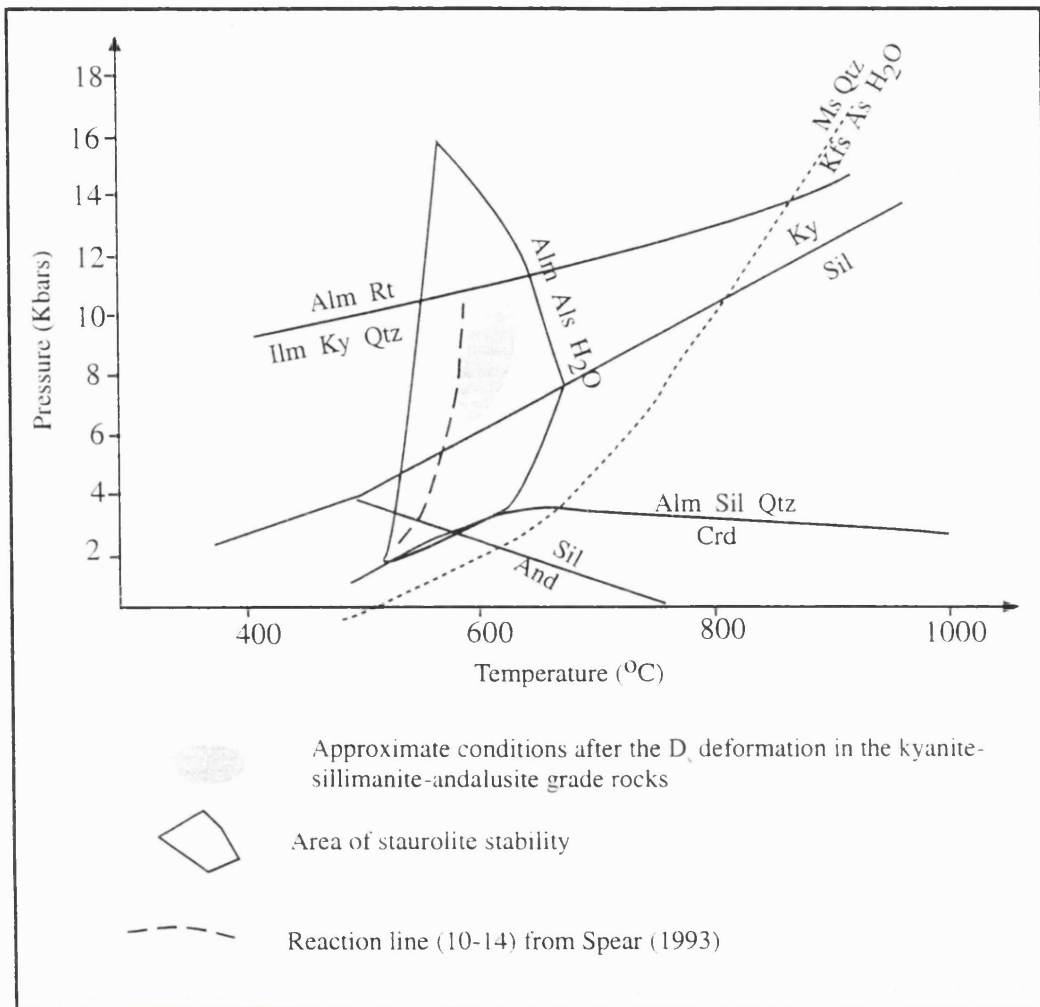


Figure 4.7 P-T plot with shaded area to indicate the likely location in P-T space of the kyanite-sillimanite-andalusite rocks after the end of the D₅ deformation event. The area of P-T space has been constrained by the stability and instability of mineral phases, assessed from the mineral-fabric relations in numerous thin-sections of rocks of kyanite-sillimanite-andalusite grade. Textures indicate that garnet may have been forming as a consequence of chloritoid breakdown, as defined by reaction (10-14) of Spear (1993), marked on this plot. Mineral stability fields of other inclusion in garnet are concordant with this deduction.

Further constraint of P-T conditions is achieved by the application of calibrated thermobarometers (section 5.5.3 & 5.5.4).

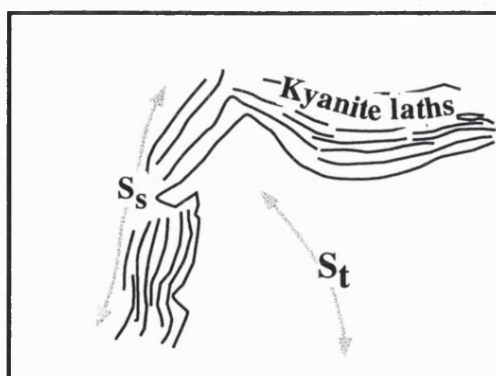


Figure 4.8 Microphotograph and interpretative sketch of textures in the matrix of kyanite-sillimanite-andalusite rocks. A kyanite lath lying within the S_s foliation (parallel to the composition boundary between the P and Q domains) has been deformed by the D_t deformation, which in this view generates a small-scale D_t fold hinge. The S_t foliation (axial planar to the D_t fold) is not pervasively developed here.

Sample LH 309. Viewed in the YZ plane.
Kyanite-sillimanite-andalusite grade.

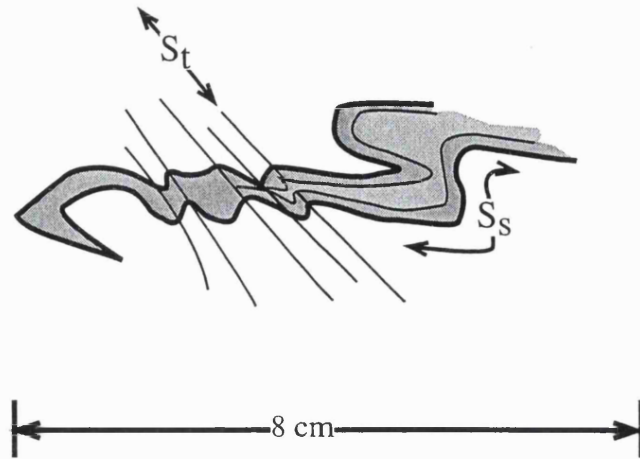
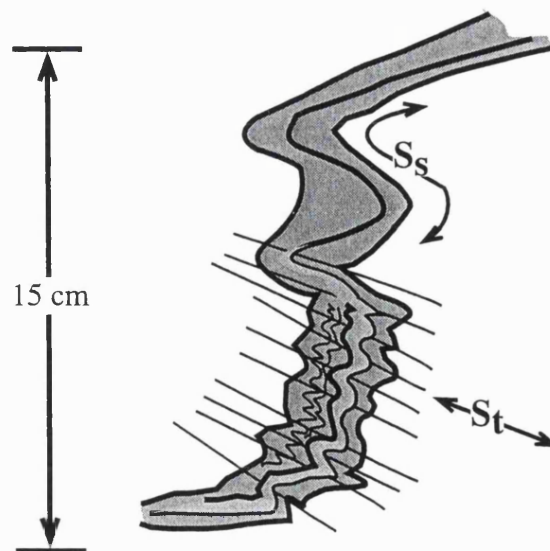


Figure 4.9a Above. Simple field sketch showing the relationship of the S_t foliation to S_s to the west of Almunecar at VF43720665. A D_5 fold hinge is seen, in quartzite-rich rock; the S_t foliation that cross-cuts S_s is widely spaced due to the high competency of the quartz-rich rock. This exposure is of non-graphitic schist and quartzite sequence.

Figure 4.9b Below. Field sketch from VF 438906669, north of Almunecar, on the road towards Jete. This exposure of graphitic schist and quartzite sequence contains a high proportion of schist. The S_t foliation is more pervasively developed here than in the quartzite-rich exposure described above. Fold closures of the D_5 folds are typically more difficult to identify in schist-rich outcrops.



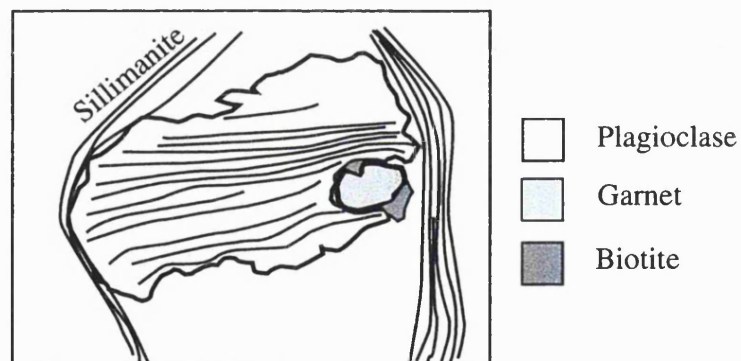
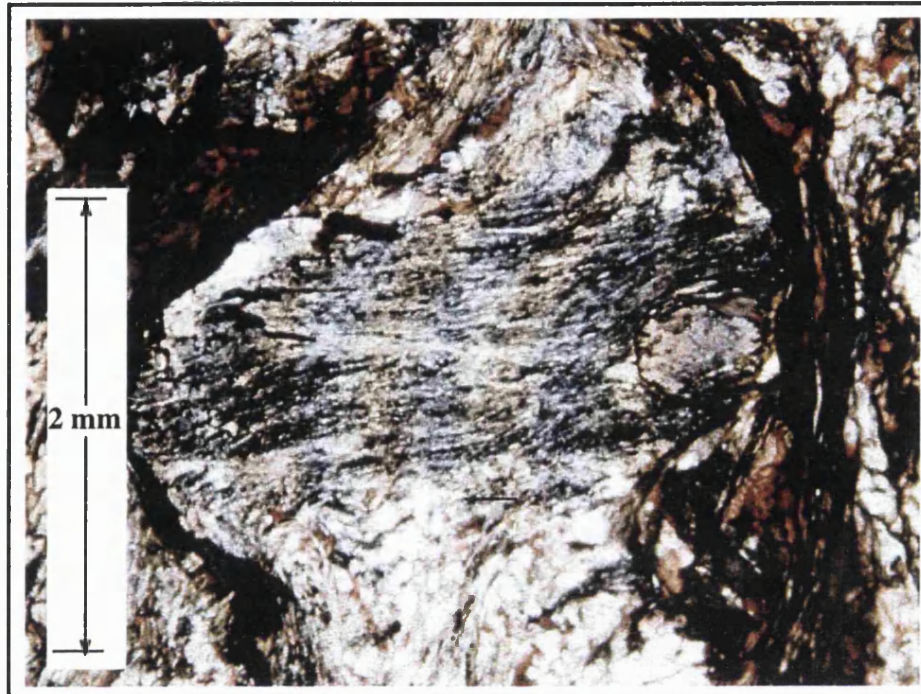


Figure 4.10 Garnet porphyroblast included in a plagioclase porphyroblast. The plagioclase porphyroblast includes a planar fabric that is S_S , indicating that this crystal grew after the end of the D_S deformation. The garnet crystal has an irregular, embayed outline (some alteration to biotite), indicating it was unstable either during and/or after the D_S deformation. Sillimanite fibres define S_T in this view, and wrap around the plagioclase porphyroblast; sillimanite is likely to have been stable during S_S , before the onset of D_T and perhaps in the early part of the D_T deformation.

Sample LH 329 - kyanite-sillimanite-andalusite grade.
View in the YZ plane.

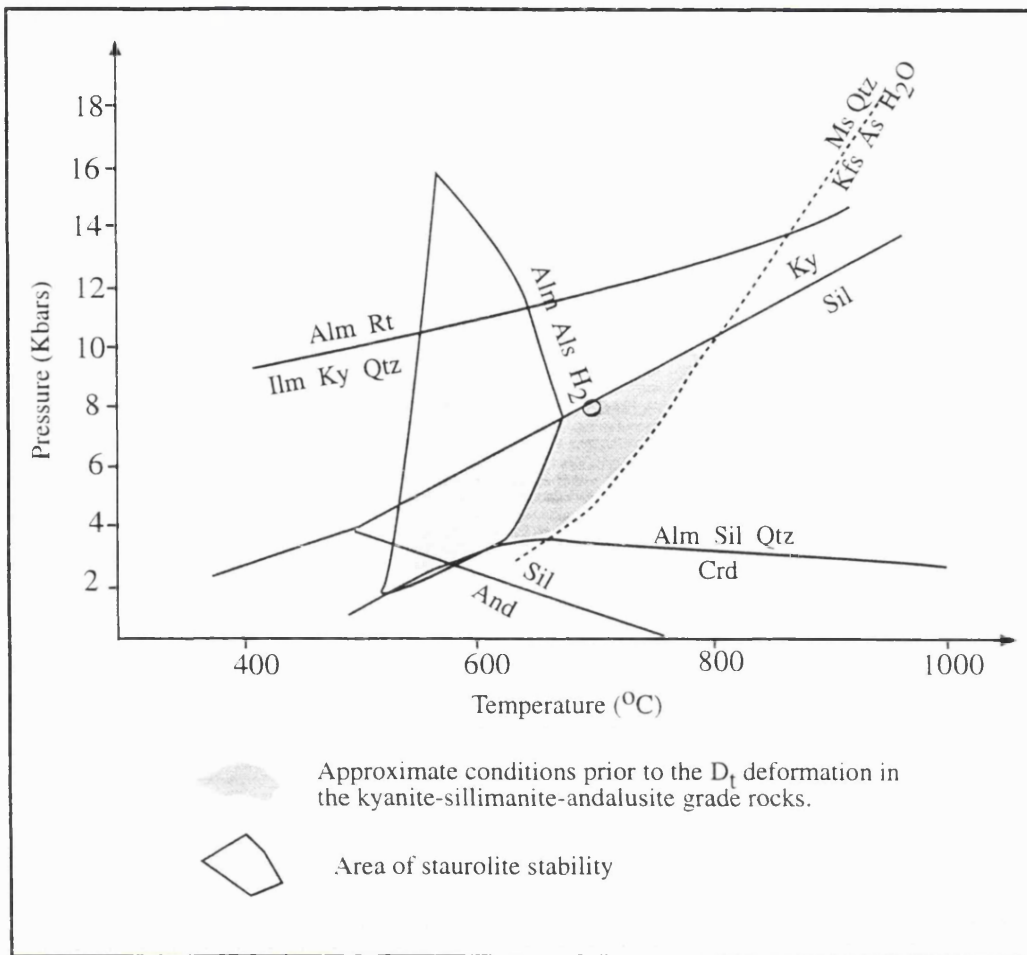


Figure 4.11 P-T plot with shaded area to indicate the likely location in P-T space of the kyanite-sillimanite-andalusite grade rocks after D₃ and before D₁. The area of P-T space has been constrained by the stability and instability of mineral phases, assessed from the mineral-fabric relations in numerous thin sections of rocks from kyanite-sillimanite-andalusite grade outcrops.

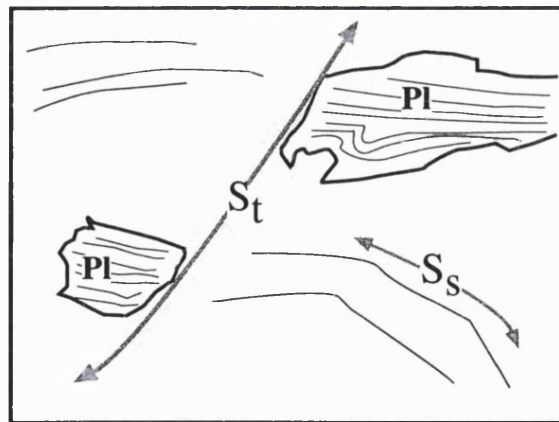


Figure 4.12 Plagioclase porphyroblast disrupted by the development of a pressure solution seam, formed parallel to the S_t foliation plane. A proportion of the plagioclase crystal has been removed by pressure solution along the seam, creating an apparent offset in the plagioclase crystal.

Sillimanite fibres lie along the trace of the solution seam, indicating that this sample was within the stability field of sillimanite at least during the early part of the D_t deformation event.

Sample LH 337. View in the YZ plane.
Kyanite-sillimanite-andalusite grade.

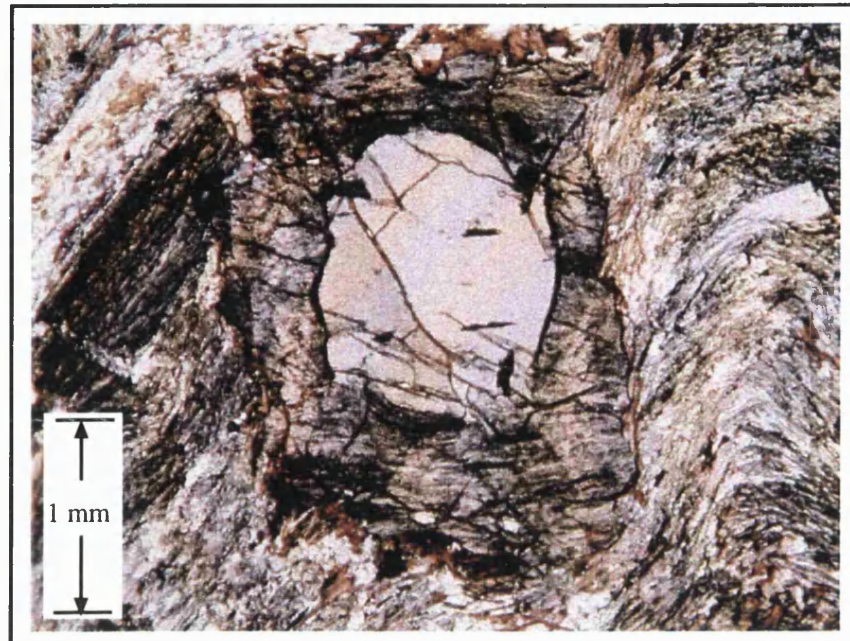
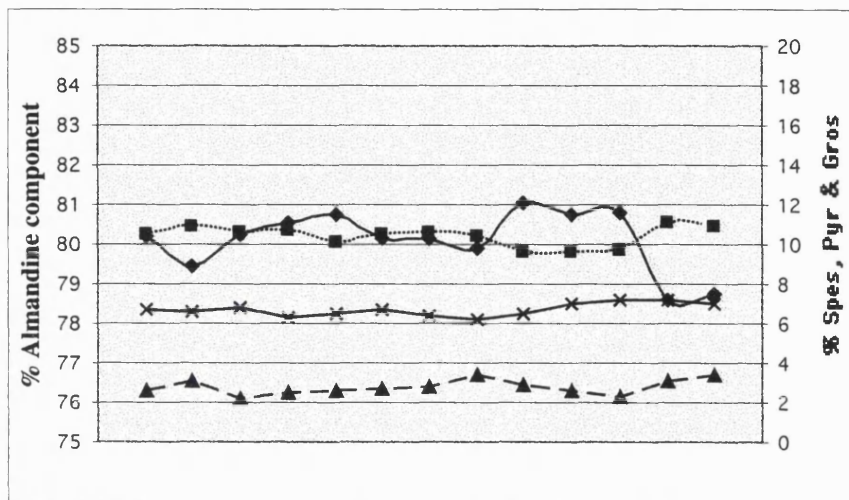


Figure 4.13a Photograph and interpretative sketch of a garnet porphyroblast with a 'core and rim' texture.

The core portion of the porphyroblast contains sparse, large inclusions of ilmenite with no apparent preferred orientation. The interface between the core and rim sectors of the garnet is irregular, suggesting that resorption of the garnet occurred at this phase.

The rim portion of the garnet contains clearly defined straight inclusion trails: this foliation is likely to be S_s . The included fabric in the rim of the porphyroblast does not pass into continuity with the trace of S_s in the matrix of the sample: the S_s fabric in the matrix has been affected by the D_t deformation which has caused rotation of its orientation. The growth of garnet at the rim of this porphyroblast, then, had stopped prior to the onset of the D_t deformation event.

Sample LH 339. Kyanite-sillimanite-andalusite grade.
View in YZ plane.



Rim Core Rim
 Distance across diameter of porphyroblast
 Rim Core Rim

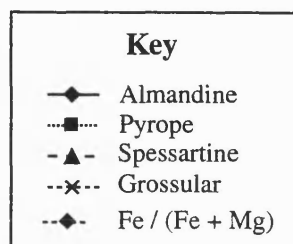
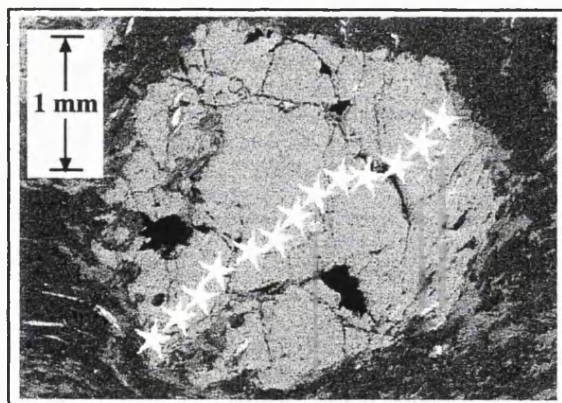
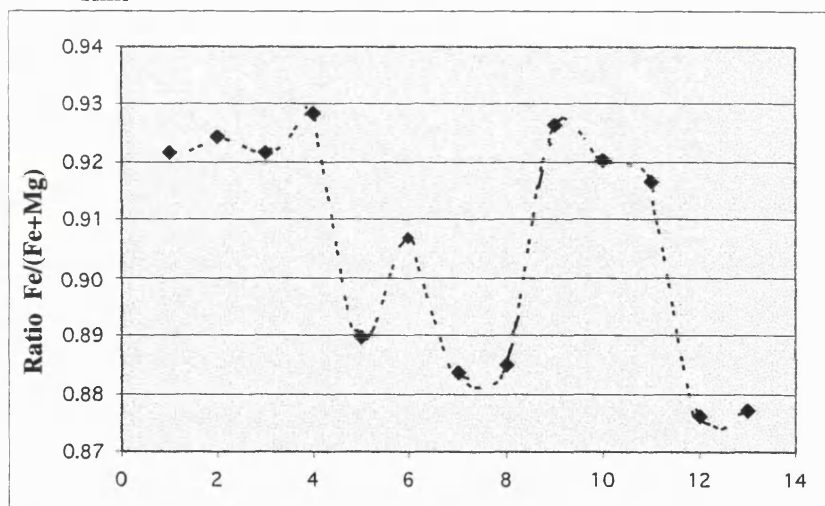


Figure 4.13b Compositional variation across porphyroblast from sample LH 309 (kyanite-sillimanite-andalusite grade) showing change of composition at core-rim boundary.

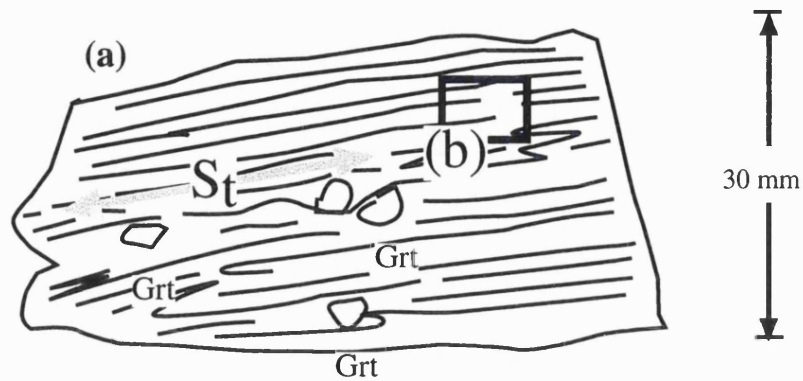
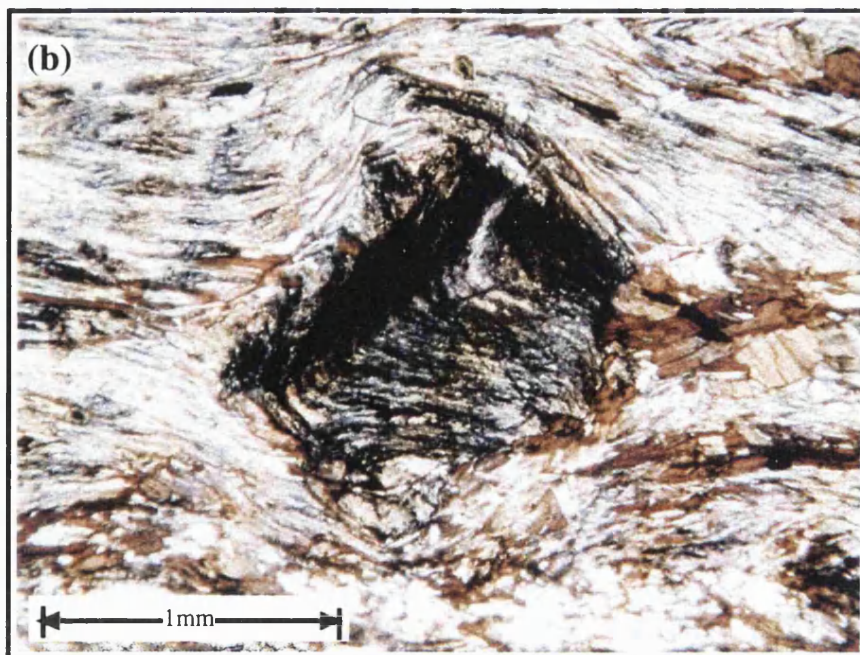


Figure 4.14a

Above Sketch of a rock slice from sample LH 339, at 90° to the $L_{S/t}$ lineation. S_t is the dominant foliation in this sample. The location of **figure 4.14b** is indicated.

Figure 4.14b

Below. Location of view as indicated in **figure 4.14a**. Subhedral staurolite crystal includes an open fold hinge, interpreted to be the early stage of S_s deformation during D_t . Continued deformation during D_t subsequently intensified the S_t foliation causing eradication of S_s in the matrix. Sample LH 339. Kyanite-sillimanite-andalusite grade. View in the YZ plane.



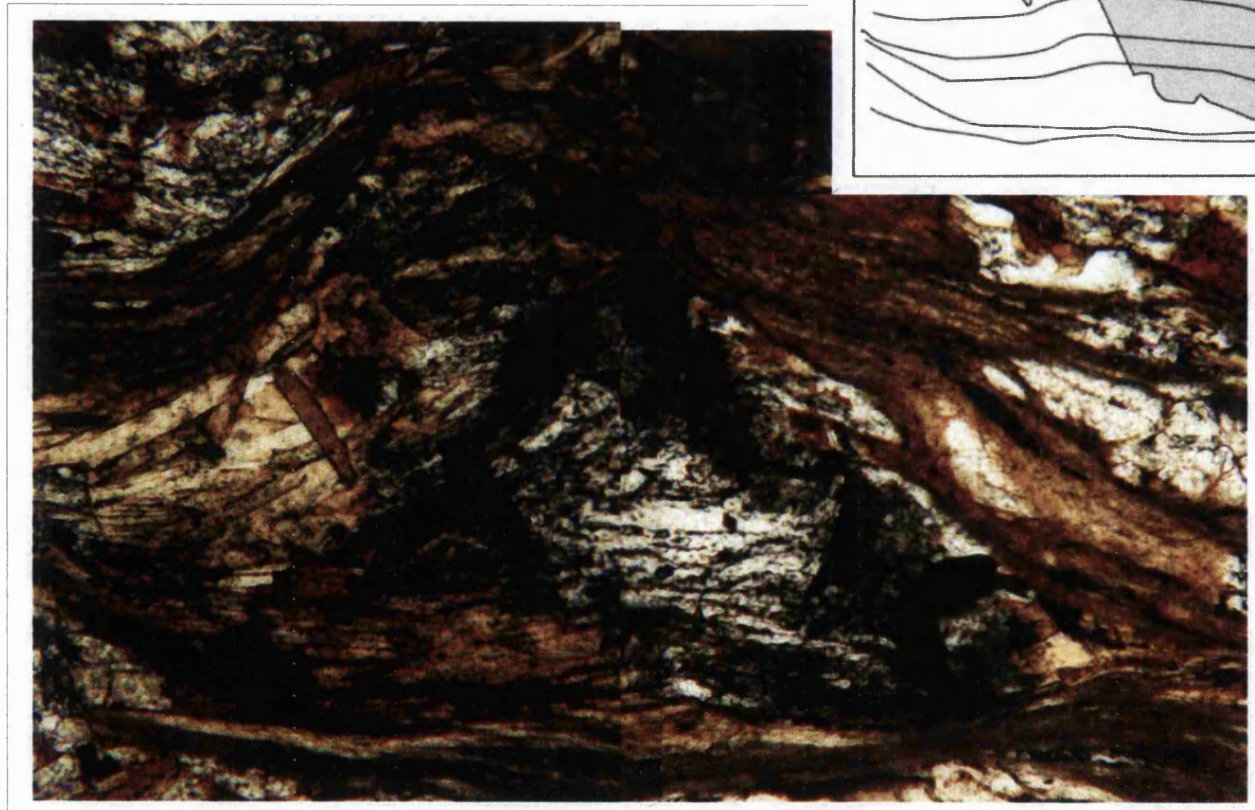


Figure 4.15

A crystal of andalusite overprints the S_1 foliation, defined by sillimanite. Sillimanite also wraps the andalusite porphyroblast, indicating that rotation of the S_1 foliation continued after the end of andalusite growth. Euhedral staurolite and biotite crystals also overprint the S_1 fabric: these textures are interpreted as indicating the staurolite and biotite grew after the end of D_1 .

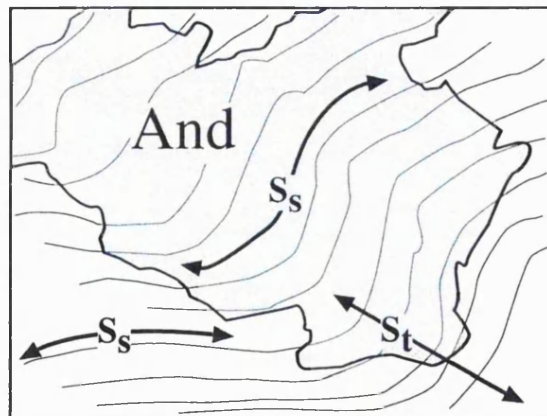


Figure 4.16 Photograph and interpretative sketch of andalusite - foliation relationship. The area covered by the andalusite crystal in the photograph is indicated in grey in the sketch beneath. The andalusite porphyroblast shows a rotational texture: the foliation in the crystal and in the matrix is S_s . This texture indicates that andalusite grew, and included the S_s foliation, during the D_t deformation event (during which the S_t foliation formed).

Section LH 123 - viewed in the YZ plane.
Kyanite-sillimanite-andalusite grade.

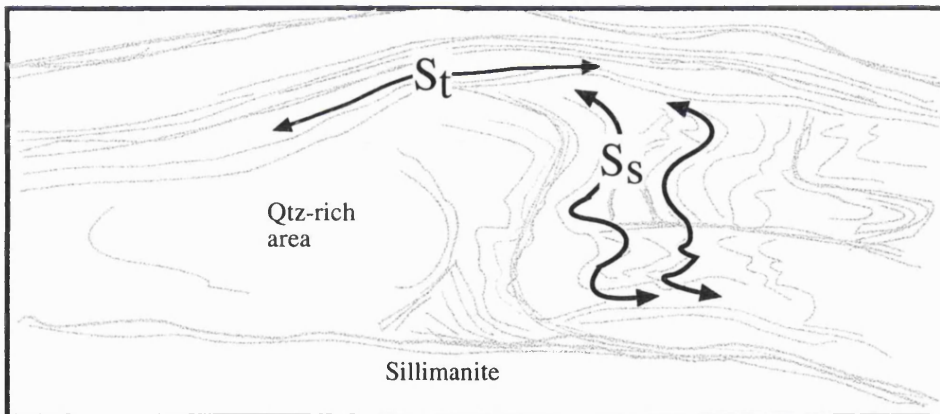
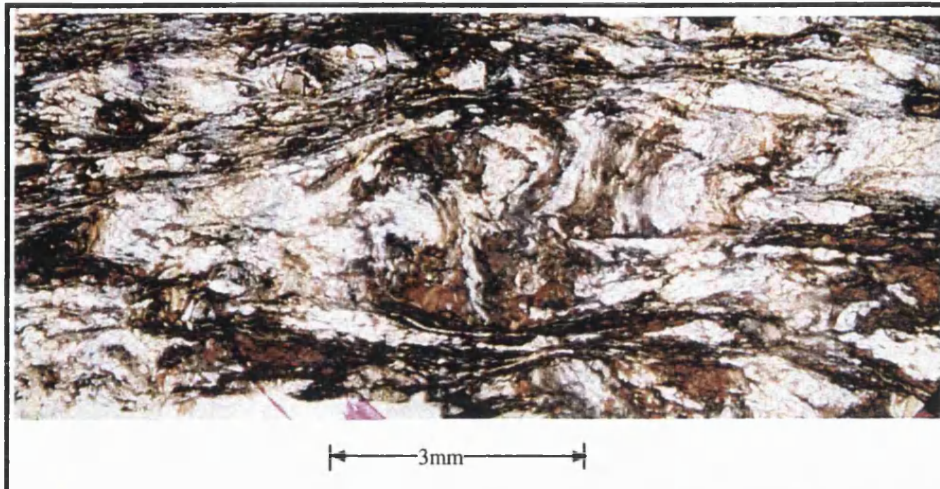


Figure 4.17 Quartz-rich area within a schistose layer. Open crenulations of the S_s fabric (deformed by D_t) are preserved in the more resistant quartz-rich area. In the surrounding, mica-rich rock, the S_t foliation is dominant, formed as a consequence of the continued crenulation of S_s by D_t , achieving eventual transposition of the S_s fabric. The S_t foliation is axial planar to the folds in the S_s surfaces.

Sample LH 335 - viewed in the YZ plane. Sillimanite-andalusite grade.

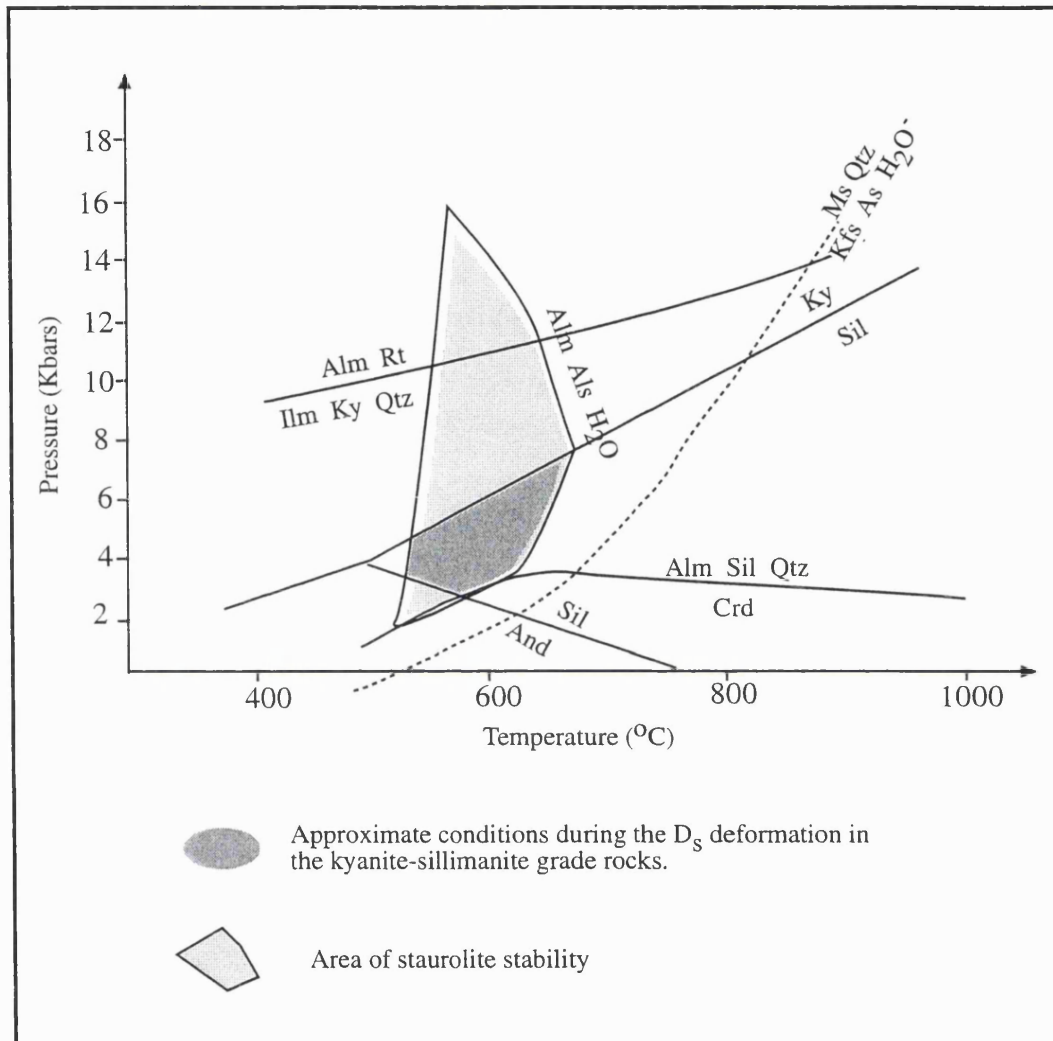


Figure 4.18 Approximate P-T conditions for the sillimanite-andalusite rocks, prior to the onset of the D_t deformation. The area in P-T space is constrained from the stability / instability of key metamorphic minerals, which has been deduced from microstructural analyses of numerous samples from the sillimanite-andalusite grade rocks, with respect to the S_s and S_t foliations. .

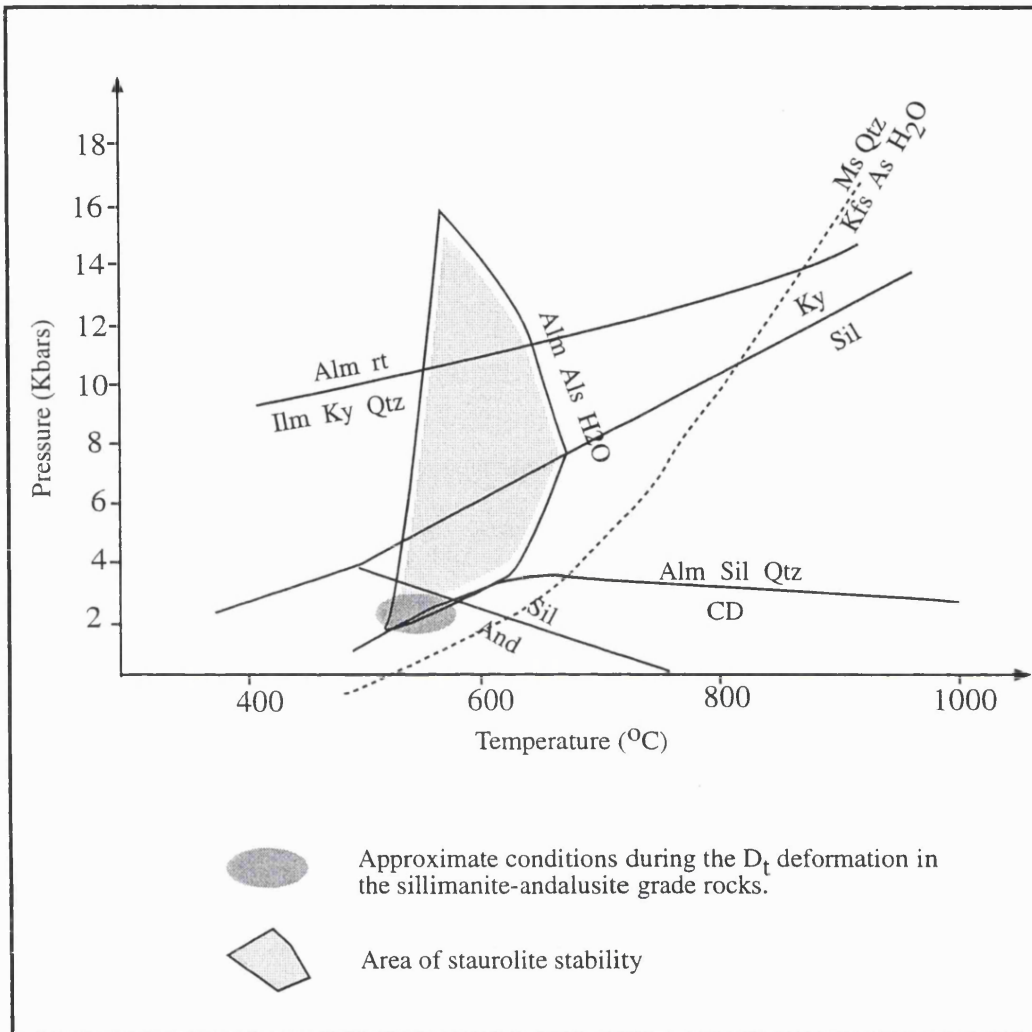


Figure 4.19 Approximate P-T conditions during the D_t deformation in sillimanite-andalusite rocks that crop out in Los Guajares and Sierra Chapparal areas. These conditions have been estimated from the mineral-foliation relationships observed in multiple thin-sections of the sillimanite-andalusite grade rocks. Staurolite and andalusite crystals show clear rotational fabrics, including the S_s foliation, developed during the period of S_t foliation growth.

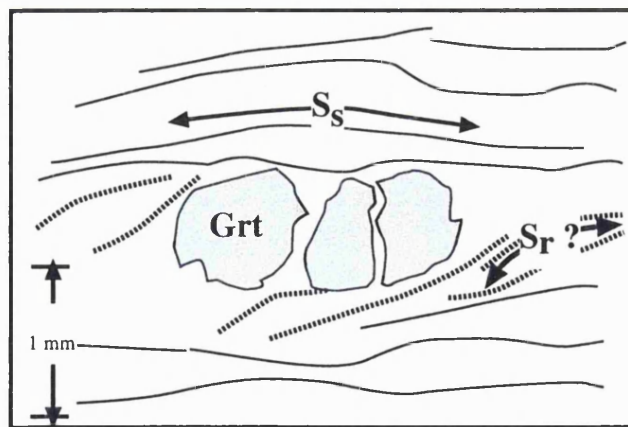
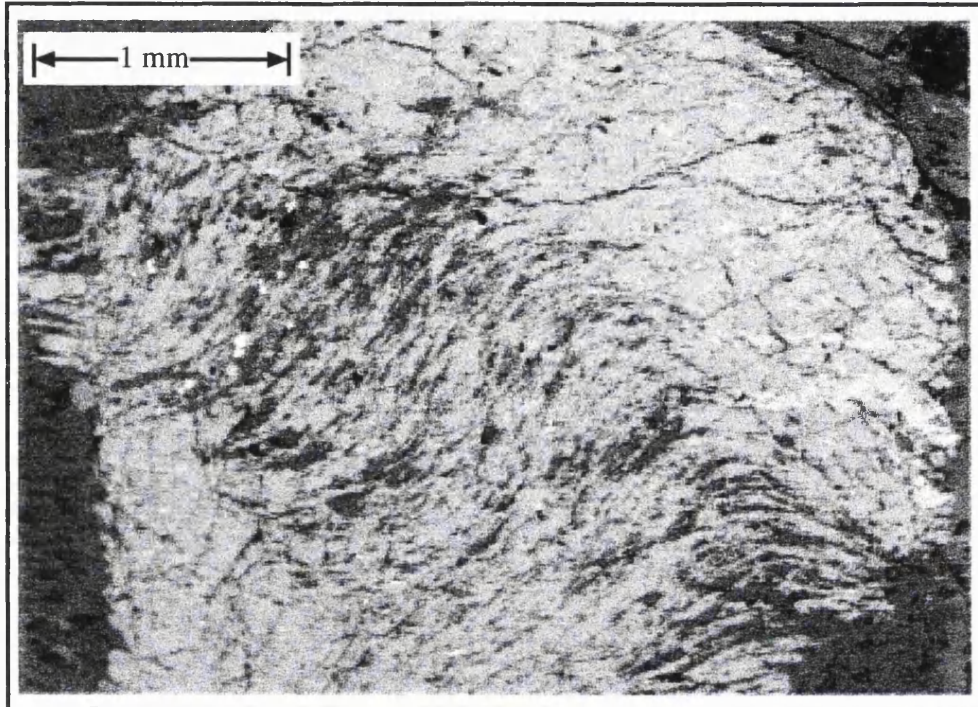


Figure 4.20

Microphotograph and interpretative sketch. Garnet porphyroblast, with apparent development of cracks at 90° to the S_s foliation, caused by extension of the garnet porphyroblast parallel to the S_s foliation. This extension may have occurred during the D_t deformation event.

Sample LH 194. View in YZ plane.
Garnet/staurolite-andalusite grade.



Key




-  Garnet
-  Quartz inclusions
-  Ilmenite / magnetite inclusions

Figure 4.21

Image from the electron microprobe and interpretative sketch

Garnet porphyroblast with curved inclusion trails of quartz and opaque minerals, indicating garnet growth during the D_S deformation event.

This sample is from near to Rio de la Miel in the west of the area (VF 42730682) where the S_t foliation is commonly weakly developed.

LH 255. View in YZ plane.
Garnet/staurolite-andalusite grade.

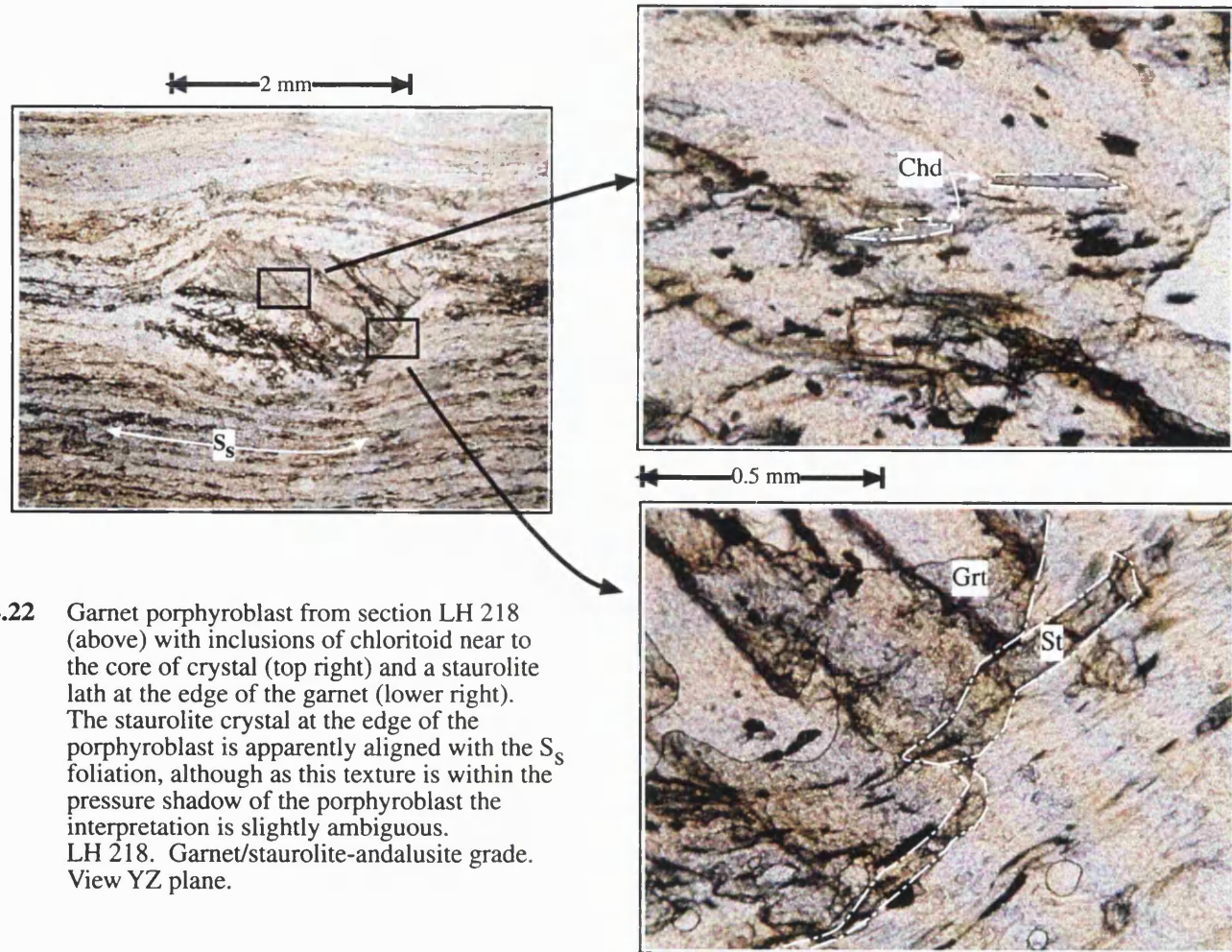


Figure 4.22 Garnet porphyroblast from section LH 218 (above) with inclusions of chloritoid near to the core of crystal (top right) and a staurolite lath at the edge of the garnet (lower right). The staurolite crystal at the edge of the porphyroblast is apparently aligned with the S_s foliation, although as this texture is within the pressure shadow of the porphyroblast the interpretation is slightly ambiguous. LH 218. Garnet/staurolite-andalusite grade. View YZ plane.

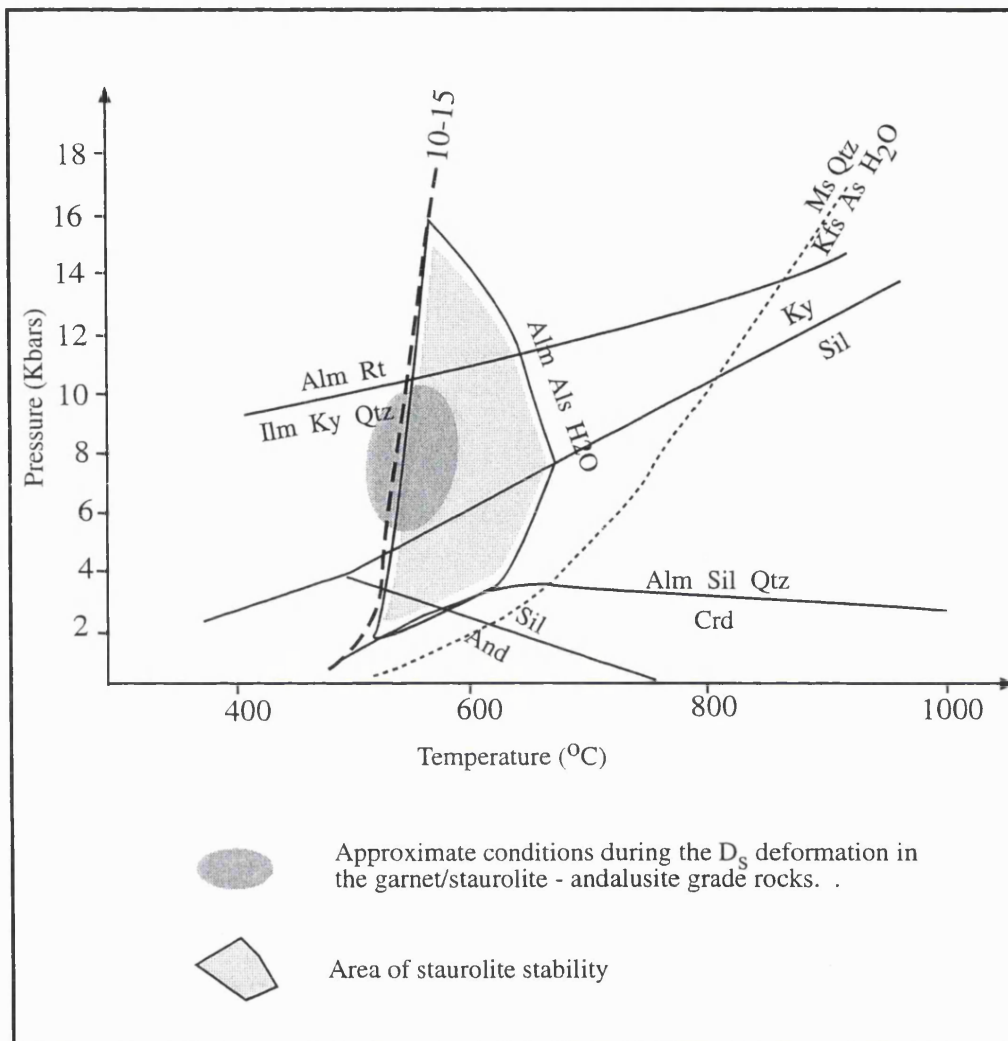
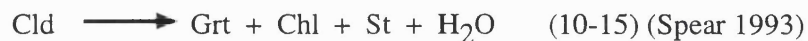


Figure 4.23 Approximate P-T space occupied by the garnet/ staurolite-andalusite grade rocks during the development of the S₅ fabric. The area of P-T space has been constrained from textures seen in garnet porphyroblasts in samples from Rio de la Miel (VF 43730682) and Rubite (VF 46700719), in which staurolite, and chloritoid and staurolite, respectively, are present as inclusions. Textures seen in these rocks indicate that chloritoid breakdown to staurolite was occurring during garnet growth, simultaneously with the D₅ deformation:



shown on the P-T plot above.
See also **Figure 4.22**.

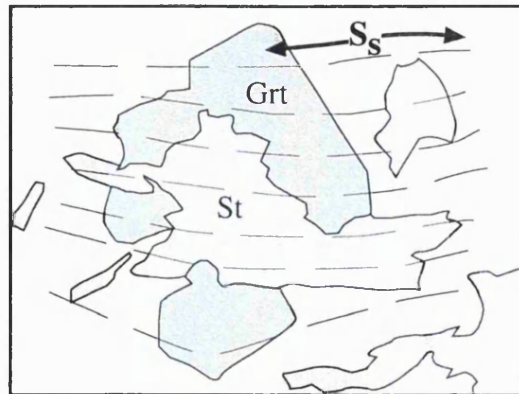
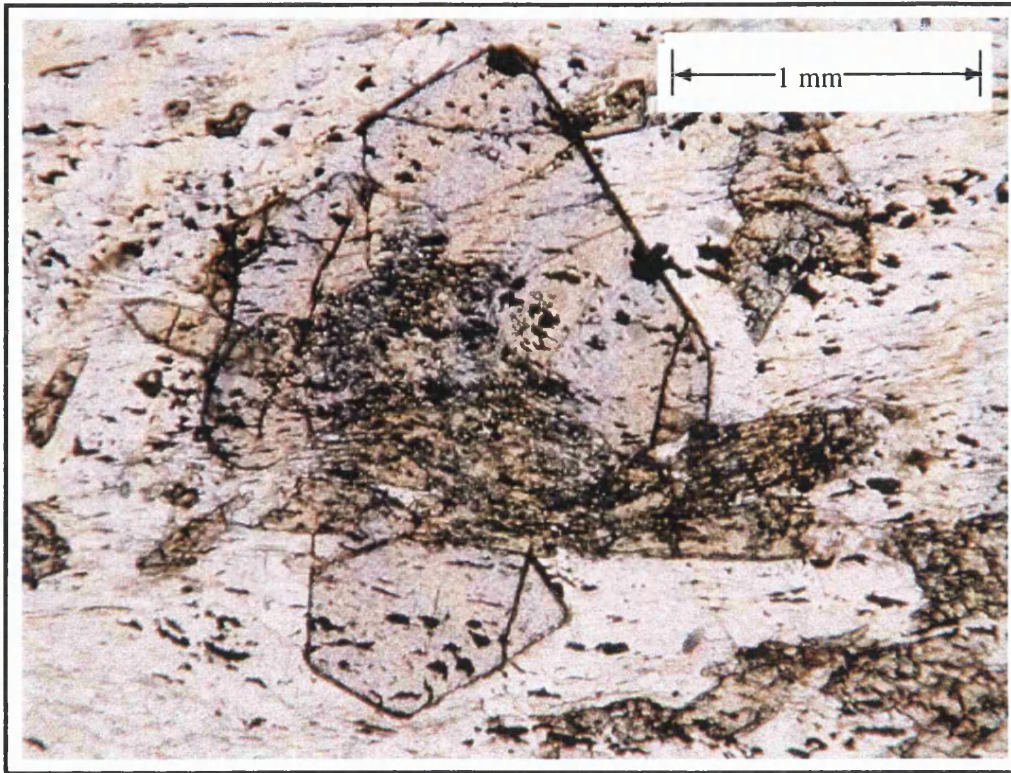


Figure 4.24 Photograph and interpretative sketch of textures between garnet and staurolite in a garnet / staurolite - andalusite grade rock from the west of Torrecuevas (VF 43560704 - LH 140). The dominant fabric in this view, defined by elongate opaque minerals, is the S_s foliation.

Prolific staurolite is present in the matrix: relationships with the garnet porphyroblasts and S_s foliation suggest that garnet and staurolite grew simultaneously after the end of the D_s deformation event and before the onset of D_t .

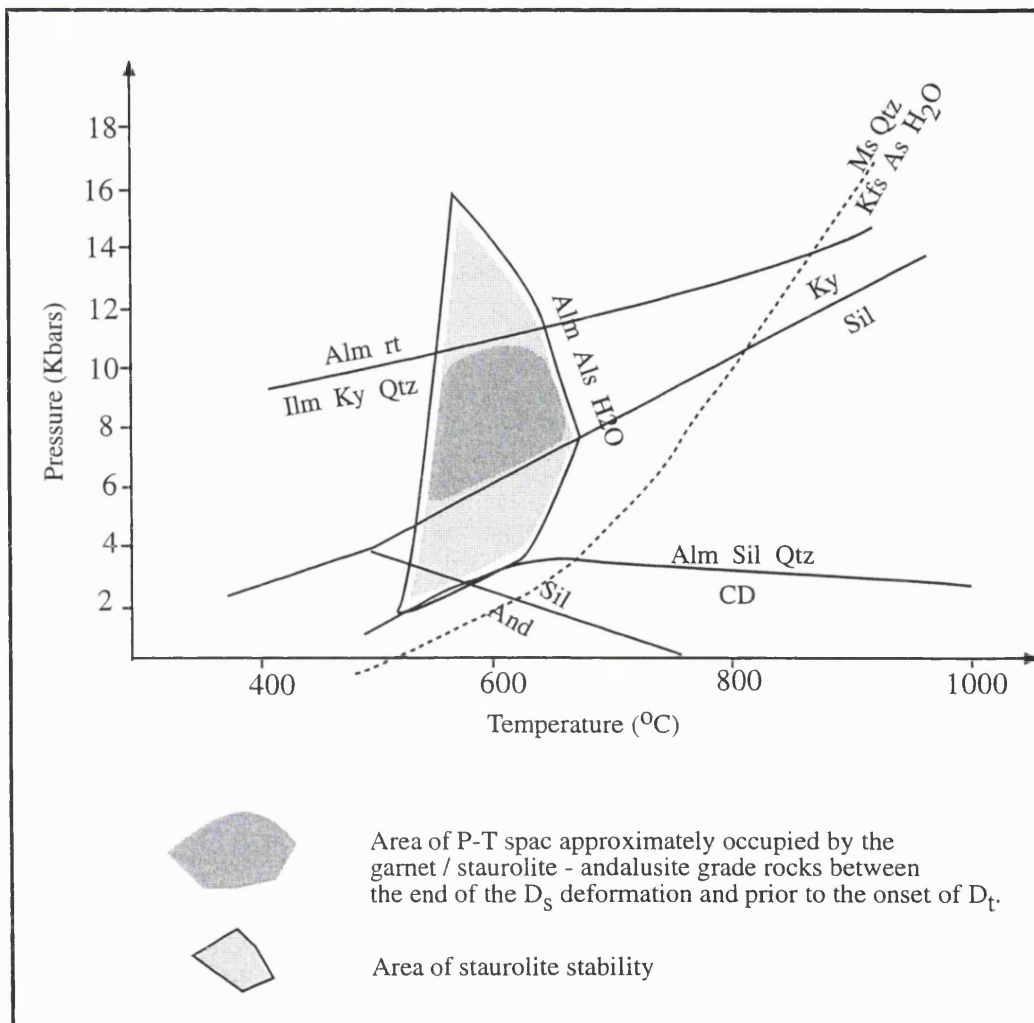


Figure 4.25 Approximate area of P-T space occupied by the garnet / staurolite - andalusite rocks at the end of the D_s deformation event and prior to the onset of D_t.

The area of P-T space has been constrained by the mineral textures with the S_s and S_t foliation surfaces seen in multiple thin sections of rocks from the garnet / staurolite - andalusite grade rocks in the studied area.

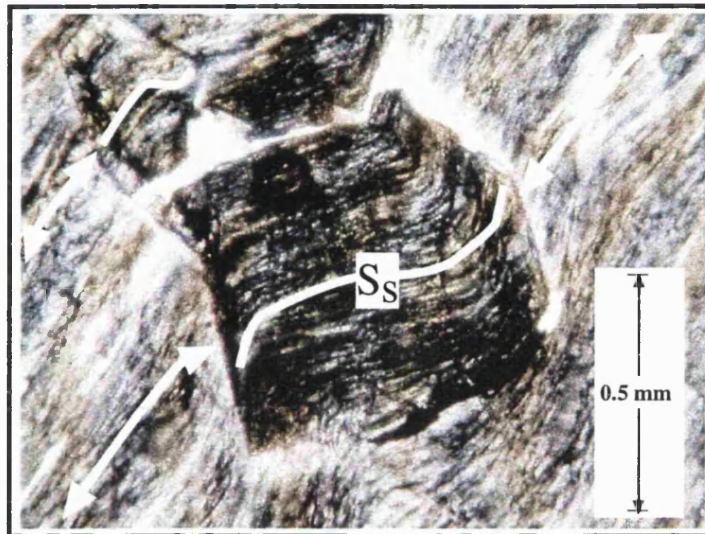
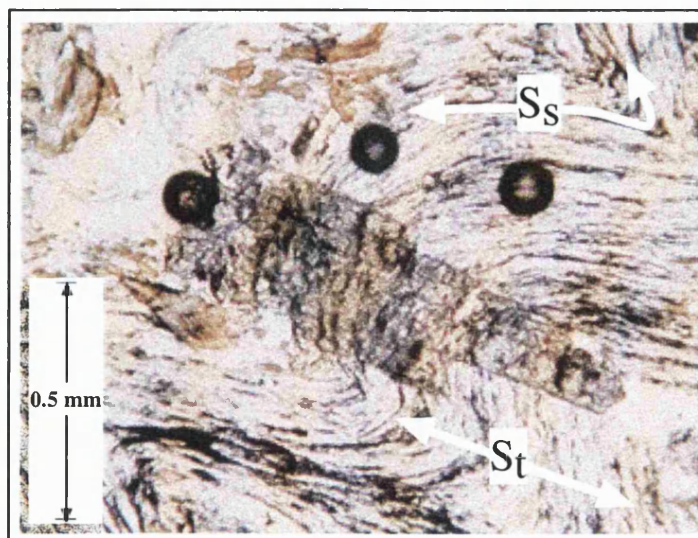


Figure 4.26a Above Euhedral staurolite crystal including the S_s foliation, with some relative rotation between the included S_s foliation in the staurolite crystal and S_s in the matrix. This texture implies that relative rotation of S_s in the matrix occurred after this staurolite porphyroblast stopped growing. The deformation of S_s is attributed to D_1 , so that this porphyroblast stopped growing before the end of the D_1 deformation event.

Figure 4.26b Below Elongate staurolite crystal including helicitic folds of the S_t fabric. This texture indicates that this staurolite porphyroblast continued growing until after the end of the D_1 deformation event. 3 air-bubbles (dark circles) disrupt this view.

Section LH 143 - Garnet / staurolite - andalusite grade.
Viewed in XZ section.



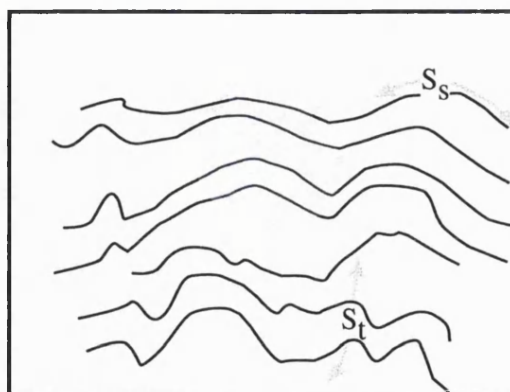


Figure 4.27 An andalusite porphyroblast showing helicitic over-printing relations with the S_s and S_t foliations: the S_t foliation is weakly developed here, and S_s is the dominant fabric. The slight distortion that the D_t event has caused to the S_s fabric in the matrix is evident in the included fabric of the andalusite porphyroblast.

Sample LH295 . View in the YZ plane.
Garnet / staurolite - andalusite grade.

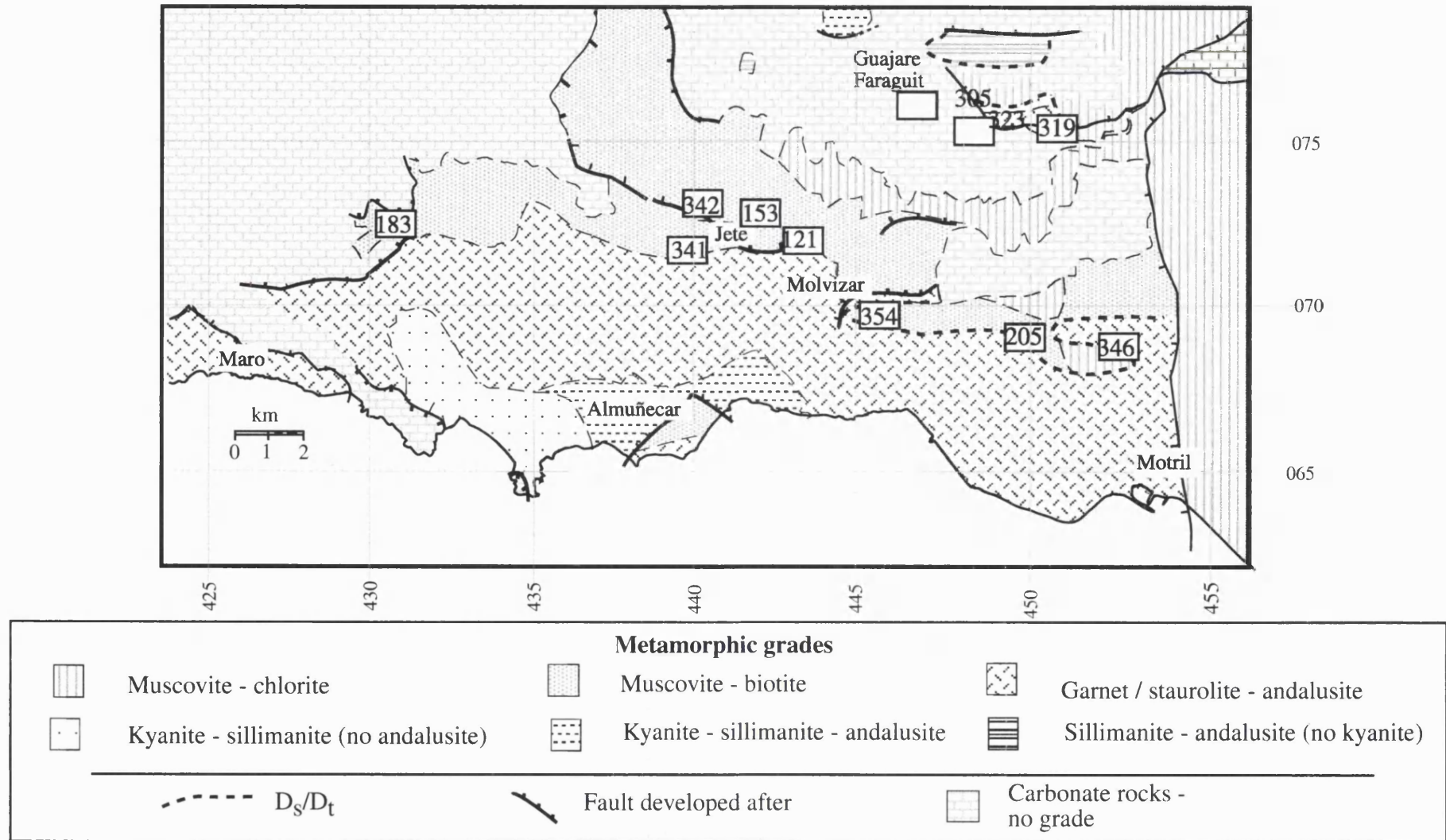


Figure 4.28 Map of the studied area showing the locations of samples within the garnet-absent assemblages that contain andalusite. Samples 121, 153, 183, 341 and 342 are close to garnet-bearing rocks: samples 205, 305, 319, 323, 346 and 354, in the east of the area, are close to the D_s/D_t tectonic contact (see key).

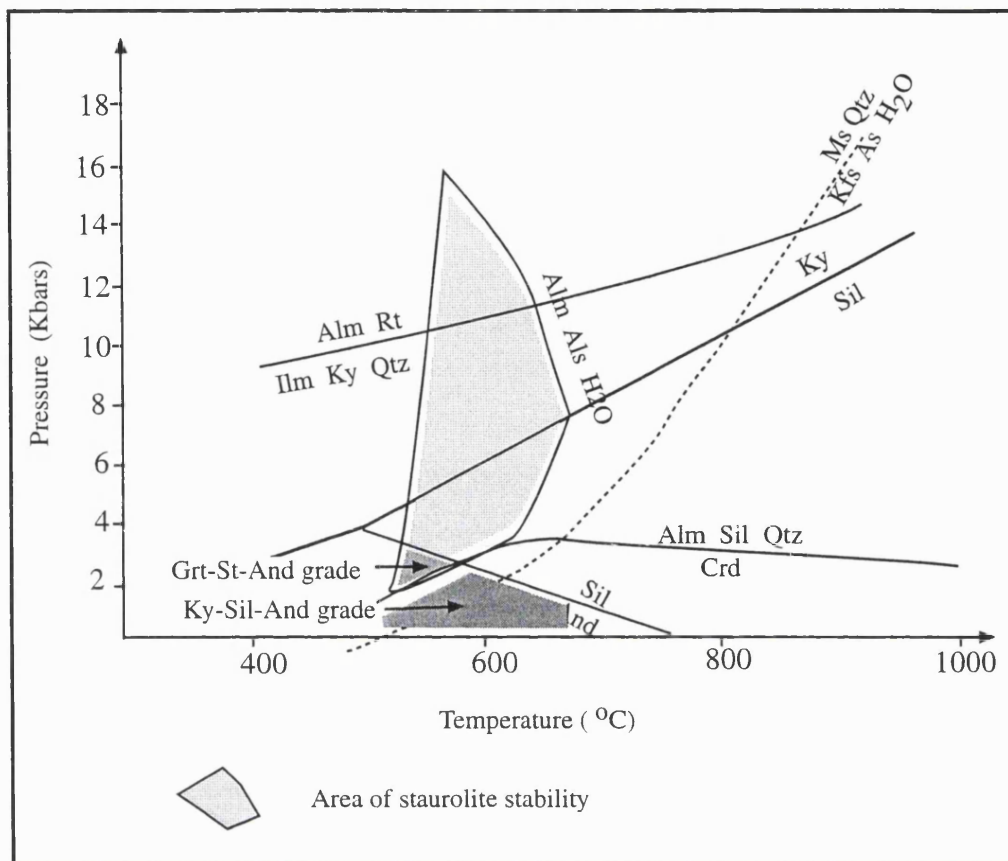


Figure 4.29 Approximate P-T space occupied by the kyanite-sillimanite-andalusite grade rocks and the garnet/ staurolite - andalusite grade rocks during the development of the S_t fabric. In the sillimanite-bearing assemblages, no staurolite crystals overprint the S_t foliation indicating that these rocks did not pass through the stability field of staurolite at this time. In the garnet/staurolite-andalusite rocks, 'late' staurolite shows textural relationships indicative of growth during and after the D_t deformation event.

The mineral - foliation relationships were deduced by analysis of numerous sections cut at 90° to the lineation.

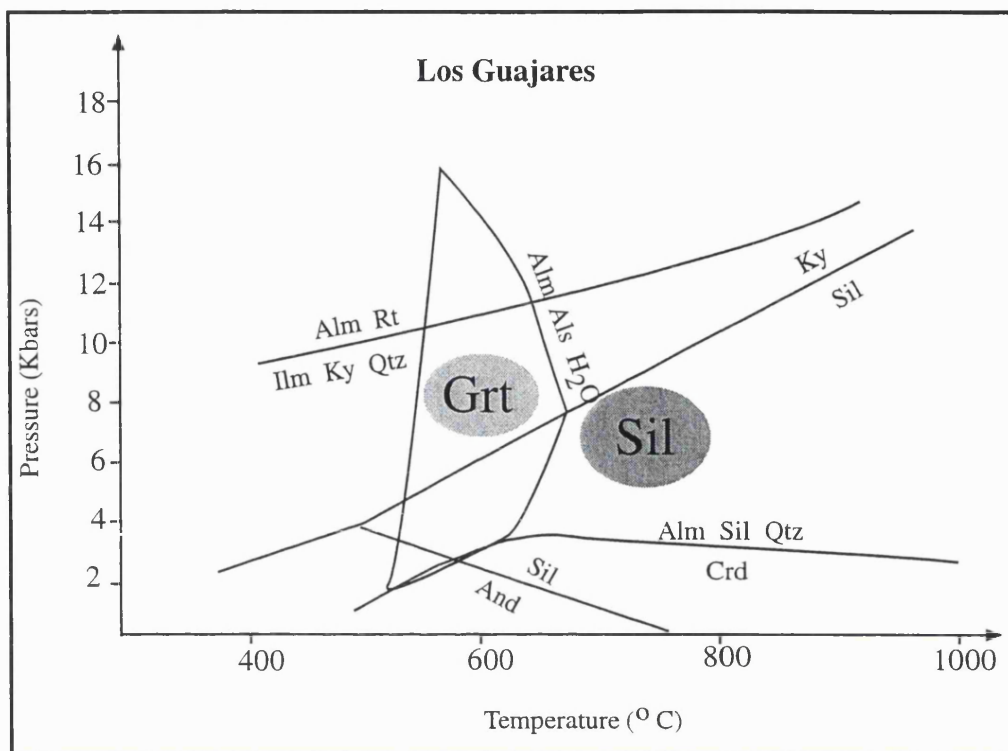


Figure 4.30 P-T axes to show the approximate positions in P-T space of two metamorphic grades seen in the Los Guajares area during the D_S deformation event. Mineral relations in the sillimanite-bearing rocks indicate that garnet and sillimanite were growing during the D_S deformation: in the garnet/staurolite-andalusite rocks, staurolite and garnet were stable. These observations represent a summary of data collected from the analysis of numerous thin sections cut in the YZ plane from rocks in the Los Guajares area.

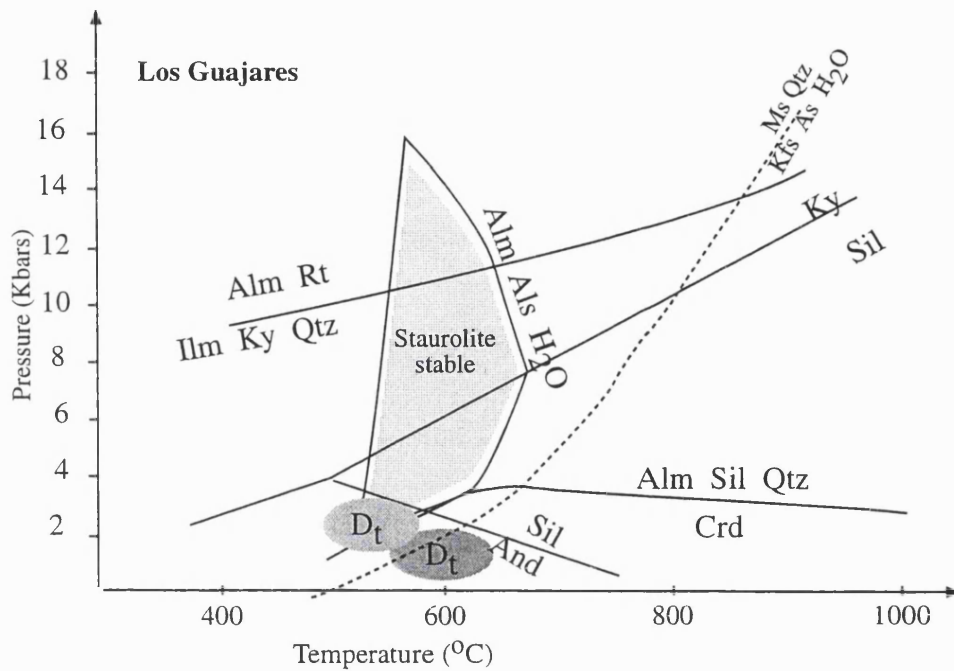


Figure 4.31a (above) P-T plot showing predicted P-T conditions for sillimanite-bearing and garnet/staurolite-andalusite rocks near to Los Guajares during the D_t deformation. The sillimanite-bearing rocks do not show evidence of having passed into the staurolite stability field in the late part of their evolution.

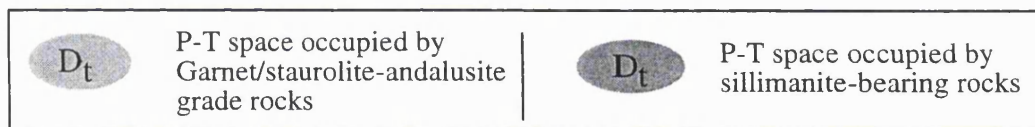
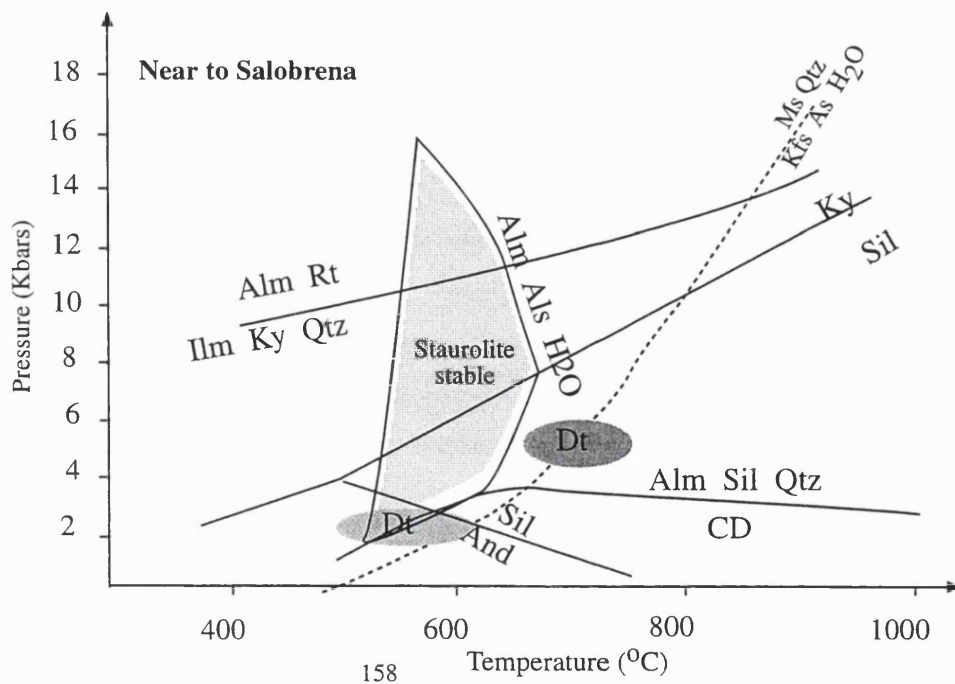


Figure 4.31b (below) P-T plot showing predicted P-T conditions for sillimanite-bearing and garnet/staurolite-andalusite rocks to the north of Salobrena during the D_t deformation. The sillimanite-bearing rocks passed into the stability field of andalusite after the end of the D_t deformation at temperatures insufficient to crystallise staurolite.



CHAPTER 5 CONSTRaining THE P-T-t PATH: QUANTITATIVE METHODS

PART 1 THERMOBAROMETRY

5.1 Introduction and methods

5.1.1 Theoretical basis of thermobarometric techniques

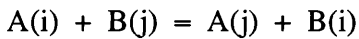
Thermobarometry uses the compositions of mineral phases within a sample that are considered to have formed in equilibrium with each other in order to elucidate an area on the pressure-temperature plot through which the assemblage has passed. As seen in Chapter 4, an area of P-T space in which a sample existed may be constrained from the mineral stability fields: precise measurements of mineral compositions enable more accurate pressure / temperature conditions to be calculated.

Depending on the mineral assemblage present and the relationships between the phases, the method of pressure / temperature estimation may be based on one of two principal types of reaction: an exchange reaction or a net-transfer reaction. An exchange reaction describes the way in which a pair of isovalent elements are interchanged between two mineral phases, while in net-transfer reactions, mineral phases are produced and consumed as a consequence of the re-distribution of elements. The suitability of a reaction as a thermometer or barometer is determined by its thermodynamic properties: exchange reactions are commonly calibrated as thermometers as they tend to have large ΔS (entropy) and ΔH (enthalpy) (i.e. are sensitive to temperature) and small values of ΔV (volume) i.e. are not sensitive to pressure. Net-transfer reactions tend to be appropriate for the estimation of pressure as they typically have a large ΔV value and are relatively insensitive to temperature (small ΔS and ΔH).

A map showing the locations of samples containing mineral assemblages to which calibrated thermometers / barometers were applied is shown in **figure 5.1**.

5.1.2 Exchange reactions

For a given exchange reaction, the distribution of the isovalent elements between two mineral phases will be determined by external conditions of pressure or temperature. A general statement for this type of reaction may be written as:



where (i) and (j) are the exchanging cations between the two phases A and B, which are in equilibrium. (Essene, 1982). This may be re-written as an equilibrium constant reaction:

$$\exp(-\Delta G / RT) = K = a_j^A a_i^B / a_i^A a_j^B$$

where K = a constant

$\Delta^\circ G$ = change of Gibbs free energy

R = gas constant

T = temperature

a_j^A = activity of component j in phase A

Substituting $a = \gamma X$

we arrive at:

$$K = (\gamma_j^A \gamma_i^B / \gamma_i^A \gamma_j^B)(X_j^A X_i^B / X_i^A X_j^B) = K_T \cdot K_D$$

where K_D = distribution coefficient

γ_T^S = activity coefficient of component S in phase T (Essene, 1989)

The value of the distribution coefficient may be determined from the chemical analyses of the minerals, measured on an electron microprobe; this was the technique used in this study (**Appendix Two**). If the activity coefficient ratio γ_i / γ_j for each phase is known (from experimental or thermodynamic data), the value of K_D will be related to the temperature at which the minerals equilibrated in an exponential way.

The most commonly used exchange thermometers involve the isovalent species Fe^{2+} and Mg^{2+} : i.e. the biotite - garnet thermometer of Ferry & Spear (1978) – discussed in section 5.4.2.

5.1.3 Net Transfer reactions

Net transfer reactions are those in which phases are produced and consumed: these reactions often generate large changes in volume (i.e. $\Delta V_{\text{reaction}}$ is large) so that they are, in general, appropriate for use as barometers. The activity of each phase in the equilibrium assemblage is calculated by measuring the chemical composition of the phases. As the values of the mineral activities are related to the K_{eq} of the reaction, where thermodynamic values such as ΔC_p (constant pressure heat capacity) and $\Delta V_{\text{reaction}}$ are known, the pressure at which the mineral assemblage equilibrated can be calculated.

5.1.4 General problems in the application of thermobarometers

Essene (1982) highlights several sources of inaccuracy inherent in the application of calibrated thermobarometers to actual metamorphic assemblages. These include the following:

5.1.4.1 Inaccurate thermodynamic models of solids

Experimental data for the a-X relationships in silicate minerals, on which the calculation of the K_D depends, are only able to be measured at temperatures of $> 700^\circ\text{C}$. At temperatures significantly lower than this (i.e. below 600°C), extrapolated a-X values are likely to introduce considerable error into the calculation of K_D , particularly for net-transfer reactions. Coefficients to model the non-ideal behaviour of complex systems serve, in part, to counteract the inaccuracies introduced from the extrapolation of a-X to low temperatures. An example of this is the discussion of the quaternary solid solution model of garnet presented in section 5.3.

5.1.4.2 Errors in normalising mineral formulae

The electron probe is not able to detect the Fe^{3+} species, or the effects of OH replacement by O^{2-} in hydrous silicates: this introduces ambiguity as to the $\text{Fe}^{2+}/\text{Fe}^{3+}$ ratio, and the amount of oxygen present in the mineral structure. This data is required to normalise the results from

the electron probe, and cannot be calculated directly for minerals that are prone to contain large numbers of cation vacancies (i.e. amphiboles and micas). Unless data for Fe^{3+} and OH^- is available from other techniques (i.e. wet chemistry), the amount of these species in a mineral phase is calculated using empirical formulae based on the stoichiometric formulae of elements present. This approach introduces a potential source of error into the results of the thermobarometers applied subsequently; errors in the amount of Fe^{3+} will influence the amount of Fe^{2+} deduced to be present in the samples, and the Fe^{2+} ion is the basis of several thermometers and barometers.

5.1.4.3 Effect of cation disorder in minerals / synthetic phases

The degree of order/disorder of cations in a mineral phase is assumed in order to calculate the value of ΔH for a mineral. Where uncertainties as to the degree of disorder exist in mineral structures (i.e. for feldspars and micas), the published values of ΔH may be inaccurate (Essene, 1982). It is difficult to remove this source of inaccuracy in the absence of sufficient thermobarometric data.

5.1.5 Special considerations of rocks showing disequilibrium textures

The fundamental assumption in the application of a calibrated thermometer or barometer to a mineral assemblage is that the mineral phases within that assemblage are in chemical equilibrium with each other. It has been demonstrated in previous sections that mineral assemblages from within the Alpujarride Complex commonly contain textures indicative of disequilibrium (e.g. sections 4.2 - 4.5). Garcia-Casco & Torres-Roldan (1996) present evidence of strong compositional disequilibrium textures in rocks from the Alpujarride Complex in the central Betics.

In view of the strongly disequilibrium textures and assemblages in the matrix of many samples from the area studied, a high proportion of the pressure and temperature estimates presented in this chapter have been obtained from inclusion suites within garnet porphyroblasts. Phases included in resistant porphyroblasts are most likely to have been 'armoured' from the subsequent changes of composition in the main body of the rock. However, re-equilibration between the inclusion and host mineral, as a consequence of diffusion and the infiltration of fluids along cracks in the porphyroblast, may permit modification of the original equilibrium compositions (section 5.5.2.5).

5.1.6 Estimating / minimising errors in pressure-temperature estimates

Kohn & Spear (2000) provide a mechanism by which results from garnet-biotite thermometry may be corrected for the effects of retrograde garnet dissolution. The upturn of the spessartine component at the rims of garnet porphyroblasts are interpreted to indicate that net-transfer reactions have been in operation during the retrograde history of the assemblage in addition to exchange reactions. Kohn & Spear (2000) recognise that biotite in the matrix will become enriched in Fe if garnet dissolution has occurred (as garnet has a higher Fe/Mg ratio than biotite). Consequently, the temperatures produced from the GARB thermometer (sections 5.5.2.5, 5.5.2.6 and 5.5.3.6) will be higher than the actual peak temperature if a correction factor is not applied.

High-resolution X-ray maps of garnet, containing Mn concentration data in the pixels of the images, have been used by Kohn & Spear (2000) to calculate the parameters that permit correction factors for the effects of garnet dissolution to be applied. In the absence of equipment able to collect the data necessary to calculate these parameters, garnet porphyroblasts with low or absent peaks of Mn near to the rim of the porphyroblasts have been selected for the application of thermobarometric techniques. It is likely that the effects of net transfer reactions are minimised in these assemblages (Spear, 1993; Kohn & Spear, 2000).

5.2 Manipulation of probe data

5.2.1 Introduction

The mineral compositions provided by the electron micro-probe (details of procedure in **Appendix Two**) are in the form of weight percent oxides. The electron ion-probe cannot distinguish between the Fe^{3+} and Fe^{2+} species, so all the iron oxide detected is assumed to be Fe^{2+} . It is known from wet chemical analysis and Mossbauer spectroscopy that Fe^{3+} ions are present in the structure of numerous ferro-magnesian oxide and silicate minerals. The quantity of Fe^{3+} present in the mineral formulae is calculated using equations derived from empirical relationships and/or assumptions of charge-balance between cations and anions in the formula unit. Subsequently, the weight percent oxide figures for the minerals may be

converted into the molecular proportions of cations, which are required in the thermobarometric calculations.

5.2.2 Cation number calculation

Conversion from weight percent values to the molecular proportion of cations, or the 'Cation number' may be achieved by a simple manual procedure, outlined below and illustrated in **table 5.1**.

Table. 5.1 Calculation of cation number values from percent oxide values – example for an olivine – from Ragland (1989)

Oxide species	Weight percent oxide	Equivalent gram formula weight	Mol proportion cation
SiO ₂	39.60	60.1	0.6589
TiO ₂	0.02	79.9	0.0002
FeO	13.90	71.8	0.1936
MnO	0.25	70.9	0.0035
MgO	45.50	40.3	1.1290
CaO	0.31	56.1	0.0055
Na ₂ O	0.03	31.0	0.0010
K ₂ O	0.01	47.1	0.0002

- 1 Division of weight percent oxide into the gram formula weight of the oxide, producing the molecular proportions of the oxide
- 2 Multiplication of molecular proportions of oxides by the number of cations in the oxide formula unit , to give the molecular proportion of cations.

The computer program 'MinProg' (Harangi, 1992) contains an option to perform this calculation prior to the calculation of Fe³⁺ (section 5.2.4). This technique has been employed for all the mineral analyses used in the calibrated thermometers and barometers (section 5.5).

5.2.3 Spinel number selection

The 'MinProg' computer program, used to calculate the cation numbers of the analyses, requires that, for the Fe-Ti mineral series, a value for the spinel number is input into the program prior to the calculation of cation values. The minerals of all three series within the Spinel group (Spinel series, Magnetite series, Chromite series) contain 32 oxygens and 24 cations: hence, the spinel number chosen for this group is 32.

5.2.4 Fe³⁺ estimation

There are several ways to correct for the erroneous assumption that all iron in the structure of a mineral is the Fe²⁺ species. Techniques include estimation of the amount of Fe³⁺ in the formula unit by stoichiometric normalisation (Spear, 1993; Droop, 1987) and other routines applicable only to specific mineral phases (i.e. Williams & Grambling, 1990, for biotite; Spear & Kimball, 1984 for amphibole). Methods that can be only used for a specific mineral phase may introduce additional error into the calculation, as different assumptions may be implicit in the various routines used to calculate Fe³⁺ in different mineral species.

An example of the **stoichiometric** method of Fe³⁺ estimation is reproduced in Spear (1993). The initial assumption is that all Fe ions present are Fe²⁺, and the molecular proportions are normalised according to the idealised number of cations in the formula unit. The amount of Fe²⁺ which is actually present in the mineral structure as Fe³⁺ ions is calculated from the deduction of the actual value of the positive charge from the ideal value of positive charge for the formula unit. A positive result from this calculation indicates that Fe³⁺ is present in the formula unit. In hydrous minerals, and in minerals where there are structural vacancies in the cation sites (i.e. amphiboles, micas), the uncertainty in using this method to calculate the quantity of Fe³⁺ present is substantially increased (Spear, 1993).

A general formula based on the stoichiometric method outlined above for the estimation of Fe³⁺ is derived by Droop (1987): this routine is applicable to garnet, ilmenite, and other minerals in which it may be assumed that there are no vacant cation sites. For minerals in which vacant cation sites are present, (i.e. mica minerals, amphiboles), the method is modified by the assumption that the total number of cations of any subset of elements in the formula has a fixed value throughout the structure. This method of Fe³⁺ estimation is a convenient one, as it may be employed with only slight modifications to the majority of

mineral species, eliminating a potential source of inconsistency were multiple techniques to be employed. This method of Fe^{3+} correction has been applied to all the relevant probe results in this study, using an option within the computer program 'MinProg' (Harangi, 1992).

5.3 Modelling the activity of garnet

The non-ideal mixing behaviour of cations within the garnet structure (i.e. Fe, Mg, Ca, Mn) requires that a correction factor be applied to the activity-composition (a-X) relations calculated from measured mineral thermodynamic data.

The proportions of the six garnet end-members in a crystal - pyrope, almandine, spessartine, grossular, andradite and uvarovite – vary throughout pressure-temperature space. Two solid solution series, pyrope-almandine (pyrope, almandine, spessartine) and ugrandite (uvarovite, grossular and andradite) exist, in which there is continuous compositional variation.

The multiplicity of cation substitutions which are possible within the garnet structure render the development of an activity model to simulate the possible range of substitutions very difficult (Deer, Howie & Zussman, 1992). Activity models for garnet are typically based on either data from purely experimental calibrations, or from the comparison of naturally occurring garnet compositions with synthetically produced materials.

A comparison of the garnet-mixing models presented by Ganguly & Saxena (1984), Hodges & Spear (1982) and those of Ferry & Spear (1978) exemplifies the way in which assumptions about the way in which garnet cations mix varies between different authors. Ganguly & Saxena (1984) assume that the spessartine, grossular and pyrope components mix in a non-ideal way, and that the remainder of the garnet solid solution constituents exhibit ideal mixing. The non-ideal mixing nature of the Fe-Mg and Fe-Mn substitutions tend to act in opposing directions, as garnets with high spessartine component have low Fe/Mg values. (Ganguly & Saxena, 1984). In contrast, Hodges & Spear (1982) propose a model in which the spessartine component is assumed to have ideal mixing properties. Ferry & Spear (1978) consider only the mixing of the almandine and pyrope components i.e. the spessartine component is not considered to influence the mixing of the Fe-Mg components.

A garnet model proposed by Berman (1990) assumes that the grossular – pyrope garnet end-members mix with only slight deviation from ideal behaviour, and spessartine mixes in an ideal way with the other garnet components. Results arising from this model have been compared with assemblages from a variety of metamorphic conditions, including a comparison with natural samples from an Al-rich pelitic assemblage, containing both sillimanite and kyanite (Spear, 1993). In the sample analysed, the homogeneity of porphyroblast minerals was considered to indicate that equilibrium conditions near to the kyanite-sillimanite transition were approached, and the results arising from the application of a biotite-garnet thermometer using the Berman (1990) garnet model replicated this data to within experimental error.

Results from the garnet models discussed above will produce different results for different compositions of garnet; the model of Ferry & Spear (1978) consistently yields lower temperatures than the results produced by the other two models. Evidently, more spessartine rich garnets will produce more disparate results for these three models than results from samples where the spessartine content is very low. The paucity of appropriate assemblages identified in the area that are deemed to be in equilibrium (i.e. suitable for the application of thermobarometric techniques) requires that results from different calibrated thermometers/barometers be compared across the area (see **figure 5.1**). In this scenario, it is extremely important to choose calibrations of exchange / net-transfer reactions which incorporate similar models of garnet activity.

5.4 Choice of calibrations for barometers and thermometers

5.4.1 Introduction

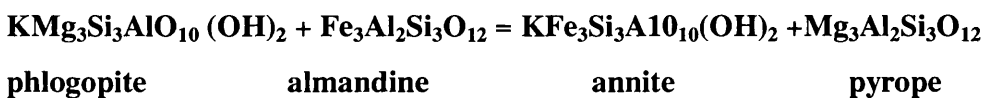
The existence of chemical equilibrium of mineral assemblages from pelitic schist within the quartzite and schist sequences was initially assessed from textural relations (sections 4.2 – 4.6). The choice of which calibrated thermometer or barometer to apply was determined by the assemblages in the rocks. Chemical analyses of the phases in equilibrium were then carried out on the electron micro-probe; at this stage many assemblages were discounted as it was apparent that alteration subsequent to metamorphism had strongly modified the composition of one or more phases. Low oxide percentage totals for a mineral were a common indication that alteration of the mineral structure had occurred.

The scarcity of appropriate assemblages suitable for the application of thermo-barometric techniques necessitated that estimates of pressure and temperature across the area were obtained from a variety of different mineral assemblages (**figure 5.1**). The comparison of pressure or temperature data obtained from different mineral assemblages is inevitably less accurate than comparing data generated from a single technique, but the rare occurrence of equilibrium assemblages made this unavoidable.

In order to minimise the error introduced by the use of multiple thermometers / barometers, the assumptions made in the calibration of each thermometer / barometer have been carefully considered (sections 5.4.2 – 5.4.5), in order to select calibrations for each assemblage with assumptions which are as concordant as possible.

5.4.2 Garnet-Biotite thermometer

A multiplicity of calibrations for exchange between garnet – biotite exist. The reaction is based on the equation:



A variety of published calibrations were applied to a single garnet-biotite pair from sample LH104; the results are shown in **figure 5.2**. The different activity models used to model the end-members of the garnet- biotite reaction, and the way in which these end-member components are assumed to interact with each other, account for the different results observed (e.g. section 5.3).

Ferry & Spear (1978) achieved the first successful experimental calibration of composition variation between biotite – garnet over a range of temperatures up to 800°C. A high ratio of garnet:biotite was used in these experiments in order to minimise the amount of compositional change that the garnet needed to accommodate during the reaction. The experiments, and hence the calibration, are restricted to use with iron-rich garnet and biotite compositions and garnets with low manganese and calcium contents (Ferry & Spear, 1978 and discussion above in section 5.3).

On the plot in **figure 5.2**, a cluster of K_{eq} lines intersect the X-axis between 630 – 680°C: this cluster includes the Ferry & Spear (1978) and Ferry & Spear (1978) with Berman (1990) garnet models. Similar results are also obtained from the Ganguly & Saxena (1984) symmetrical garnet model; slightly higher temperatures are yielded by the Holdaway *et al* (1997) calibration.

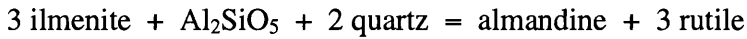
The garnet-biotite (GARB) model of Holdaway *et al* (1997) includes factors that attempt to simulate numerous sources of inconsistency not considered in other calibrations. These include: accounting for the effect of the non-ideal nature of the Fe-Mg substitution; the presence of Fe^{3+} in natural systems; and a re-assessment of garnet and biotite mixing properties (Holdaway *et al*, 1997). Results from this model produce slightly higher temperatures (at a fixed pressure) than the results from the calibration of Ferry & Spear with Berman (1990). Comparison of results from this thermometer with garnet-biotite compositions from natural staurolite-bearing assemblages yielded temperatures higher than those given from other thermometers (see table 9 in Holdaway *et al*, 1997).

The GARB calibration of Indares & Martingole (1985), with either the Ganguly & Saxena (1984) or Hodges & Spear (1982) garnet mixing model produces the lowest estimations of temperature (**figure 5.2**). The calibration of Indares & Martingole (1985) incorporates compensation factors for Al^{vi} and Ti substitutions occurring in biotite at high temperatures, as this thermometer was calibrated in granulite facies rocks, where sillimanite was the only aluminium silicate mineral present. In samples at lower grade, these compensation factors are likely to be invalid and consequently the results from this calibration will produce anomalous results compared to other calibrations.

The Berman (1990) garnet model incorporated into the Ferry & Spear (1978) calibration of the garnet-biotite model is plotted on **figure 5.2**. As mineral compositions from the experimental study are coincident with those of natural biotite and garnet compositions in a sample containing both sillimanite and kyanite, this strongly suggests that the model of Berman (1990) is an appropriate analogue for the activity of garnet in Al-rich pelites.

From this comparative study, it may be concluded that either the calibration of Ferry & Spear with Berman (1990) or Holdaway *et al* (1997) yield the most appropriate values for

GRAIL is a net-transfer barometer is based on the reaction between the almandine component of garnet and the rutile and ilmenite members of the Fe-Ti oxide group. The net transfer reaction on which this barometer is based is:



The assemblage garnet – ilmenite – rutile – Al-silicate and quartz is multivariant due to extensive solid solution in garnet and some solid solution behaviour in ilmenite. To a first approximation, the pressures deduced from this barometer are a function of the garnet composition at a given temperature (Bohlen *et al*, 1983).

In common with other calibrated thermometers and barometers, the assumption that all the phases in the GRAIL assemblage formed in equilibrium with each other is of paramount importance to the accuracy of the pressures estimated. To avoid the possibility of measuring titanium oxide phases that have undergone late-stage oxidation, inclusion suites within garnet porphyroblasts have been exclusively used for the application of the GRAIL barometer in this study. Consistent values for the ilmenite and rutile compositions included within a single garnet porphyroblast serve to increase confidence that the inclusion suite has not been modified by late-stage local alteration.

Further important consideration is the selection of a suitable solution model with which to model the garnet behaviour. At high grades, the Fe-Mg interactions are the most important, with those of Ca and Mn components constituting a minority of the garnet volume (Spear, 1993). In the GRAIL calibration of Bohlen *et al* (1983), the garnet-mixing model proposed by Perkins (1979) is used. This model is based on empirical evaluations against natural, almandine - grossular samples, and yields P-T estimates consistent with the aluminium silicate phase present in the samples. The almandine-grossular model is likely to provide a good approximation to the behaviour of garnet in the study area, as the composition of garnet analysed for this barometer is dominated by Fe, with some Ca component) e.g. **figure 5.24**). Fe-Mn, Ca-Mn and Mg-Mn interactions are assumed to be ideal (Bohlen *et al*, 1983). The calibration of the GRAIL barometer established by Bohlen *et al* (1983) will be used for garnet-ilmenite-aluminium silicate assemblages in this study.

5.5 Results from thermobarometry

5.5.1 Introduction

A study of the microstructures in thin section, described in the previous chapter, enabled the timing of mineral growth relative to the regional foliations S_s and S_t to be established (**table 4.1**). Regions of P-T space through which rocks of different metamorphic grades passed during the structural evolution were estimated; this data is summarised for the sillimanite-bearing and garnet/staurolite-andalusite assemblages in **figure 5.3** and **figure 5.4**, respectively.

Compositions of mineral phases have been accurately measured using the electron microprobe (see **Appendix Two**); in this chapter, mineral chemistry data is used to further constrain the P-T history of rocks from the Alpujarride Complex, using two principle methods.

(1) Garnet profiles

Variation of the percentage of major garnet components (almandine, pyrope, spessartine and grossular) and the ratio $Fe/(Fe+Mg)$ are related to the changes in pressure and temperature that have occurred during the growth of the garnet. Diffusion in garnet is slow, so that garnet accumulated at the edge of a porphyroblast does not equilibrate with the pre-existing garnet. Consequently, the P-T history during the growth of garnet is recorded in successive 'layers' of the porphyroblast crystal (e.g. Yardley, 1977; Spear *et al*, 1990). These composition profiles are susceptible to subsequent modification by diffusion which may destroy some or all of the P-T history recorded in the garnet. Diffusion is most likely to be an important factor in garnet porphyroblasts exposed to high temperature conditions (e.g. Yardley, 1977).

Spear (1993) summarises the effect of pressure and temperature variation on the garnet composition from three different mineral assemblages in plots of X_{Fe}^{Grt} contours (**figure 5.5**). An equivalent plot for the rocks from this study could be generated using a program by Spear (1993) but this requires that a well-constrained point in P-T space is stipulated, and an accurate composition of garnet is known at these pressure-temperature conditions. Data from this study does not permit sufficient constraint of the pressure-temperature conditions, so plots taken from Spear (1993) for analogous assemblages have been used to interpret zoning profiles from this study. Isopleths of the molar abundance of garnet have been calculated

from mass balance equations for the same mineral assemblages shown in **figure 5.5**. These are presented in **figure 5.6**. Together, these two types of diagram provide a framework in which to interpret the variation of major elements and Fe/(Fe+Mg) across the diameter of garnet porphyroblasts.

(2) Calibrated thermometers and barometers

In appropriate assemblages, calibrated thermometers and barometers were applied to rocks of varying metamorphic grade. The textural relationship of the minerals to each other was the principal evidence on which the assumption of equilibrium was based, and the composition of mineral phases provided additional information as to whether apparent equilibrium assemblages had been affected by subsequent modification (section 5.5.3.2).

Data illustrating the variation of composition across garnet porphyroblasts and the results from the application of calibrated thermometers / barometers to assemblages assumed to have equilibrated are presented below. These data confirm and refine the P-T-t history of rocks from the Alpujarride Complex indicated by the mineral relations with the regional fabrics S_s and S_t .

5.5.2 Sillimanite-bearing assemblages

5.5.2.1 Garnet zoning profiles

Variation of composition across the diameter of garnets from the kyanite-sillimanite grade rocks was measured in several samples: a typical example of compositional in LH 125 (**figure 5.7**). The absence of compositional zoning in garnet from sample LH125 also characterises garnet profiles from sample LH 28B (kyanite-sillimanite-andalusite grade) **figure 5.8**.

Mineral assemblages in the sillimanite-bearing rocks do not suggest that these samples have experienced high temperatures for a sustained duration (section 2.4); as seen in **figure 5.3**, the maximum temperature experienced by these samples is estimated to have been $\leq 700^\circ\text{C}$. The possibility that growth-zoning profiles in these garnets have been destroyed during diffusion is remote, as the diffusivity of garnet at temperatures $< 600^\circ\text{C}$ is negligible (Spear, 1993). Alternative hypotheses in which unzoned porphyroblasts may be generated include rapid growth under constant conditions of pressure and temperature, or garnet growth during

decreasing pressure and increasing temperature along a path in P-T space sub-parallel to the series of Fe/(Fe+ Mg) isopleths (**figure 5.5a**).

5.5.2.2 Pressure estimates - Introduction

The only estimates of pressure that were available from rocks within the sillimanite-bearing assemblages were obtained from the application of the GASP barometer (**section 5.4,4**). The GRAIL barometer could not be applied to these rocks due to the absence of rutile.

The most likely explanation as to why rutile is present in sillimanite—absent assemblages (see **section 5.5.3.4**) but absent in sillimanite-bearing rocks is that rutile crystals present in the earlier part of the history of these samples have back-reacted to ilmenite prior to the growth of garnet porphyroblasts. Alternative hypotheses, such as the possibility that these rocks followed a P-T evolution at pressures lower than the garnet-andalusite rocks, are unlikely as structural relations in this area and elsewhere in the Betics suggest that temperature is related to structural depth in the Alpujarride Complex (i.e. Argles *et al*, 1999). The presence of prolific ilmenite indicates that Ti was plentiful in these samples, ruling out the possibility that insufficient Ti was present to permit rutile to stabilise.

5.5.2.3. Application of the GASP barometer

The GASP barometer was applied to three samples in the kyanite-sillimanite grade rocks (LH17, LH 125 and LH134) and one sample of kyanite-sillimanite-andalusite grade (LH 28B). In three of these samples (LH125, LH 17 and LH28B), no plagioclase inclusions were armoured within garnet porphyroblasts and in these cases it was assumed that plagioclase crystals in the matrix of the samples were in equilibrium with the edges of the garnet porphyroblasts. In sample LH 134, quartz and plagioclase inclusions define a planar internal fabric in the garnet porphyroblasts (**figure 4.3**): the composition of a plagioclase inclusion and that of the garnet adjacent to the inclusion were assumed to be in equilibrium.

Results obtained from the application of the GASP barometer to garnet-plagioclase pairs in the kyanite-sillimanite grade rocks are shown in **figures 5.9, 5.10 and 5.11**. K_{eq} lines of the GASP barometer for sample LH 28B (kyanite-sillimanite-andalusite grade are presented in **figure 5.12**.

Application of the GASP barometer, to plagioclase included in garnet in sample LH134 generate K_{eq} lines that are more widely spaced than those from other samples (e.g. compare **figure 5.10** with **figure 5.11**). Detailed analysis of the plagioclase inclusions in garnet from sample LH 134 shows that they have an irregular shape and that the composition of the crystals varies widely (**figure 5.13**). It seems likely that these plagioclase crystals have not equilibrated with the surrounding garnet, or that the composition of some or all of the plagioclase inclusions have been altered, perhaps as a consequence of fluid penetrating the crystal along cracks or adjacent to the numerous quartz inclusions.

K_{eq} lines from the application of GASP to matrix plagioclase and rim garnet compositions (i.e. sections LH 125, LH 17 and LH 28B) probably estimate pressure at the end of garnet growth.

5.5.2.4 Temperature estimation – Introduction

Distinct disequilibrium textures in the sillimanite-bearing assemblages have severely restricted the number of samples to which the assumption of equilibrium between phases could plausibly be applied. In the sillimanite-bearing rocks, garnet porphyroblasts were commonly altered to aggregates of plagioclase-sillimanite-quartz, and local garnet porphyroblasts were completely replaced by this assemblage.

5.5.2.5. Application of the GARB thermometer

Two attempts were made to apply the garnet-biotite thermometer to apparent biotite inclusions in garnet.

A garnet porphyroblast from LH104 (kyanite-sillimanite grade), with apparent biotite inclusions, is shown in **figure 5.14**. A plot of composition variation across the porphyroblast, is shown in **figure 5.15**; there is no significant variation of composition from the core to the rim of this porphyroblast, indicating that it is likely to have grown during decompression and/or conditions of increasing temperature (**figure 5.5**). A plot of the Fe/(Fe+Mg) ratio for biotite grains both included in garnet and in the matrix of sample LH104 is shown in **figure 5.16**. Most of the biotite inclusions from within the garnet porphyroblasts have a similar Fe/(Fe+Mg) ratio as the biotite grains in the matrix of the sample. Exceptions to this trend are inclusions at sites 01 and 03; at these sites, the Fe/(Fe+Mg) ratio is significantly lower.

It is likely that the composition of most of the biotite inclusions in this sample has been modified after the growth of garnet; different compositions seen at sites 01 and 03 may represent biotite compositions closer to that which equilibrated with garnet. K_{eq} lines for the GARB thermometer, using the calibration of Ferry & Spear (1977) with Berman (1990) are plotted in **figure 5.17**; the K_{eq} lines corresponding to garnet-biotite maineral pairs from sites 01 and 03 indicate that temperature in this sample was between 600-700°C while it was experiencing pressures of around 6 kbar.

Sample **LH 56** – (kyanite-sillimanite-andalusite grade) – appeared to contain a single biotite crystal included in a garnet porphyroblast. No compositional zoning was evident across the diameter of the garnet (**figure 5.18a**), suggesting that this porphyroblast may have grown rapidly, or in conditions of increasing temperature and decreasing pressure (i.e. following a path in P-T space sub-parallel to the X (Fe) contours on **figure 5.5a**).

Application of the garnet-biotite thermometer to the included biotite and adjacent garnet composition from LH56 generated fairly concordant K_{eq} lines (**figure 5.18b**). A plot of Fe/(Fe+Mg) for compositions of biotite included in the garnet and biotite within the matrix reveals that there is no variation of composition between garnet in these two different locations (**figure 5.18c**). This may indicate that the Fe:Mg exchange has been operative and has modified the compositions of the biotite crystals; an alternative scenario, in which the Fe:Mg ratio of biotite has not changed significantly during garnet growth may be plausible, as the K_{eq} lines in **figure 5.18b** are concordant. In this case, the temperature estimate from the application of GARB to sample LH56 may reflect temperature conditions during garnet growth.

5.5.3 Garnet/staurolite-andalusite assemblages

5.5.3.1 Garnet zoning profile

A transect of composition points across a garnet porphyroblast from sample LH 255 reveals a maximum value of grossular in the core of the crystal, an increase of grossular component in the centre of the crystal followed by a sharp decrease towards the edge (**figure 5.19a**). The spessartine and pyrope components show no regular pattern of zoning, except that one side of the transect records a significant drop in spessartine content which is accompanied by a

corresponding rise in almandine. Apart from this fluctuation, the almandine content and the Fe/(Fe+Mg) ratio both show a 'saucer' shaped curve with minimum values at the core and maxima at either side. There is a gradual decrease of almandine and Fe/(Fe+Mg) toward the rims.

The contours of garnet composition for the MnNCKFMASH system plotted by Spear *et al* (1990) (**figure 5.20**) may be used to interpret the observed patterns of Fe/(Fe+Mg) and grossular variation. The peak of grossular component at the core of the crystal indicates that the pressure decreased, or the temperature increased, from a maximum at the onset of garnet growth (**figure 5.20d**). The increase of Fe/(Fe+Mg) at the 'rim' in the centre of the crystal may imply a decrease in temperature, while the decreasing trend of Fe/(Fe+Mg) towards the rim of the crystal may indicate the growth of staurolite in the assemblage (Spear, 1993). The drop in grossular and spessartine at one edge of the profile that is accompanied by an increase in almandine is likely to signify a drop in pressure near the end of porphyroblast growth.

Sequential points of composition across the diameter of a garnet porphyroblast from sample LH 154 shows the typical compositional variation that is seen in garnets from the garnet/staurolite-andalusite grade rocks (**figure 5.21**). No significant variation is seen in the grossular, almandine, spessartine or pyrope components and, consequently, the Fe/(Fe+Mg) ratio shows no zoning. From the X(Fe) and M(Grt) contours shown in **figure 5.5** and **figure 5.6** it seems most likely that garnet growth followed a P-T path sub-parallel to the X(Fe) contours and with a slightly negative gradient, tracing a path of increasing temperature and decreasing pressure.

5.5.3.2 Pressure estimates – Introduction

In some sillimanite-absent assemblages, garnet porphyroblasts are locally equant and do not show extensive evidence of resorption at the rims. This texture suggests that the composition of the garnet porphyroblast rims may be in equilibrium with minerals in the matrix of the samples.

5.5.3.3 Application of the GASP barometer

In sample **LH 255** (VF 42880675), garnet porphyroblasts and plagioclase crystals exhibit curved inclusion trails that are oblique to the main fabric in the sample (**figure 4.21**). These textures suggest that both mineral phases grew during the development of the main fabric (S_s) in this area (section 4.5.2). A transect of composition across a garnet porphyroblast from this rock is seen in **figure 5.19a**.

Mineral pairs of corresponding core and rim locations in both the garnet and plagioclase porphyroblasts were used in the GASP barometer (Ganguly & Saxena, 1984). The locations at which the garnet compositions were measured is shown in **figure 5.22a**; composition data for the plagioclase crystals in the matrix is presented in **figure 5.22b**.

Results from the application of the GASP barometer are shown in **figure 5.23**.

5.5.3.4. Application of the GRAIL barometer

Intergrowth textures between ilmenite and rutile were identified as inclusions in garnet porphyroblasts in samples **LH138** and **LH311** (garnet/stauroilite-andalusite grade). A plot of the compositional variation across a garnet porphyroblast in sample LH311 is seen in **figure 5.24**; no significant variation of the major components is identified.

The elongate rutile/ilmenite intergrowths were aligned parallel to the internal foliation of the garnet porphyroblasts (**figure 5.25** and **figure 5.26**). Spear (1993) suggests that intergrowths between ilmenite and rutile are a consequence of early rutile converting to ilmenite prior to the growth of garnet. Alignment of the rutile needles to the internal foliation within the garnet is concordant with rutile growth predating the growth of garnet. Although these minerals (garnet, ilmenite, rutile) did not, then, grow simultaneously, their close association was used as the basis for assuming equilibrium and the GRAIL barometer was applied. In this case, the pressures obtained from GRAIL will constrain the minimum pressure value for a given temperature.

K_{eq} plots for GRAIL assemblages in samples LH 138 and LH 311 are shown in **figures 5.27a** and **5.27b**, respectively.

At 550°C, the K_{eq} lines from the GRAIL barometer estimates a pressure of 2 kbar less than those estimated from GASP at the same temperature (e.g. compare **figure 5.22** and **figure 5.27**). This variation appears to confirm that the rutile/ilmenite intergrowths included within the garnet porphyroblasts in samples LH138 and LH311 did not grow in equilibrium with the garnet; as a consequence of this, results from the GRAIL barometer do not generate results that can be reliably interpreted.

5.5.3.5. Temperature estimates - Introduction

No examples of biotite inclusions in garnet were identified within the garnet/staurolite – andalusite assemblages. Where staurolite was absent, and little evidence of garnet resorption at the edges of the porphyroblasts was present, it was assumed that due to the absence of other Fe / Mg phases in the rock the Fe:Mg ratio of the matrix biotite would have maintained a constant value since the end of garnet growth. Based on this assumption, compositions of garnet taken from the rim of the garnet porphyroblasts and average biotite compositions from the matrix were used in the garnet-biotite thermometer of Ferry & Spear with Berman (1990). These calculations will yield estimates of the ambient temperatures prevailing near to the end of garnet growth.

5.5.3.6. Application of the GARB thermometer

The garnet-biotite thermometer was applied, with the assumption discussed above, to three samples - LH61, LH 154 and LH349. Plots of the K_{eq} lines for these samples are presented in **figures 5.28 - 30**.

The K_{eq} lines generated from the application of GARB to each sample cluster close together, and a comparison of the results from the three individual samples reveals that the K_{eq} lines of each sample all plot in similar positions on the P-T plot. For a pressure of 600 kbar, the GARB barometer indicates that the garnet/staurolite-andalusite grade rocks were in the temperature range 600-650°C.

5.5.3.7 Application of the Garnet-amphibole thermometer

Sample **LH255** (VF 42880675), from the garnet/staurolite-andalusite grade rocks, contains large porphyroblasts of garnet and amphibole, both of which exhibit curved inclusion trails. These textures indicate that both garnet and amphibole grew during the D_s deformation event (section 4.5.2) and it is reasonable to assume that these phases were in equilibrium with each other during their growth. Sequential point analyses, parallel to the curved inclusion trails in the porphyroblasts, have been made across the diameter of both the garnet and amphibole crystals in this section. The interpretation of the garnet profile is discussed above (section 5.5.3.1); the plot of composition across the amphibole porphyroblast shows no variation of the Fe/(Fe+Mg) ratio (**figure 5.31**).

The garnet-amphibole thermometer of Graham & Powell (1984) has been applied to mineral pairs taken from the core, intermediate areas within the crystals and from rims of the garnet and amphibole porphyroblasts. K_{eq} lines for the thermometer, obtained from the program of Spear (1991) are shown in **figure 5.32**. It appears from these results that no change in temperature occurred during the growth of the garnet porphyroblasts; this is concordant with the absence of compositional zoning in the porphyroblasts noted above (**figure 5.19**).

5.5.4 Summary

The results obtained from the application of barometry and thermometry to the sillimanite-bearing and garnet/staurolite-andalusite assemblages from the Alpujarride Complex help to constrain the P-T history of the rocks of different metamorphic grades. Relationships of minerals to the regional foliations S_s and S_t have been explored in sections 4.2 – 4.5; a summary of the results from the micro-structural studies is presented in **table 4.1**. The results from thermobarometry are most usefully interpreted in terms of the structural evolution of the rocks.

In the kyanite-sillimanite grade rocks, garnet growth ended prior to the generation of the S_s foliation (**table 4.1**); the pressure-temperature conditions of 7.5 – 10.5 kbar and 650 - 750°C predicted from **figure 5.33** relate to the conditions prevailing before D_s affected these rocks. In kyanite-sillimanite-andalusite grade rocks, garnet growth continued during the D_s deformation (**table 4.1**); the pressure-temperature conditions constrained on **figure 5.34** for these rocks (i.e. 7.5 – 9.5 kbar and 600-700°C) indicate the ambient conditions during the D_s

phase of deformation. The results for both the kyanite-sillimanite and kyanite-sillimanite-andalusite grade rocks, considered together, suggest that these rocks experienced similar conditions of pressure and temperature during the early part of their metamorphic history.

Garnet/staurolite-andalusite grade rocks were at conditions of approximately 9 kbar and 650°C (**figure 5.35**) after the end of the D_s phase of deformation (**table 4.1**). The garnet/staurolite-andalusite grade rocks probably followed a path of lower pressure and temperature than the sillimanite-bearing rocks; this is compatible with other studies in the Alpujarride Complex that suggest rocks of lower metamorphic grade originate from structurally higher positions in the metamorphic pile (e.g. Argles *et al*, 1999).

Andalusite grew in the kyanite-sillimanite-andalusite and garnet/staurolite-andalusite rocks during and after the D_t deformation (**table 4.1**); these rocks must have experienced a rapid period of decompression between the D_s deformation and the onset of D_t .

PART 2 DATING TECHNIQUES

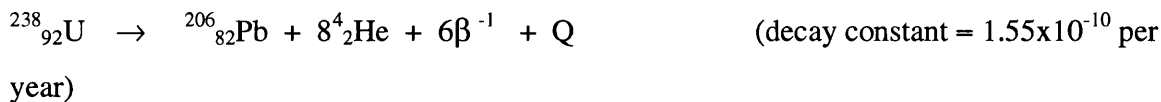
5.6 Introduction

Three methods of geochronology have been applied to rocks within this area of study and have yielded useful results that help to constrain the timing of the metamorphic and structural evolution of the Alpujarride Complex described in previous sections. A map showing the location of the samples used for geochronology is presented in **figure 5. 36**; the techniques used, and the results arising from the application of these techniques are set out in the following sections.

5.7 U-Pb technique

5.7.1 Introduction to the technique

The radioactive uranium isotopes ^{238}U and ^{235}U decay to ^{206}Pb and ^{207}Pb , respectively via the series represented below;



Lead has four naturally-occurring isotopes (^{204}Pb , ^{206}Pb , ^{207}Pb and ^{208}Pb). The ^{208}Pb isotope is regarded as being non-radiogenic, as it has a half-life of $\geq 1.4 \times 10^{17}$. The three remaining isotopes are the decay products of uranium and thorium. The natural abundances of the isotopes are:

$$^{208}\text{Pb} = 52.4\%$$

$$^{206}\text{Pb} = 24.1\%$$

$$^{207}\text{Pb} = 22.1\%$$

$$^{204}\text{Pb} = 1.4\%$$

The ratio U:Pb for a given mineral is related to the time 't' since the mineral system become closed to the incorporation of lead and uranium isotopes. This may be expressed by an equation that includes a term for the decay constant of the uranium isotope, the measured ratio of lead isotopes at the time of analysis and the projected initial ratio of lead isotopes. For a mineral that contains ^{238}U and ^{204}Pb the equation is;

$$\frac{{}^{206}\text{Pb}}{{}^{204}\text{Pb}} = \frac{({}^{208}\text{Pb})_i}{{}^{204}\text{Pb}} + \frac{{}^{238}\text{U}}{{}^{204}\text{Pb}} (\exp(\lambda_1 \cdot t) - 1)$$

where

- ${}^{208}\text{Pb}/{}^{204}\text{Pb}$ = isotope ratio in mineral when analysed
- $({}^{208}\text{Pb}/{}^{204}\text{Pb})_i$ = initial isotope ratio in mineral
- λ_1 = decay constant of ^{238}U
- ${}^{238}\text{U}/{}^{204}\text{Pb}$ = isotope ratio in mineral when analysed
- t = time since the closure of the mineral to uranium, thorium, lead and other daughter products.

An isochron may be plotted for this equation (and for each of the equations using the other isotope ratios) in terms of co-ordinates of ${}^{206}\text{Pb}/{}^{204}\text{Pb}$ and ${}^{238}\text{U}/{}^{208}\text{Pb}$. The slopes of these isochrons will show the age of the sample suite examined, provided that the samples are from closed systems that contain identical ratios of lead isotope ratios.

The values of the isotopes at the time of analysis are determined by the values from ion-probe results, and the values of initial ratios are obtained from published standards of known age. Similar equations may be written for the ratios ${}^{235}\text{U}/{}^{204}\text{Pb}$ and ${}^{232}\text{Th}/{}^{204}\text{Pb}$; the concordance of results from all three equations for a single analysis confirms the accuracy of the data obtained. In practise the loss or gain of lead, uranium and/or thorium does occur and the results from these three equations may diverge.

Zircon is favoured for the application of the U-Pb analysis technique as it tends to contain high concentrations of U and Th (average concentrations of 1330 and 560 ppm, respectively). The cation sites in thorium prohibit the incorporation of lead into the structure, so that at the time of formation it typically contains low amounts of lead but high U/Pb and Th/Pb ratios. (Bowen, 1988).

5.7.2 Analytical procedure

The application of the U-Pb technique was performed by John Platt and Martin Whitehouse, using the Cameca IMS1270 ion-probe facility based at the Swedish Museum of Natural History (NordSIM facility), Stockholm. A description of the analytical procedure and the results produced are contained in Platt & Whitehouse (1999); salient parts of this literature are summarised below.

The first stage in the preparation of samples for ion probe analysis is the extraction of zircons from the parent rock. This is effected by mechanical crushing of the sample to a coarse powder and followed by hand picking (using a binocular microscope) of the zircon grains. These zircon grains are then polished, and mounted in epoxy resin.

Polished surfaces of the mounted grains were viewed with a cathodoluminescence (CL) imaging system on a Philips SEM to reveal the internal structures in the grains (e.g. oscillatory planar growth banding, planar growth structure). This technique permitted the beam of the ion-microprobe to be accurately positioned at known localities within the zircon grain. Calibrations of initial Pb/U and Pb/Th ratios were achieved using the 1065 Ma Geostandards zircon 91500 (Wiedenbeck *et al*, 1995) and the presence of non-radiogenic Pb was monitored using ^{204}Pb . The amount of ^{204}Pb was small, so that the results are fairly insensitive to the assumed composition of the Pb contaminant. The present-day terrestrial Pb-isotope composition of Stacey & Kramers (1975) has been used (i.e. $^{207}\text{Pb}/^{206}\text{Pb} = 0.83$), and the data have been presented through the Tera-Wasserburg concordia representation ($^{207}\text{Pb}/^{206}\text{Pb}$ vs $^{238}\text{U}/^{206}\text{Pb}$) with regression through the assumed common Pb composition.

5.7.3 Description of the sample

A sample of high grade pelitic rock (reference number PB342) from Punta de la Mona yielded the zircon crystals that were analysed with the U-Pb technique. The location of the sample, at VF 43480655, is marked on **figure 5.36**. Sample PB342 contains an assemblage of quartz + plagioclase + biotite + muscovite + fibrolitic sillimanite, in addition to corroded relics of kyanite and garnet and accessory phases of apatite, zircon and ilmenite (Platt & Whitehouse, 1999).

Zircon grains from sample PB342 were generally idiomorphic prisms up to 200 μm long. Viewed with cathodoluminescence, many of the grains were revealed to have oscillatory planar growth banding in the cores of the crystals (**figure 5.37**), indicative of zircons generated by igneous processes. Some of these zoned zircon crystals have been broken, suggesting that they passed through a sedimentary cycle prior to being enclosed by the growth of prismatic zircon. The texture of the zircon overgrowth (metamorphic zircon dated in this study) is typically patchy, although locally some slight compositional bands are seen (i.e. grains 6 and 12 in **figure 5.37**).

5.7.4. Results

The raw data generated by the U-Pb technique on sample PB342 has been published by Platt & Whitehouse (1999) and is reproduced in **Appendix Three**.

Ages from eleven of the twelve analyses are in the range 18.7 – 20.1 Ma; the remaining grain produces an age of 25.6 Ma. Regression of the eleven concordant ages using an assumed common Pb value from Stacey & Kramers (1975) produces an intercept with concordia corresponding to an age of 19.3 ± 0.3 Ma (95% confidence, MSWD = 1.9, n=11) – **figure 5.38**. The abundance of inclusions and the lack of zonation in these zircon crystals strongly suggest that they are metamorphic in origin, although the mineral assemblage of this rock indicates that it has not experienced temperatures of $> 700^\circ\text{C}$, which is well below the closure temperature for zircon (Platt & Whitehouse, 1999). The age obtained from this technique is therefore interpreted as a crystallisation age; it is hypothesised that the breakdown of garnet may have initiated the growth of zircon (Platt & Whitehouse, 1999).

U-Pb data from the cores of these zircons (presumed igneous origin, as mentioned above) provide age estimate of 300Ma (2 analyses; Hercynian age); 600 Ma (2 analyses); 1000 Ma and 1800 Ma. These core ages are the same as those calculated from cores of zircons from the Torrox gneiss (Zeck & Whitehouse, 1999) (Platt & Whitehouse, 1999).

5.8 Ar-Ar technique

5.8.1 Introduction to the technique

The decay of the naturally occurring isotope ^{40}K to ^{40}Ar provides the basis for both the Ar-Ar and the K-Ar dating techniques. The latter of these techniques requires that potassium and argon measurements be made on separate aliquots of the same sample: flame photometry and wet chemistry are the standard techniques with which to measure potassium. In contrast, the Ar-Ar technique permits data collection on a single aliquot of a sample, and the only analytical technique employed is that of mass spectrometry.

^{39}Ar is generated by neutron bombardment of ^{39}K in a nuclear reactor. The reaction may be written as:



The ratio of the two naturally occurring potassium isotopes ^{39}K and ^{40}K is essentially constant in nature. As a result, the ratio of ^{40}Ar (from the natural radioactive decay of ^{40}K) to ^{40}K will be proportional to the $^{40}\text{Ar}^*/^{39}\text{Ar}$ ratio (i.e. the ratio between the product of nuclear bombardment and that of natural radioactive decay, respectively). It may be shown that the ratio of natural radiogenic argon ($^{40}\text{Ar}^*$) to reactor-generated argon (^{39}Ar) is proportional to the age of the sample, when a dimensionless irradiation-related parameter, J , is known. The age of the sample is calculated from a ratio of $^{40}\text{Ar}^*/^{39}\text{Ar}$ using a standard material of known age which is irradiated along with the sample.

Gas released from impingement of a laser onto a polished thick section of the sample (see section 5.8.2 below) is transmitted into a mass spectrometer for analysis, following a 'cleaning' process to remove active gases (such as H_2O , CO_2 , CH_4 , N_2 and H_2) present in the mixture. Removal of these gases is necessary to prevent scattering effects occurring in the mass spectrometer and is achieved by passing the gas mixture over 'getters': filaments of fine-grained metals or alloys (i.e. Zr-Al) which react with the active species. To ensure thorough cleaning of the gas, two 'getters' – one at 450°C and a second at room temperature – are used.

Naturally occurring isotopes of argon (^{36}Ar , ^{38}Ar and ^{40}Ar) and isotopes produced during bombardment in the nuclear reactor (^{39}Ar and ^{37}Ar) are measured in the mass spectrometer. The value of ^{36}Ar is used to correct for the presence of atmospheric argon in the sample, using the present-day $^{40}\text{Ar}/^{36}\text{Ar}$ ratio (295.5; Steiger & Jager, 1977). The values of ^{36}Ar , ^{39}Ar and ^{40}Ar will contain a component of gas produced by interference reactions involving calcium during the bombardment of the sample: pure salts of Ca and K (i.e. CaF_2 and K_2SO_4) irradiated with each batch of samples permit correction factors for these reactions to be calculated. In addition, a correction factor to accommodate for the decay of ^{37}Ar (produced by neutron capture of Ca) that occurs between the date of irradiation and the date of analysis is applied. This isotope has a half-life of 35 days, so that the precision of the ages obtained from calcium-rich minerals or whole-rock may be affected if the sample is not analysed within 6 months of irradiation.

5.8.2 Apparatus and sample preparation

Suitable areas of samples were selected in thin section, and were used to prepare aliquots for Ar-Ar analysis. Sample consisted of polishing a 5mm x 5 mm area of the slide to a thickness of approximately 300 microns (more friable material may be left slightly thicker) and ensuring that the top surface had acquired a high-quality polish. Each 5 x 5 mm thick section was then cleaned ultrasonically in alternate methanol and de-ionised water, then packaged in Al-foil.

The samples were irradiated at the McMaster reactor in Canada for 25 hours on the 15th November 2000, and the GA 1550 biotite standard with an age of 98.79 ± 0.7 Ma (Renne *et al*, 1998) was irradiated with the samples. The J factor calculated from this run was 0.00637 and the irradiation correction factors for the McMaster reactor are as follows:

$$^{39}\text{Ar} / ^{37}\text{Ar} = 0.00065 \pm 0.5 \%$$

$$^{36}\text{Ar} / ^{37}\text{Ar} = 0.000234 \pm 0.5 \%$$

$$^{40}\text{Ar} / ^{39}\text{Ar} = 0.0085 \pm 0.5 \%$$

The results presented here were obtained using the Ar-Ar laboratory at The Open University, under the guidance of Dr Simon Kelley and Dr Sarah Sherlock. The apparatus used was a Spectron Laser System SL902 CW Nd-YAG. The laser beam is generated from a Nd-YAG source (i.e. a solid state laser), and has a wavelength of 1064 nm, in the infrared spectrum. The laser was set in continuous wave mode (CW), generating a continuous beam of light as a consequence of repeated pumping of the emitted photons through the laser rod. The spot size is easily controlled to generate a range of densities, to produce laser pits of 50–100 µm in a range of minerals with various absorption, reflectance and refraction parameters.

The laser beam was directed through a standard petrographic microscope using an arrangement of mirrors. A video camera was directed with its field of view parallel to that of the laser beam, so that the image on an adjacent monitor provided a view of the sample area at which the laser was aimed. Three single laser shots, each of 50 milliseconds duration, were used for each analysis: an automated system subsequently passed the released gas into the vacuum chamber where it was cleaned by the 2 SAES AP 10 getter system (see section 5.8.1) and then passed into the mass spectrometer for analysis.

Once in the mass spectrometer chamber, the gas sample was analysed by an ion beam scanning across mass peaks of 35 to 41. Each peak was measured 10 times during every analysis. The analysis of each sample of gas is begun immediately upon the introduction of the sample into the mass spectrometer chamber, and an automated system back-extrapolates the peak heights measured at the specified mass values to the time at which the gas was let in. This procedure serves to minimise the error produced by argon adsorption and / or desorption onto the metal walls of the gas chamber. 'Blank runs' i.e. analyses of gas in the spectrometer without firing the laser, were performed after every two analyses in order to calibrate the cumulative effects of argon adsorption / desorption.

5.8.3 Results

Locations of the Ar-Ar samples are shown in **figure 5.36**. The results are summarised in **table 5.2** below; the full analytical results are presented in **Appendix Three**. The precision of these results, however, is determined by several parameters, including sample size (larger samples are less affected by errors on the blanks) and the amount of argon able to be initially

incorporated into a mineral or rock is controlled by composition, temperature, grain size and cooling rate.

As the Ar-Ar technique aims to estimate the time since argon became trapped in the mineral or rock ('closure' or 'blocking' temperature), it is apparent that if the quantity of argon contained within the rock or mineral structure is altered subsequent to the passage of the material through this blocking temperature, erroneous dates will be obtained. Argon loss may occur as a consequence of alteration and weathering of the sample and in metamorphic rocks loss of argon from the mineral / rock is promoted by slow rates of cooling.

In low-grade samples analysed in this study, the average size of the muscovite crystals is ~ 72 μm . Empirical equations that relate grain size to closure temperature have been applied (Mathcad program incorporating closure temperature parameters of Dodson (1973) and diffusion parameters of Hames & Bowring (1994) - from these calculations it is estimated that the closure temperature from these samples is 320°C (i.e. the Ar-Ar date for these samples estimates the time that they passed through the 320°C isotherm. Ar-Ar dates yielded by muscovite grains with an average diameter of 198 μm in sample PB342 (kyanite-sillimanite grade; data in Appendix Three) represents the passage of this sample through the 408°C isotherm – the larger mineral grains in this sample increase the value of the estimated closure temperature. Ar-Ar dates from biotite grains with an average diameter of 223 μm , also taken from PB342, are calculated to represent the time at which the sample passed through the 360°C isotherm. Difference in composition between muscovite and biotite presumably controls the closure temperatures for these minerals; accurate calculations to quantify the relationship between closure temperature and composition have not yet been published.

Table 5.2 – Results from Ar-Ar

Sample	Grid Reference	Age (Ma)
LH172	44930764	20.02±0.4
PB535	43860753	16.67±0.6
PB536	43870762	20.50±0.4

5.9 Apatite Fission track technique

5.9.1 Introduction to the technique

Damage caused by the traverse of charged nuclear particles through insulating solids generate paths of disrupted atoms; fission of the uranium isotope ^{238}U is almost exclusively responsible for the formation of these 'fission tracks' in natural minerals. As the process of fission occurs at a statistically constant rate, the number of fission tracks present in a sample is proportional to the time over which the tracks have been accumulating. If the concentration of ^{238}U in a sample is known, and the effect of thermal annealing (shortening) of the fission tracks is taken into account, the study of fission tracks in apatite may provide an insight into the low-temperature ($\sim 60\text{-}120^\circ\text{C}$ for geological time-scales) thermal history of a sample.

Fission track analysis is analogous to other methods of radioactive dating; the ^{238}U isotope is the 'parent' species and the fission tracks are the 'daughter' product of the decay. It is necessary to estimate the relative abundance of the both the parent and daughter species; methods by which this may be achieved are discussed below.

5.9.1.1 Estimating the concentration of fission tracks

The quantity of spontaneous fission tracks within a given sample is recorded by direct observation i.e. counting the number of fission tracks that intersect the polished surface of a mineral grain. Latent (i.e. natural) fission tracks are between 3 and 14 nm wide (Gallagher et al, 1998); the process of chemical etching serves to widen the tracks so that they are easier to observe with an optical microscope. The density of natural spontaneous fission tracks, and sample age, is governed by the length distribution of tracks. All newly formed tracks have the same initial length ($\sim 66\ \mu\text{m}$); exposure to elevated temperatures leads to progressive track shortening. The length of a track is related to the likelihood of it intersecting the plane of observation (short tracks are less likely to impinge on the surface) therefore reduced track lengths lead to lower track densities and younger apparent ages. Thus, it is essential to quantify the range of track length and age distribution for each sample. This is achieved by measuring the length of horizontal (with respect to the surface of observation) confined tracks.

Confined tracks are etched by passage of fluid into them via fractures or fission tracks that intersect the mineral surface. Mineral grains (typically 15-40 per analysis) are viewed in a consistent orientation with respect to the mineral axes as the etching properties of apatite (for example) vary with the optical orientation of the mineral.

5.9.1.2 Estimating the concentration of ^{238}U

Abundance of ^{238}U may not be observed directly; the quantity of ^{238}U is assessed from either (1) population analysis or (2) external detector technique. The latter of these has been used in the analysis of apatite grains for this study; it is described in detail in Hurford *et al*, (1999), and the salient features of the procedure are briefly outlined below.

The polished surface of an apatite crystal, cut parallel to the c-axis of the mineral, is firstly etched to reveal the spontaneous fission tracks. These tracks are counted, and the lengths of confined tracks are measured. A medium that acts as a detector (e.g. muscovite mica or plastic foil) is then sealed against the polished surface and the detector/sample pair is irradiated along with a dosimeter. The dosimeter serves to monitor the neutron flux in the reactor so that the creation of fission tracks by fission of ^{232}Th can be avoided.

Fission of the ^{235}U isotope is achieved by irradiation with low energy neutrons; ‘induced fission tracks’ that impinge on the detector material attached to the sample surface are generated by this process. The number of induced fission tracks recorded on the detector surface provide an estimate of the amount of ^{235}U in the sample (and the distribution of its concentration); as the ratio of $^{235}\text{U}/^{238}\text{U}$ is constant, this permits the abundance and distribution of ^{238}U in the sample to be predicted.

The equation that relates the parameters measured during this procedure to the age of the sample is given by;

$$t = (1 / \lambda_d) L n (\lambda_d (\rho_s / \rho_T) \rho_d \cdot \zeta g + 1)$$

where	t =	age of sample	λ_d =	the alpha decay constant of ^{238}U
	ρ_d =	track density in dosimeter	g =	geometry factor
			ζ =	proportionality constant, zeta

(see below)

The constant of proportionality ‘ ζ ’ in the above equation incorporates parameters resulting from the analytical procedure, including the fission decay constant and neutron capture cross-section. The value of ‘ ζ ’ is obtained by rearranging the above equation for a sample of known age; as the calculation of this parameter involves fission track counts, this parameter also implicitly incorporates some of the variation that will occur between calculations performed by different workers.

5.9.1.3 Fission-track length information

As mentioned above, the length of fission tracks within a sample shorten as the sample is heated; between $\sim 60 - 120^\circ\text{C}$ the rate of annealing of fission tracks in apatite increases with increasing temperature, and above $\sim 120^\circ\text{C}$ most fission tracks have completely healed. Below 60°C significant modification of fission track length does not occur. Analysis of fission tracks, then, can provide important information about the thermal history of a sample between $60-120^\circ\text{C}$.

The annealing process forms the basis of relating the length of the fission track population to the age of the sample. Age of the sample is determined by counting the number of fission tracks. The track length after initial formation is related to temperature and time by an Arrhenius-type equation, as temperature and time are of primary and secondary importance, respectively, among the factors that cause annealing in geologically important samples (Fleischer *et al*, 1965). The shape of the track-length distribution is constructed using only confined tracks – this distribution may contain significant information about the thermal history of the sample (Gallagher *et al*, 1998).

5.9.2 Analytical procedure

Andrew Carter at the London Fission Track Centre (Research School of UCL and Birkbeck College) has processed samples collected for fission track analysis in this study. Spontaneous and induced fission track counts were counted using a Zeiss Axioplan microscope with a total magnification of 1250; irradiation of the samples was carried out at the D-3 thermal facility of the Riso Reactor, National Research Centre, Denmark (Hurford *et al*, 1999). The zeta

calibration method was used (as described above) with a zeta value for dosimeter glass CN-5 estimated as 339 ± 5 . This parameter was calculated from 33 analyses by Dr A Carter from: Fish Canyon Tuff, Colorado; Durango deposit, Cerro de Mercado, Mexico; and the Mount Dromedary banatite, New South Wales. The length of the confined fission tracks were measured with a Houghton Instruments digitising tablet; calibration of the tablet against a stage micrometer provided a direct measure of each track length, with an accuracy of $\pm 0.1 \mu\text{m}$ (Hurford *et al*, 1999).

5.9.3 Results from Apatite Fission Track analysis

Locations of the sites for which apatite fission track ages were successfully obtained are shown in **figure 5.36**. The results obtained are presented in **table 5.3**; full analytical results are presented in **Appendix Three**.

Table 5.3 – results from apatite fission track analysis

Sample	Grid reference	Central Age (Ma)	Mean track length
LH166	44850776	12.7 ± 2.3	n/a
LH351	43500715	18.6 ± 1.5	n/a
PB342	43490656	19.8 ± 1.9	14.98 ± 0.21 (10 tracks)

The results seen in **table 5.3** above for samples LH351 and PB342 are within error of each other: the result from sample LH166 is younger.

Ages presented in table 5.3 are central or modal ages, calculated from the population of singular grain ages. If the single grain ages belong to a single Poissonian population, the central ages is truly representative. However, if there is significant extra poissonian variation in grain ages, the central age may not have a direct meaning. Whether a sample comprises a statistically single age population is measured by the χ^2 (chi) test and relative error. If a sample has a mixed population of grain ages due to variable annealing or bad analysis, χ^2 will be $< 5\%$ and relative error will be $> 20\%$.

Of the three samples analysed. LH166 fails these tests and has extra dispersion. Examination of the individual grain ages on a radial plot (**figure 5.39**) shows that this dispersion is not caused by any systematic spread in grain ages, and therefore this dispersion is not considered significant. The central age, in this case, is representative of the age population in this sample. One feasible scenario in which the track lengths in this sample may be shortened (hence generating a younger fission track age) is if the sample is 'paused' in the annealing zone ($60^{\circ}\text{C} < T < 120^{\circ}\text{C}$) for a period sufficient to allow the fission track lengths to be reduced.

Length data for confined tracks within the apatite crystals was only available for one sample (PB342, in **table 5.3**, above) because of inherently low spontaneous track densities in the other crystals. The long length of the tracks, and the small range of track lengths, suggests that this sample cooled rapidly through the partial annealing zone. Since ~ 19 Ma these samples have remained below $\sim 60^{\circ}\text{C}$.

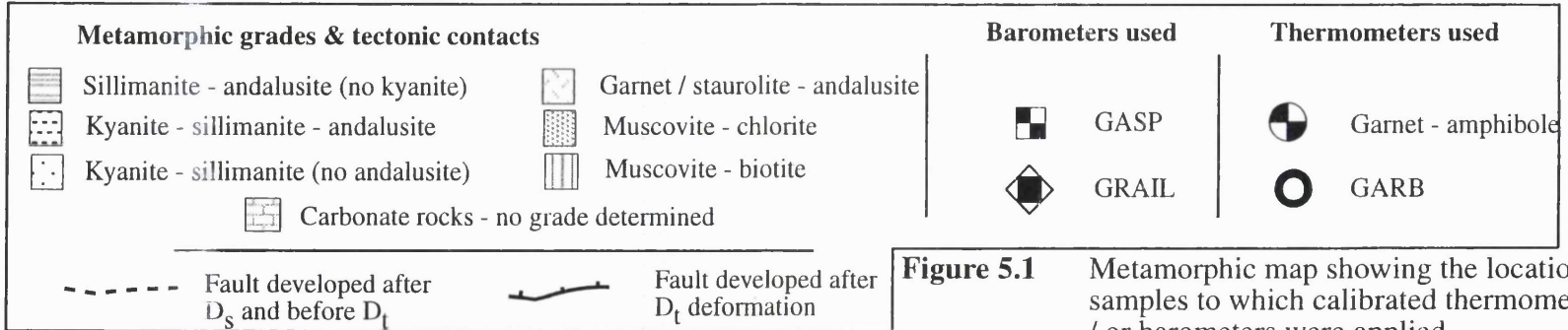
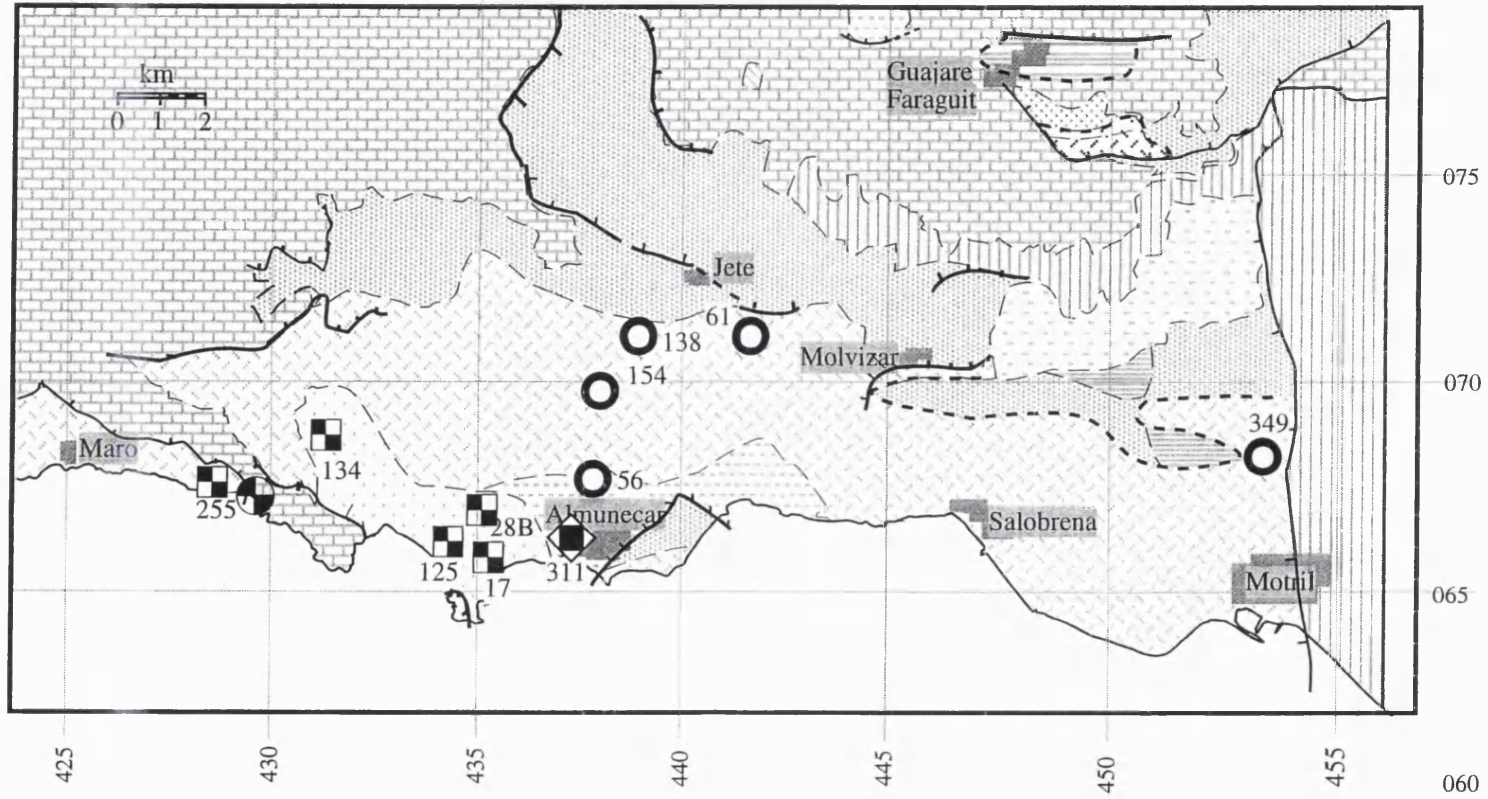


Figure 5.1 Metamorphic map showing the locations of the samples to which calibrated thermometers and / or barometers were applied.

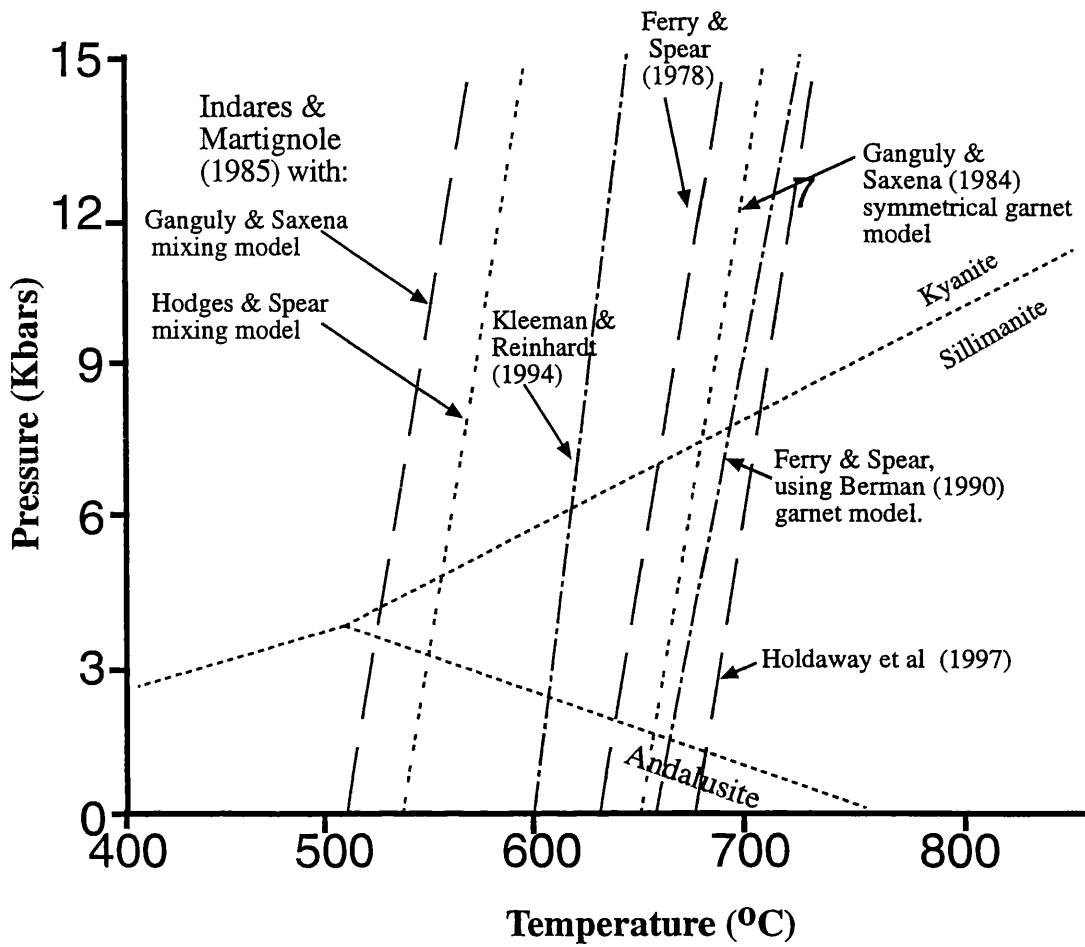
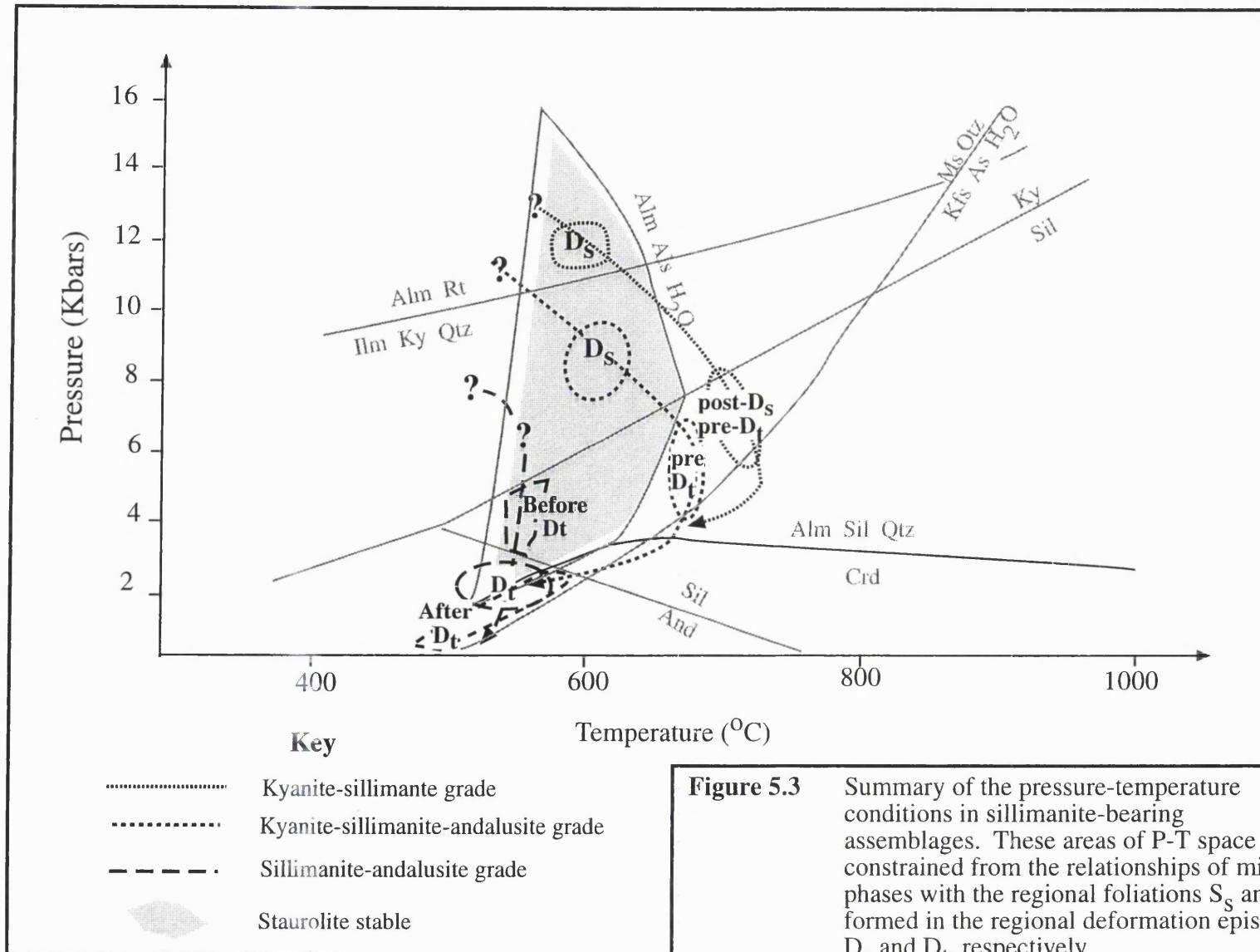
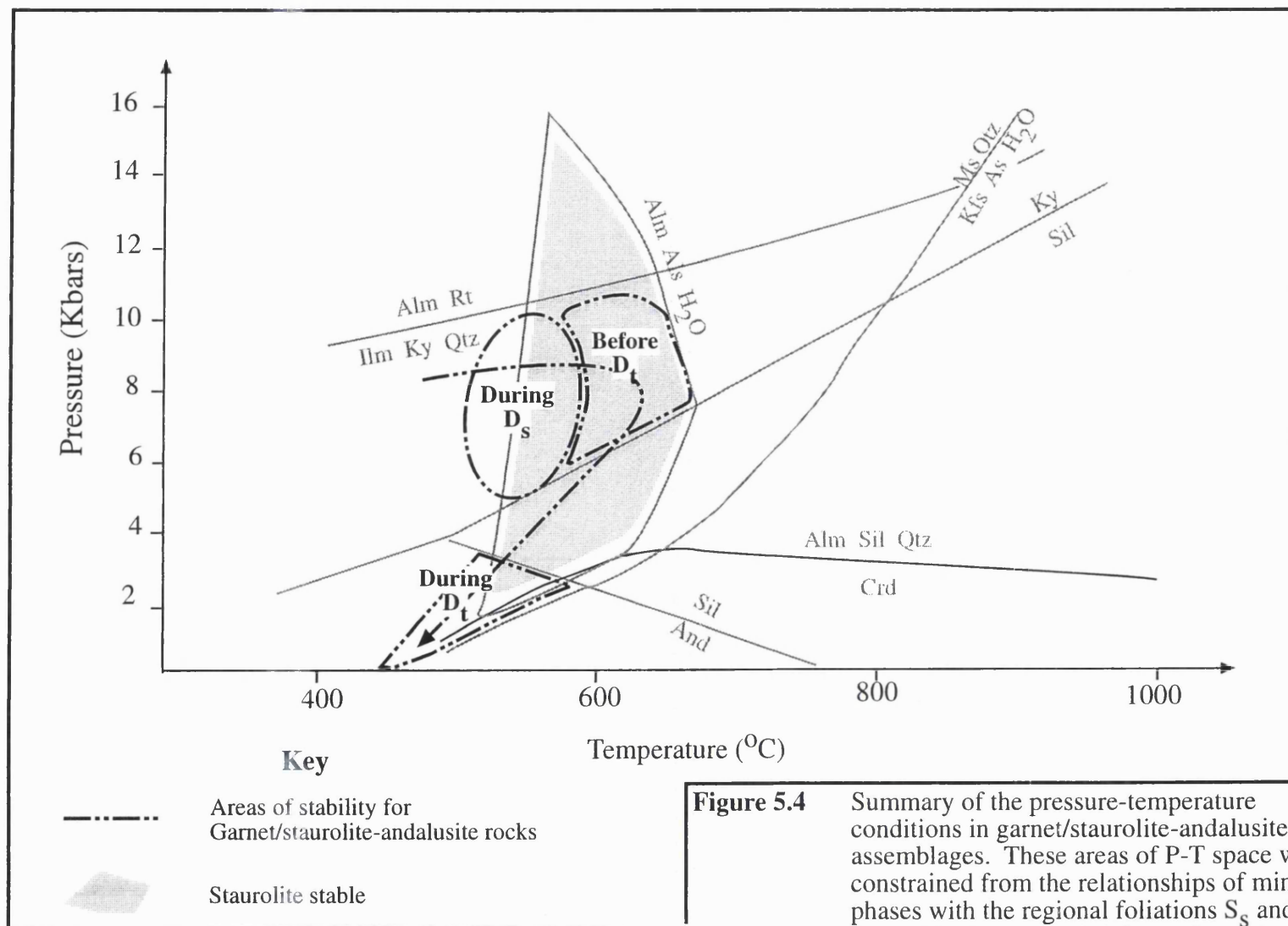


Figure 5.2 K_{eq} lines from the GARB (garnet-biotite) thermometer. Various calibrations of this thermometer were applied to a single mineral pair (from sample LH 56). The wide variation of positions is a consequence of the varying assumptions made in different calibrations of this thermometer.





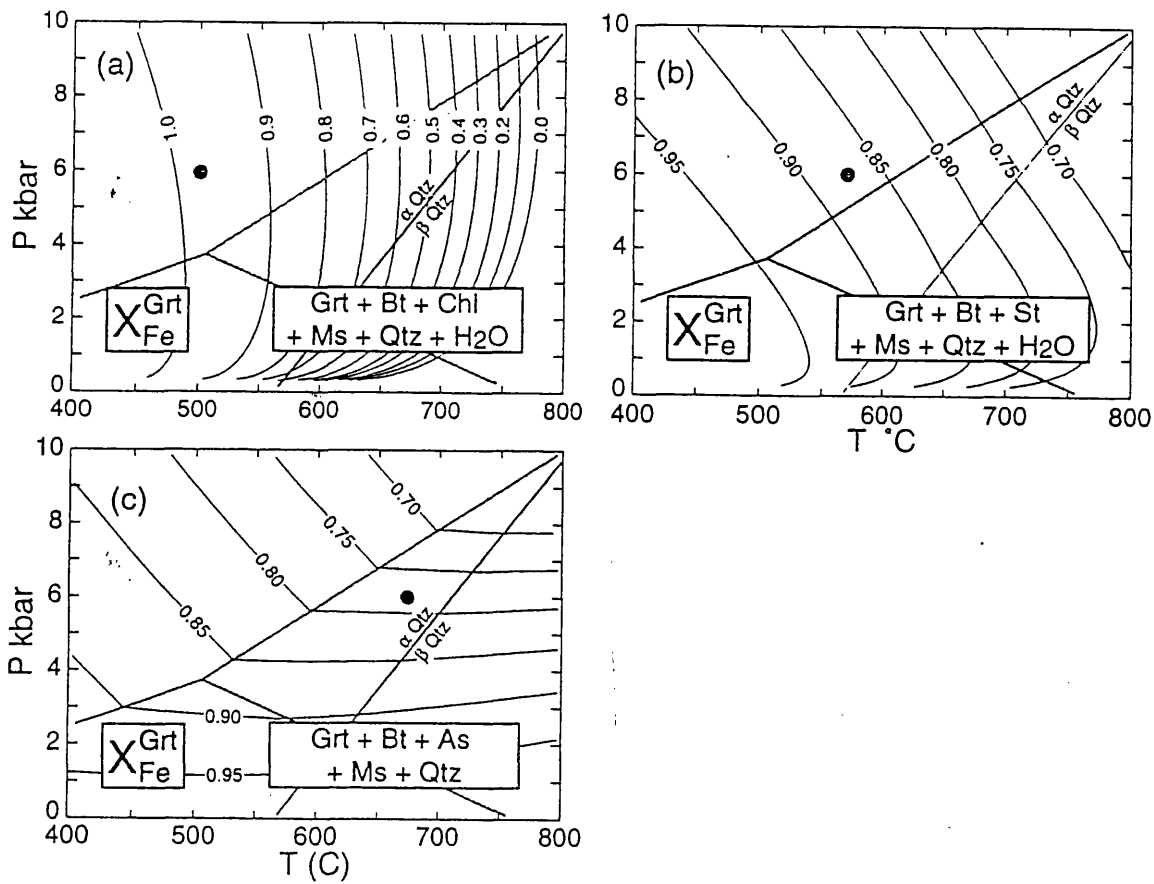


Figure 5.5 P-T plots showing contours of X_{Fe}^{Grt} for assemblages, as marked.

These plots were constructed from independent variables, starting from a set of known mineral compositions at a reference value of P and T. It was assumed that all mineral phases were un-zoned (i.e. that fractional crystallisation did not occur). As a consequence, these diagrams show the effects of phase equilibria and mass balance on composition and mode. From Spear (1993)

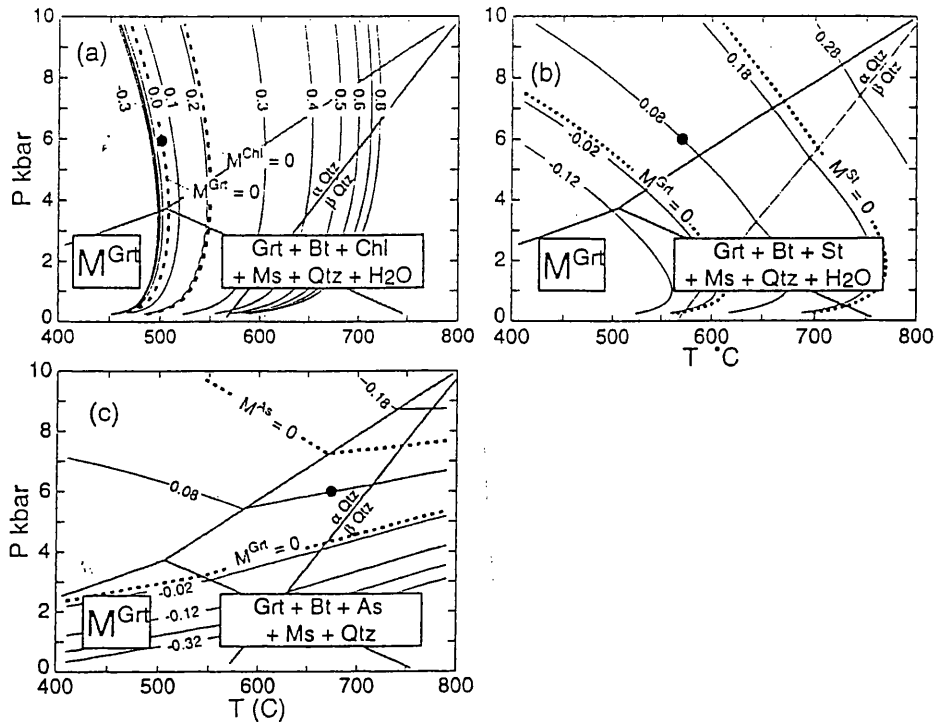


Figure 5.6 P-T plots showing contours of the molar abundance of garnet (M^{Grt}) for assemblages, as marked.

Contours that lie close together indicate reactions that will produce more garnet for a given increment in pressure than from reactions with more widely-spaced contours i.e. the assemblage Grt + Bt + Chl + Ms + Qtz + H₂O is responsible for the majority of garnet formed in pelitic rocks.

Dotted lines show the locus of points along which the molar abundance of one phase in the assemblage becomes 0. Hence, the stability range of garnet in each plot is bound by the lower stability limit ($M^{\text{Grt}}=0$) and the upper stability limit ($M^{\text{Chl/St/As}}$).

From Spear (1993)

Sample LH 125 - Kyanite-sillimanite grade

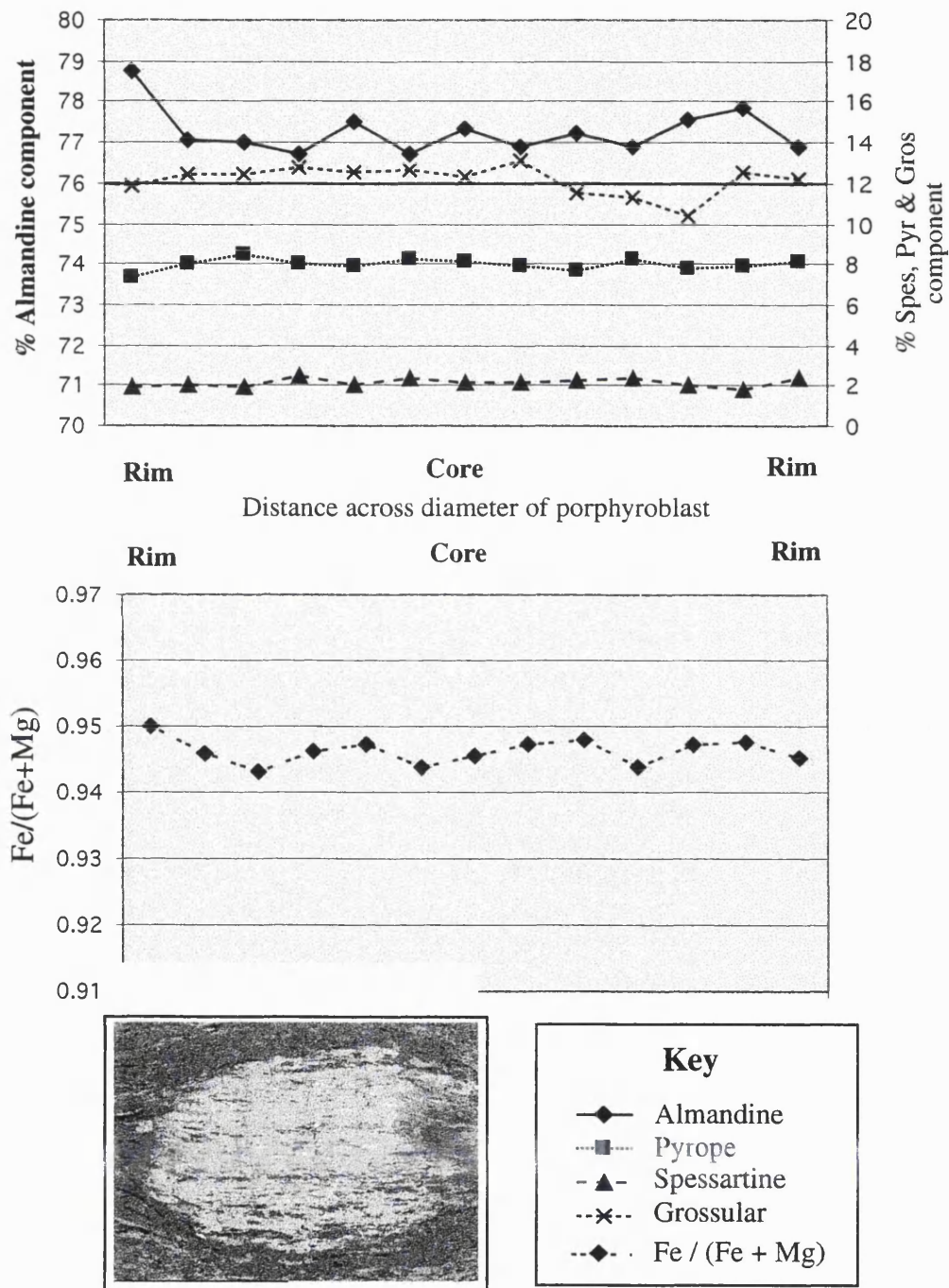


Figure 5.7 Variation of composition across the diameter of a typical garnet porphyroblast from sample LH 125. An image of the garnet across which this transect was made is shown. No systematic variation of composition across the garnet is identified.

Sample LH 28B - Kyanite-sillimanite-andalusite grade

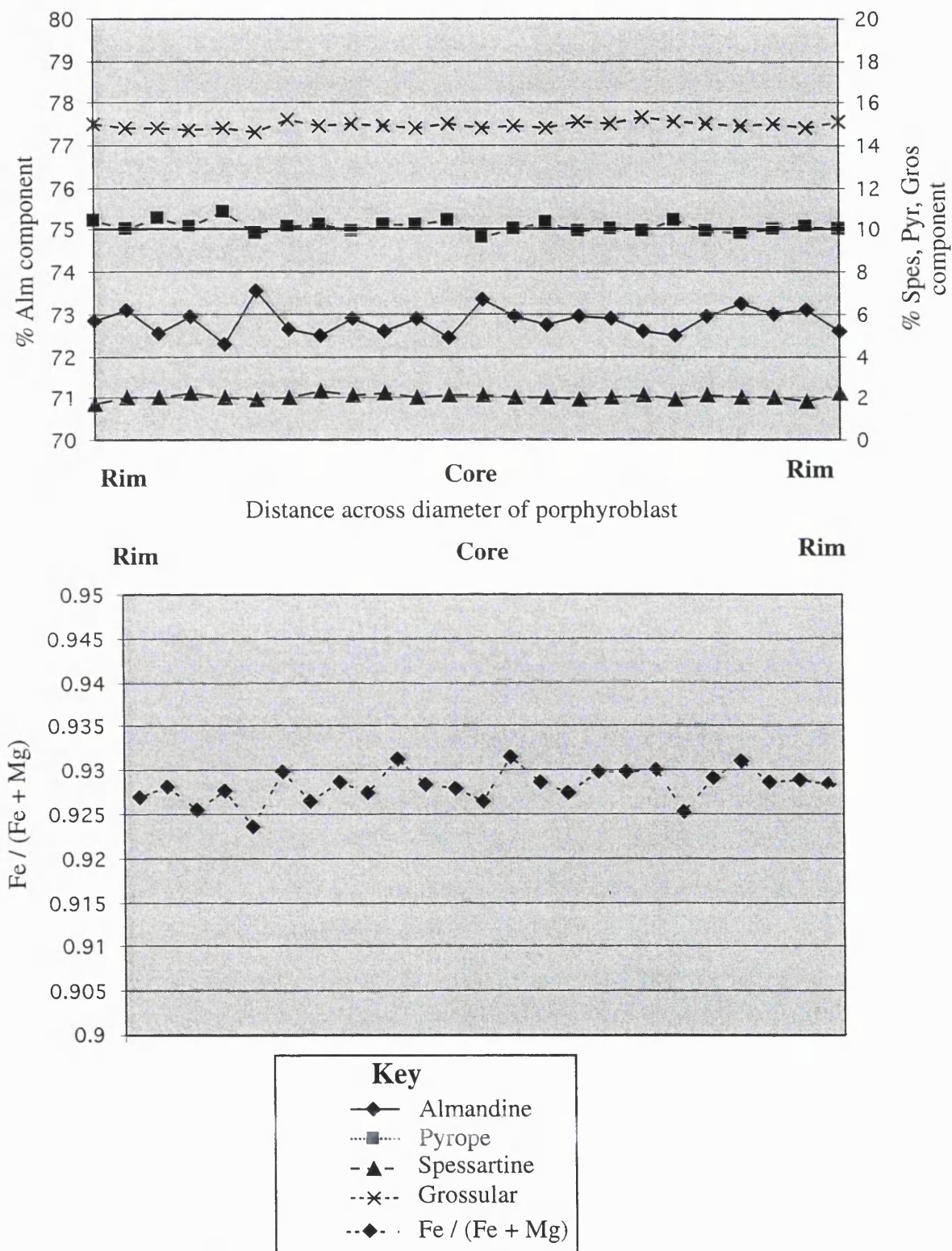
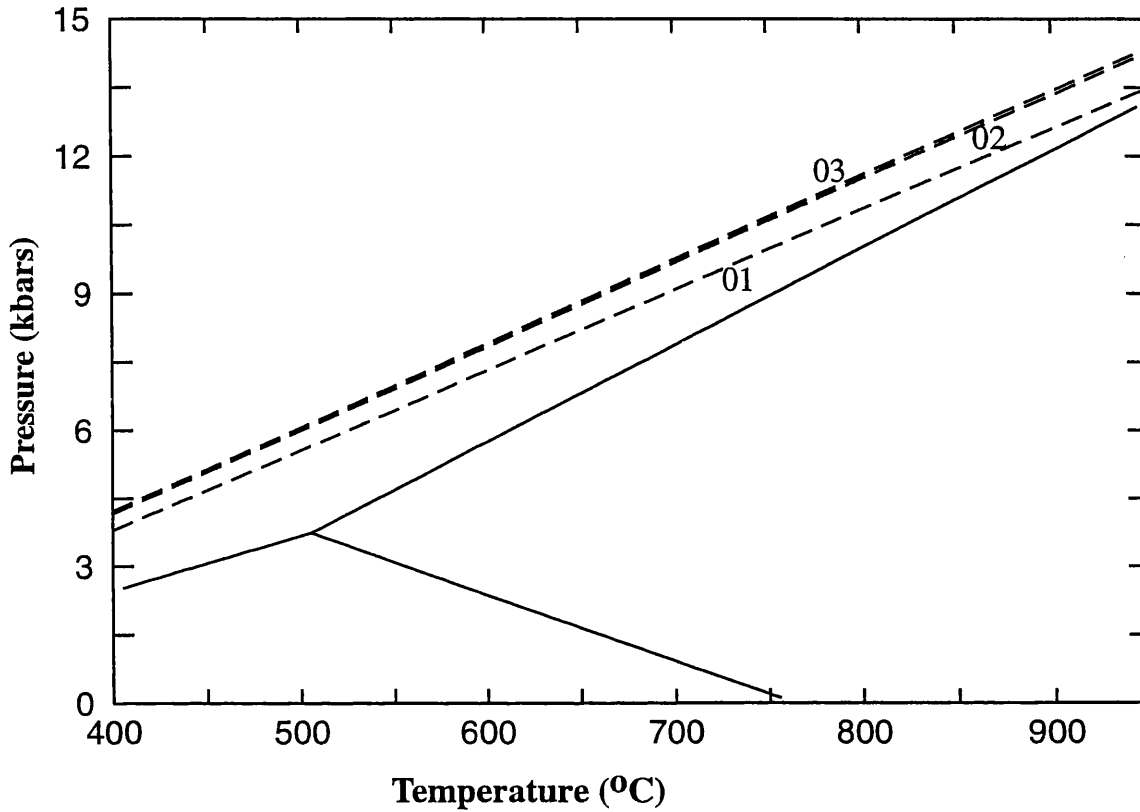


Figure 5.8 Variation of composition across a garnet porphyroblast from sample LH 28B. No significant change of composition is seen from core to rim.

**Sample LH 17 - Kyanite-sillimanite grade
GASP barometer (Kyanite field)
Ganguly & Saxena (1984)**

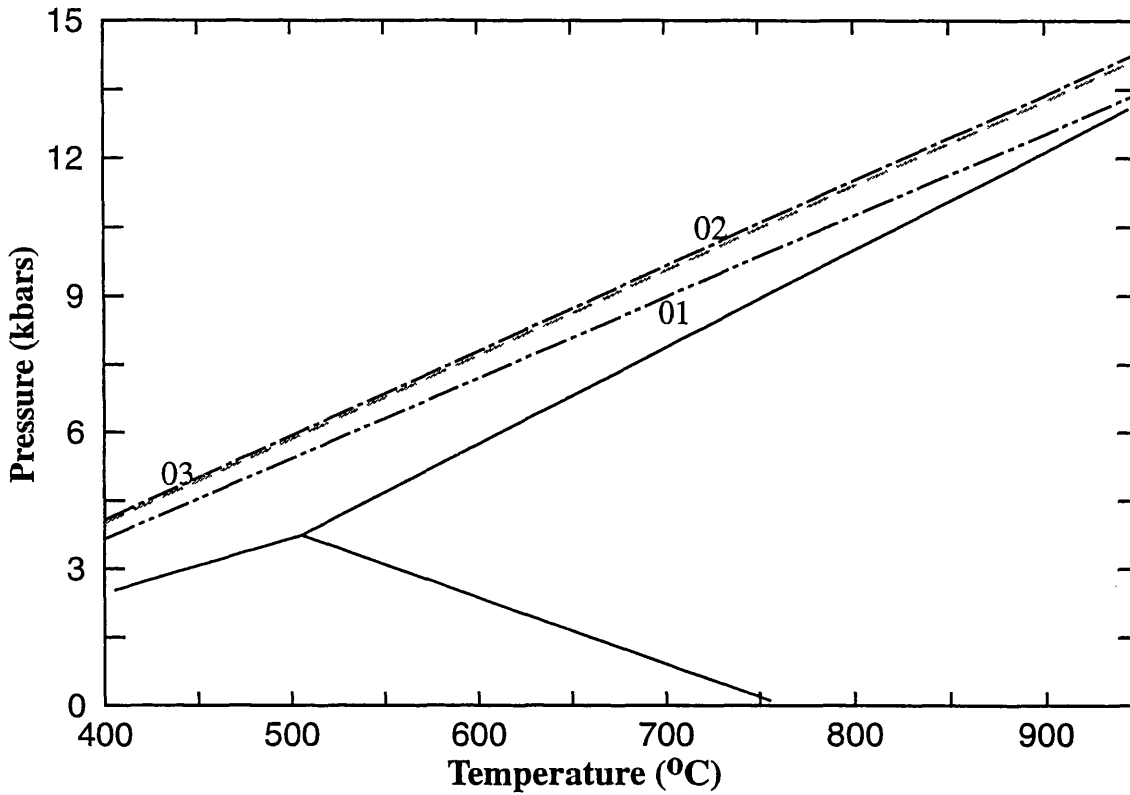


Line	Grs in Grt (%)	point	An in Plag. (%)	point
01	13.73	17rim	45.94	loc 1
02	13.73	17rim	37.62	loc 2
03	13.73	17 rim	38.71	loc 3

Figure 5.9 K_{eq} plot from the program of Spear (1991) for the GASP barometer (Ganguly & Saxena, 1984). Mineral pairs of garnet from the rim of the porphyroblast and plagioclase in the matrix have been used to plot these K_{eq} lines. The results of the barometer are fairly consistent, and indicate that the pressure was between 6-7 kbars at a temperature of $\sim 550^{\circ}\text{C}$

Full chemical analyses of each point may be found in Appendix Two.

**Sample LH 125 - Kyanite-sillimanite grade
GASP barometer (Kyanite field)
Ganguly & Saxena (1984)**



Line	Grs in Grt (%)	Point	An in Plag (%)	Point
01	12.99	125rim	42.87	125m1
02	12.99	125rim	35.05	125m2
03	12.99	125rim	34.08	125m3

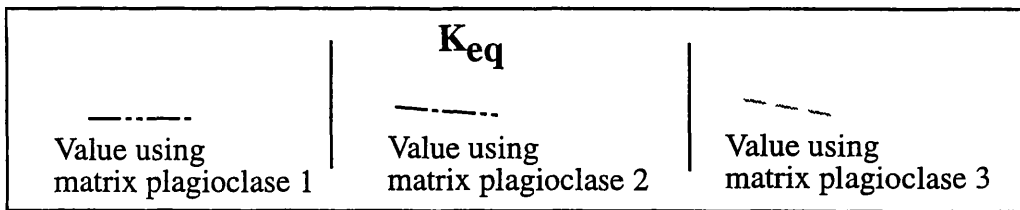
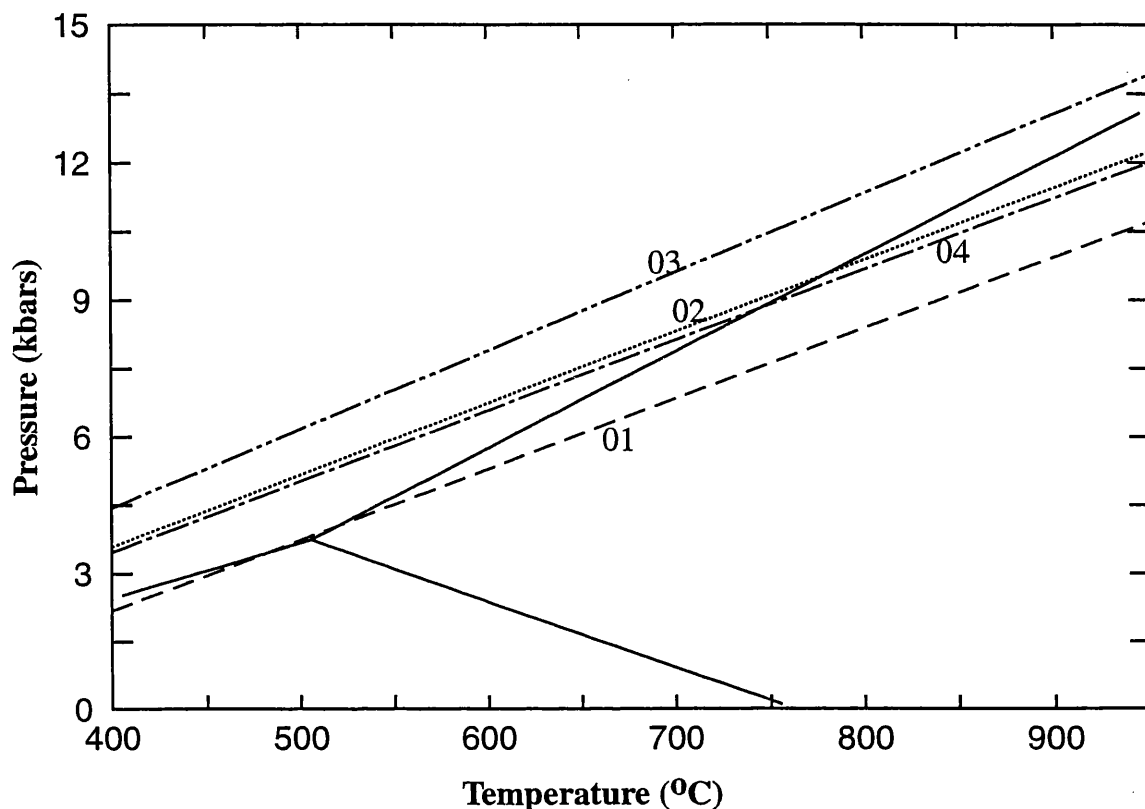


Figure 5.10

K_{eq} plot from the program of Spear (1991) for the GASP barometer (Ganguly & Saxena, 1984). The distribution of the K_{eq} lines on the P-T plot seem to be dictated by the composition of the crystal of plagioclase from the matrix which is used in the calculation. Calculations using plagioclase compositions with lower An content predict a higher pressure for a given temperature than calculations using plagioclase with higher An content.

Full chemical analyses of each point may be found in Appendix Two.

**Sample 134 - Kyanite-sillimanite grade
GASP barometer (kyanite field)
Ganguly & Saxena (1984)**



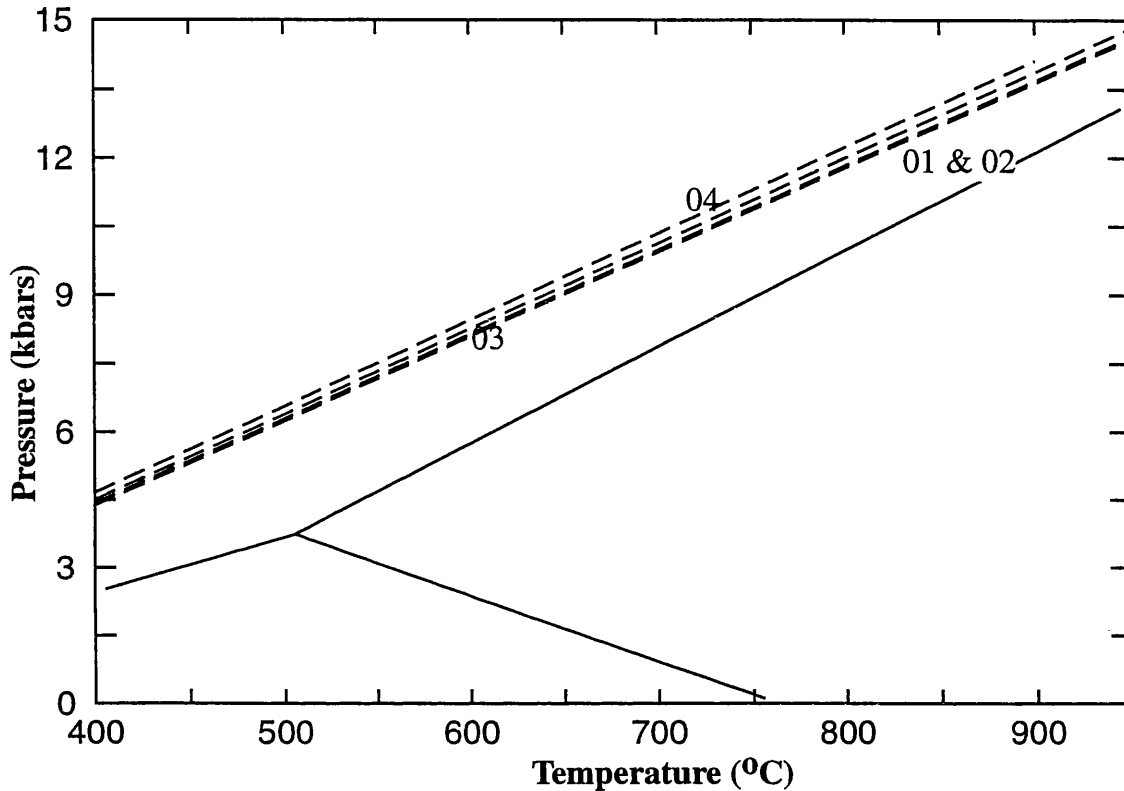
K_{eq}		Line	Grs in Grt (%)	Point	An in Plag (%)	Point
Garnet 1:						
site A - at core	-----					
site C - intermediate	01	9.10	grt4a	49.05	pl-locA
site D - nearest rim	-.-.-.-	02	17.27	grt4c	92.38	pl-locC
Garnet 2:						
site E - intermediate	-.-.-.-	03	7.72	grt6d	67.86	pl-locD
		04	11.33	grt6e	92.71	pl-locE

Figure 5.11

K_{eq} plot from the program of Spear (1991) for the GASP barometer (Ganguly & Saxena, 1984). Both garnet and plagioclase compositions vary in a non-regular way: the prediction of the highest pressure (at a given temperature) is produced when the ratio of An (feldspar) : Grs (garnet) is highest. For detailed information about the locations and composition of the plagioclase inclusions, see **figure 5.13**.

Full chemical analyses of each point may be found in Appendix Two.

**Sample LH 28B - Kyanite-sillimanite-andalusite grade
GASP barometer (kyanite field)
Ganguly & Saxena (1984)**

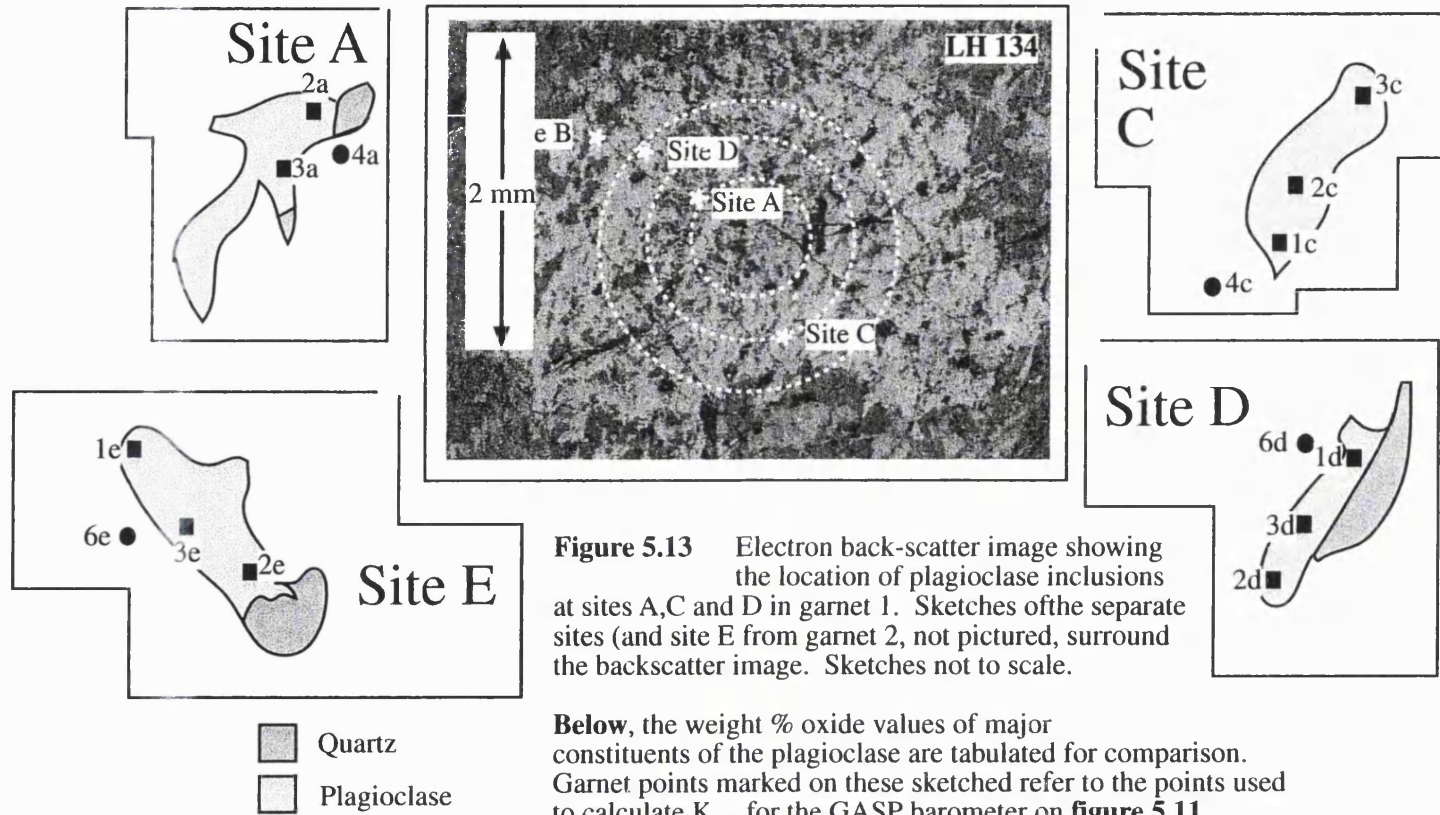


Line	Grs in Grt (%)	Point	An in Plag (%)	Point
01	14.92	28rim	38.04	28bplm3
02	14.92	28rim	40.52	28bplm2
03	14.92	28rim	36.51	28bplm1
04	14.92	28rim	38.44	28bplm4

Figure 5.12

K_{eq} plot from the program of Spear (1991) for the GASP barometer (Ganguly & Saxena, 1984). Garnet compositions are taken from the rim of the porphyroblast and are assumed to be in equilibrium with plagioclase crystals in the matrix of the sample. The composition of matrix plagioclase does not vary significantly: all the K_{eq} lines from this sample are concordant. See also figure 3.8.

Full chemical analyses of each point may be found in Appendix Two.



Point	1a	2a	3a	1c	2c	3c	1d	2d	3d	1e	2e	3e
Na ₂ O	5.43	5.29	5.18	0.83	0.91	0.77	2.79	3.94	3.47	0.77	0.88	0.74
Al ₂ O ₃	27.92	28.15	28.35	35.54	35.46	35.49	32.40	30.65	31.61	35.79	35.45	35.71
SiO ₂	57.10	56.80	56.32	44.97	44.72	44.16	49.86	52.12	51.51	44.69	45.16	44.15
CaO	9.01	9.14	9.54	17.96	18.21	18.87	14.21	12.30	12.43	18.07	17.92	18.78

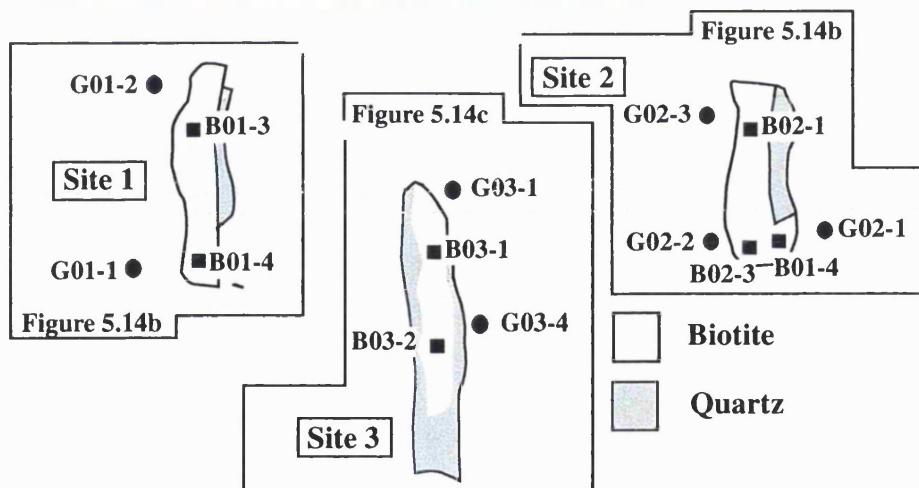
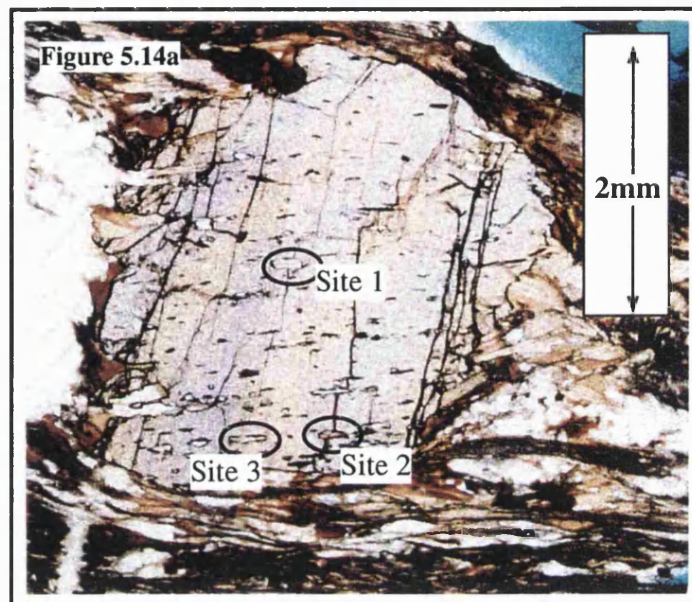


Figure 5.14a Image of garnet porphyroblast from sample LH104 (kyanite-sillimanite grade) with elongate inclusions of biotite included parallel to other inclusions (mainly ilmenite) within the crystal. The sites of the three biotite inclusions from which measurements on the electron micro-probe were taken are marked.

Figure 5.14b Sketch to show detail of site 1, and the locations of biotite and garnet analyses taken for GARB.

Figure 5.14c Sketch to show detail of site 2, and the locations of biotite and garnet analyses taken for GARB.

Figure 5.14d Sketch to show detail of site 3, and the locations of biotite and garnet analyses taken for GARB.

The results of analyses at sites 1, 2 and 3 are tabulated in **figure 5.16** - full analyses in Appendix Two

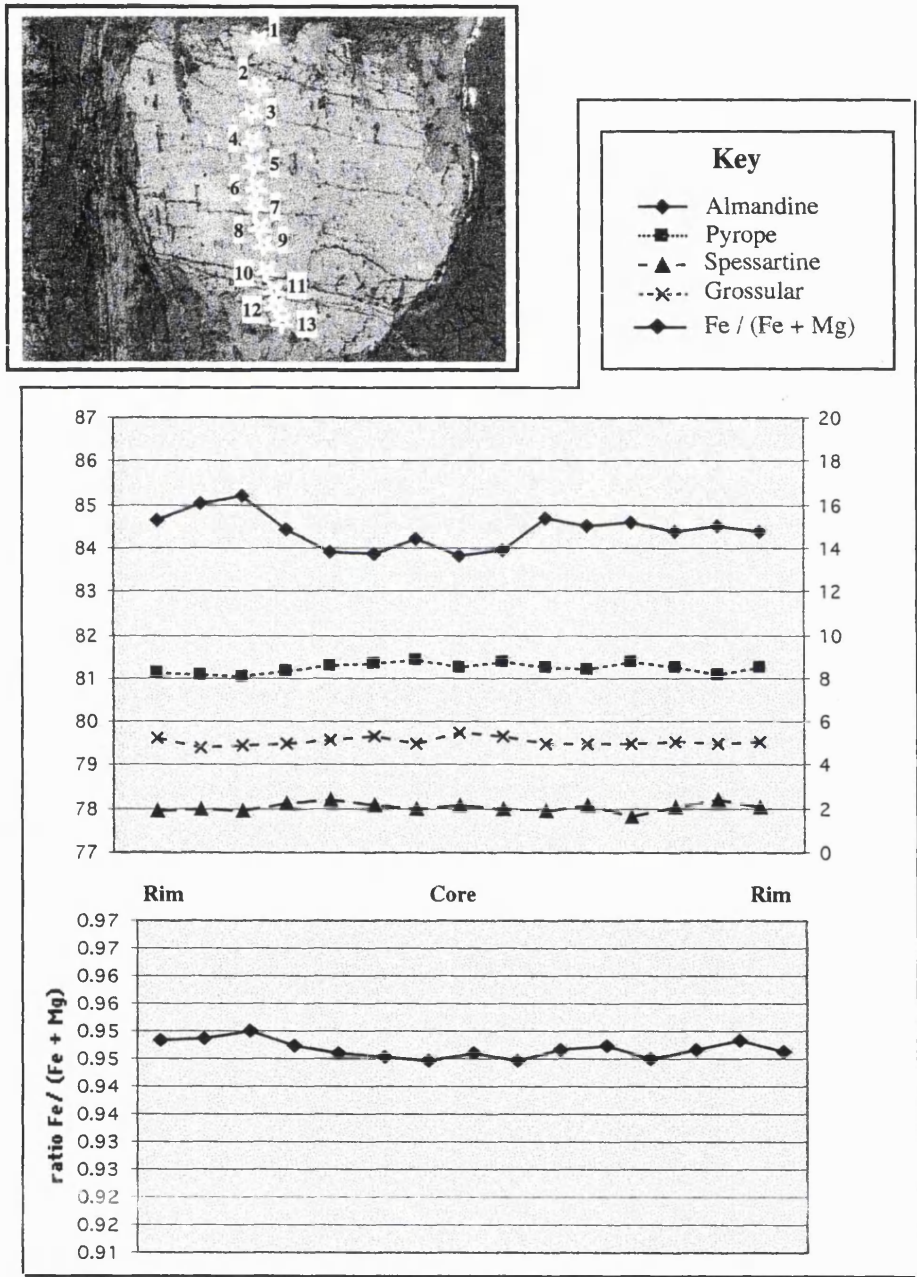


Figure 5.15 Image of garnet porphyroblast from sample LH104 (kyanite-sillimanite zone) from which the composition of biotite inclusions were measured, and plots of the variation of major components across the diameter of the porphyroblast. In common with other garnet profiles from kyanite-sillimanite-grade rocks e.g. sample LH125, in figure 5.8), there is no significant variation of composition from core to rim, indicating this garnet probably grew during decompression and/or conditions of increasing temperature.

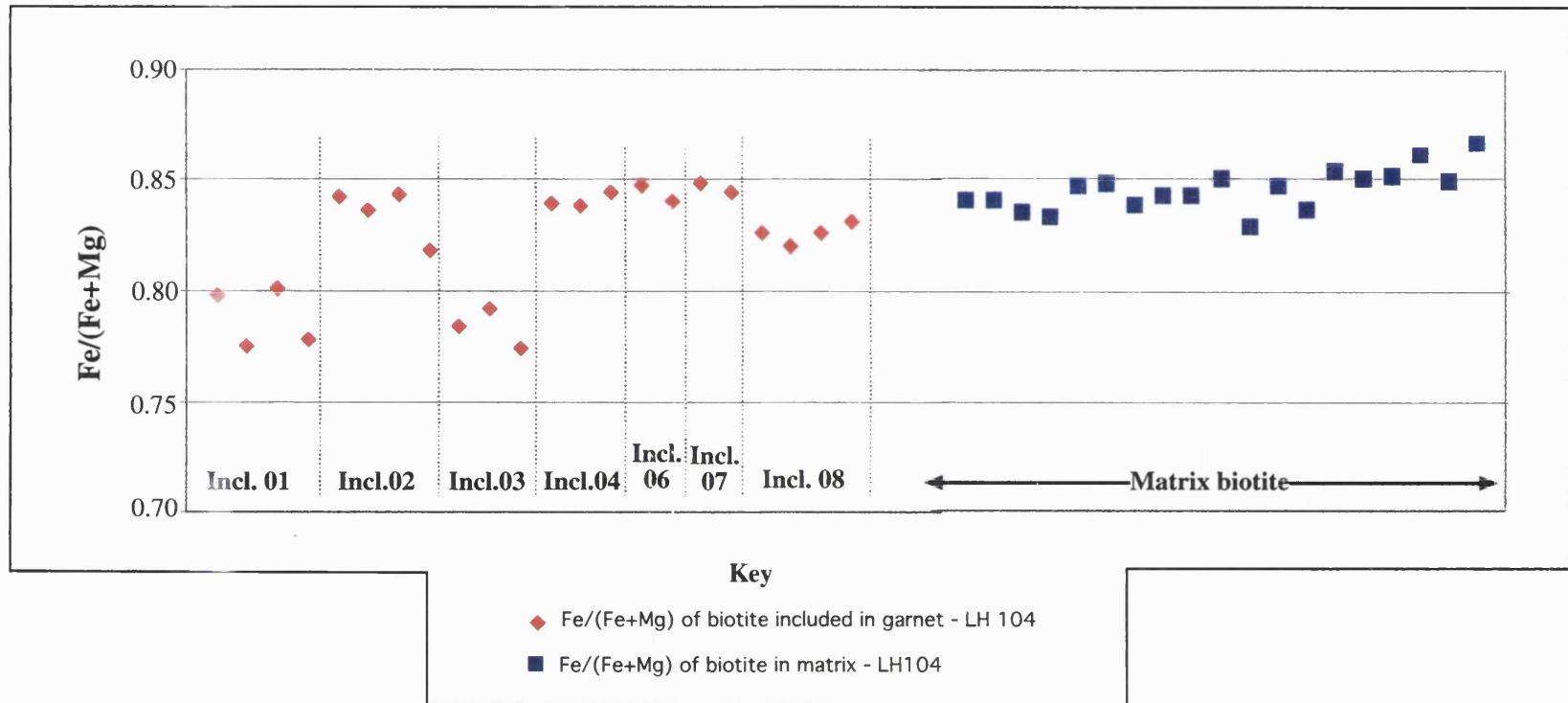
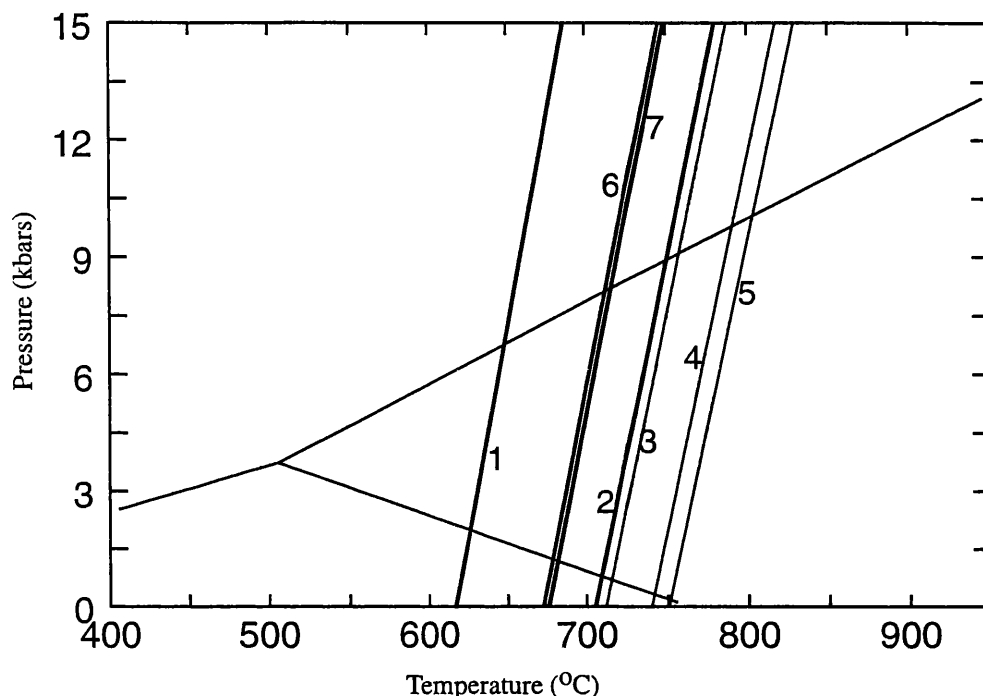


Figure 5.16

Plot of the ratio $\text{Fe}/(\text{Fe}+\text{Mg})$ for all the biotite grains included in garnet porphyroblasts within sample LH104 (kyanite-sillimanite grade). The compositions of these included grains is compared with the ratio of $\text{Fe}/(\text{Fe}+\text{Mg})$ calculated for a selection of biotite grains in the matrix of the sample, located at the edge of garnet porphyroblasts and grains lying parallel to foliations.

From this plot it seems likely that the composition of the majority of biotite inclusions within the garnet porphyroblasts has been modified to a composition similar to that of biotite in the matrix. Biotite inclusions at sites 01 and 03 show distinctly different $\text{Fe}/(\text{Fe}+\text{Mg})$ ratios, indicating that biotite at these sites has been least affected by exchange reactions operating after the growth of the garnet.

**Sample LH 104 - Kyanite-sillimanite grade
Garnet-Biotite thermometer
(Ferry & Spear with Berman, 1990)**

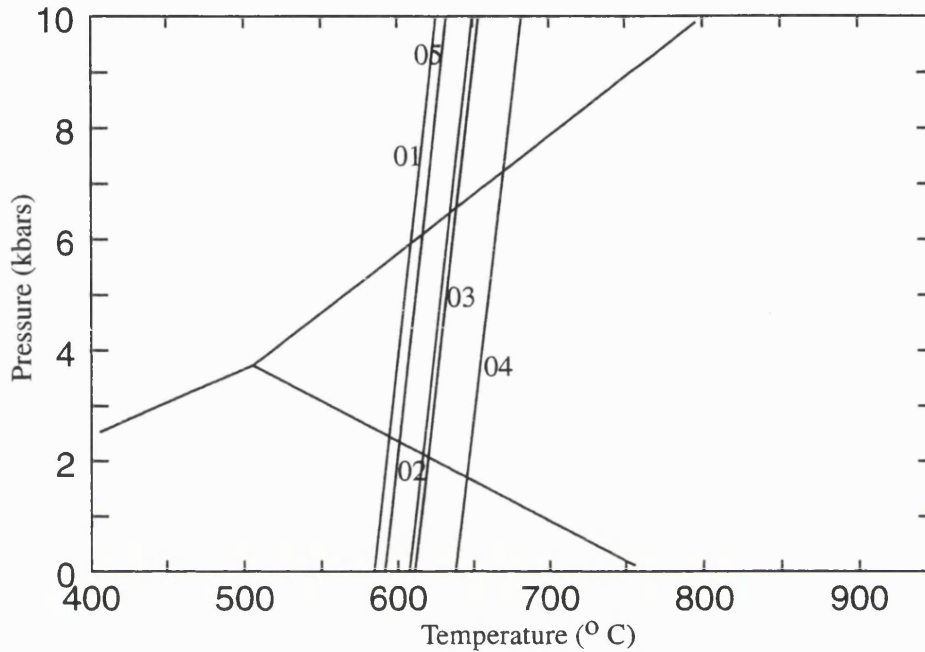


Line	Fe/(Fe+Mg) Garnet	Point	Fe/(Fe+Mg) Biotite	Point
01	0.9533	G01-1	0.801	B01-3
02	0.9420	G01-2	0.800	B01-1
03	0.9493	G02-1	0.818	B02-4
04	0.9533	G02-2	0.843	B02-3
05	0.9532	G02-3	0.842	B02-1
06	0.9421	G03-1	0.784	B03-1
07	0.9439	G03-4	0.792	B03-2

Figure 5.17 K_{eq} plot from the program of Spear (1991) for the GARB thermometer, calibration of Ferry & Spear (1978) with garnet mixing model of Berman (1990). Following on from the conclusions shown on figure 5.16, values of the mineral pairs taken from biotite inclusions at sites 01 and 03 are highlighted in bold in the table, and the K_{eq} lines corresponding to these values are indicated by broader lines than K_{eq} lines relating to other sites. These lines are most likely to represent the temperature experienced by the sample at a given pressure.

Full chemical analyses of each point may be found in Appendix Two.

**Sample LH 56 - Kyanite-sillimanite-andalusite grade.
Garnet - Biotite thermometer
Ferry & Spear with Berman (1990)**



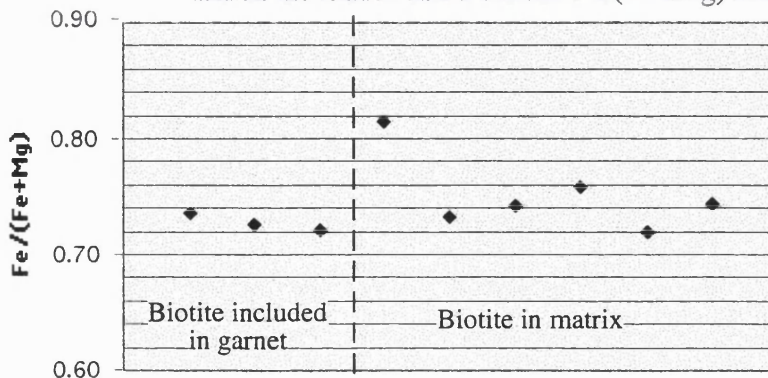
Line	Alm in Grt (%)	Point	Fe / (Fe+Mg) in Biotite	Point
01	78.52	G3	0.62	B03
02	78.52	G3	0.64	B04
03	77.42	G1	0.60	B02
04	79.42	G5	0.71	B01
05	77.76	G4	0.59	B05

Figure 5.18b

Above K_{eq} lines for the application of the GARB thermometer, as calibrated by Ferry & Spear with Berman (1990). The resulting K_{eq} lines plot quite closely together, and provide a useful constraint for the temperature of equilibration.

Figure 5.18c

Below. The composition of biotite included in garnet and in the matrix has a similar Fe/(Fe+Mg) ratio.



Sample LH 255 - garnet/staurolite-andalusite grade

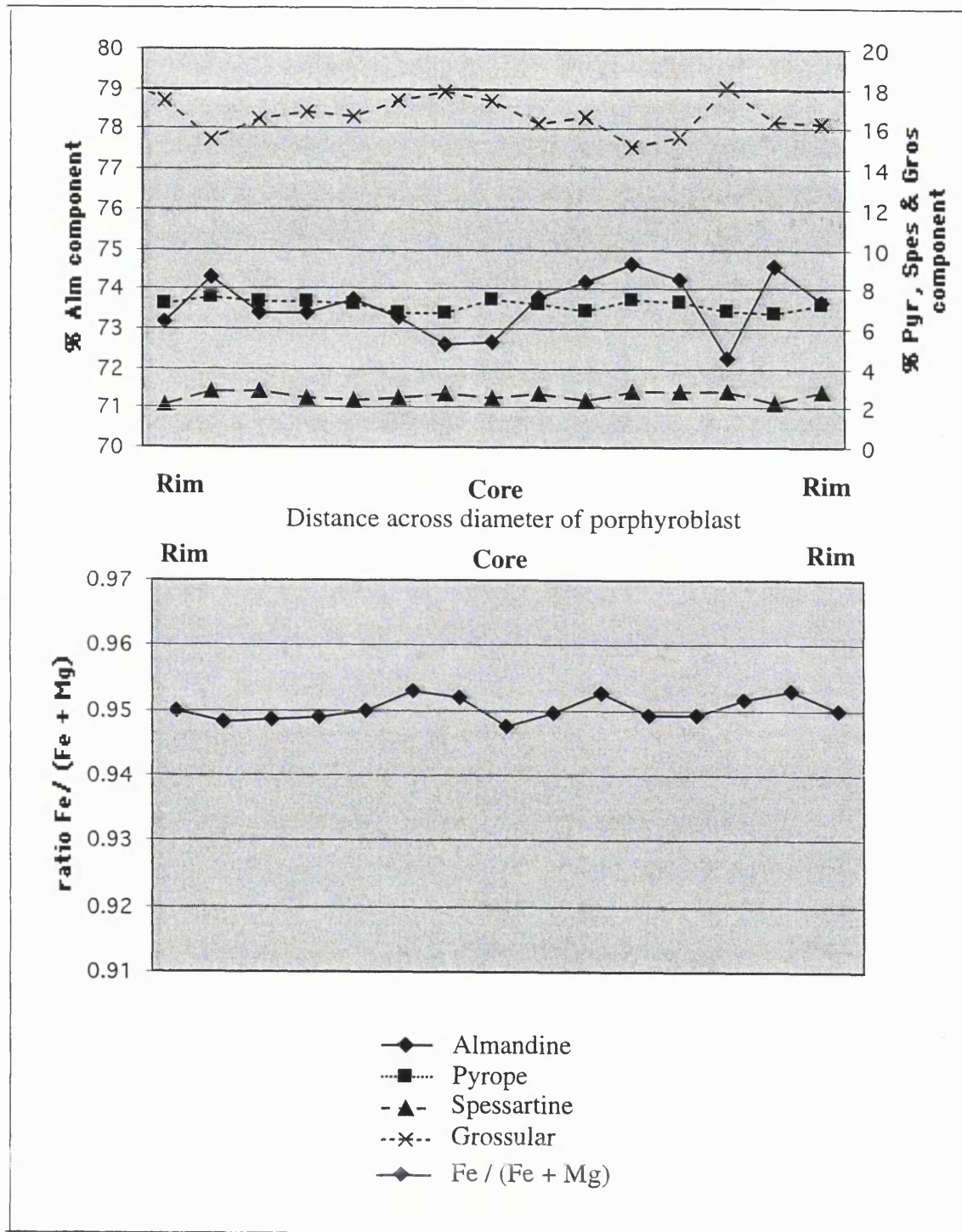


Figure 5.19 Composition variation across a garnet porphyroblast from sample LH 255. The grossular component shows a slight maximum at the core, indicating higher pressure/ temperature in the early part of garnet growth. No other significant zoning.

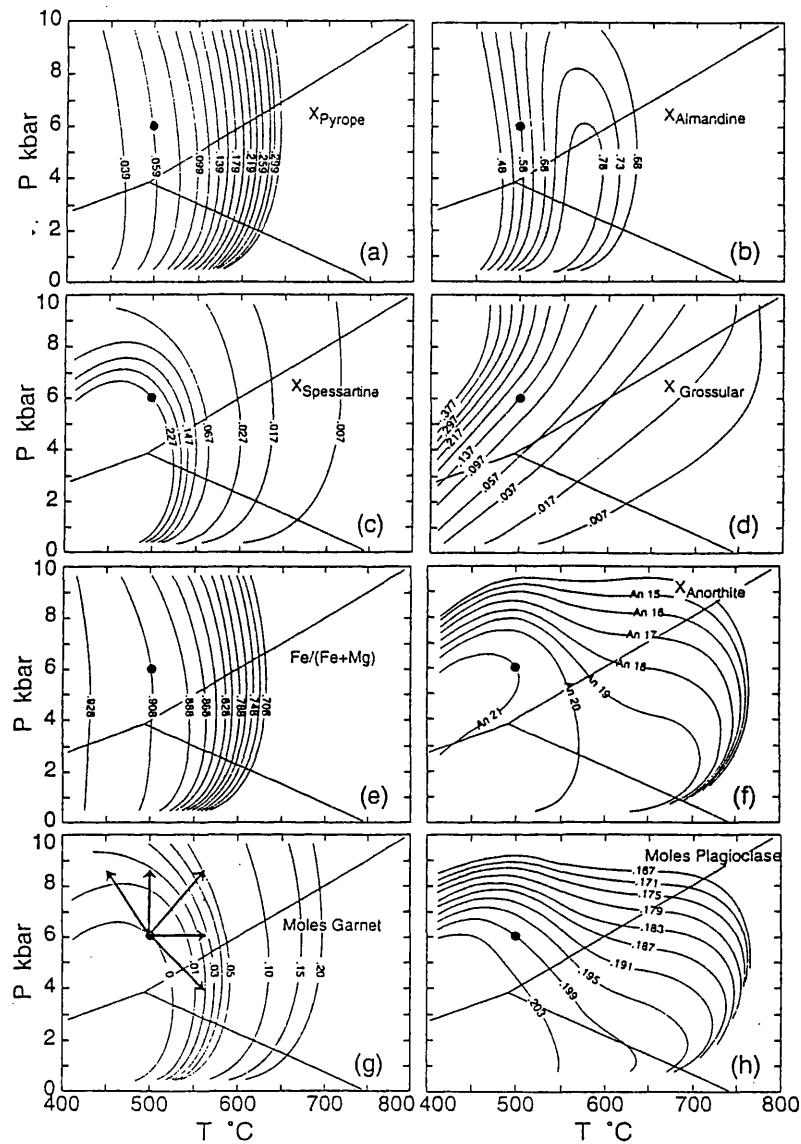


Figure 5.20 Contours of garnet composition (a-e), plagioclase composition (f) and plagioclase molar abundance (g-h) for the assemblage garnet + biotite + chlorite + plagioclase + muscovite + quartz in the MnNCKFMASH system. The black dot indicates the location of the reference P-T conditions.

From Spear (1993)

Sample LH 154 - garnet/staurolite - andalusite grade

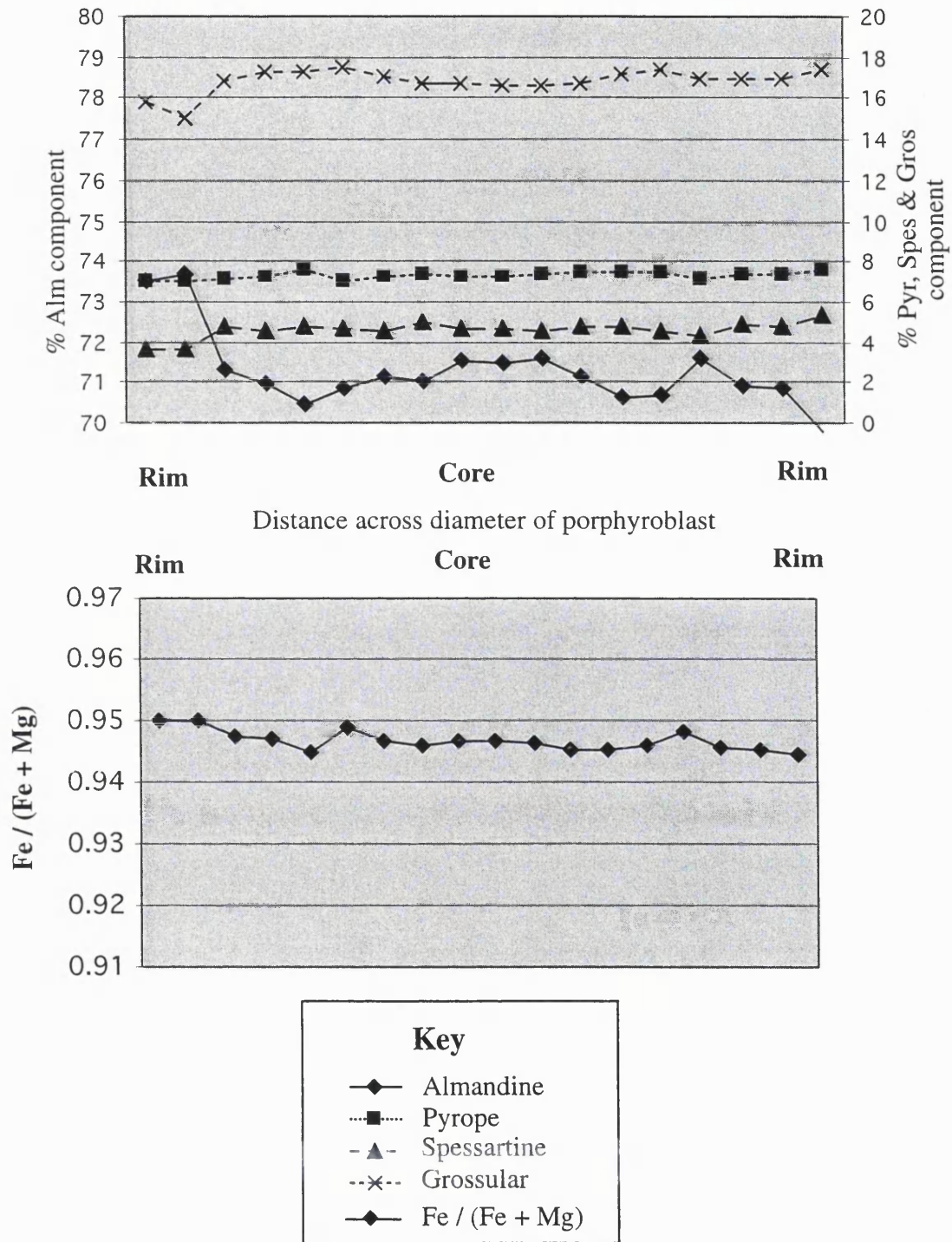


Figure 5.21 Variation of garnet composition across a garnet porphyroblast from sample LH 154 (garnet/staurolite - andalusite grade). The almandine component may show a decrease from the core to the rim, followed by an increase towards the rim of the crystal, and a sharp decrease at the furthest rim.

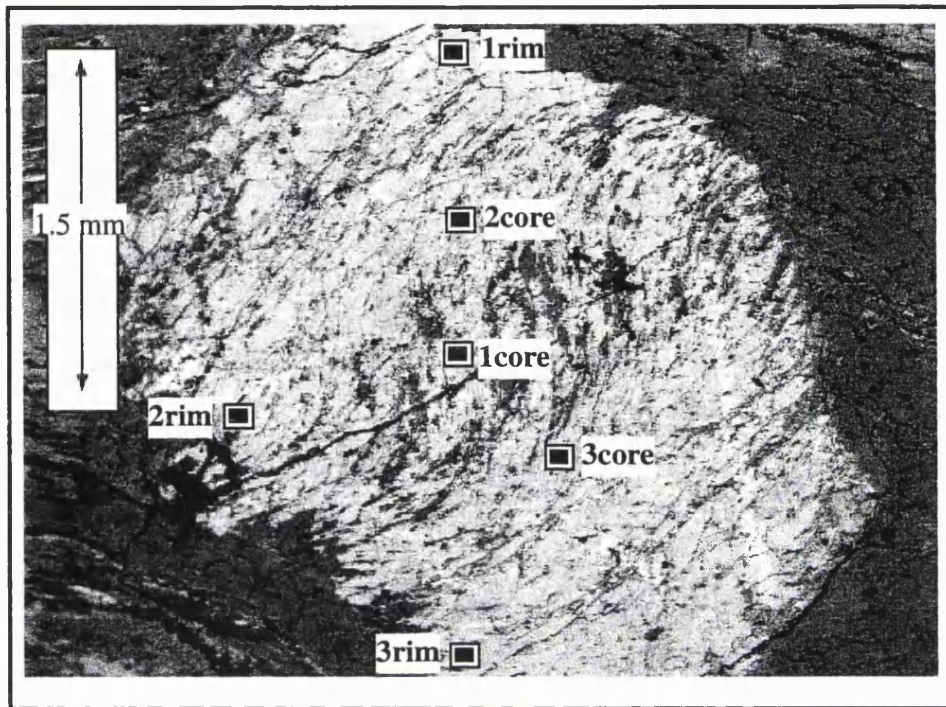
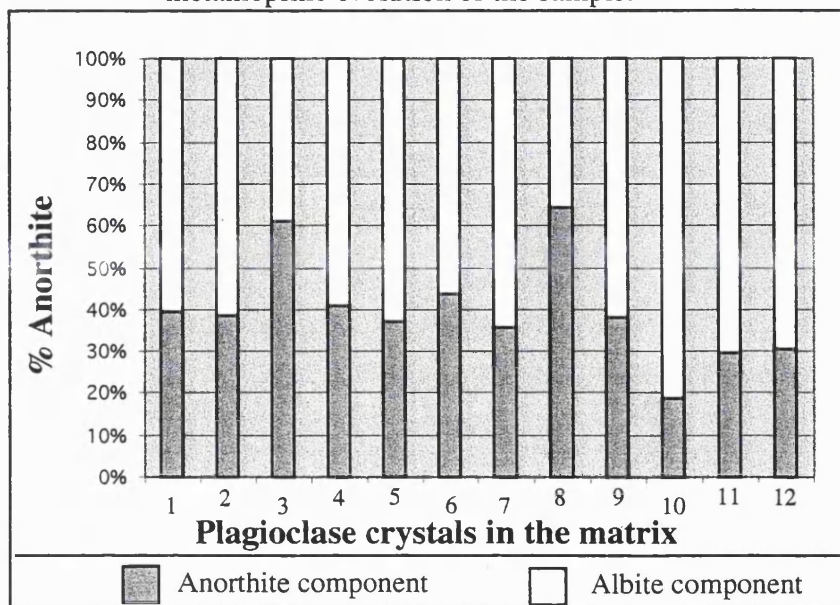


Figure 5.22a

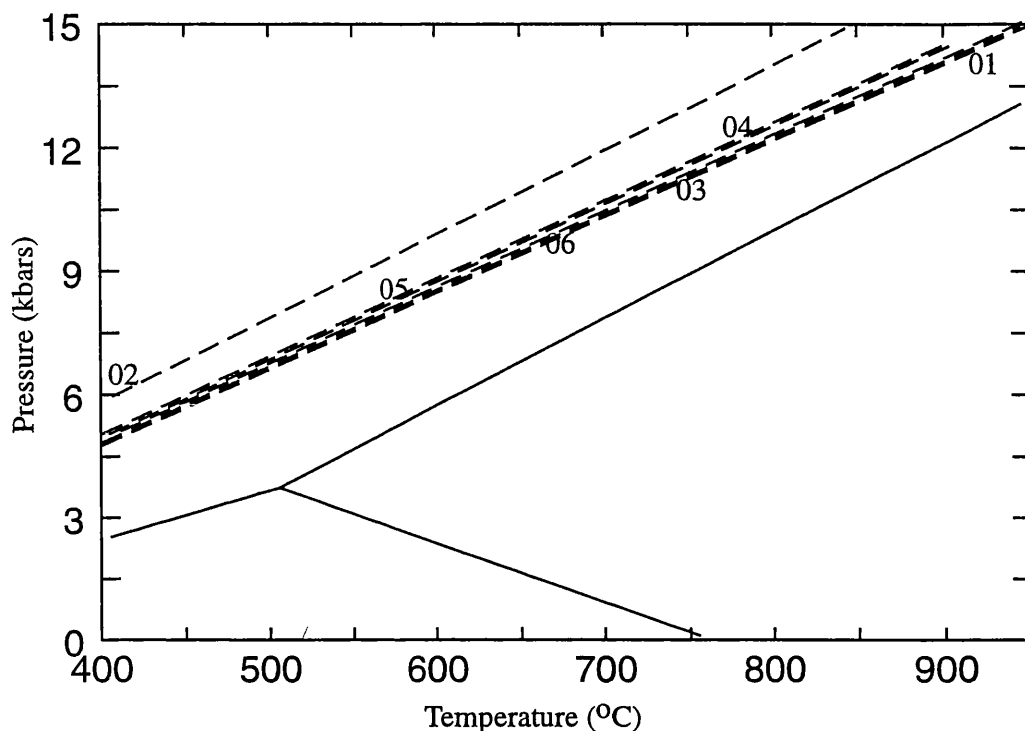
Above. Electron backscatter image of a garnet porphyroblast in sample LH255 (garnet/staurolite-andalusite grade) with the locations of point analyses of garnet indicated. Results from these analyses are tabulated in **figure 5.23**.

Figure 5.22b

Below Plot to show the variation of composition of plagioclase in the matrix of sample LH255. The wide variation of composition may indicate that plagioclase has not equilibrated during the metamorphic evolution of the sample.



**Sample LH 255 - Garnet/staurolite-andalusite grade
GASP barometer - (Ganguly & Saxena, 1984).**



- . - . - .	Mineral pairs using garnet values from the porphyroblast core
- - - - -	Mineral pairs using garnet values from the porphyroblast rim
(All plagioclase values are from crystals in the matrix)	

Line	Grs in Grt (%)	Point	An in Plag (%)	Point
01	11.26	3rim	48.19	pl255-2
02	11.26	3rim	29.34	pl255-4
03	14.91	2rim	43.70	pl255-1
04	14.91	2rim	38.17	pl255-3
05	17.83	1rim	43.70	pl255-1
06	17.83	1rim	48.19	pl255-2

Figure 5.23 K_{eq} lines resulting from the application of the GASP barometer to sample LH 255 (Garnet/staurolite-andalusite field). The results from these calculations tightly constrain the conditions of pressure at a given temperature. Locations of the point analyses and a plot of varying plagioclase composition is given in **figure 5.22**. A range of plagioclase compositions representing the variation in the matrix have been used in the GASP barometer.

Full mineral analyses in Appendix Two. .

Sample LH 311- garnet/staurolite-andalusite grade

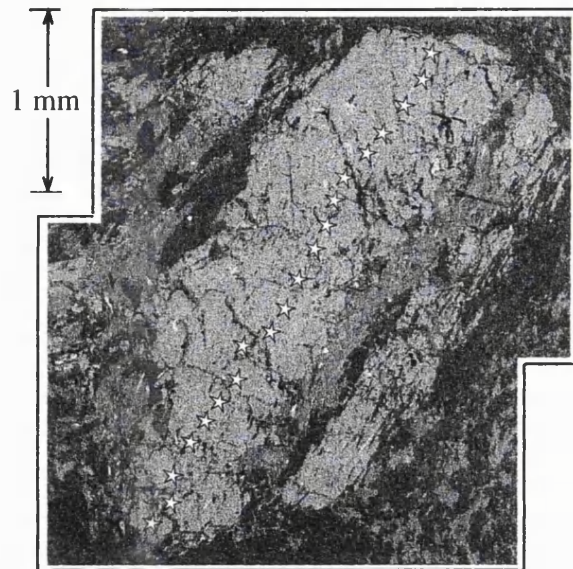
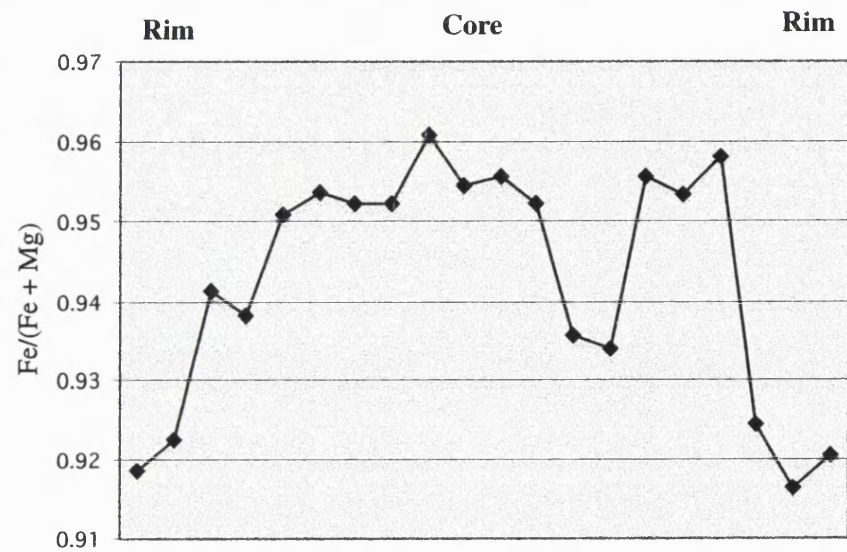
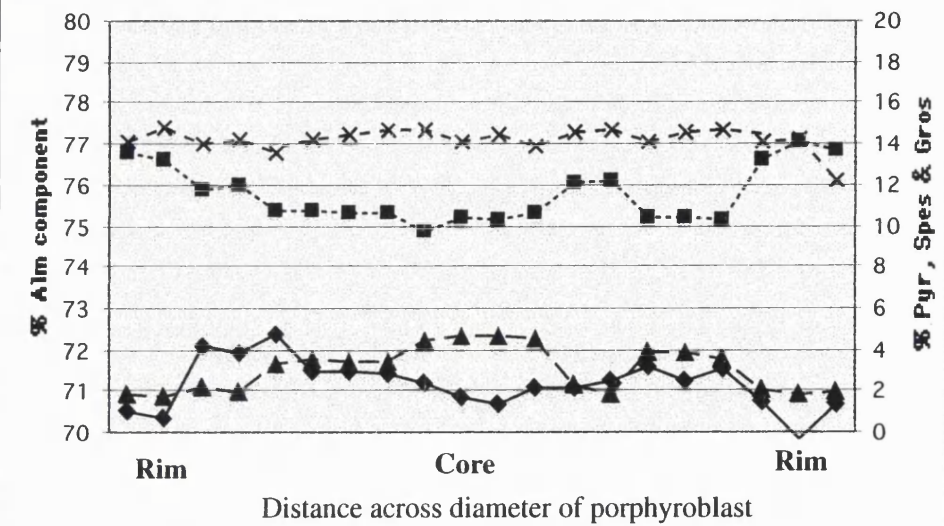


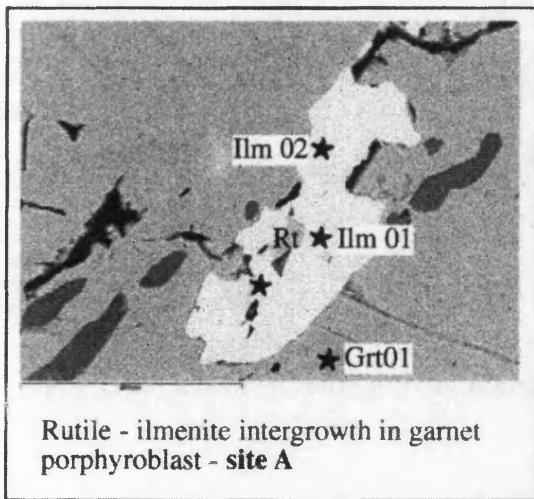
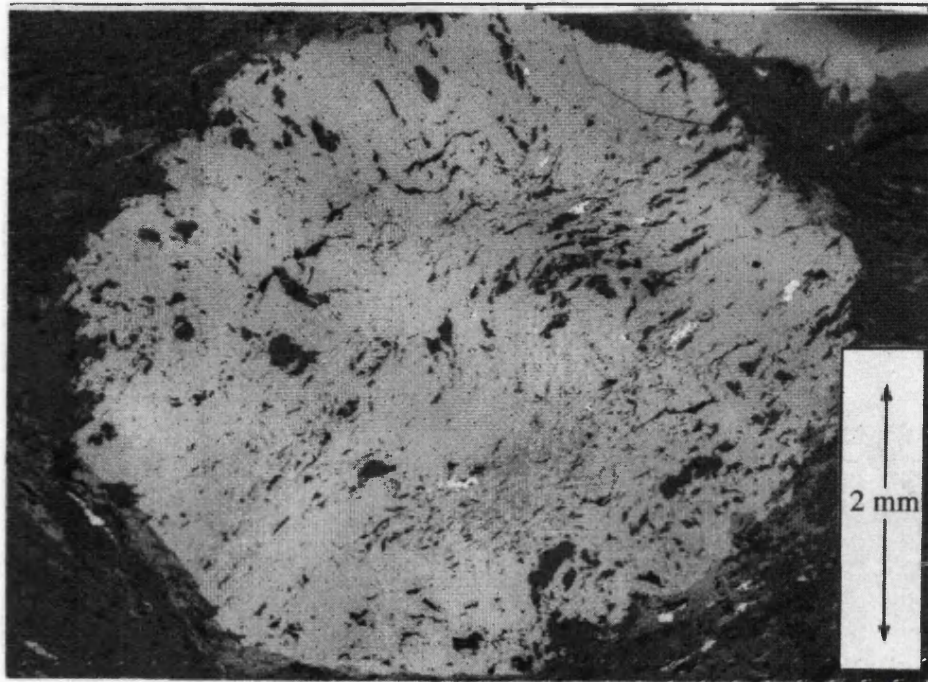
Figure 5.24a Above Image of garnet porphyroblast from sample LH 311, across which composition readings were taken.

Figure 5.24b Right. Composition variation across porphyroblast. Fe/(Fe + Mg) shows a decrease from core to rim; other components do not show significant variation.

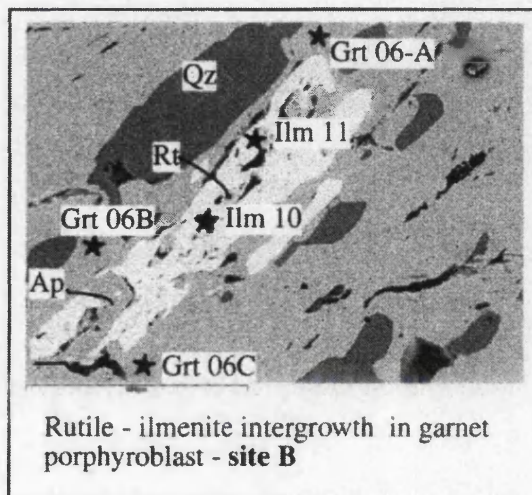


- ◆ Almandine
- Pyrope
- ▲ Spessartine
- × Grossular
- ◆ Fe / (Fe + Mg)

Figure 5.25a **Below.** Backscatter image from the electron micro-probe of garnet porphyroblast from sample LH 138. This image shows the locality of the ilmenite-rutile intergrowths seen in detail in 5.25 b (below).



Rutile - ilmenite intergrowth in garnet porphyroblast - **site A**



Rutile - ilmenite intergrowth in garnet porphyroblast - **site B**

Figure 5.25b **Above.** Detailed images showing rutile - ilmenite intergrowths at the locations marked on the photograph in figure 5.15a. The localities where measurements of ilmenite, rutile and garnet composition were made are indicated by asterisks.

Arrow indicates location of close-up view of a rutile-ilmenite intergrowth in garnet.

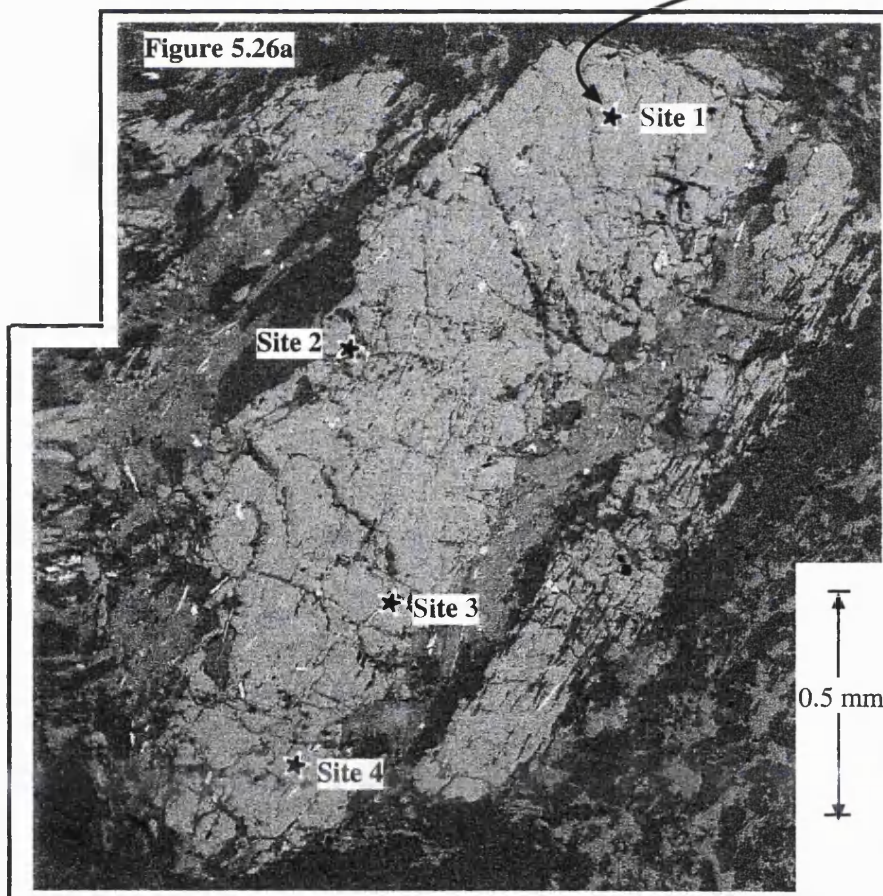
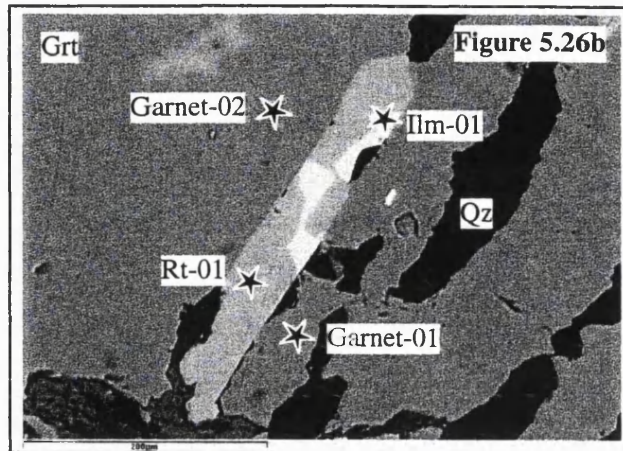


Figure 5.26a Above. Back-scatter image of garnet porphyroblast in section LH311, with sites where ilmenite-rutile intergrowths occur as inclusions marked. Arrow indicates location of inset - **figure 5.26b**.

Figure 5.26b Top. A detailed view of a rutile-ilmenite intergrowth at site 1. Large asterisks mark the positions where mineral analyses were made for GRAIL

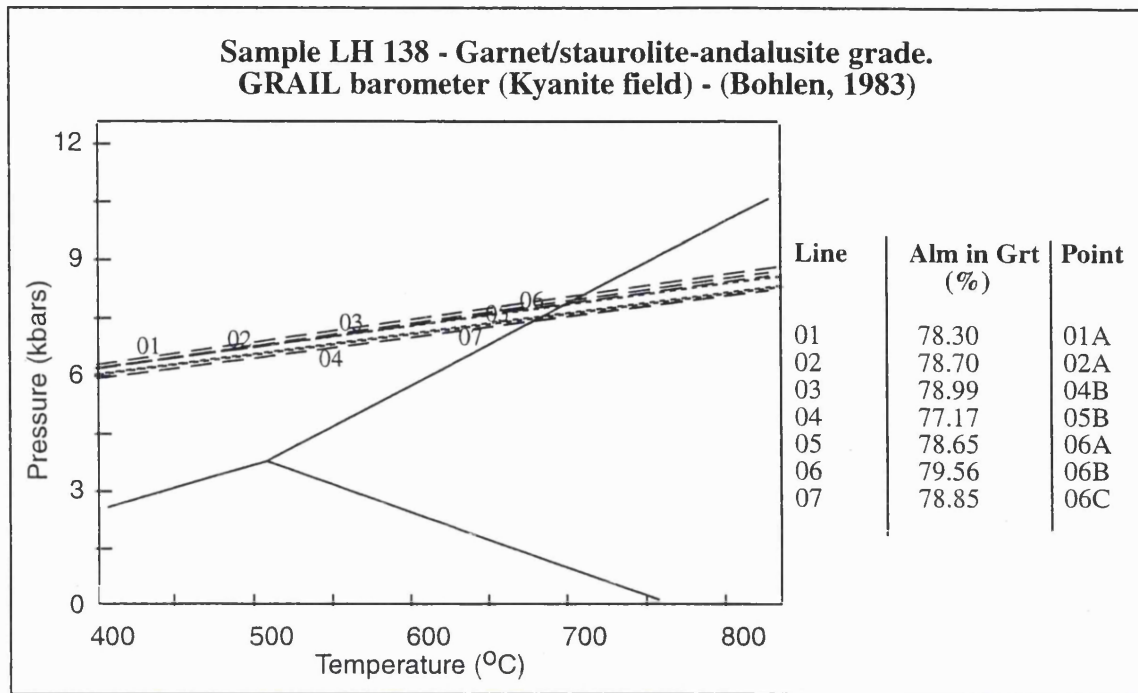
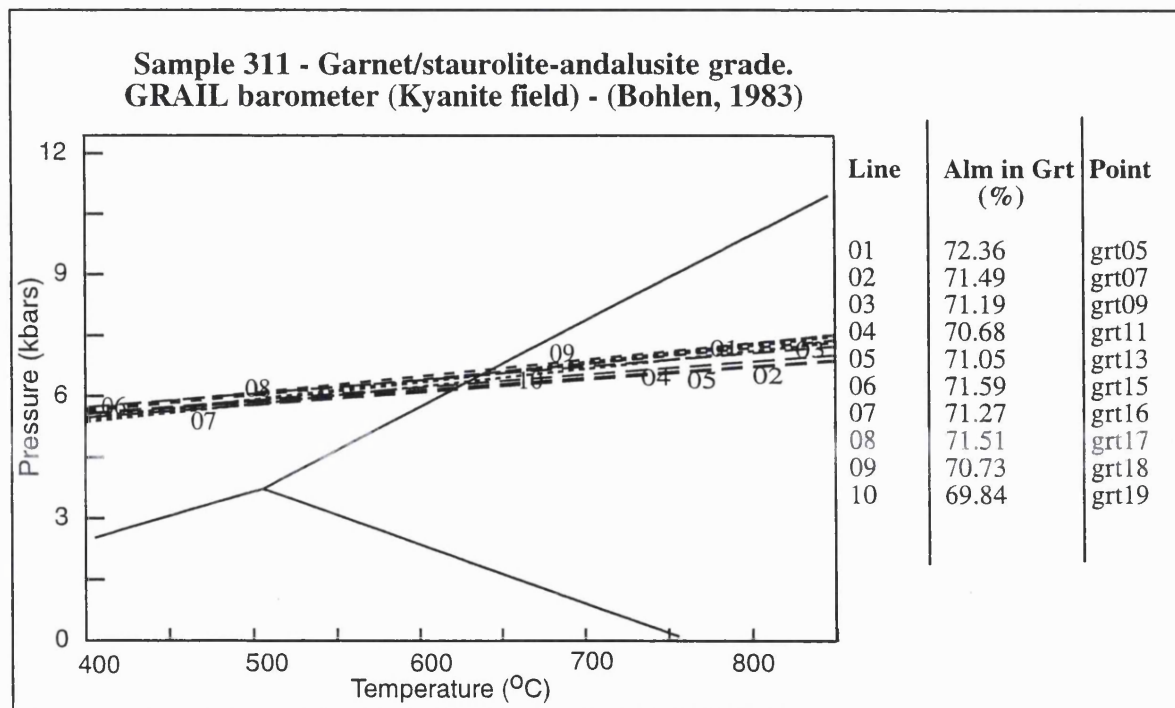
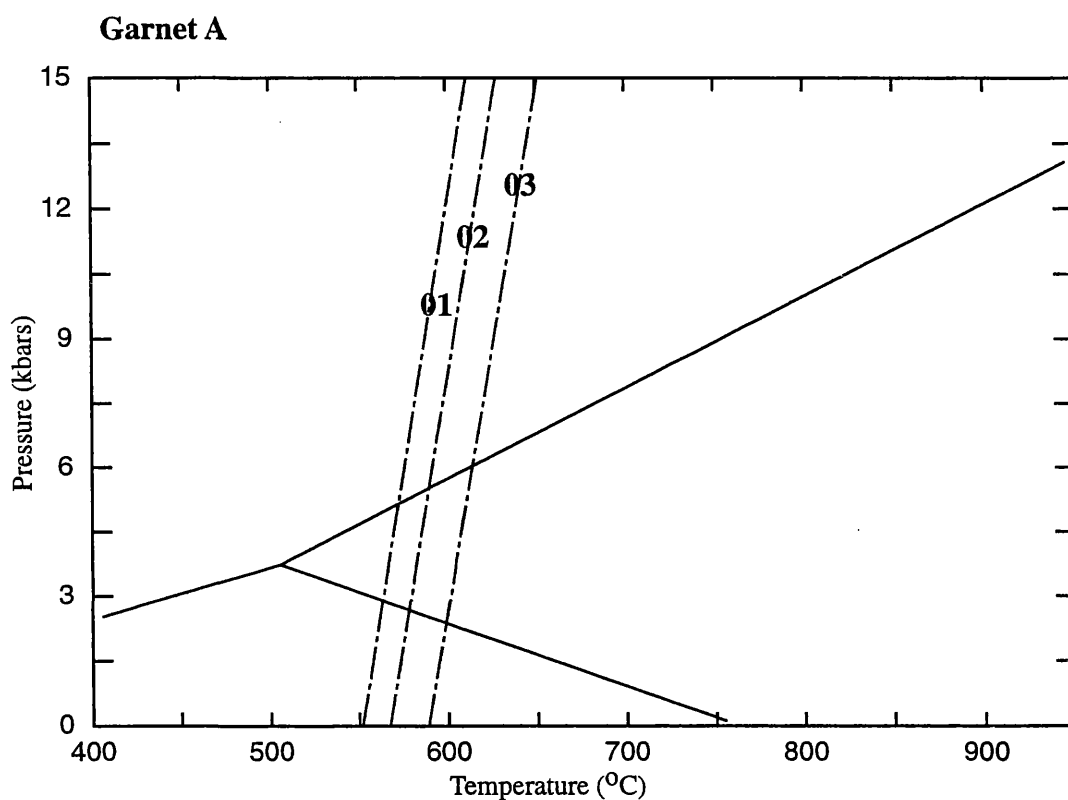


Figure 5.27a Above. GRAIL calibration of Bohlen (1983) applied to rutile-ilmenite in garnet from LH 138. Almandine contents of garnet used in calculations are also shown.

Figure 5.27b Below. GRAIL calibration of Bohlen (1983) applied to rutile-ilmenite in garnet for LH 311. Almandine contents of garnet used in calculation also shown.



**Sample LH 61 - garnet/ staurolite - andalusite grade
GARB thermometer (Ferry & Spear with Berman (1990))**



Line	Alm in Grt (%)	Point	Fe/(Fe+Mg) in biotite	Point
01	78.20	rimA	0.56	RimA
02	78.20	rimA	0.58	matr1
03	78.20	rimA	0.58	matr1

Figure 5.28a

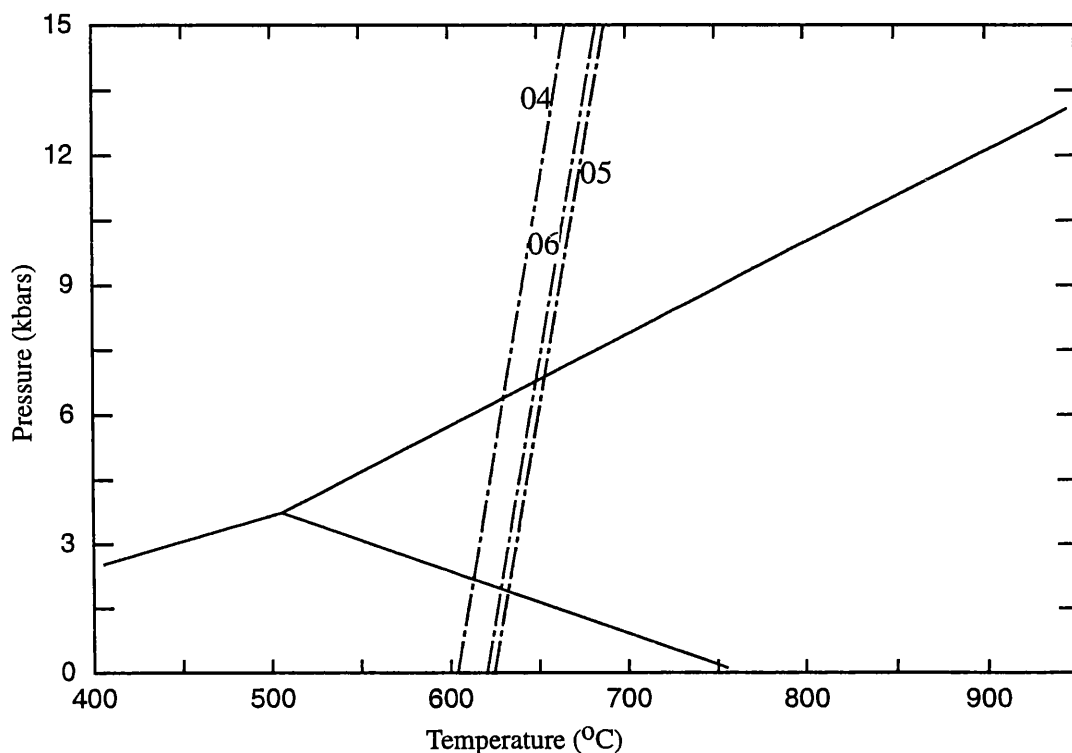
K_{eq} plot of data from sample LH61, garnet/staurolite-andalusite grade. **Garnet A.**

The K_{eq} lines plotted using garnet compositions from the rim of the porphyroblast and compositions of biotite from the matrix provide a fairly tight constraint for temperature at a known pressure; at 6 kbar, the GARB thermometer predicts that the temperature was between 550 - 600 °C

Full mineral analyses in Appendix Two..

**Sample LH 61 - garnet/ staurolite - andalusite grade
GARB thermometer (Ferry & Spear with Berman (1990))**

Garnet B



Line	Alm in Grt (%)	Point	Fe/(Fe+Mg) in biotite	Point
04	75.19	rimB	0.58	61rimB
05	75.19	rimB	0.59	matrix2
06	75.19	rimB	0.59	matrix3

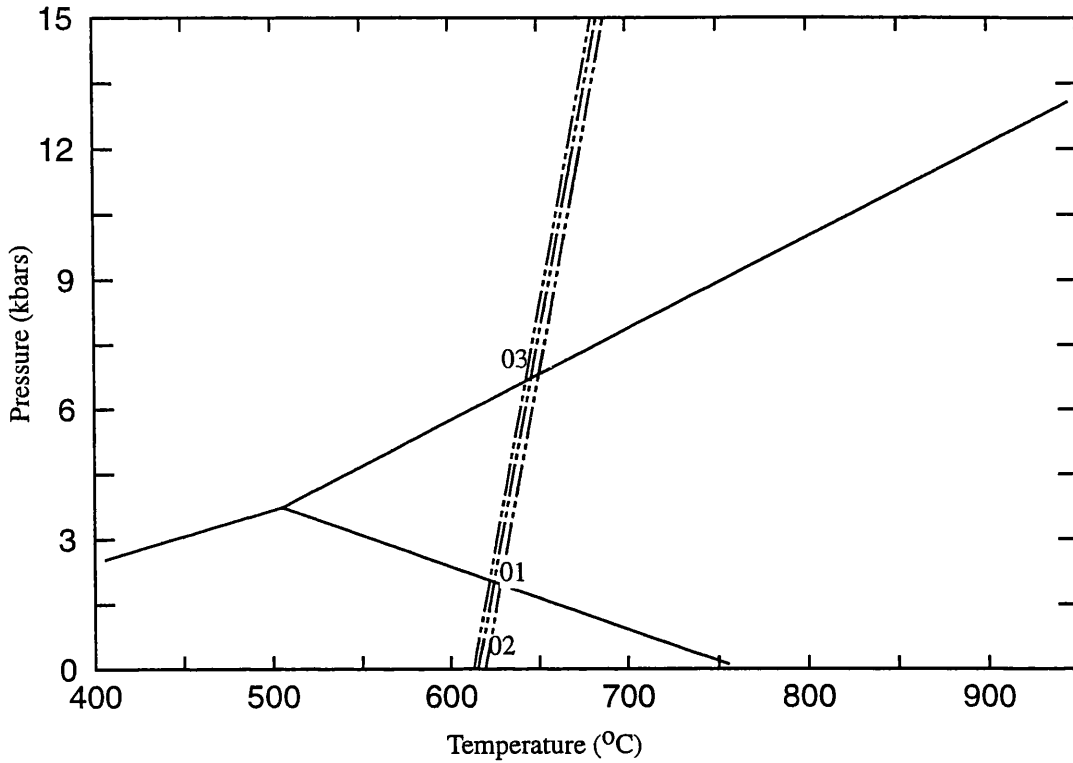
Figure 5.28b

K_{eq} plot of data from sample LH61, garnet/staurolite-andalusite grade. **Garnet B**. Some variation of composition is detected from core to rim.

The K_{eq} lines plotted for this garnet predict slightly higher temperatures than those from Garnet A; at 6 kbar, the GARB thermometer predicts that this garnet was at or just above 600°C.

Full mineral analyses in Appendix Two.

**Sample LH 349 - garnet/ staurolite - andalusite grade
GARB thermometer (Ferry & Spear with Berman (1990))**



Line	Alm in Grt (%)	Point	Fe/(Fe+Mg) in biotite	Point
01	74.66	rimAv	0.64	rimAv
02	74.66	rimAv	0.63	M1
03	74.66	rimAv	0.63	M2

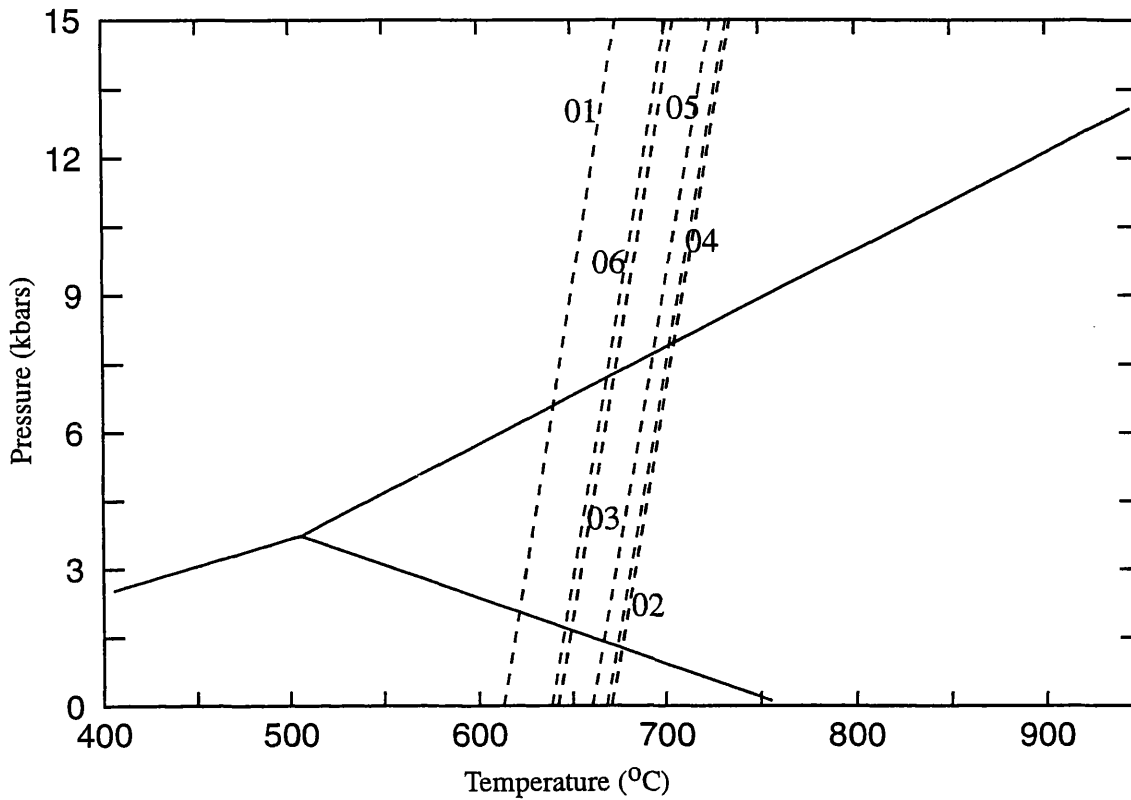
Figure 5.29

K_{eq} plot of data from sample LH349 - garnet/staurolite-andalusite grade.

The K_{eq} lines plotted using garnet compositions from the rim of the porphyroblast and compositions of biotite from the matrix yield uniform estimates of temperature. At 6 kbar, the results above suggest that this sample was at approximately 600°C.

Full mineral analyses in Appendix Two.

**Sample LH 154 - garnet/ staurolite - andalusite grade
GARB thermometer (Ferry & Spear with Berman (1990))**



Line	Alm in Grt (%)	Point	Fe/(Fe+Mg) in biotite	Point
01	71.08	grt07	0.54	154b1
02	71.08	grt07	0.57	154b6
03	70.21	grt09	0.54	154b2
04	70.21	grt09	0.56	154b5
05	71.28	grt01	0.57	154b3
06	71.28	grt01	0.54	154b1

Figure 5.30

K_{eq} plot of data from sample LH 154 - garnet/staurolite-andalusite grade. No significant variation of composition is observed across the diameter of the porphyroblast.

The locations of garnet compositions used in these calculations are from the intermediate area between the rim and the core of the porphyroblast. The biotite compositions used are from the matrix of the sample. There is some variability in the spread of K_{eq} line position: this appears to be due to variations in the composition of biotite: these variations may reflect true change of temperature during garnet growth, or some re-equilibration of Fe:Mg in biotite as a consequence of retrograde reactions.

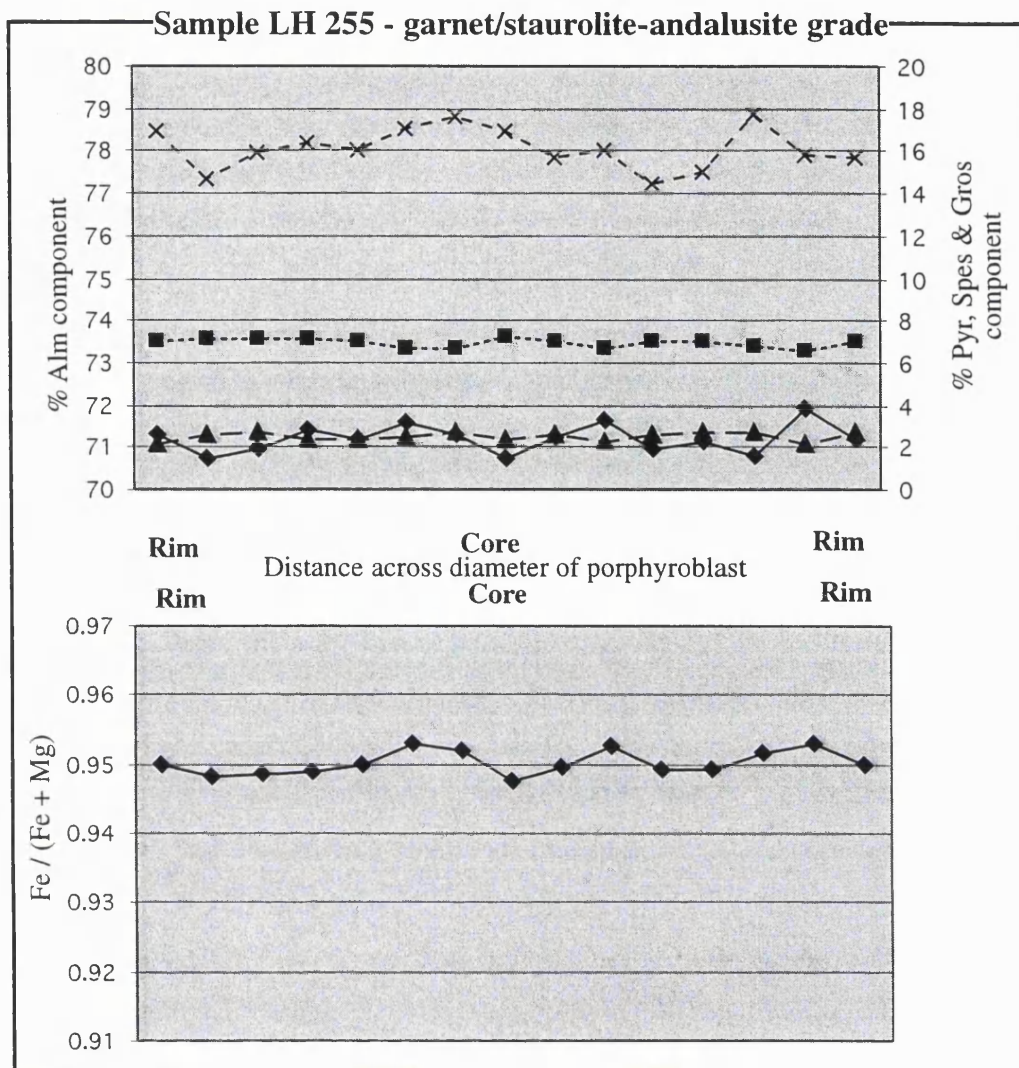
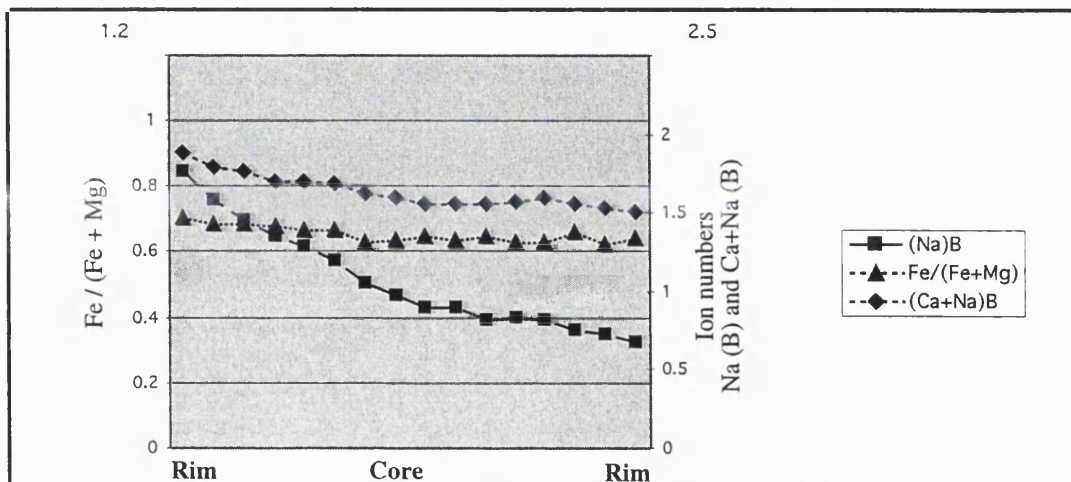


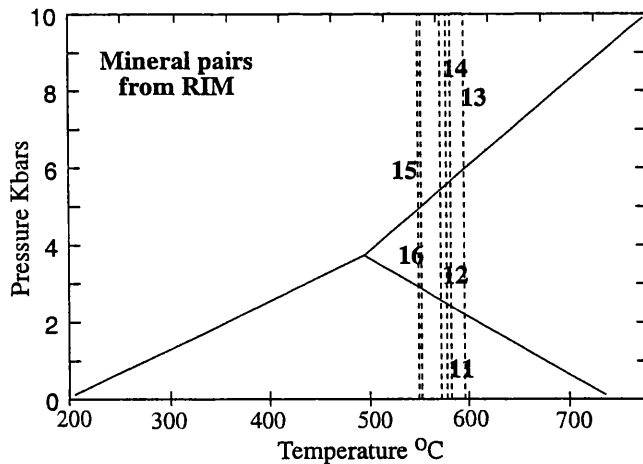
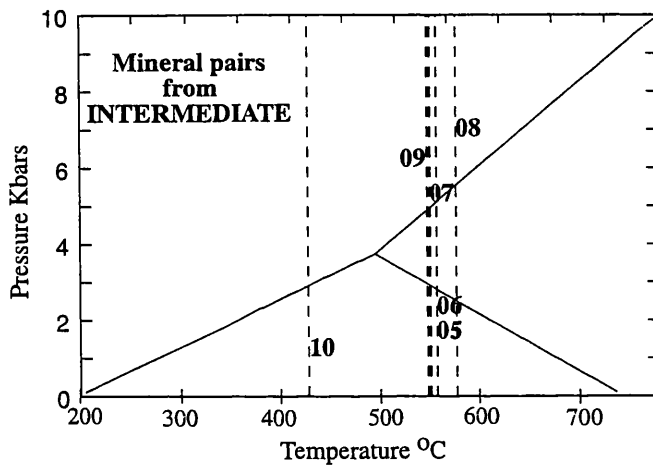
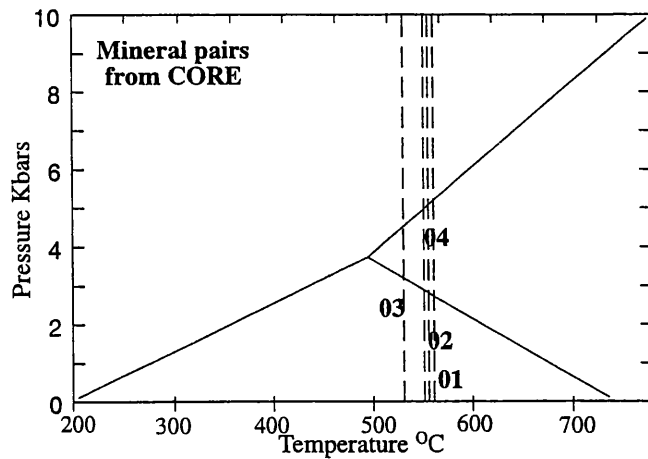
Figure 5.31a Above Composition variation across a garnet porphyroblast in sample LH 255.

Figure 5.31b Below Composition variation across an amphibole porphyroblast in sample LH 255.

- ◆ Almandine
- Pyrope
- ▲ Spessartine
- × Grossular
- ◆ Fe / (Fe + Mg)



**Sample LH 255 - Garnet-Hornblende thermometer
(Graham & Powell, 1984)**



GARNET

Line	% Alm	Point
01	71.65	grt10
02	71.42	grt04
03	71.29	grt07
04	70.74	grt08
05	70.96	grt11
06	70.96	grt11
07	71.28	grt09
08	71.28	grt09
09	71.18	grt05
10	71.56	grt06
11	71.15	grt12
12	70.81	grt13
13	71.91	grt14
14	70.95	grt03
15	70.75	grt02
16	71.29	grt01

AMPHIBOLE

Line	Fe/ (Fe+Mg)	Point
01	0.66	amp05
02	0.65	amp12
03	0.63	amp08
04	0.63	amp09
05	0.57	amp13
06	0.63	amp14
07	0.63	amp11
08	0.64	amp10
09	0.67	amp06
10	0.47	amp07
11	0.68	amp03
12	0.69	amp02
13	0.70	amp01
14	0.66	amp15
15	0.62	amp16
16	0.64	amp17

Figure 5.32 K_{eq} lines plotted for garnet - amphibole mineral pairs from sample LH 255, (Garnet/staurolite-andalusite grade), using the program of Spear (1991). Compositional data, given in tables to the right of the plots indicate that there is no significant compositional variation across the diameter of either the garnet or amphibole porphyroblast. The K_{eq} lines reflect this consistency: the results suggest that no variation of temperature occurred during the growth of the porphyroblasts. Full mineral analyses in Appendix Two.

**Kyanite-sillimanite grade rocks - estimate of P-T
after the end of garnet growth.**

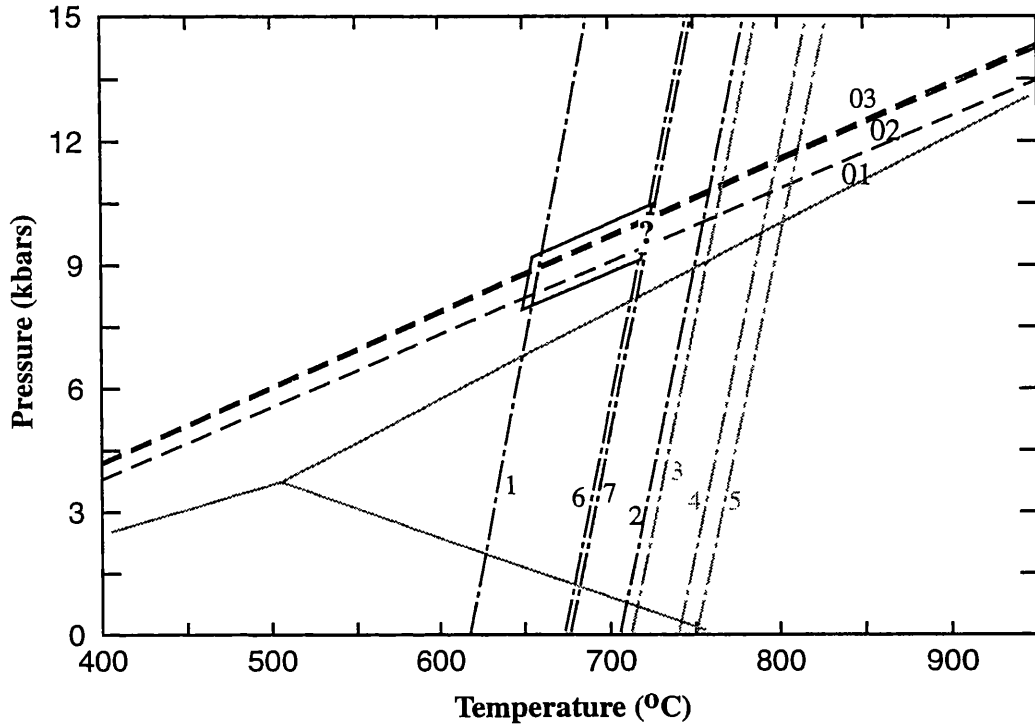


Figure 5.33 Estimate of pressure and temperature in the kyanite-sillimanite grade rocks at the end of garnet growth. Pressure constraint is from the application of the GASP barometer to sample LH17 (see **figure 5.9**) - calibration of Ganguly & Saxena (1984). Temperature constraint is from the application of the GARB thermometer (Ferry & Spear with Berman, 1990) to sample LH104; the K_{eq} lines plotted from the mineral pairs most likely to be in equilibrium are shown by black lines, with other values in grey (see **figure 5.17**).

This plot estimates that after the end of garnet growth, pressure conditions in the kyanite-sillimanite grade rocks were between 7.5 - 10.5 kbar, while the temperature lay in the range 650°C - 750°C. These conditions prevailed prior to the growth of sillimanite. Mineralogy in the rock suggests that temperature has not exceeded ~ 650°C; the results from the GARB barometer seem to be slightly high.

Kyanite-sillimanite-andalusite grade rocks - estimate of P-T after the end of garnet growth.

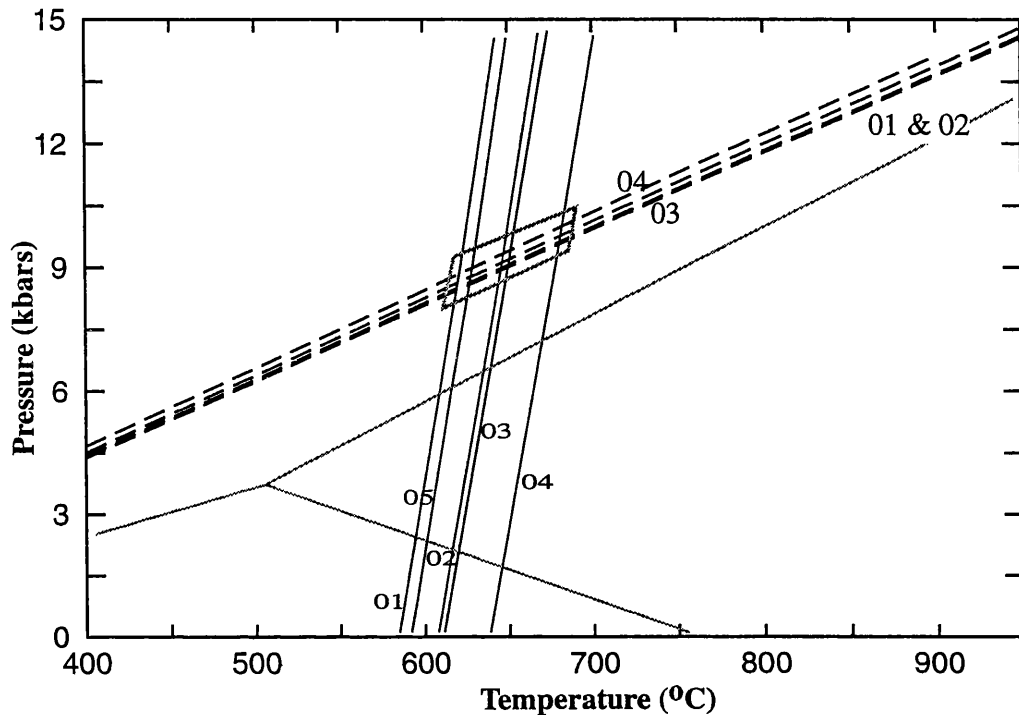


Figure 5.34 Estimate of pressure and temperature in the kyanite-sillimanite grade rocks at the end of garnet growth. Pressure constraint is from the application of the GASP barometer to sample LH28 (see figure 5.12) - calibration of Ganguly & Saxena (1984). Temperature constraint is from the application of the GARB thermometer (Ferry & Spear with Berman, 1990) to sample LH56 (see figure 5.18).

This plot estimates that after the end of garnet growth, pressure conditions in kyanite-sillimanite-andalusite grade rocks were between 7.5 - 9.5 kbar, while the temperature lay in the range 600°C - 700°C. These conditions prevailed prior to the growth of sillimanite.

Garnet / staurolite-andalusite grade rocks - estimate of P-T after the end of garnet growth.

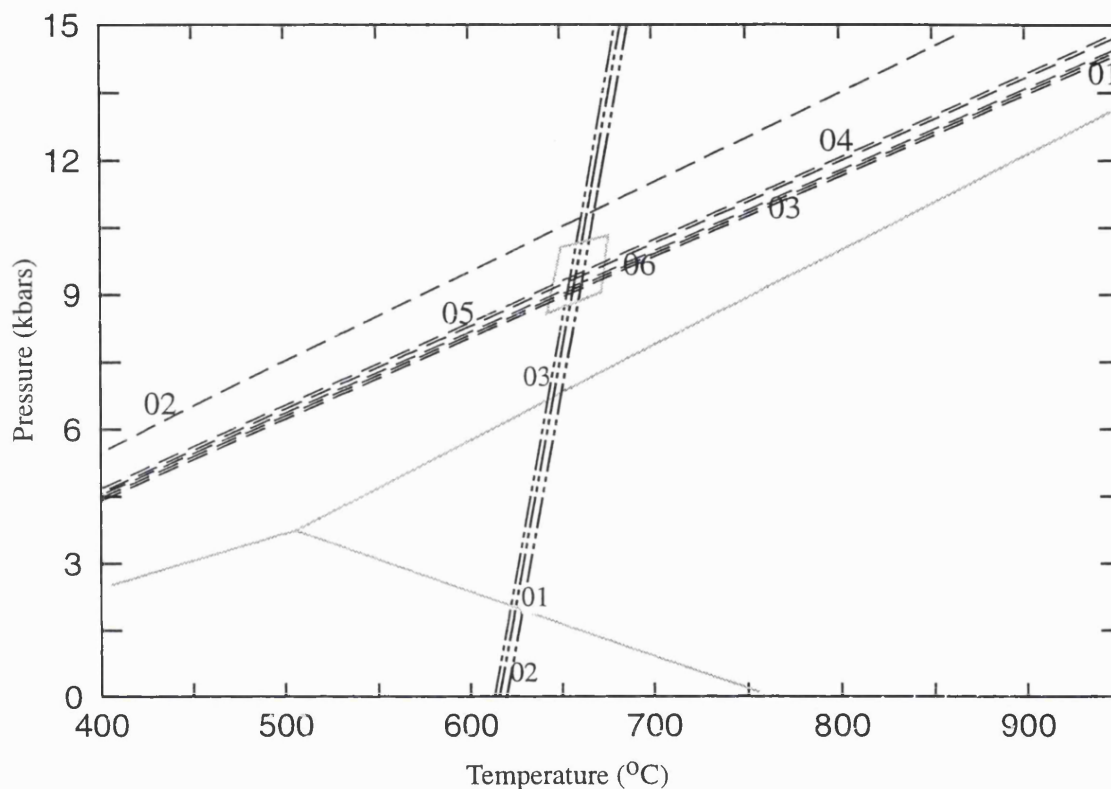
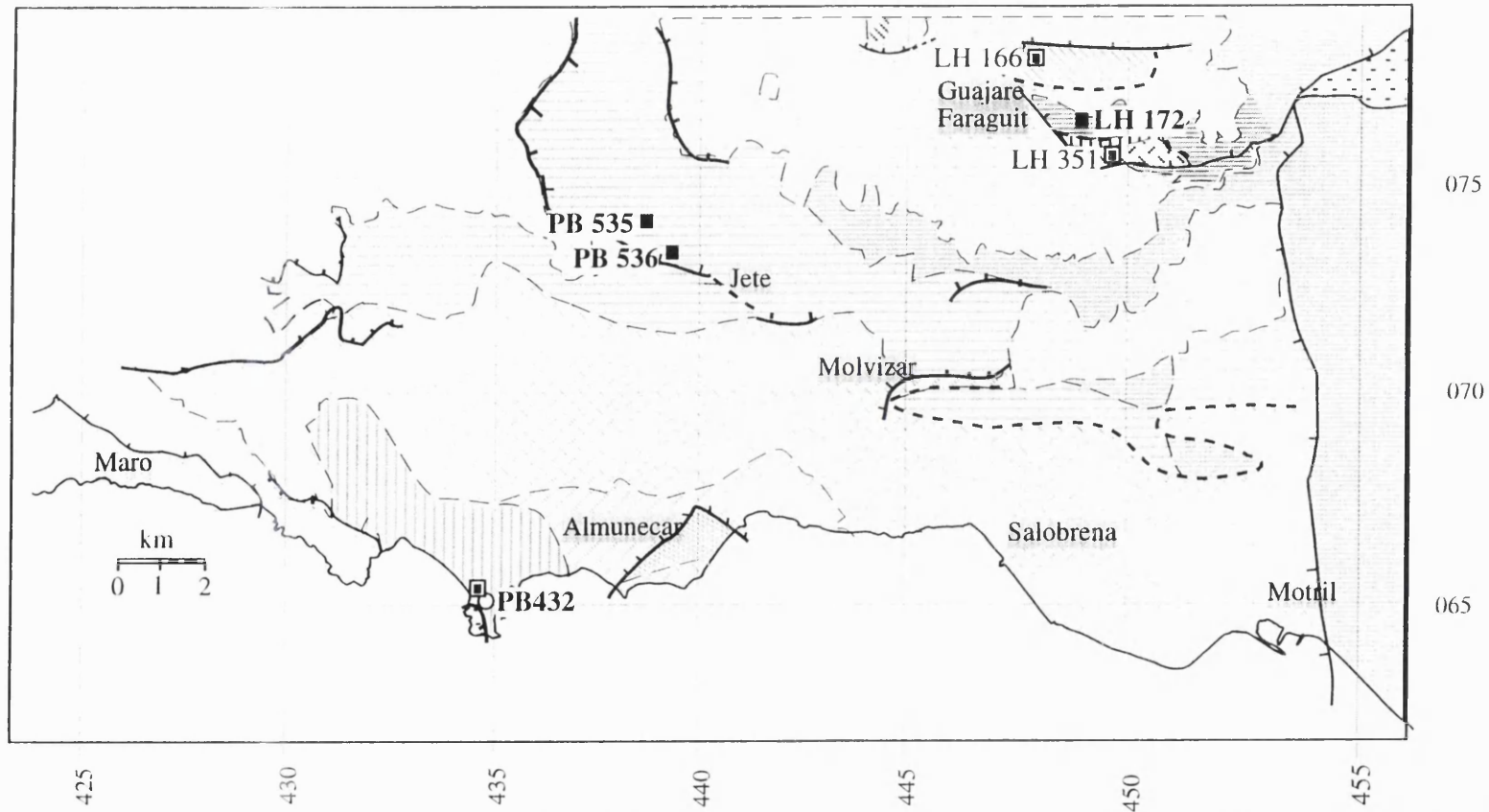

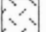

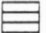

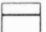



Figure 5.35 Estimate of pressure and temperature conditions in the garnet/staurolite-andalusite grade rocks at the end of garnet growth. Pressure constraint is from the application of the GASP barometer to sample LH 255 (see **figure 5.23**) - calibration of Ganguly & Saxena (1984). Temperature constraint is from the application of the GARB thermometer (Ferry & Spear with Berman, 1990) to sample LH349 (**figure 5.29**). The results from the application of the GARB thermometer to this sample are used in this plot as they provide a well-constrained estimate of temperature.

This plot estimates that after the end of garnet growth, the pressure in the garnet/staurolite-andalusite grade rocks was approximately 8.5 - 9 kbars, while the temperature was close to 650°C.



Metamorphic grades & tectonic contacts

	Sillimanite - andalusite (no kyanite)		Garnet / staurolite - andalusite
	Kyanite - sillimanite - andalusite		Muscovite - chlorite
	Kyanite - sillimanite (no andalusite)		Muscovite - biotite
	Carbonate rocks - no grade determined		

--- Fault developed after D_s and before D_t

— Fault developed after D_t deformation

Key to symbols for dating technique

- U-Pb (section 5.7)
- Ar-Ar on muscovite (section 5.8)
- ▣ Apatite fission track (section 5.9)

Figure 5.36 Metamorphic map of the area showing the locations of the samples to which geochronological techniques have been applied.

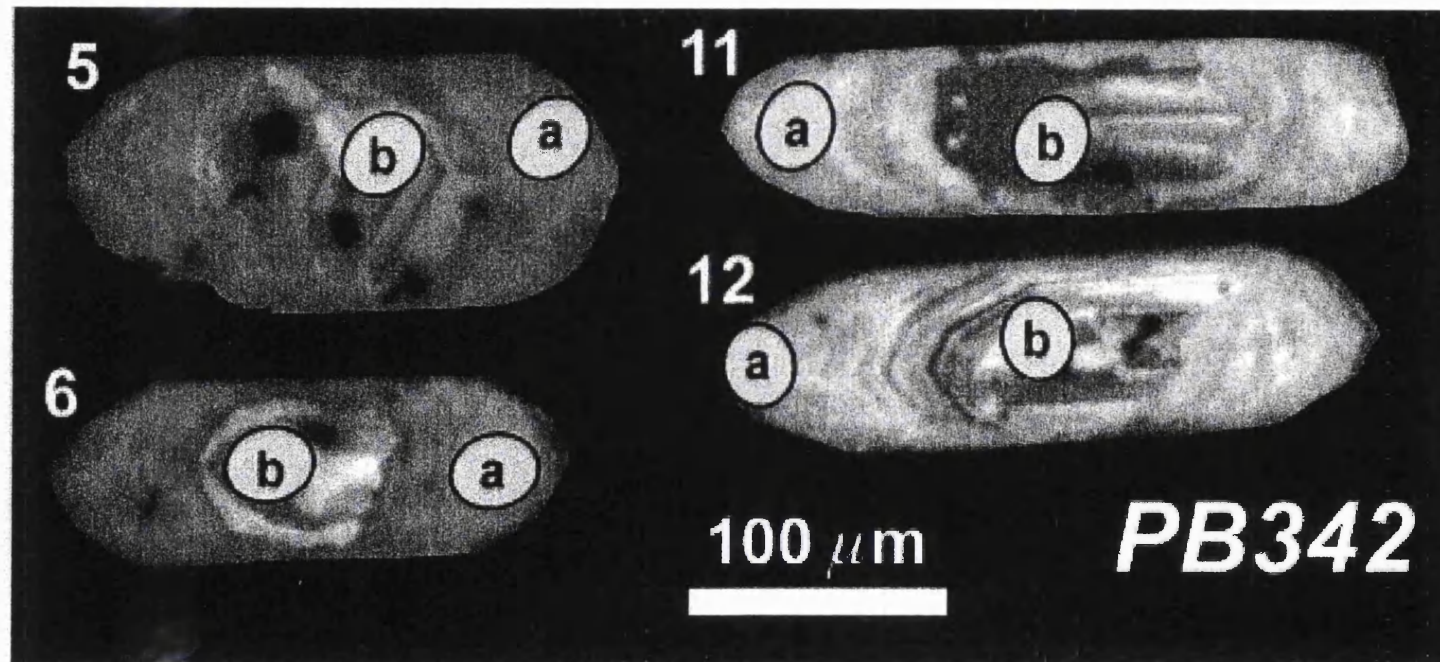


Figure 5.37

Images of zircon grains taken from sample PB342. The grains are typically idiomorphic prisms up to 200 micrometers in length, with well-defined oscillatory zoning in the core of the crystals indicating likely growth from an igneous fluid. Overgrowths of zircon that grew during metamorphism include these zoned cores; the metamorphic zircon typically shows patchy growth, although there is very local evidence of planar growth bands in crystals 6 and 12.

From Platt & Whitehouse (1999)

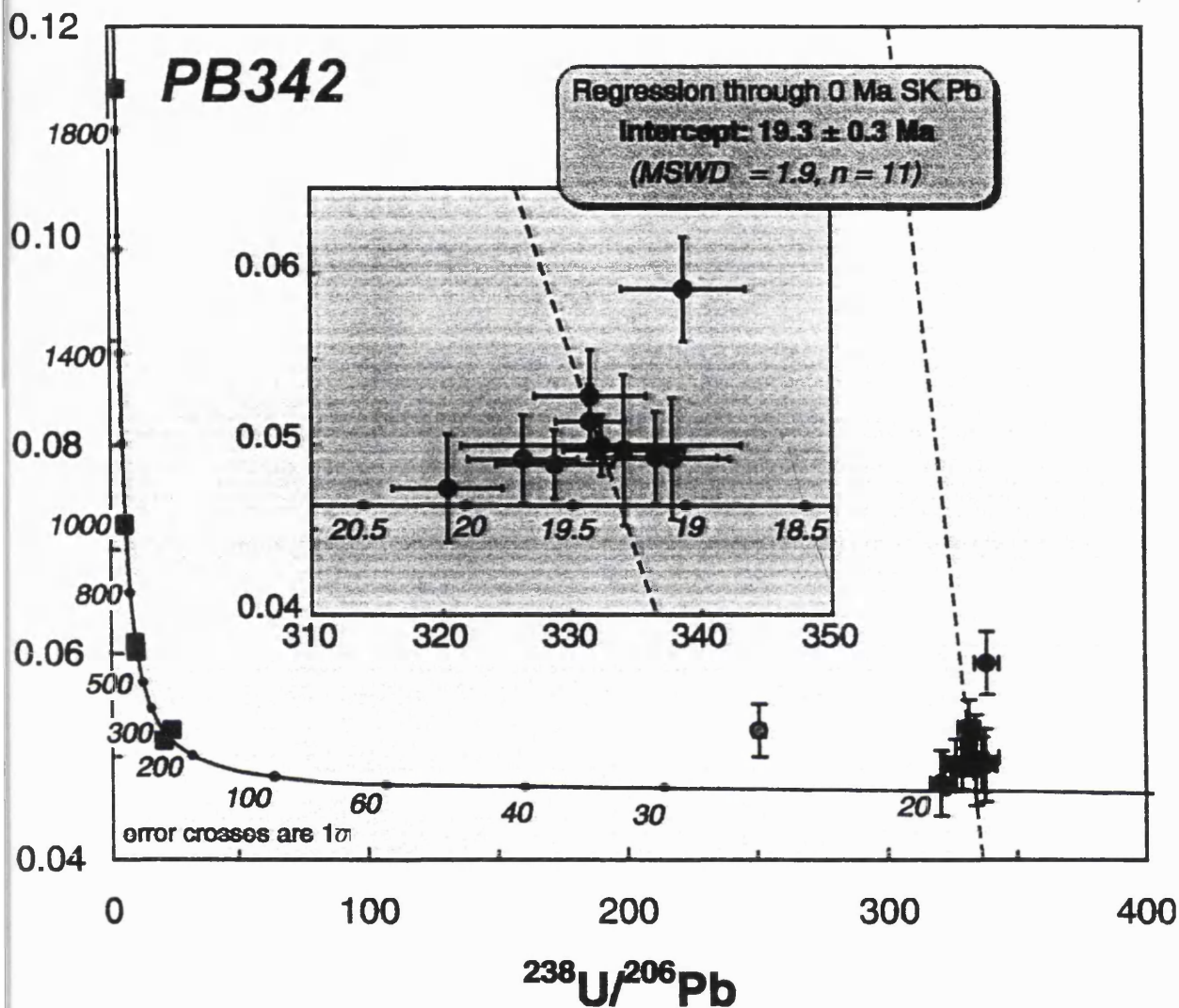


Figure 5.38

Concordia plot of all data from sample PB 342. Circles represent the outermost growth phase of the zircon, plotted uncorrected for common Pb. Shaded circles have been excluded from the regression. Squares represent analyses from the cores of the crystals are plotted as common Pb corrected data where appropriate.

The data from the cores of the crystals yield a range of concordant or near-concordant ages at ca. 300 Ma (Hercynian - 2 analyses), 600 Ma (2 analyses), 1000 Ma and 1800 Ma.

From Platt & Whitehouse (1999)

LH 166

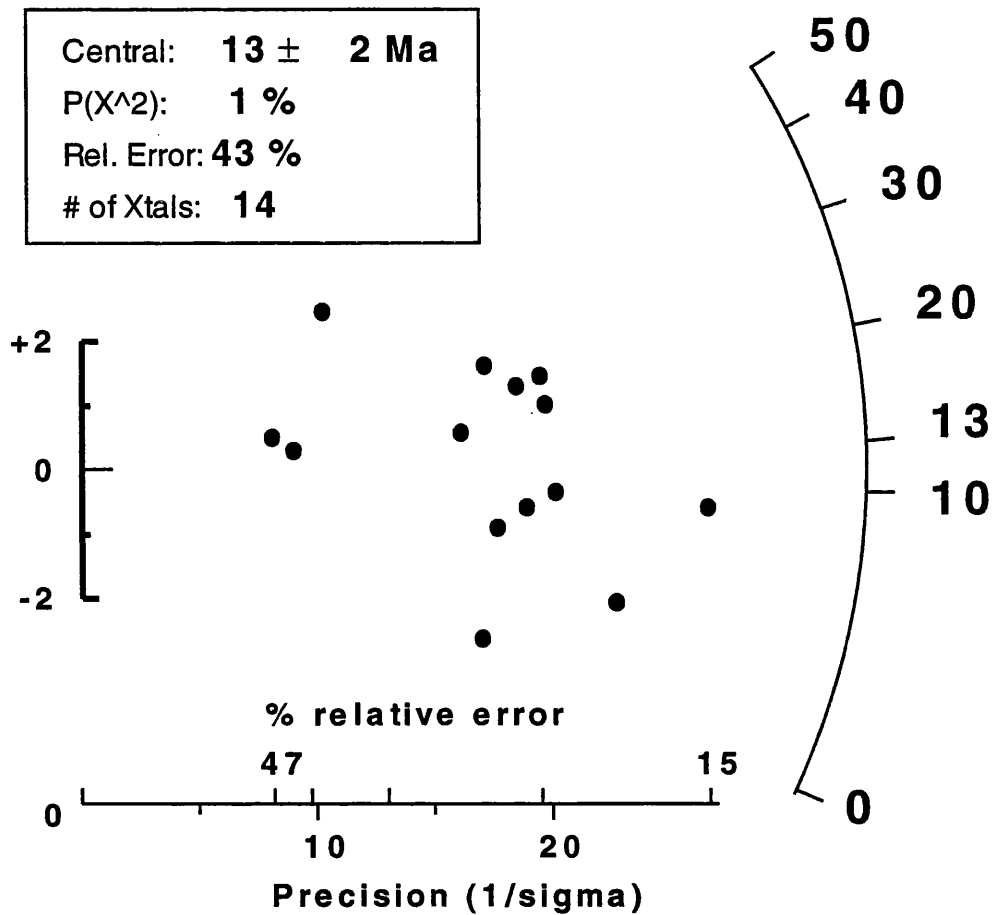


Figure 5.39

Radial plot of fission track data from sample LH166. Each point represents the data from a single apatite crystal. The location of each point indicates the precision (well-constrained data points plot close to the origin of the plot, on the left) and age (a line connecting the data point and the origin of the plot intersects the radial scale, on the right, at the age of the sample) of data from each crystal. (Galbraith, 1990)

In this plot, the distribution of points indicates that the dates from individual crystals appears diverse, but most ages are within error of each other. Thus, the central age (quoted on this diagram and in **table 5.3**) is suitably representative of this data set.

Plot constructed by Dr A Carter.

CHAPTER 6 CONCLUSIONS AND DISCUSSION

6.1 Summary of the structural evolution in the Alpujarride Complex

Pelitic schist and quartzite sequences around Almuñecar and Guajare Faraguit, 50 km south of Granada, contain disequilibrium mineral assemblages (many high grade rocks contain Ky + Sil + And + Grt + St) and two foliations of regional extent, S_s and S_t , that are readily identified at outcrop and in thin section.

6.1.1 Initial phase of contraction

In thin section the S_s foliation, that dips gently to the north or south, may locally be identified as a crenulation cleavage, alluding to the existence of an ' S_r ' foliation that has subsequently been almost entirely eradicated (**figure 2.2**). Tectonic contacts that juxtapose rocks of different types, and across which no variation of metamorphic grade occurs, are present in the area; these contacts formed prior to the high temperature metamorphism, probably as thrust contacts during D_r , which is postulated to be the episode of crustal thickening that occurred in the initial stages of orogenic development. A foliation S_r may be expected to have lain parallel or sub-parallel to the strike of the mountain chain (i.e. E-W / NE-SW), predisposing subsequent fabrics to adopt this orientation (**figure 3.14** and **figure 3.20**).

6.1.2 D_s – ductile deformation in an extending orogen

S_s is commonly the most dominant fabric identified at outcrop. The S_s foliation is sub-parallel to schist and quartzite layers and is cross cut by the S_t foliation at varying angles of obliquity (**figure 3.17**). Where the D_t phase of deformation is not strongly developed, lineations relating to the D_s deformation are seen to be refolded by the D_t fold axes (**figure 3.15**); the L_s lineation is a stretching lineation and is defined by sillimanite in the high-grade rocks that predominately parallel to the fold axes generated during the D_s and D_t phases of deformation. Elsewhere, the dominant lineation at outcrop is an intersection lineation of S_t with S_s (L_{st} - **figure 3.19**) that trends approximately NE-SW, except to the north of Motril (VF 54350675; **figure 3.37**). Areas of north and south vergence of the D_s folds form roughly east-west trending domains (**figure 3.13**). Stretching lineations and fold axes relating to the

D_s phase of deformation generated a strong anisotropy in the rocks; this is likely to have controlled the orientation of D_t structures.

Evidence that normal faulting occurred during and after the D_s deformation (section 3.5) indicates that the D_s deformation occurred in an extensional setting. This deduction is supported by various other lines of evidence, most significantly the evident down-pressure trajectory that was experienced during D_s which has been elucidated by microstructural studies (Chapter 4). Similar textures and paths through P-T space have been described within the Alpujarride Complex by other workers (i.e. Garcia-Casco *et al*, 1993; Sanchez-Gomez *et al*, 1998).

6.1.3 D_t – continued ductile deformation during decompression

Km-scale folds, generated during the D_t phase of deformation, cause significant modification of the earlier (pre-D_t) metamorphic sequence in the Alpujarride Complex near to Almuñecar (cross sections in **figures 3.2 – 3.10**). The S_t foliation is axial planar to these folds and clearly over-prints S_s (**figure 2.3**). Vergence of S_t with respect to S_s at outcrop scale permits identification of the D_t structures at regional scale. D_t folds cause inversion of the metamorphic sequence and pre-existing structures in the overturned limbs. Faults that developed during and after the D_s phase of deformation and juxtapose high and low grade rocks (section 3.5) generate an apparent superposition of high grade rocks structurally above low grade rocks where these faults crop out in the overturned limbs of D_t folds (**figure 3.9**). The configuration is associated with faults that have normal-sense displacement (i.e. were generated in response to extensional tectonics); in combination with micro-structural evidence, it is deduced that the D_t phase of deformation also occurred within an extensional regime.

Faults that formed after the end of metamorphism exhibit hanging wall movement to the north, with the exception of the Cerro Caleta and Cerro Escalate faults (**figure 3.1**). The hanging walls of these contacts move to the south and WNW, respectively and the configuration of rock-types near to the Cerro Caleta fault suggest that earlier normal movement occurred along this fault with hanging wall movement to the north. Syn -to-post

D₁ shear features in the low grade phyllite and quartzite sequence also indicate displacement to the north - **figure 3.40**.

6.2 Temperature and time constraints for deformation

6.2.1 Thermobarometry

Together, the data from mineral assemblages (**figures 5.3 & 5.4**) and thermobarometry (**figures 5.33 – 5.35**) provide well-constrained P-T paths for sillimanite and garnet-bearing assemblages during metamorphism (**figure 6.1**). This plot shows that the main metamorphic assemblages in rocks of all metamorphic grades formed during decompression. An increase of temperature of between 100-150°C during the D_s deformation is evidenced for the kyanite-sillimanite, kyanite, sillimanite-andalusite and garnet/staurolite-andalusite grade rocks; the sillimanite-andalusite grade rocks that crop out only locally (**figure 2.7**) apparently experienced isothermal decompression. Assuming that each deformation event D_s and D_t imposed a foliation (S_s / S_t) on the metamorphic stack simultaneously, the diachroneity of the temperature increase identified through the metamorphic pile may represent the passage of a thermal 'pulse' structurally upwards through the stack, prior to the onset of the D_t deformation.

6.2.2 Geochronology

Results from U-Pb, apatite fission track and Ar-Ar geochronology techniques are presented in **tables 5.2, 5.3** and **figure 5.38**, respectively. As discussed in section 5.9.4, the age obtained for the U-Pb technique in this case (19.3 ± 0.3 Ma) dates the crystallisation of zircon during metamorphism, and not the passage of the rock through the closure temperature of the U-Pb system (Platt & Whitehouse, 1999). Fraser *et al* (1997) suggest that the growth of zircon may occur as a consequence of the breakdown of garnet (a phase relatively rich in zirconium). This is likely to occur at conditions of peak temperature; for this sample, this is estimated to have been ~ 700°C, occurring after the end of the D_s deformation phase and prior to the onset of D_t (**figure 6.1**). The data from the U-Pb technique provides the maximum date at which the S_t foliation formed in the kyanite-sillimanite grade rocks.

A minimum age for the S_t foliation may be constrained by Ar-Ar data on muscovite; this technique has a closure temperature of 408°C for sample PB342 (section 5.8.3); it is evident from **figure 6.1** that temperatures in this range only prevailed after the end of the D_t deformation event. A sample of white mica from sample PB342 was dated at the Ar-Ar facility at OU by Prof. J Platt and yielded an age of 19.01 ± 0.66 Ma. The raw data from this analysis is collated in Appendix Three. Together with the U-Pb date obtained from this sample, the time period in which the S_t foliation formed may be constrained as 19.6 – 18.25 Ma. A minimum rate of cooling during the period 19.6 Ma and 18.25 Ma of 216°C km/m.y. has been calculated, using maximum and minimum possible dates for the U-Pb and Ar-Ar muscovite ages, respectively.

Cooling rates of the Alpujarride rocks during the low-temperature part of their history may be constrained using the data from Ar-Ar dates on muscovite and biotite from sample PB342 (Appendix Three; data collected by Prof J Platt) and fission track data on apatite (**table 5.3**). The closure temperature for the Ar-Ar system applied to muscovite for these samples has been calculated to be 408°C and the closure temperature of Ar-Ar in biotite has been estimated as 360°C (from equations of Dodson (1973) and diffusion parameters of Hames and Bowring (1994) - section 5.8.3). Apatite fission track data yields the date at which the samples passed through the 60°C isotherm (Gallagher *et al*, 1998).

Using data from samples PB342 (Ar-Ar on biotite) and PB342 (apatite fission track), a minimum cooling rate of 89°C / m.y. is obtained for the cooling rate of these rocks in the latter part of their exhumation trajectory. Using Ar-Ar on white mica from PB342 and the apatite fission track data from this sample yields an estimate of the minimum cooling rate of 95°C / m.y. Similar calculations using Ar-Ar and apatite fission track data from low-grade samples in this area (table 5.2 and table 5.3) yield a minimum cooling rate estimates in the low-temperature part of the exhumation of 49°C / m.y.

A summary of the structural and metamorphic evolution of the Alpujarride Complex in the area near to Almuñecar is shown in **figure 6.2**.

6.3 The scenario of deformation

Mechanisms proposed for the formation of folds in an extensional setting include: shearing of layers originally oblique to a shear plane (Malavielle, 1987); bulk vertical thinning from the shortening of steeply dipping layers (Froitzheim, 1992) and coupled extension and shortening occurring simultaneously or episodically during overall extension (Avigad *et al*, 2001). In the latter of these works, Avigad *et al* (2001) describe fibrous sillimanite crystallised in steeply inclined cleavage planes, axial planar to a metamorphic dome structure on the Greek island of Naxos. This area is widely accepted to have been affected by vertical thinning and horizontal NE-SW-directed stretching during the last 15-20 m.y.; the presence of sillimanite in cleavage planes indicates that shortening occurred at mid-crustal levels. Elsewhere, Avigad *et al* (2001) describe textures indicative of extension parallel to fold axes, including mineral stretching lineations and shear criteria.

It is envisaged that the structural fabrics identified in the Alpujarride Complex near to Almunecar, and the progressive metamorphic evolution during the development of these structural fabrics deduced from microstructural studies, may be accounted for in an extensional regime similar to that described by Avigad *et al* (2001).

That vertical shortening of the Internal Zones was occurring during the early Miocene is clearly established (this work; Monie *et al*, 1991; Platt *et al*, 1998) and palaeogeographic studies indicate that N-S / NW-SE convergence between the African and Eurasian plate was still operative (Dewey *et al*, 1989). These two sets of forces provide constraining boundaries on the structural evolution, which was accompanied by extension approximately along NE-SW (perhaps controlled by the anisotropy of the pre-existing foliations). Resolution of the force exerted by the NE-SW directed extension on to the constraining margins of Africa and Eurasia generates anticlockwise and clockwise rotations of the Betic and Rif belts, respectively (**figure 6.3**). The presence of opposing senses of palaeo-rotation in the Betic-Rif arc has been extensively documented (i.e. Platzman *et al*, 1993); it is proposed that the extension of the Internal Zones may have provided the driving force for this rotation, and have contributed to the generation of the present-day tightly arcuate geometry of the orogenic belt.

6.4 Consideration of scenarios for crustal evolution

This study has shown that the co-axial phases of deformation D_s and D_t that produced the S_s and S_t foliations occurred during decompression, and that the rocks of the Alpujarride Complex experienced an increase of temperature during their exhumation (figure 6.1). Conditions of moderate temperature (500-550°C) persisted to relatively low (3-4 kbar) pressures (this study; Comas *et al*, 1999; Platt *et al*, 1998; Soto & Platt, 1999).

Evocation of a model for crustal evolution on the scale of the orogen as a consequence of this study in a restricted area of the Betics, is undesirable but, considered together with geochronological and structural / mineralogical data from other studies, it is feasible to propose a model for the evolution of the Betic Cordillera that plausibly fits with the observed phenomena.

Data from geochronology studies provides an important constraint as to the evolution of the Betic-Rif orogen; the convergence of data from U-Pb, Ar-Ar and Fission Track techniques for samples widely distributed over the mountain belt to a range of 22.7 – 19.3 Ma (Platt *et al*, in press; Monie *et al*, 1991; 1994) tightly constrains the exhumation of the Internal Zones to the early Miocene. There is also evidence that denudation / erosion rates in the area were very high (Sosson *et al*, 1998). These data are supported by heavy mineral (Lonergan & Mange-Rajetzky, 1994) and micro-paleontology (Lonergan, 1993) and seem to preclude on temporal grounds, the possibility that the process of extension evidenced in the early Miocene during the opening of the Alboran Basin (Comas *et al*, 1999) was interrupted by an intervening period of compression (models proposed by Balanya *et al*, 1997; Azanon *et al*, 1994; Azanon & Crespo-Blanc, 2000). Furthermore, the evidence from metamorphic assemblages from rocks within the Internal Zones clearly demonstrate that exhumation occurred during conditions of continual decreasing pressure and that temperatures within these rocks remained elevated to above 400-450°C to low (3-4 kbar) pressures (this work; Garcia-Casco *et al*, 1993; Garcia-Casco & Torres-Roldan, 1996). In addition, the occurrence of a renewed phase of thrusting would be expected to cause heating of the rock-pile and the generation of mineral assemblages that had re-equilibrated at depths greater than those recorded earlier in the P-T evolution (i.e. prior to the episode of thrusting). No evidence of increased pressure late in the

structural evolution of these rocks is present, and this seems to further invalidate the proposal that a late phase of compressional tectonics has affected the rocks in the Alpujarride Complex.

Within the constraints imposed by the data outlined above, a plethora of possible mechanisms exist within which the present day configuration of the Betic-Rif arc in general, and the metamorphic-structural evolution of the Internal Zones in particular, may have evolved. Recent works have proposed that the orogen evolved as a consequence of subduction roll back (Lonergan & White, 1998) or as a consequence of lithospheric delamination (Platt *et al*, 1998). Modelling of the mechanical and thermal consequences of these competing hypotheses by Platt *et al* (1998) is suggestive that a process of lithospheric delamination most readily generates the observed features of textural and chemical disequilibrium preserved in rocks from the Internal Zones. However, it is conceivable that these textures could also be produced by the process of subduction zone roll-back or, perhaps, by a process that was intermediate between these two 'end-member' processes. A study of the volcanic rocks within the Betic Rif arc by Turner *et al* (1999) reveals that there is no linear trend of volcanic type within the arc, as would be expected if the evolution of the orogen had proceeded by a process of 'slab-detachment' (de Jong, 1991) yet consideration of the temporal evolution of the whole Mediterranean region is conducive to an explanation of subduction zone roll-back (Lonergan & White, 1998).

Although the precise nature of the crustal processes that led to the evolution of the Betic-Rif arc are difficult to ascertain at the orogen-wide scale, this work has helped to constrain and refine the regional scale metamorphic and structural processes that were operating coevally during the exhumation of the Alpujarride Complex.

6.5 Further work

A detailed structural and mineralogical study of the low grade rocks to the east of this area (Albuñol geological sheet; 20-44: IGME) would be permit further constraint of the timing and amount of movement that has occurred along the Escalate fault zone (**figure 3.1**). It may be possible to relate the km-scale folds described in this area to morphologically similar structures in low-grade rocks to the east, described by Orozco *et al* (1998)

Pilot samples for calcite-dolomite thermometry (e.g. Nesbit & Essene, 1982) were collected during this study, but appropriate samples (i.e. containing both calcite and dolomite) were not identified. Application of this technique to the carbonate bodies in this area, and comparison with established grades of metamorphism with adjacent schist, may permit the relative timing of movement along the brittle faults to be crudely estimated (i.e. whether movement occurred before, during or after the high temperature metamorphism). No reliable indication of the accuracy of the calcite-dolomite thermometer compared with thermometers applied to pelitic rocks is available; at the least, a study of carbonate bodies would enable regional-scale structures within carbonate to be identified. This could be coupled with the use of mineralogical techniques applicable to low-grade samples (i.e. measurements of d_{001} basal spacing in phengite, paragonite and chlorite; determinations of the illite crystallinity index) to determine the presence of structures in the phyllite and quartzite sequence.

The distribution of rock types and the occurrence of metamorphic grades have been considered as independent from one another in this study; the present-day arrangement of rock types is considered as arising from the structural evolution, during which varying conditions of metamorphism developed. This approach contrasts with that adopted on the geological sheets (e.g. IGME, Motril sheet; 19-44) and in the work of other authors (e.g. Azañon *et al*, 1994; Balanya *et al*, 1997). In these studies, the imposition of a metamorphic grade on a rock type in an area is characterised as belonging to a specific 'nappe' (IGME) or 'allocthonous tectonic unit' (Azañon *et al*, 1994) that are assumed to have regional significance. This approach to the classification of rock types within the Alpujarride Complex confuses the identification of metamorphic grade changes and large-scale structures across an area. Reconsideration of the 'nappe' units within the Alpujarride Complex, in terms of their component metamorphic grade and rock-types, may permit more coherent trends of structure and metamorphism to be identified in the Complex across the orogen.

Figure 6.1 P-T plots to show the conditions through which rocks in the Alpujarride Complex have passed during their structural evolution.

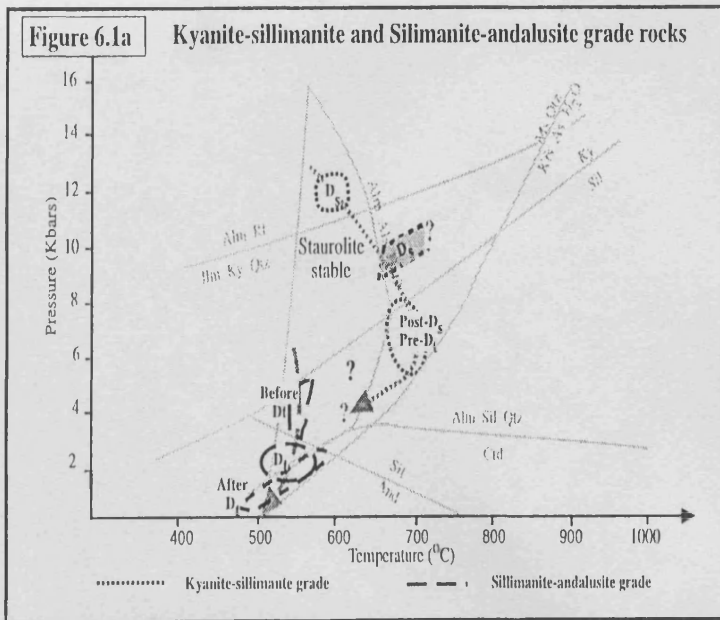


Figure 6.1a

Kyanite-sillimanite grade rocks. Conditions of P-T during the D_5 deformation estimated from the mineral assemblage (figure 4.4) and from thermobarometry (figure 5.33) vary. The presence of disequilibrium textures suggests that the estimations may illustrate the change of conditions during this event (i.e. that both estimations are valid). P-T conditions after D_5 and before D_1 are deduced from mineral relations (figure 4.6). An arrow that indicates an increase in temperature during decompression traces the most likely P-T evolution of these rocks, with peak temperatures prevailing after D_5 and before D_1 .

Sillimanite-andalusite grade rocks. No thermobarometric data is available for these rocks, but the mineral assemblages related to the S_5 and S_1 foliations (figure 4.18) constrains a path of almost isothermal decompression during D_5 and D_1 .

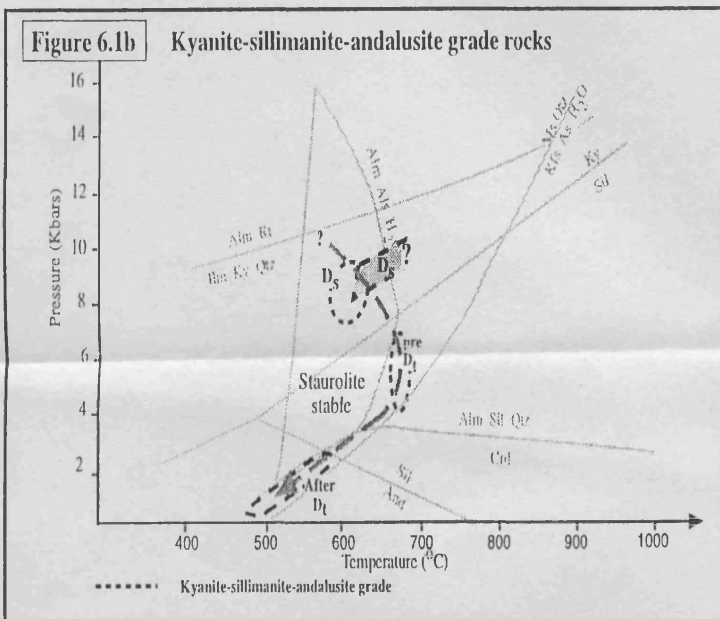


Figure 6.1b

Kyanite-sillimanite-andalusite grade rocks. Relations of S_5 and S_1 to mineral assemblages (figures 4.7, 4.11 and 4.16), combined with results from thermobarometry (figure 5.34) tightly constrain the trajectory in P-T space of these rocks. Maximum temperature (growth of sillimanite) is attained after D_5 and prior to D_1 , in the context of continued decompression.

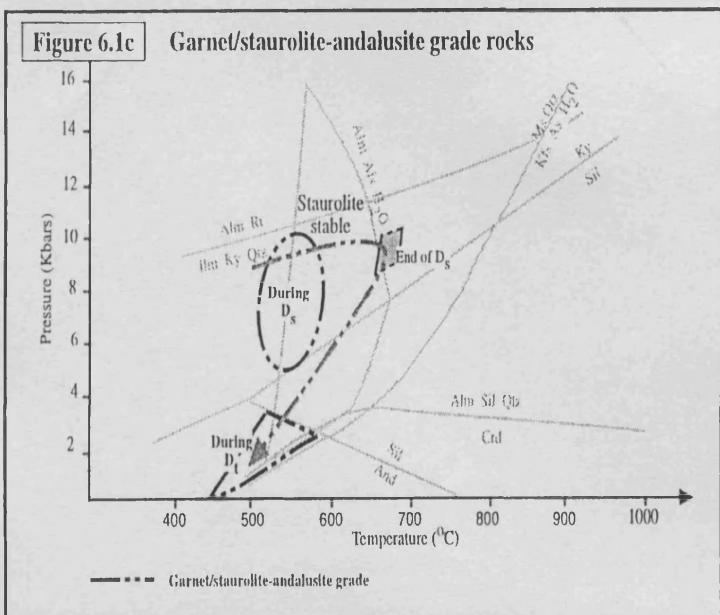
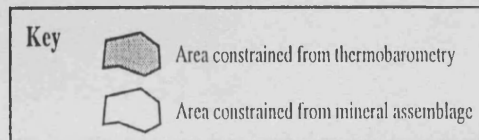


Figure 6.1c

Garnet/staurolite-andalusite grade rocks. A combination of results from mineral/foliation relationships (figures 4.23, 4.25 and 4.27) and the application of thermobarometry (figure 5.35) provide well-defined constraint for the P-T trajectory of these rocks during the structural evolution. Pressure in the early part of the path is poorly constrained, but it is evident that temperature increased during D_5 . Maximum temperature occurs at the end of the D_5 deformation, and is followed by cooling and decompression before and during the D_1 episode.



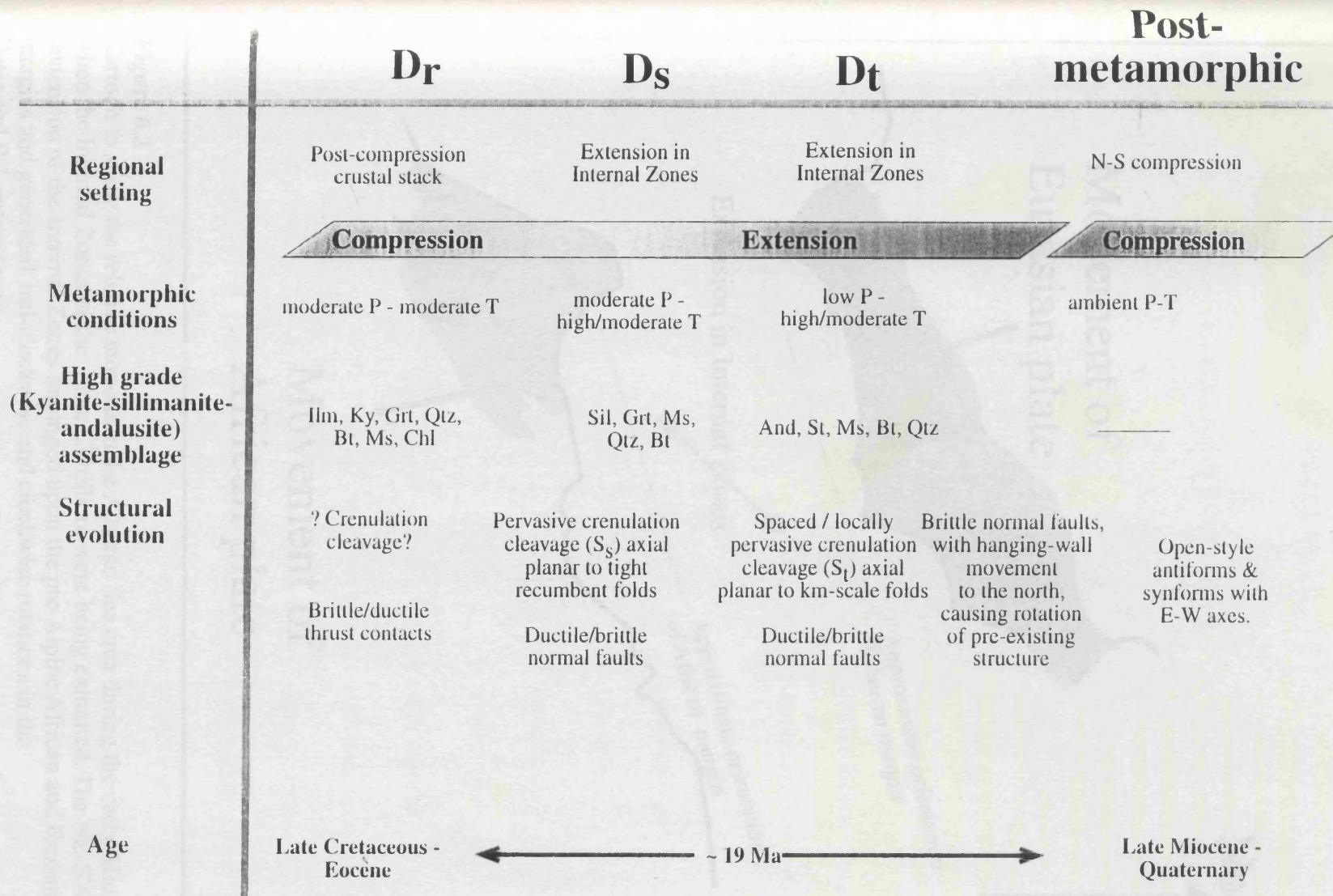


Figure 6.2 Summary sketch of the metamorphic and structural evolution of the Alpujarride Complex during the Alpine-age orogenic event. Mineral abbreviations are as in Appendix One.

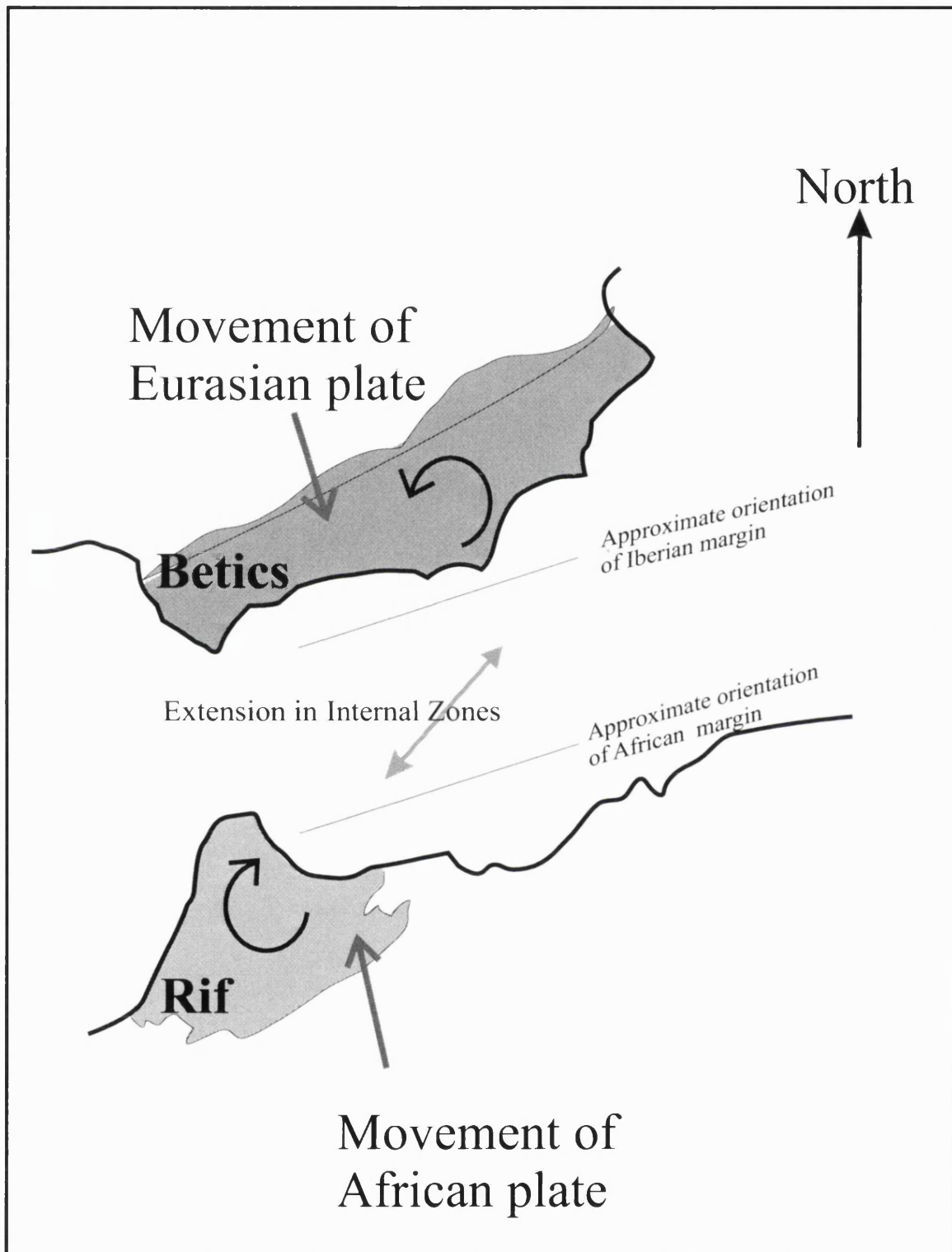


Figure 6.3
 Cartoon to show the relative motions in the Alboran Sea area during the early Miocene, when the Internal Zones of the Betic Cordillera were being exhumed. The NE-SW extension of the Internal Zones impinged upon the pre-Alpine African and Iberian margins and generated anti-clockwise and clockwise rotations in the Betic and Rif, respectively.

APPENDIX ONE MINERAL ABBREVIATIONS AND MINERAL ASSEMBLAGES

PART 1 MINERAL ABBREVIATIONS

Alm	almandine	Hbl	hornblende
Amp	amphibole	Ilm	ilmenite
And	andalusite	Kfs	K feldspar
Ann	annite	Ky	kyanite
An	anorthite	Mag	magnetite
Ap	apatite	Ms	muscovite
Cal	calcite	Or	orthoclase
Chl	chlorite	Pl	plagioclase
Cld	chloritoid	Pry	pyrope
Crd	cordierite	Qtz	quartz
Di	diopside	Rt	rutile
Dol	dolomite	Sil	sillimanite
Ep	epidote	Spn	sphene
Grt	garnet	Sps	spessartine
Gr	graphite	St	staurolite
Grs	grossularite	Tr	tremolite
Hem	hematite	Zr	zircon

From *Kretz, 1983*, with modifications

PART 2

MINERAL ASSEMBLAGES

SAMPLE	GRID REF.	MINERALOGY
1	43790666	Ms Ky Sil And St Bt Qtz Gr
8	43550659	Ms Ky Sil St Bt Qtz
10	43520659	Ms Ky Sil St Grt Bt Chl Qtz Ilm
11	43520659	Ms Ky Sil And Bt Cld Pl Amp Ep Qtz
12	43520658	Ms Ky Sil Bt Qtz Ilm
15	43490657	Ms Sil Bt Chl Pl Qtz Ilm
16	43490655	Ms Sil Bt Pl Qtz Ilm
17	43500655	Ms Sil Ky St Grt Bt Pl Qtz Ilm
18	43500655	Ms Ky Sil St Grt Bt Pl Qtz Ilm
19	43470652	Ms Ky Sil Bt Pl Qtz
23	43440652	Ms Sil Bt Chl Pl Qtz
28	43730665	Ms Ky Sil And St Grt Bt Chl Qtz
29	43710665	Ms Ky And St Grt Bt Pl Qtz
33	43880667	Ms Ky Sil St Grt Bt Qtz Gr
35	43330670	Ms Ky Sil Bt Chl Pl Qtz
37	43350676	Ms Ky Sil Bt Chl Qtz Ilm
43	43810652	Ms Ky St Bt Pl Qtz Ilm
44	43640657	Ms Ky And St Grt Bt Qtz Ilm
45	43980656	Ms St Grt Bt Chl Qtz Ilm
48	43980665	Ms Chl Pl Ep Qtz Ilm
52	43890670	Ms Ky Sil And St Grt Bt Pl Qtz
56	43860681	Ms Ky Sil And St Grt Bt Pl Qtz
58	43920697	Ms Ky St Grt Bt Qtz
59	43940704	Ms Ky St Grt Bt Chl Pl Qtz Ilm
61	44060721	Ms Grt Bt Chl Qtz Gr
62	44060729	Ms Ky Bt Pl Qtz Ilm
64	44070731	Ms St Bt Chl Qtz Ilm

66	44070733	Ms Chl Pl Qtz Ilm Cal/Dol
70	43720659	Ms Ky And Grt Bt Qtz Ilm
71	43720659	Ms Ky Sil St Bt Qtz
75	43650707	Ms Ky St Grt Bt Qtz Gr
80	43740659	Ms St Grt Bt Chl Qtz
90	43950655	Ms St Ep Act Bt Chl Qtz Ilm
92	43680656	Ms Ky Sil And Bt Qtz
95	43260666	Ms Ky Sil And Bt Pl Qtz
97	44460671	Ms And St Grt Bt Pl Qtz Gr
99	44320670	Ms Sil St Grt Bt Qtz Gr
102	44210677	Ms Sil Ky And St Grt Bt Qtz Ilm Gr
104	43490656	Ms Ky Sil St Grt Bt Qtz Ilm
105	43480953	Ms Sil Grt Bt Pl Qtz Ilm
107	43890678	Ms Ky And St Grt Bt Qtz Gr
108	43890679	Ms Ky And St Grt Bt Qtz Ilm
109	43900674	Ms Ky Sil Grt Bt Qtz Gr
110	44620669	Ms And St Grt Bt Qtz Gr
111	44000662	Ms Bt Chl Pl Qtz Ilm
114	44640678	Ms Bt Qtz Pl Grs
115	44690686	Ms Bt St Pl Qtz Ilm
117	44570713	Ms Bt Qtz Chl Pl Cal/Dol
118	44570713	Ms And Bt Pl Qtz Ilm Zr
119	43890670	Ms Ky Sil St Grt Bt Pl Qtz Ilm Gr
120	44310728	Ms Bt Pl Qtz Gr
121	44330723	Ms Bt Pl Qtz Ilm Zr
123	44210670	Ms Ky Sil And St Grt Bio Qtz Gr
124	44150672	Ms Ky Sil And St Grt Bt Qtz Ilm Gr
125	43520659	Ms Ky Sil St Grt Bt Pl Qtz
128	43490656	Ms Ky Sil Bt Pl Qtz Ilm
129	43510656	Ms Sil St Bt Pl Qtz Ilm
131	43250671	Ms Ky Sil St Bt Pl Qtz
132	43220667	Ms Bt Chl Pl Qtz Ilm

133	43220672	Ms Bt Chl Amp Ep Pl Qtz
134	43140680	Ms Ky Sil St Grt Bt Chl Pl Qtz
135	43310704	Ms Ky Bt Qtz Gr Hem
136	43310745	Ms Ky Bt Chl Qtz Ilm
138	43760691	Ms Ky St Grt And Bt Qtz Gr Ilm
139	43760691	Ms Ky St Grt Bt Qtz Gr
140	43560704	Ms St Grt And Bt Pl Qtz Ilm
142	43700699	Ms And St Grt Bt Chl Qtz Gr
143	43650712	Ms St Grt Bt Qtz Gr
144	43530706	Ms St Grt Bt Qtz Ilm Gr
145	43930698	Ms Ky St Grt Bt Qtz Gr
146	44060736	Ms Pl Ep Qtz Cal/Dol
147	44080736	Ms Cld Chl Qtz Ilm
148	44030740	Ms Chl Pl Qtz Cal/Dol
149	44020740	Ms Pl Chl Qtz Cal/Dol
150	??	Ms Chl Qtz Zr Cal/Dol
151	44620669	Ms And St Grt Bt Qtz Gr
152	44280731	Ms Bt Pl Qtz
153		Ms Bt And Pl Qtz
154	43940704	Ms Ky St Grt Bt Chl Qtz
155	43920702	Ms St Grt Bt Qtz Ilm
156	43740665	Ms Ky Sil And St Grt Bt Qtz Gr
157	43060679	Ms Bt Chl Pl Qtz Ilm
160	43890669	Ms Ky Sil And Grt Bt Pl Qtz Gr Ilm
161	44020714	Ms And St Bt Qtz Ilm Gr
162	43570655	Ms Ky Sil St Grt Bt Qtz
163	43520660	Ms Sil Bt Pl Qtz Ilm
165	43290668	Ms Ky Sil St Bt Pl Qtz Ilm Zr
166	44850716	Ms Sil And St Grt Bt Pl Qtz
168	44990756	Ms Ky Sil St Grt Bt Pl Qtz Gr
169	45060755	Ms And St Grt bio qz C
170	45090747	Ms Bt Chl Qtz Ilm

171	44930761	Ms And Bt Chl Qtz Mag
172	44930764	Ms And Bt Chl Qtz Ilm Zr
174	44920765	Ms Bt Chl Pl Qtz Mag Zr Spn
175	43520712	Ms And St Grt Bt Qtz Mag Gr
176	43410727	Ms Ky St Bt Qtz Ilm
184	43100726	Ms Pl Bt Qtz Ilm Mag
185	43150723	Ms Bt Pl Qtz Mag
186	43020677	Ms And Bt Pl Qtz Gr
187	43020677	Cal/Dol
188	42990688	Ms Ky Sil St Bt Qtz Ilm Mag Zr
189	43010683	Ms Bt Chl Amp Ep Qtz Mag Zr
190	43670717	Ms Ky And St Bt Qtz Gr Ilm
191	43680723	Ms Bt Ep Qtz Cal/Dol
192	44840767	Ms And Chl Pl Qtz
193	43510656	Ms Ky Sil St Grt Bt Pl Qtz Mag Zr
194	44520670	Ms And St Grt Bt Qtz Gr
195	44630701	Ms And St Grt Bt Qtz
196	45120669	Ms St Bt Ab Qtz Zr Gr
197	45120669	Ms And St Grt Bt Qtz Gr
198	45300679	Ms And Grt St Bt Chl Ab Qtz Gr
199	45370684	Ms Pl Bio Qtz Gr
200	45470701	Ms Chl Pl Qtz Mag Ilm
205	45060690	Ms And Bt Pl Qtz Mag Ilm
206	45500784	Ms Ep Pl Qtz Chl Zr Mag Cal/Dol
207	44950756	Ms Ky And Grt St Bt Ilm Gr
208	44870776	Ms Sil Grt St Pl Qtz Ilm Gr
210	44910768	Ms St Grt Bt Pl Qtz Ilm
218	46700719	Ms St Grt Bt Cld Ep Chl Mag Qtz
227	43490664	Ms Ky Bt Chl Pl Qtz Mag
228	43320677	Ms Ky St Pl Bt Chl Qtz Ilm
229	43310673	Ms Ky Sil And Bt Pl Qtz Mag
237	44020714	Ms Bt Pl Qtz Ilm Mag Gr Zr

238	44060721	Ms Chl Qtz Gr Zr
239	44060723	Ms St Grt Bt Qtz Ilm Mag Zr
240	43150670	Ms And Qtz Hem Mag
241	47330722	Ms Ky And St Grt Bt Qtz Gr
242	47330722	Ms Ky St Grt Bt Qtz Mag Gr
243	43960710	Ms Bt Ep Cld Chl Pl Pl Qtz Mag Ilm
245	44050737	Ms Chl Qtz Gr Cal/Dol
246	44020714	Ms Bt Chl Ep Cld Qtz Mag Ilm
247	44070733	Ms Chl Pl Qtz Ilm Mag
248	43870761	Ms Chl Qtz Mag
249	43830753	Ms Qtz Cal/Dol
250	43830755	Ms Chl Qtz Mag
251	43280665	Ms Sil Bt Qtz Pl Ilm Mag
252	43060680	Ms Bt Chl Pl Qtz Ilm Gr
253	43020676	Ms Pl Qtz Mag Gr
254	42820676	Ms Grt Bt Ab Chl Qtz Ilm Cal/Dol
255	42880675	Ms Grt Amp Bt Chl Pl Qtz Cal/Dol
256	42900678	Ms Pl Bt Chl Qtz Ilm
257	42910675	Ms Ep Pl Chl Qtz Ilm
258	42910675	Ms Bt Chl Pl Amp Qtz Ep Ilm Mag
260	42820698	Ms Sil And St Grt Bt Pl Qtz
261	42820698	Ms Ky St Grt Bt Qtz
262	43470643	Cal/Dol
263	43500655	Ms Cld Amp Pl Qtz Zr
264	44480789	Ms Amp Ep Chl Pl Cal/Dol Qtz
265	42650684	Ms And Grt Bt Chl Qtz
266	44360783	Cal/Dol
267	44420778	Ms Pl Chl Qtz Mag
268	43920697	Qtz Zr
269	43700758	Zr
270	44050736	Zr
271	43890670	Ms Qtz Zr

272	43570655	Ms Ky Sil St Grt Bt Pl Qtz Mag
273	43260666	Ms Ky Sil And Bio Pl Qtz
277	42860674	Ms Bt Grt Amp Qtz
278	42720680	Amp Bt Pl Ep Qtz
279	42720680	Ms Bt Grt And Qtz Gr
280	42710681	Ms Bt Grt St And Pl Qtz Gr
281	43270627	Ms Bt Chl Qtz Mag
283	43340669	Act Amp Qtz Pl Spn Zr
284	43720665	Ms Sil Ky Grt St Bt Qtz Ilm
287	44050669	Ms Bt Sil Ky St Grt Qtz Gr
288	44600671	Ms Bt Grt St Qtz Gr
289	44290676	Ms Ky St And Grt Bt Qtz Mag Gr
290	44170681	Ms Sil Grt St Bt Gr
291	44020669	Ms Bt Pl Chl Qtz
292	44020669	Ms Bt Tr-Act Ep Pl Qtz
293	43570669	Ms Ky St Grt Bt Chl Qtz Pl
294	44190678	Ms Sil Ky And Grt Bt St Pl Qtz Gr
295	44590672	Ms And Grt Bt Ep Mag Qtz
298	45730747	Ms Chl Pl Qtz Mag Ilm
299	44950774	Ms Sil Grt St And Bt Pl Qtz Ilm Mag
300	44480789	Ms Sil Grt St Bt Qtz
302	43920697	Ms Ky St Grt Bt Ab Qtz
303	44860776	Ms Sil And St Grt Bt Pl Qtz Gr Mag
304	44920764	Cal/Dol
305	44930762	Ms And Bt Chl Pl Qtz
307	45220743	Ms Ep Qtz Cal Ilm
309	43860684	Ms Ky Sil And Grt St Bt Pl Qtz Ilm
310	43710666	Ms Sil Ky Grt St Bt Ilm Mag Qtz
311	43720665	Ms Ky Grt St Chl Bt Pl Qtz
312	43730665	Ms Sil Ky And Grt St Ab Bt
314	44740713	Ms Chl Ep An Qtz Ilm
315	44560714	Ms Bt Pl Qtz Gr

316	43670706	Ms Ky Grt St Bt Pl Qtz Ilm
318	45130745	Ms Qtz
319	45080751	Ms And Bt Pl Pl Qtz
320	45070752	Ms Sil And Grt Bt Qtz
321	45060756	Ms And Grt St Bt Ab Qtz
322	45010755	Ms Sil Ky Grt St Bt Pl Qtz Gr
323	44940756	Ms And Ep Bt Mag Qtz
324	44940757	Ms Sil St Ky Grt Qtz
325	42890675	Ms Ilm Qtz Pl Chl
326	42890675	MS GRT ACT BT AB QTZ
328	43260666	Ms Sil Ky Bt Qtz
329	44040671	Ms Sil And Grt St Bt Ab Qtz Gr Mag
330	44850776	Ms Sil And Grt St Pl Qtz
333	44030779	Ms Qtz Cal/Dol
335	44170775	Ms Sil And Grt St Bt Pl Qtz Gr
336	42890675	Ms, grt, bio, pl qz MAG
337	44200678	Ms Ky Sil And Grt St Bt Pl Qtz Gr Mag
339	43880680	Ms Ky Sil And Grt St Bt Ab Qtz Gr
340	43970710	Ms Chl Ep Pl Qtz
341	44050720	Ms And Bt Qtz Gr
342	44060731	Ms Pl Qtz
343	44060731	Ms Cal/Dol Qtz
344	44040740	Ms Cal Qtz Gr Mag
345	45290670	Ms And St Grt Bt Qtz
346	45270682	Ms And Ep Pl Qtz
347	45390687	Ms Grt Bt St Qtz Gr
348	45410686	Ms Chl Qtz Cal Ilm
349	45380691	Ms Grt Bt Qtz Gr
350	43520712	Ms Grt St Qtz Gr
351	43500715	Ms Grt St Bt Ab Pl Qtz
351/5	44630678	Ms Sil And Grt St Bt Pl Qtz
352	44460789	Ms Sil Ky And Bt Qtz

353	44870770	Ms Sil And Grt St Bt Ab Qtz
354	44590698	Ms And Bt Qtz Ilm Mag
355	44630703	Ms Sil And Grt Bt Ab Qtz Ilm Mag

APPENDIX TWO - PROBE DATA

Part One – Apparatus and technique

Major elemental and mineral analyses were obtained using a Jeol 733 Superprobe, with Oxford Instruments ISIS energy dispersive system. This facility is based at the Research School of UCL and Birkbeck College, and is supervised by Dr A. Beard.

Data was collected at ~ 15 kV for 100 seconds time count with a 2 µm beam/spot diameter. These results were corrected using a SEMQuant (ZAF4) program. The microprobe was calibrated using Specpure® cobalt metal (99.999 % Co) and profile standardisation material including natural and synthetic silicates and oxides (In table A2-01 below).

Table A2-01 - Major element compositions of electron microprobe standard silicates, oxides and metals used for analyses in this study.

Standard Ref.	Olivine UCOL1	Olivine UCOL2	Wollastonite BKWOLL	Orthoclase UCORTH	Jadeite BKJAD	Apatite UCAPA
wt % oxide						
SiO ₂	41.54	35.04	51.51	64.26	59.40	0
TiO ₂	0	0	0	0	0	0
Al ₂ O ₃	0	0	0.02	19.19	25.10	0
FeO	6.78	40.35	0.42	0.09	0.15	0
MnO	0	0.48	0.12	0	0	0
NiO	0.38	0.18	0	0	0	0
MgO	51.03	23.70	0.10	0.10	0.10	0
CaO	0	0.07	47.77	0.11	0.06	56.35
Na ₂ O	0	0	0	0.92	15.10	0
K ₂ O	0	0	0	15.30	0	0
P ₂ O ₅	0	0	0	0	0	43.31
Total	99.73	99.82	99.94	99.99	99.91	99.88

Thin sections for probe analysis were prepared by Mr Sean Houlding, then polished and carbon coated using facilities at Birkbeck College, under the supervision of Dr A Beard.

Part Two – Garnet Compositions

Samples LH17,28 & LH61

	17rim	28rim	61rimA	61rimB
SiO ₂	37.91	37.98	37.04	37.08
TiO ₂	0.14	0.19	0.00	0.09
Al ₂ O ₃	20.77	20.88	20.42	20.56
Fe ₂ O ₃	0.00	0.00	0.00	0.00
FeO	33.23	32.40	35.10	33.83
MnO	0.75	0.88	0.79	0.85
MgO	2.59	2.53	2.22	2.34
CaO	4.61	5.14	3.71	4.58
Sum:	100.00	100.00	99.29	99.33

Sample LH104

	g01-1	g01-2	g02-1	g02-2	g02-3	g03-1	g03-4
SiO ₂	36.68	36.11	36.42	36.89	36.47	36.58	36.74
TiO ₂	0.08	0.10	0.15	0.00	0.04	0.00	0.11
Al ₂ O ₃	20.58	20.89	20.72	20.82	20.75	20.94	20.99
Fe ₂ O ₃	0.00	0.00	0.00	0.00	0.00	0.00	0.00
FeO	38.04	37.85	37.10	36.62	37.09	37.22	37.38
MnO	1.74	1.06	2.15	2.27	2.33	1.37	1.20
MgO	1.86	2.33	1.98	1.79	1.82	2.29	2.22
CaO	1.01	1.66	1.49	1.56	1.51	1.48	1.40
Na ₂ O	0.00	0.00	0.00	0.00	0.00	0.00	0.00
Sum:	99.99	100.00	100.01	99.95	100.01	99.88	100.04

Samples LH 125 & LH134

	125rim	4a	4c	6d	6e
SiO ₂	38.05	36.65	36.67	36.61	35.50
TiO ₂	0.07	0.00	0.06	0.14	0.09
Al ₂ O ₃	21.20	20.34	20.72	20.60	20.13
Fe ₂ O ₃	0.00	0.00	0.00	0.00	0.00
FeO	33.26	34.43	31.52	30.89	30.09
MnO	0.92	0.98	0.98	1.91	1.67
MgO	2.08	2.47	1.66	1.56	1.42
CaO	4.42	3.24	5.78	5.49	6.13
Na ₂ O		0.00	0.00	0.60	0.58
Sum:	100.00	98.11	97.39	97.80	95.61

Sample LH 138

	grt01A	grt02A	grt03A	grt04B	grt05B	grt06-A	grt06-B	grt06-C
SiO ₂	37.27	37.46	37.67	37.65	37.17	36.39	36.12	36.41
TiO ₂	0.29	0.42	0.07	0.27	0.49	0.46	0.39	0.28
Al ₂ O ₃	21.34	21.19	21.25	21.48	21.16	20.64	20.58	20.61
Fe ₂ O ₃	0.00	0.00	0.00	0.00	0.00	0.00	0.00	0.00
FeO	35.34	35.65	35.18	35.44	34.69	34.45	34.76	34.47
MnO	1.05	1.21	1.04	1.24	1.39	0.81	0.81	0.70
MgO	2.65	2.57	2.51	2.20	2.18	2.43	2.49	2.33
CaO	3.08	2.85	3.23	3.32	3.74	3.18	2.76	3.36
Sum:	101.02	101.35	100.95	101.60	100.82	98.36	97.91	98.16

Sample LH154

	grt07	Grt09	grt01
SiO2	36.62	36.77	36.67
TiO2	0.20	0.11	0.14
Al2O3	20.96	21.03	21.24
Fe2O3	0.00	0.00	0.00
FeO	32.31	31.83	31.27
MnO	1.44	1.39	1.20
MgO	2.59	2.66	2.83
CaO	5.19	5.45	4.95
Sum:	99.31	99.24	98.30

Sample LH255

	3rim	1rim	2rim
SiO2	36.41	36.86	36.66
TiO2	0.03	0.02	0.07
Al2O3	20.67	20.74	20.67
FeO	33.58	32.00	32.68
MnO	0.99	1.02	1.06
MgO	1.69	1.57	1.61
CaO	76.30	7.07	6.71
Sum:	99.67	99.28	99.46

Sample LH 311

	grt05	grt07	grt08	grt09	grt11	grt13	grt15	grt16	grt17	grt18	grt19
SiO2	36.62	36.62	36.45	36.27	36.14	36.43	36.27	36.24	35.81	36.58	36.37
TiO2	0.24	0.32	0.33	0.64	0.40	0.31	0.29	0.35	0.47	0.21	0.45
Al2O3	20.26	20.39	20.24	20.15	20.09	20.20	19.98	20.27	19.68	20.27	20.17
Fe2O3	0.00	0.00	0.00	0.00	0.00	0.00	0.00	0.00	0.00	0.00	0.00
FeO	31.13	31.32	30.89	30.59	30.54	30.56	30.90	30.74	30.84	30.72	30.72
MnO	1.39	1.46	1.43	1.86	1.93	0.96	1.62	1.61	1.45	0.85	0.78
MgO	2.59	2.58	2.54	2.33	2.44	2.89	2.47	2.50	2.40	3.17	3.37
CaO	4.54	4.85	4.89	4.87	4.80	4.87	4.65	4.86	4.77	4.71	4.73
Sum:	96.77	97.54	96.77	6.71	96.42	96.22	96.18	96.57	95.42	96.51	96.59

Sample LH 349

	rimav
SiO2	36.88
TiO2	0.00
Al2O3	20.42
Fe2O3	0.00
FeO	33.64
MnO	5.80
MgO	2.24
CaO	1.03
Na2O	0.00
Sum:	100.00

Part Two – Biotite compositions

Sample 56

	B01	B03	B04	B05
SiO ₂	27.44	31.03	28.57	32.45
TiO ₂	0.32	0.33	0.32	0.42
Al ₂ O ₃	20.55	19.72	19.12	19.64
Fe ₂ O ₃	0.00	0.00	0.00	0.00
FeO	28.27	21.94	24.40	20.12
MnO	0.16	0.03	0.16	0.01
MgO	6.45	7.63	7.78	7.88
CaO	0.21	0.14	0.20	0.18
Na ₂ O	0.83	0.90	0.88	0.99
K ₂ O	2.57	5.75	4.47	7.79
Sum:	86.80	87.47	85.90	89.48

Sample LH 61

	6lrimA	6lrimB	6lmatr1	6lmatr2	6lmatr3
SiO ₂	37.15	38.24	7.14	37.10	37.59
TiO ₂	2.01	1.43	1.98	2.00	2.18
Al ₂ O ₃	21.64	21.96	20.67	20.62	20.68
Fe ₂ O ₃	0.00	0.00	0.00	0.00	0.00
FeO	21.50	21.35	22.63	22.61	21.87
MnO	0.00	0.03	0.01	0.00	0.01
MgO	9.36	8.85	9.28	8.74	8.65
CaO	0.39	0.37	0.24	0.17	0.24
Na ₂ O	0.88	0.81	0.94	0.88	0.81
Sum:	92.93	93.04	92.90	92.13	92.02

Sample LH104

	b011	b014	b021	b023	b024	b031	b032
SiO2	34.98	35.46	35.79	35.31	35.67	35.28	35.66
TiO2	3.49	3.36	2.96	3.24	3.03	3.39	3.35
Al2O3	21.45	21.76	21.43	21.92	21.50	21.51	21.31
Fe2O3	0.00	0.00	0.00	0.00	0.00	0.00	0.00
FeO	23.74	22.51	24.75	25.04	24.61	23.18	23.56
MnO	0.30	0.00	0.14	0.13	0.00	0.01	0.13
MgO	6.02	6.44	4.65	4.67	5.46	6.39	6.18
CaO	0.31	0.33	0.04	0.00	0.13	0.23	0.24
Na2O	0.00	0.00	0.00	0.00	0.00	0.00	0.00
K2O	9.70	10.15	10.25	9.78	9.60	10.00	9.57
Sum:	99.99	100.01	100.01	100.09	100.00	99.99	100.00

Sample LH154

	154b1	154b2	154b3	154b4	154b5	154b6
SiO2	37.78	38.68	37.80	37.40	37.53	37.91
TiO2	2.96	2.74	3.07	3.39	2.87	3.23
Al2O3	20.58	21.27	20.66	19.35	19.78	19.06
Fe2O3	0.00	0.00	0.00	0.00	0.00	0.00
FeO	18.45	17.65	18.51	20.60	20.12	20.26
MnO	0.12	0.16	0.21	0.06	0.13	0.25
MgO	8.97	8.34	8.56	8.15	8.77	8.44
CaO	0.03	0.06	0.02	0.08	0.05	0.14
Na2O	0.68	0.65	0.66	0.76	0.84	0.70
Sum:	89.57	89.55	89.49	89.79	90.10	89.99

Sample LH349

	M1	M2	rimAv
SiO2	36.42	36.64	36.51
TiO2	1.60	1.25	1.55
Al2O3	21.41	21.27	21.14
Fe2O3	0.00	0.00	0.00
FeO	23.70	23.62	24.08
MnO	0.03	0.08	0.08
MgO	7.79	7.84	7.74
CaO	0.23	0.12	0.20
Na2O	0.79	0.89	0.84
Sum:	91.97	91.71	92.13

Part 3- Plagioclase Compositions

Sample LH17

	loc1	loc2	loc3
SiO2	59.70	61.27	60.92
TiO2	0.06	0.04	0.03
Al2O3	26.08	25.24	25.36
Fe2O3	0.00	0.00	0.00
FeO	0.18	0.05	0.02
MnO	0.06	0.05	0.00
MgO	0.00	0.00	0.00
CaO	8.31	6.88	7.15
Na2O	5.40	6.31	6.25
Sum:	99.80	99.85	99.73

Sample 125

	125m1	125m2	125m3
SiO2	59.58	61.52	62.14
TiO2	0.03	0.03	0.07
Al2O3	26.35	25.08	24.84
Fe2O3	0.00	0.00	0.00
FeO	0.05	0.05	0.17
MnO	0.05	0.03	0.00
MgO	0.00	0.00	0.00
CaO	7.91	6.33	6.06
Na2O	5.83	6.48	6.47
Sum:	99.79	99.52	99.76

Sample 134

	locA	locC	locD	locE
SiO2	56.74	44.62	51.16	44.67
TiO2	0.00	0.00	0.00	0.00
Al2O3	28.14	35.49	31.55	35.65
Fe2O3	0.00	0.00	0.00	0.00
FeO	0.60	0.71	0.89	0.61
MnO	0.00	0.00	0.01	0.04
MgO	0.00	0.00	0.00	0.00
CaO	9.23	18.35	12.98	18.26
Na2O	5.30	0.84	3.40	0.79
Sum:	100.00	100.00	100.00	100.01

Sample LH255

	255-1	255-2	255-3	255-4	28bplm1	28bplm2	28bplm3	28bplm4
SiO2	60.13	57.95	60.63	63.10	61.24	60.28	60.91	61.50
TiO2	0.03	0.02	0.09	0.03	0.03	0.09	0.00	0.02
Al2O3	26.06	27.19	25.61	24.23	25.28	25.89	25.74	25.46
Fe2O3	0.00	0.00	0.00	0.00	0.00	0.00	0.00	0.00
FeO	0.28	0.14	0.13	0.18	0.09	0.04	0.01	0.22
MnO	0.02	0.08	0.02	0.03	0.04	0.00	0.00	0.00
MgO	0.00	0.00	0.00	0.00	0.00	0.00	0.00	0.00
CaO	7.60	9.13	7.05	5.26	6.64	7.43	6.90	6.61
Na2O	5.41	5.42	6.31	7.00	6.38	6.03	6.21	5.85
Sum:	99.53	99.92	99.84	99.82	99.72	99.77	99.77	99.65

APPENDIX THREE – GEOCHRONOLOGY DATA

PART 1 – U-Pb DATA

PB-342

9	sub-p-o-pz	182	0.5	0.8	0	2150 (0.9)	0.034 ± 0.003	0.00290 ± 0.00004	18.7 ± 0.3
3	eu-p-o-pz	315	1	1.6	0.01	3300 (0.6)	0.059 ± 0.003	0.00295 ± 0.00004	19.0 ± 0.3
6a	eu-p-o-pz*	302	0.9	1.9	0.01	>1e6 (>0.1)	0.049 ± 0.003	0.00296 ± 0.00004	19.1 ± 0.2
12a	eu-p-o-pz*	401	1.3	2.1	0.01	4350 (0.4)	0.049 ± 0.002	0.00297 ± 0.00004	19.1 ± 0.3
8a	sub-p-o-pz	169	0.5	0.8	0	1310 (1.4)	0.049 ± 0.004	0.00299 ± 0.00011	19.3 ± 0.7
4	eu-p-o-pz	691	2.2	4.4	0.01	760 (2.5)	0.050 ± 0.001	0.00301 ± 0.00004	19.4 ± 0.2
5a	sub-p-o-	286	0.9	1.8	0.01	2770 (0.7)	0.052 ± 0.002	0.00302 ± 0.00004	19.4 ± 0.3
2b	sub-p-o-pz	253	0.8	1.2	0	2920 (0.6)	0.051 ± 0.002	0.00302 ± 0.00002	19.4 ± 0.2
11a	sub-p-o-	222	0.7	1.2	0.01	2120 (0.8)	0.048 ± 0.002	0.00304 ± 0.00004	19.6 ± 0.3
10	eu-p-s-pz	265	0.9	1.2	0	3520 (0.5)	0.049 ± 0.002	0.00306 ± 0.00004	19.7 ± 0.3
7	sub-p-s-pz	196	0.7	1	0.01	800 (2.3)	0.047 ± 0.003	0.00312 ± 0.00004	20.1 ± 0.3
1	sub-r-s-pz	268	1.2	3.1	0.01	1360 (1.4)	0.052 ± 0.002	0.00398 ± 0.00004	25.6 ± 0.2

PART 2 – AR-AR DATA

Sample	Mineral	Run-code	40Ar	+-	39Ar	+-	38Ar	+-	37Ar	+-	36Ar	+-	40Ar*/39Ar	+-	Age (Ma)	+-
PB536	white mica	LHA 01	0.450253	0.001447	0.212964	0.000275	0.002893	2.65E-05	0.007038	7.32E-05	0.000198	1.41E-05	1.839283	0.020902	21.38	0.26
PB536	white mica	LHA 02	0.597034	0.001322	0.282658	0.000584	0.003618	3.16E-05	0.009081	7.32E-05	0.000298	1.41E-05	1.801093	0.015947	20.94	0.21
PB536	white mica	LHA 03	0.973111	0.001641	0.451119	0.0003	0.005989	3.87E-05	0.041758	0.000117	0.000489	1.41E-05	1.836809	0.010027	21.35	0.16
PB536	white mica	LHA 04	0.879944	0.001789	0.423687	0.000369	0.005478	3.87E-05	0.012914	0.000117	0.000467	1.41E-05	1.751447	0.010837	20.37	0.16
PB536	white mica	LHA 05	0.288834	0.001679	0.117223	0.000176	0.00233	2.65E-05	0.009902	7.33E-05	0.000257	1.41E-05	1.815148	0.038516	21.10	0.46
PB536	white mica	LHA 06	1.899759	0.003262	1.00033	0.000945	0.013175	5.57E-05	0.231766	0.000613	0.000559	2.24E-05	1.734058	0.007546	20.17	0.13
PB536	white mica	LHA 07	2.135469	0.00486	1.157668	0.000565	0.015863	3.16E-05	0.830432	0.001831	0.000681	2.24E-05	1.670861	0.007132	19.43	0.13
PB536	white mica	LHA 08	1.917818	0.00449	0.8597	0.0007	0.011529	5.57E-05	0.057201	0.000234	0.001315	5.1E-05	1.778835	0.018346	20.68	0.24
PB536	white mica	LHA 09	2.603575	0.010137	1.330314	0.0014	0.016435	7.42E-05	0.130594	0.000234	0.001306	4.12E-05	1.667119	0.012043	19.39	0.17
PB536	white mica	LHA - 10 - QUARTZ	1.794137	0.005987	0.850979	0.000603	0.011325	5.57E-05	0.092047	0.000174	0.000536	5.83E-05	1.922301	0.021479	22.34	0.27
PB536	white mica	LHA - 11	4.881191	0.015757	2.494876	0.001311	0.033831	7.42E-05	0.321368	0.001032	0.001465	7.62E-05	1.782949	0.011051	20.73	0.16
PB536	white mica	LHA - 12	0.533091	0.001456	0.269411	0.000201	0.003495	4.74E-05	0.016323	0.000133	0.000266	1.41E-05	1.687307	0.016474	19.62	0.21
PB536	white mica	LHA - 13	0.357141	0.00142	0.169547	0.000168	0.002145	4.74E-05	0.020389	0.000145	0.000135	1.41E-05	1.871826	0.026098	21.76	0.32
PB536	white mica	LHA - 14	0.569568	0.001549	0.277609	0.000176	0.003566	4.74E-05	0.008308	0.000163	0.000298	1.41E-05	1.734688	0.016092	20.17	0.21
PB536	white mica	LHA - 15	0.57787	0.001504	0.259031	0.000168	0.003586	4.74E-05	0.012036	0.000163	0.000377	1.41E-05	1.801014	0.017186	20.94	0.22
PB536	white mica	LHA - 15	0.974497	0.001472	0.472921	0.000688	0.006295	5.24E-05	0.02594	0.000239	0.000353	1.41E-05	1.839928	0.009744	21.39	0.16

Mean = 20.50±0.44 (2.1%) 95% conf.

Wtd by data.pt errs only. 0 of 16 rej.

MSWD = 19. probability = 0.0

Sample	Mineral	Run-code	40Ar	±	39Ar	±	38Ar	±	37Ar	±	36Ar	±	40Ar ^r /39Ar ^r	±	Age (Ma)	±
LH 215	white mica	LHA - 01	0.808844	0.006722	0.210159	0.000602	0.005155	5.34E-05	0.004612	0.000162	0.001759	1.41E-05	1.375739	0.037867	16.02	0.45
LH 215	white mica	LHA - 02	2.376411	0.007354	0.774418	0.001465	0.017399	7.97E-05	0.027023	0.000163	0.003883	4.12E-05	1.587029	0.01862	18.46	0.23
LH 215	white mica	LHA - 03	2.616379	0.004627	0.671535	0.000286	0.019525	9.57E-05	0.017523	0.000178	0.005645	3.16E-05	1.411946	0.01554	16.44	0.20
LH 215	white mica	LHA - 04	0.921691	0.002992	0.263851	0.00075	0.006085	6.05E-05	0.004618	0.000163	0.001489	1.41E-05	1.825865	0.020158	21.23	0.26
LH 215	white mica	LHA - 05	2.391013	0.022522	0.545394	0.004462	0.016244	0.000187	0.012019	0.000178	0.005737	0.0001	1.27574	0.069132	14.86	0.81
LH 215	white mica	LHA - 06	0.974997	0.002638	0.221895	0.000143	0.006013	6.05E-05	0.004754	0.000153	0.002189	2.24E-05	1.479179	0.032077	17.22	0.38
LH 215	white mica	LHA - 07	2.218917	0.003575	0.535081	0.000149	0.01559	5.62E-05	0.015366	0.000163	0.005086	2.83E-05	1.338154	0.016993	15.58	0.21
LH 215	white mica	LHA - 08	1.616459	0.003042	0.470359	0.000465	0.011257	0.00015	0.009553	0.000179	0.002807	3.61E-05	1.672869	0.023615	19.46	0.29
LH 215	white mica	LHA - 09	1.299287	0.003174	0.388681	0.000259	0.008517	6.6E-05	0.008662	0.000153	0.002088	2.24E-05	1.7556	0.018896	20.41	0.24
LH 215	white mica	LHA - 11	2.265313	0.002422	0.587464	0.000485	0.016275	7.97E-05	0.010629	0.000153	0.004547	2.24E-05	1.568807	0.012049	18.25	0.17
LH 215	white mica	LHA - 12	1.432957	0.003644	0.564918	0.000553	0.010245	5.62E-05	0.015307	0.000179	0.001756	1.41E-05	1.618061	0.009942	18.82	0.15
LH 215	white mica	LHA - 13	1.740819	0.003376	0.461868	0.000398	0.011625	7.25E-05	0.008349	0.000153	0.003308	2.83E-05	1.652778	0.019569	19.23	0.25

Mean = 18.3 ± 1.1 (5.7%) 95% conf.

Wtd by data-pt errs only. 0 of 12 rej.

MISWD = 51, probability = 0.0

Type	Mineral	Run-code	40Ar	±	39Ar	±	38Ar	±	37Ar	±	36Ar	±	40Ar*/39Ar	±	Age (Ma)	±
LH 172	white mica	LHA - 01	0.496736	0.001438	0.264122	0.000482	0.007757	5.24E-05	0.00065	0.000132	0.00015	1.41E-05	1.713082	0.017023	19.92	0.22
LH 172	white mica	LHA - 02	0.995657	0.003802	0.533632	0.001035	0.019306	5.24E-05	0.002972	0.000132	0.000329	2.24E-05	1.683509	0.014654	19.58	0.20
LH 172	white mica	LHA - 03	0.692613	0.002156	0.372133	0.000797	0.013685	5.87E-05	0.00321	0.000132	0.000109	1.41E-05	1.774521	0.013195	20.63	0.18
LH 172	white mica	LHA - 04	0.477751	0.002588	0.260721	0.000337	0.007859	5.24E-05	0.002975	0.000132	0.000169	1.41E-05	1.640634	0.018973	19.08	0.24
LH 172	white mica	LHA - 05	1.928222	0.003029	0.991148	0.001155	0.038051	7.38E-05	0.009417	0.000163	0.000848	1.41E-05	1.692765	0.005568	19.69	0.12
LH 172	white mica	LHA - 06	0.81239	0.001612	0.422426	0.000218	0.015514	7.38E-05	0.003349	0.000133	0.000319	2.24E-05	1.699923	0.016125	19.77	0.21
LH 172	white mica	LHA - 07	0.278266	0.001417	0.141159	0.000133	0.005784	4.41E-05	0.000482	0.000133	7.99E-05	1.41E-05	1.80409	0.031306	20.97	0.38
LH 172	white mica	LHA - 08	1.902103	0.001562	0.991657	0.003672	0.031029	9.08E-05	0.005038	0.000133	0.000559	1.41E-05	1.751629	0.007893	20.37	0.14
LH172	white mica	LHA - 10	0.452303	0.001459	0.243704	0.000404	0.008247	4.74E-05	0.005755	0.000133	0.000158	1.41E-05	1.663791	0.018371	19.35	0.23
LH172	white mica	LHA - 11	2.396204	0.001511	1.350274	0.000492	0.044317	0.000166	0.009474	0.000145	0.000377	1.41E-05	1.691993	0.003348	19.68	0.11
LH172	white mica	LHA - 12	0.304289	0.001447	0.151872	0.000201	0.004977	4.41E-05	0.000484	0.000133	2.99E-05	1.41E-05	1.945462	0.029232	22.61	0.36
LH172	white mica	LHA - 13	0.749265	0.001426	0.359148	0.00029	0.012458	5.87E-05	0.001837	0.000133	0.00031	1.41E-05	1.831567	0.012384	21.29	0.18

Mean = 20.02 ± 0.44 (2.2%) 95% conf.

Wtd. by data-pt errs only. 0 of 12 rej.

MISWD = 16, probability = 0.0

Sample	Mineral	Run-code	40Ar	+-	39Ar	+-	38Ar	+-	37Ar	+-	36Ar	+-	40Ar*/39Ar r	+-	Age (Ma)	+-
PB 535	white mica	LHA - 01	0.58761	0.010805	0.185644	0.000586	0.002882	4.97E-05	0.002661	0.000142	0.000909	3.16E-05	1.717871	0.07714	19.97806	0.897691
PB 535	white mica	LHA - 02	0.80349	0.003063	0.279317	0.000208	0.004252	4.97E-05	0.004756	0.000142	0.001099	0.00001	1.714222	0.01529	19.93586	0.202859
PB 535	white mica	LHA - 05	0.415024	0.001026	0.090587	0.000226	0.001594	4.97E-05	0.001771	0.00013	0.000847	2.24E-05	1.818684	0.073957	21.14362	0.861248
PB 535	white mica	LHA - 06	0.555396	0.00156	0.17115	0.00011	0.003312	4.65E-05	0.002356	0.000162	0.000859	1.41E-05	1.76132	0.026088	20.48049	0.318439
PB 535	white mica	LHA - 07	0.631047	0.001197	0.270494	0.000293	0.003996	4.65E-05	0.003943	0.00013	0.000569	0.00001	1.711385	0.011931	19.90304	0.169969
PB 535	white mica	LHA - 08	0.528194	0.001114	0.200718	0.000255	0.003046	4.97E-05	0.002842	0.00013	0.000689	0.00001	1.616804	0.015866	18.80881	0.20619
PB 535	white mica	LHA - 09	0.303509	0.001024	0.096424	0.000147	0.001502	4.97E-05	0.001602	0.00013	0.00022	2.24E-05	2.474731	0.069446	28.71028	0.811942
PB 535	white mica	LHA - 10	0.598733	0.001138	0.207464	0.000164	0.003025	4.65E-05	0.003051	0.00013	0.000869	1.41E-05	1.647933	0.020917	19.16901	0.260216
PB 535	white mica	LHA - 11	0.338137	0.001042	0.130434	0.000139	0.002167	4.65E-05	0.00219	0.00013	0.000309	1.41E-05	1.891393	0.033081	21.9838	0.397557
PB 535	white mica	LHA - 12	0.597246	0.001133	0.219065	0.000302	0.003342	4.97E-05	0.003846	0.000143	0.000429	1.41E-05	2.147675	0.019986	24.94208	0.261833
PB 535	white mica	LHA - 13	0.839361	0.001425	0.278821	0.000164	0.004293	4.65E-05	0.00447	0.000143	0.001009	1.41E-05	1.941228	0.015876	22.55942	0.215065
PB 535	white mica	LHA - 14	0.57305	0.001091	0.309073	0.000236	0.0111	5.45E-05	0.000639	0.000126	0.00017	0.00001	1.691717	0.010273	19.67555	0.154101
PB 535	white mica	LHA - 15	0.56438	0.001183	0.308419	0.000571	0.00972	3.7E-05	0.000945	6E-05	0.00026	1.41E-05	1.581044	0.014383	18.3949	0.190101
PB 535	white mica	LHA - 16	0.38695	0.001393	0.215649	0.000238	0.008626	6.38E-05	0.009452	6E-05	5.72E-05	1.41E-05	1.716038	0.020515	19.95687	0.257289
PB 535	white mica	LHA - 17	1.470782	0.00298	0.785081	0.000929	0.031235	8.29E-05	0.003993	8.49E-05	0.000539	1.41E-05	1.670557	0.00683	19.43078	0.125028
PB 535	white mica	LHA - 18	0.531856	0.001224	0.286035	0.000206	0.010231	0.000102	0.010442	8.49E-05	0.000257	1.41E-05	1.593654	0.015267	18.54087	0.199443

Mean = 19.67±0.62 (3.1%) 95% conf.

Wtd. by data-pt errs only. 2 of 16 rej.

MSWD = 25. probability = 0.0

Type	mineral	Run-code	40Ar	+/-	39Ar	+/-	38Ar	+/-	37Ar	+/-	36Ar	+/-	40Ar*/39Ar	+/-	Age (Ma)	+/-
PB342	biotite	1	0.622006	0.003095	0.306939	0.00033	0.006645	4.3E-05	0.000226	0.000134	0.000124	3.61E-05	1.907101	0.036205	18.50125	0.360473
PB342	biotite	2	0.503644	0.00302	0.245695	0.00031	0.00548	4.3E-05	9.51E-05	0.000139	0.000102	2.24E-05	1.927196	0.029668	18.6952	0.299967
PB342	biotite	3	0.299094	0.003021	0.151109	6.07E-05	0.003262	4.3E-05	0.000205	0.000133	0.000024	2.24E-05	1.932391	0.048087	18.74533	0.472642
PB342	biotite	4	0.764804	0.003063	0.384105	0.00067	0.008638	4.84E-05	-0.0001	0.000159	0.000164	2.24E-05	1.864965	0.019238	18.09452	0.204919
PB342	biotite	5	0.434996	0.003023	0.20808	9.04E-05	0.004509	4.3E-05	0.000205	0.000134	6E-05	1.41E-05	2.005317	0.024802	19.44896	0.256711
PB342	biotite	6	0.625755	0.001195	0.305949	0.00031	0.006126	0.000109	-0.00014	0.000217	5.2E-05	1.41E-05	1.995065	0.01435	19.35005	0.166542
PB342	biotite	7	0.17664	0.000999	0.088642	7.19E-05	0.001782	0.000109	0.000483	0.000217	0.00002	1.41E-05	1.926061	0.0485	18.68424	0.476512

Mean = 18.88±0.53 (2.8%) 95% conf.

Wtd by data-pt errs only. 0 of 7 rej.

MSWD = 4.9. probability = 0.0

PB342 M	white mica	1	0.503827	0.001127	0.221672	0.00032	0.002947	0.000107	1.42E-05	0.000217	0.000102	2.24E-05	2.136875	0.030396	20.7176	0.309309
PB342 M	white mica	2	0.4698	0.001206	0.213226	0.0003	0.002988	0.000111	8.13E-05	0.000218	0.000204	2.24E-05	1.920584	0.031617	18.63138	0.317891
PB342 M	white mica	3	0.29308	0.001018	0.130107	0.000121	0.001905	0.000109	0.000193	0.000218	0.000072	2.24E-05	2.089074	0.051422	20.25674	0.505199
PB342 M	white mica	4	0.488238	0.001083	0.223813	0.000271	0.003142	0.000109	0.000283	0.000218	0.000156	2.24E-05	1.975488	0.030012	19.16119	0.303724
PB342 M	white mica	5	0.61724	0.001012	0.299987	0.000151	0.004133	0.000107	0.000149	0.000218	0.00017	2.24E-05	1.890097	0.022303	18.33713	0.23248
PB342 M	white mica	6	0.82	0.001338	0.392511	0.00083	0.005411	0.000111	0.000104	0.000218	0.00019	1.41E-05	1.946072	0.011913	18.87735	0.146198
PB342 M	white mica	7	0.409198	0.001764	0.192148	0.000241	0.002753	0.000107	0.000261	0.000218	0.000126	2.24E-05	1.935824	0.035674	18.77846	0.355796

Mean = 19.01±0.66 (3.5%) 95% conf.

Wtd. by data-pt errs only. 0 of 7 rej.

MSWD = 8.0. probability = 0.0

PART 3 – APATITE FISSION TRACK DATA

Sample No./ Field No	No. of crystals	Dosimeter pd Nd	Spontaneous ps Ns	Induced pi Ni	Age Dispersion $P\chi^2$ RE%	Central Age (Ma) $\pm 1\sigma$	Age	Mean Track length (μm)	S.d.	No. of tracks			
Apatite only;													
1H 149								Bad - magnetite inclusions					
1H 151								Uranium too low to analyse					
1H 166	14	1.393	3775	0.118	58	2.322	1136	<1	43.4	12.7\pm2.3	No length data		
1H 338											Trace of apatite only		
1H 351	20	1.403	3775	0.116	180	1.478	2290	20	2.9	18.6\pm1.5	No length data		
PB 342	24	1.161	6429	0.182	120	1.804	1193	99	0	19.8\pm1.9	14.98 \pm 0.21	0.62	10

Table 1: Fission track apatite analytical data

Notes:

- (i). Track densities are ($\times 10^6 \text{ tr cm}^{-2}$) numbers of tracks counted (N) shown in brackets;
- (ii). analyses by external detector method using 0.5 for the $4\pi/2\pi$ geometry correction factor;
- (iii). ages calculated using dosimeter glass CN-5; analyst Carter $\zeta_{\text{CN5}} = 338 \pm 4$; CN-2; $\zeta_{\text{CN2}} = 124 \pm 4$ calibrated by multiple analyses of IUGS apatite and zircon age standards (see Hurford 1990);
- (iv). $P\chi^2$ is probability for obtaining χ^2 value for ν degrees of freedom, where $\nu = \text{no. crystals} - 1$;
- (v). Central age is a modal age, weighted for different precisions of individual crystals (see Galbraith 1992);

REFERENCES

Argles T W, Platt J P, Waters D J, 1999. Attenuation and excision of a crustal section during extensional exhumation: the Carratraca Massif, Betic Cordillera, Southern Spain. *J. Geol. Soc. London* 156, 149-162

Aldaya F, Garcia-Duenas V, Nevarro-Villa F, 1979. Los Mantos Alpujarrides del tercio central de las Cordilleras Beticas: Ensayo de correlacion, tectonica de los Alpujarrides. In homenatge a Lluís Sole i Sabaris, *Acta Geol. Hisp.* 14, 154-166

Avigad D, Ziv A, Garfunkel Z, 2001. Ductile and brittle shortening, extension-parallel folds and maintenance of crustal thickness in the central Aegean (Cyclades, Greece). *Tectonics* 20, 277-287.

Azañon J M, Garcia-Duenas V, Martinez-Martinez J M, Crespo-Blanc A, 1994. Alpujarride tectonic sheets in the central Betics and similar eastern allochthonous units (SE Spain). *C.R. Acad. Sci. Paris Ser.II* 318, 667-674

Azanon J M & Crespo-Blanc A, 2000. Exhumation during a continental collision inferred from the tectonometamorphic evolution of the Alpujarride Complex in the central Betics (Alboran Domain, SE Spain). *Tectonics* 19 (3), 549-565.

Azañon J M, Garcia-Duenas V, Goffe B, 1998. Exhumation of high pressure metamorphic metapelites and coeval crustal extension in the Alpujarride Complex (Betic Cordillera). *Tectonophysics* 285, 231-252.

Azanon J M, Crespo-Blanc A, Garcia-Duenas V, 1997. Continental collision, crustal thinning and nappe-forming during the pre-Miocene evolution of the Alpujarride Complex (Alboran Domain, Betics)). *J. Struct. Geol.* 19, 1055-1072.

Bakker H E, De Jong K, Helmers H, Biermann C, 1989. The geodynamic evolution of the Internal Zone of the Betic Cordilleras (south-east Spain): A model based on structural analysis and geothermobarometry. *J. Metam. Geol.* 7, 359-381.

Balanya J C, Azanon J M, Sanchez-Gomez M, Garcia-Duenas V, 1993. Pervasive ductile extension, isothermal decompression and thinning of the Jubrique unit in the Palaeogene (Alpujarride Complex, western Betics, Spain). *C.R. Acad. Sci. Paris* 316, 1595-1601.

Balanya J C, Campos J, Garcia-Duenas V, Orizco M, Simancas J F, 1987. Generaciones de cabalgamientos y pliegues recumbentes en los Mantos Alpujarrides entre Ronda y Almeria, Cordilleras Beticas. *Geogaceta* 2, 51-53

Balanya J C, Garcia-Duenas V, Azanon J M, Sanchez-Gomez M, 1997. Alternating contractional and extensional events in the Alpujarride nappes of the Alboran Domain (Betics, Gibraltar arc). *Tectonics* 16, 226-238.

Berman R G, 1990. Internally-consistent thermodynamic data for minerals in the system Na₂O-Al₂O₃-SiO₂-TiO₂-H₂O-CO₂. *J. Petrol* 29, 445-452.

Blanco M J, Spakman W, 1993. The P-wave velocity structure of the mantle below the Iberian Peninsula: evidence of subducted lithosphere below southern Spain. *Tectonophys.* 221, 13-34.

Bohlen S R, Wall V J, Boettcher A L, 1983. Experimental investigations and geological applications of equilibria in the system FeO-TiO₂-Al₂O₃-SiO₂-H₂O. *Am. Min.* 68, 1049-1058.

Bowen, 1988 *Isotopes in the Earth Sciences – Elsevier Applied Science*

Burg J P, Chaudry M N, Ghazanfar M, Anczkiewicz R, Spencer D, 1996. Structural evidence for back sliding of the Kohistan arc in the collisional system of northwest Pakistan. *Geology* 24, 739-742.

Calvert A, Sandvol E, Seber D, Barazangi M, Roecker S, Mourabit T, Vidal F, Alguacil G, Jabour N, 2000. Geodynamic evolution of the lithosphere and upper mantle beneath the Alboran region of the western Mediterranean: Constraints from travel time tomography. *J. Geophys. Res.* 105, 10871-10898.

Comas M C, Garcia-Dueñas V, Jurado M J, 1992. Neogene tectonic evolution of the Alboran Basin from MCS data. *Geo-Mar. Lett.* 12, 157-164.

Comas M C, Platt J P, Soto J I, Watts A B, 1999. The origin and tectonic history of the Alboran Basin: insights from Leg 161. In: Zahn R, Comas M C, Klaus A (Eds) – *Proceedings of the Ocean Drilling Program, Scientific Results, Vol 161.*

Comas M C, Zahn R, Klaus A *et al*, 1996. *Proc. ODP Initial reports 161: College Station, TX*

(Ocean Drilling Program)

Crespo-Blanc A, Orozco M, Garcia-Duenas V, 1994. Extension versus compression during the Miocene tectonic evolution of the Betic chain. Late folding of normal fault systems. *Tectonics* 13, 78-88

Crespo-Blanc A, 1995. Interference pattern of extensional fault systems: a case study of the Miocene rifting of the Alboran basement (North of Sierra Nevada, Betic Chain). *J Struct. Geol.* 17, 1559-1569

Darot M, 1974. Cinematique de l'extrusion a partir du manteau, des peridotites de la Sierra Bermeja (Serrania de Ronda, Espagne). *Comptes Rendus de l'Academie des Sciences, Paris* 278 (Serie D), 1673-1676.

De Jong K, 1991. Tectonomoetamorphic studies and radiometric dating in the Betic Cordillera (SE Spain) with implications for the dynamics of extension and compression in the western Mediterranean area. PhD dissertation 204pp. Free Univ. Amsterdam.

de Larouziere F D, Bolze J, Bordet P, Hernandez J, Montenat C, Ott d'Estevou P, 1988. The Betic segment of the lithospheric trans-Alboran shear zone during the late Miocene. *Tectonophys.* 152, 41-52.

Deer W A, Howie R A, Zussman J, 1992. *The rock-forming minerals*. 2nd Ed. John Wiley & Sons Inc. pp696.

Dewey J F, Helman M L, Turco E, Hutton D H W, Knott S D, 1989. Kinematics of the western Mediterranean. *Geol. Soc. Spec. Pub.* 45, 265-283.

Di Battistini G, Toscani L, Iaccarino S, Villa I M, 1987. K/Ar ages and the geological setting of calc-alkaline volcanic rocks from Sierra de Gata, SE Spain. *Neues. Jahrb. Minerla.* 8, 369-383.

Dodson, MH. 1973. Closure temperature in cooling geochronological and petrological systems. *Contribs. Min. Pet.*, 40, 259-274.

Droop G T R, 1987. A general equation for estimating Fe³⁺ concentrations in ferromagnesian silicates and oxides from microprobe analyses using stoichiometric criteria. *Min. Mag.* 51, 431-435.

Egler C G & Simon O J, 1969. Orogenic evolution of the Betic Zone (Betic Cordillera, Spain) with emphasis on the nappe structures. *Geol. Mijnbouw* 48, 296-305.

Ellis D J, Green D H, 1979. An experimental study of the effect of Ca upon garnet-clinopyroxene Fe-Mg exchange equilibria. *Contrib. Min. Pet.* 71, 13-22.

Essene E J, 1989. The current state of thermobarometry in metamorphic rocks. In: *Evolution of metamorphic belts*; Daly J S, Cliff R A & Yardley B W D (Eds.) *Geol. Soc. Spec. Pub.* 43, 1-44.

Ferry J M, Spear F S, 1978. Experimental calibration of the Partitioning of Fe and Mg between Biotite and Garnet. *Contrib. Min. Pet.* 66, 113-117.

Fleuty M J, 1964. Textonic slides. *Geol. Mag.* 101, 452-456.

Fraser G, Ellis D, Eggins S, 1997. Zirconium abundance in granulite-facies minerals with implications for zircon geochronology in high-grade rocks. *Geology* 25, 607-610.

Frizon de Lamotte D, Andrieux J, Guezou J, 1991. Cinématique des chevauchements néogènes dans l'Arc bético-rifain: discussion sur les modèles géodynamiques. *Société Géologique de France Bulletin* 162, 611-626.

Froitzhem, N. 1992. Formation of recumbent folds during synorogenic crustal extension (Austroalpine nappes, Switzerland). *Geology* 20, 923-926.

Garcia-Casco A, Torres-Roldan R, 1996. Disequilibrium induced by fast decompression in St-Bt-Grt-Ky-Sil-And metapelites from the Betic Belt (Southern Spain). *J. Petrol.* 37, 73-85.

Garcia-Casco A, Sanchez-Navas A, Torres-Roldan R L, 1993. Disequilibrium decomposition and breakdown of muscovite in high P-T gneisses, Betic alpine belt (southern Spain). *Am. Min.* 78, 158-177.

Garcia-Dueñas V, Martinez-Martinez J M, Orozco M, Soto J I, 1988. Plis-nappes cisaillements syn- a post-metamorphiques et cisaillements ductiles-fragiles en distension dans les Nevado-Filabrides (Cordillères bétiques, Espagne). *C.R. Acad. Sci. Paris Ser. II* 307, 1389-1395.

- Gallagher K, Brown R, Johnson C, 1998. Fission track analysis and its applications to geological problems. *Annu. Rev. Earth Plan. Sci.* 26, 519-572.
- Ganguly J, Saxena S K, 1984. Mixing properties of aluminosilicate garnets: constraints from natural and experimental data, and applications to geothermo-barometry. *Am. Min.* 69, 88-97.
- Ghent E D, Robbins D B, Stout M Z, 1979. Geothermometry, geobarometry, and fluid composition of metamorphosed calc-silicates and pelites, Mica Creek, British Columbia. *Am. Min.* 64, 874-885.
- Gomez-Pugnaire M T, Fernandez-Soler J M, 1987. High pressure metamorphism in metabasites from the Betic Cordilleras (SE Spain) and its evolution during the Alpine orogeny. *Contrib. Min.Pet.* 95, 231-244.
- Graham C M, Powell R, 1984. A garnet-hornblende geothermometer: calibration, testing and application to the Pelona Schist, Southern California. *J Metam. Geol* 2, 13-31.
- Hames, WE, Bowring, SA. 1994. An empirical study of the argon diffusion geometry in muscovite. *Earth Planet. Sci. Lett.* 124, 1
- Heinrich C A, 1986. Eclogite facies regional metamorphism of hydrous mafic rocks in the central alpine Adula nappe. *J. Petrol.* 27, 123-154.
- Hodges K V, Crowley P D, 1985. Error estimation and empirical geothermobarometry for pelitic systems. *Am. Min.* 70, 702-709.
- Hodges K V, Spear F S, 1982. Geothermometry, geobarometry and the Al_2SiO_5 triple point at Mt. Moosilake, New Hampshire. *Am. Min.* 67, 1118-1134.
- Holdaway M J, Mukhopadhyay B, Dyar M D, Guidotti C V, Dutrow B L, 1997. Garnet-biotite geothermometry revised: New Margules parameters and a natural specimen data set from Maine. *Am. Min.* 82, 582-595.
- Hurford A J, Platt J P, Carter A, 1999. Fission-track analysis of samples from the Alboran Sea Basement. In: Zahn, Comas & Klaus (Eds): *Proceedings of the Ocean Drilling Program, Scientific Results, Vol 161.*

IGME, 1972 . Mapa Geologico de España, 1:50,000. Motril (1,055). Instituto Geologica y Minero de España.

IGME: 1972. Mapa Geologico de España, 1:50,000. Albuñol (1,056). Instituto Geologica y Minero de España.

Indares A, Martingole J, 1985. Biotiite-garnet geothermometry in the granulite facies: the influence of Ti and Al in biotite. *Am. Min.* 70, 272-278.

Jabaloy A, Galindo-Zaldivar J, Gonzalez-Lodiero F, 1993. The Alpujarride-Nevado-Filabride shear zone, Betic Cordillera, SE Spain. *J. Struct.Geol* 15, 555-569.

Kelley S, 1995. Ar-Ar dating by laser microprobe. In: *Microprobe techniques in the Earth Sciences*: Potts, Bowles, Reed, Cave (Eds). Chapman & Hall, London

Kerrick D M, 1990. The Al₂SiO₅ polymorphs. *Rev. in Min.* Vol. 22. Min. Soc.Am. (Series Ed: P H Ribbe).

Kirker A, Platt J P, 1998. Unidirectional slip vectors in the western Betic Cordillera: implications for the formation of the Gibraltar arc. *J. of Geol. Soc. London* 155, 193-207.

Kohn M J, Spear F, 2000. Retrograde net transfer reaction insurance for pressure-temperature estimates. *Geology* 28, 1127-1130.

Kohn M, Spear F S, 1996. Thermobarometry (computer program) Version 2.0.

Koziol A M, 1989. Recalibration of the garnet-plagioclase-Al₂SiO₅-quartz (GASP) barometer and application to natural parageneses. *EOS Trans. Am. Geophys. Union* 70:493.

Koziol A M, Newton R C, 1988. Redetermination of the anorthite breakdown reaction and improvement of the garnet-plagioclase-Al₂SiO₅-quartz geobarometer. *Am. Min.* 73, 216-223.

Kozur H, Simon O J, 1972. Contribution to the Triassic microfauna and stratigraphy of the Betic Zone (southern Spain). *Rev. Esp. Micro. num. extra 30 aniv. ADARO*, 143-148.

Kretz R, 1959. Chemical study of garnet, biotite and hornblende from gneisses of southwestern Quebec, with emphasis on distribution of elements in coexisting minerals. *J. Geol.* 67, 371-403.

Kretz R, 1983. Symbols for rock-forming minerals. *Am Miner.* 68, 277-279.

Leake B E, 1972. Garnetiferous striped amphibolites from Connemara, western Ireland. *Min. Mag.* 38, 649-665.

Leake B E, 1968. A catalogue of analysed Calciferous and Subcalciferous Amphiboles together with their nomenclature and Associated minerals. *Spec. Paper Geol. Soc. AM.* 98.

Lonergan L & White N, 1997. Origin of the Betic-Rif mountain belt. *Tectonics* 16(3), 504-522.

Lonergan L & Platt J P, 1995. The Malaguide-Alpujarride boundary: A major extensional contact in the Internal Zone of the eastern Betic Cordillera, SE Spain. *J. Struct. Geol.* 17, 1655-1671.

Lonergan L & Mange-Rajetzky M, 1994. Evidence for Internal Zone unroofing from foreland basin sediments, Betic Cordillera, SE Spain. *J. Geol. Soc. London* 151, 515-529.

Lonergan L, 1993. Timing and kinematics of deformation in the Malaguide Complex, Internal Zone of the Betic Cordillera, Southeast Spain. *Tectonics* 12, 460-476.

Loomis T P, 1972. Contact metamorphism of pelitic rock by the Ronda ultramafic intrusion, southern Spain. *Geol. Soc. Am. Bull.* 83, 2449-2474.

Malavielle J, 1987. Extensional shear deformation and kilometer-scale 'a' type folds in a Cordilleran metamorphic core complex (Raft River Mountains, northwestern Utah). *Tectonics* 6, 423-448.

Martinez-Martinez J M & Azañon J M, 1997. Mode of extensional tectonics in the southeastern Betics (SE Spain): Implications for the tectonic evolution of the peri-Alboran orogenic system. *Tectonics* 16(2), 205-225.

Martin-Perez J A, Viseras C, 1994. Sobre la posicion estratigrafica de las 'Margas de Gor', Sierra de Baza, Cordillera Betica. *Geogaceta* 15, 63-66.

Martin J M, Braga J C, 1987. Alpujarride carbonate deposition (southern Spain) – marine sedimentation in a Triassic Atlantic. *Palaeogeog Palaeoclim.* 59, 243-266.

Matte P, 1991. Accretionary history and crustal evolution of the Variscan belt in Europe. *Tectonophys.* 196, 309-337.

Michard A, Goffe B, Bouybaouene M L, Saddiqi O, 1997. Late Hercynian-Mesozoic thinning in the Alboran Domain: metamorphic data from the northern Rif, Morocco. *Terra Nova* 9, 171-174.

Molnar P, Lyon-Caen H, Clarke-Sydney P, 1988. Processes in continental lithospheric deformation. Burchfield B Clark (Ed.). *Spec. Paper Geol. Soc. Am.* 218, 170-207.

Monie P, Torres-Roldan R L, Garcia-Casco A, 1994. Cooling and exhumation of the Western Betic Cordilleras, $^{40}\text{Ar}/^{39}\text{Ar}$ thermochronological constraints on a collapsed terrane. *Tectonophysics* 238, 353-379.

Monie P, Galindo-Zaldivar J, Gonzalez-Lodeiro G, Goffe B, Jaloboy A, 1991. $^{40}\text{Ar}/^{39}\text{Ar}$ geochronology of Alpine tectonism in the Betic Cordilleras (southern Spain). *J. Geol. Soc. London* 148, 289-297.

Montenat C P, Ott d'Estevou P, de Larouziere D, Bedu P. Originalite geodynamique des bassins Neogenes de domaine Betique oriental. *Notes Mem. Total Cen. Explor. Prod.* 21. 11-41.

Nesbit H W & Essene E J, 1982. Metamorphic thermometry and barometry in a portion of the Southern Blue Ridge Province. *Am. J. of Science* 282, 701-729.

Orozco M, Alonso-Chaves F M, Nieto F, 1998. Development of large north-facing folds and their relation to crustal extension in the Alboran Domain (Alpujarras region, Betic Cordillera, Spain). *Tectonophys.* 298, 271-295.

Passchier C W, Trouw R A J, 1996. *Micro-tectonics.* Springer-Verlag. pp289.

Perkins D III, (1979). Application of new thermodynamic data to mineral equilibria. Unpublished Ph.D thesis, The University of Michigan.

Platt J P, 1998. Comment on 'Alternating contractional and extensional events in the Alpujarride nappes of the Alboran Domain (Betics, Gibraltar Arc) by Juan C Balanya et al. *Tectonics* 17(6), 973-976.

Platt J P, Whitehouse M J, 1999. Early Miocene high-temperature metamorphism and rapid exhumation in the Betic Cordillera (Spain): evidence from U-Pb zircon ages. *Earth Planetary Science Letters* 171, 591-605

Platt J P, Soto J I, Whitehouse M J, Hurford A J, Kelley, S P, 1998. Thermal evolution, rate of exhumation, and tectonic significance of metamorphic rocks from the floor of the Alboran extensional basin, western Mediterranean. *Tectonics* 17, 671-689.

Platt J P, Soto J I, Comas M C and Leg 161 Shipboard Scientists, 1996. Decompression and high temperature/low pressure metamorphism in the exhumed floor of an extensional basin, Alboran Sea, western Mediterranean. *Geology* 24, 447-450.

Platt J P, Vissers R L M, 1989. Extensional collapse of thickened continental lithosphere: a working hypothesis for the Alboran Sea and Gibraltar arc. *Geology* 17, 540-543.

Platt J P, Behrman J H, 1986. Structures and fabrics in a crustal-scale shear zone, Betic Cordillera, SE Spain. *J Struct. Geol.* 8, 15-34

Platt J P, Eeckhout B, Jansen E, Konert G, Simon O J, Weijermars R, 1983. The structure and tectonic evolution of the Aguilon fold-nappe, Sierra Alhamilla, Betic Cordilleras, SE Spain. *J. Struct. Geol.* 5, 519-538.

Platzman E, Platt J P, Kelley S P, Allerton S, 2000. Large clockwise rotations in an extensional allochthon, Alboran Domain (southern Spain). *J. Geol. Soc. London* 157, 1187-1197.

Platzman E S, Platt J P, Olivier P, 1993. Palaeomagnetic rotations and fault kinematics in the Rif Arc of Morocco. *J. of Geol. Soc. London* 8, 707-718.

Preim H N A, Boelrijk N A I M, Hebeda E H, Verschure R H, 1966. Isotope age determination on tourmaline granite gneisses and a metagranite in the eastern Betic Cordilleras (southeastern Sierra de los Filabres) SE Spain. *Geol. Mijnbouw* 45, 184-187.

Ragland P C 1989 *Basic analytical petrology* – Oxford University Press

Renne P R, Swisher, C C, Deino A L, De Paolo D J, 1998. Intercalibration of standards, absolute ages and uncertainties in $^{40}\text{Ar}/^{39}\text{Ar}$ dating. *Chem. Geol.* 145, 117-152.

Sanz de Galdeano C, Vera J, 1992. Stratigraphic record and paleogeographical context of the Neogene Basins in the Betic Cordillera, Spain. *Basin Res.* 4, 21-36.

Sanchez-Gomez M, Azanon J M, Garcia-Duenas V, Soto J I, Platt J P, 1999. Correlation between the metamorphic rocks recovered from Site 976 and the Alpujarride rocks of the western Betics. *Proc. Ocean Drill. Program, Sci. Results* 161, 307-317.

Seber D, Barazangi M, Ibenbrahim A, Demanti A, 1996. Geophysical evidence for lithosphere delamination beneath the Alboran Sea and Rif-Betic mountains. *Nature* 379, 785-790.

Simancas J F, Campos J, 1993. Compression NNW-SSE tardi a postmetamorfica y extensio subordina en el Complejo Alpujarrid (Dominio de Alboran, Orogeno Betico). *Rev. Soc. Geol. Esp* 6, 23-35.

Sosson M, Morillon A C, Bourgois J, Feraud G, Popeau G, Saint-Marc M, 1998. Late exhumation stage of the Alpujarride Complex (western Betic Cordilleras, Spain): New thermochronological and structural data on los Reales and Ojen nappes. *Tectonophys.* 285, 253-273.

Soto J I, Platt J P, 1999. Petrological and structural evolution of high-grade metamorphic rocks from the floor of the Alboran Sea basin, W. Mediterranean. *J. Petrol.* 10, 21-60.

Spear F, 1993. Metamorphic Phase Equilibria and Pressure-Temperature-Time paths. *Min. Soc. Am.* pp 799.

Spear F S, 1991. On the interpretation of peak metamorphic temperatures in light of garnet diffusion during cooling. *J. Metam. Geol.* 9, 379-388.

Spear F S, Kohn M J, Florence F, Menard T, 1990. A model for garnet and plagioclase growth in pelitic schists: Implications for thermobarometry and P-T path determinations. *J. Metam. Geol.* 8, 683-696.

- Spear F S, Kimball, K L, 1984. RECOMP – A FORTRAN IV program for estimating Fe³⁺ contents in amphiboles. *Comp. in Geol.* 10, 317-325.
- Stacey J S, Kramers J D, 1975. Approximation of terrestrial lead isotope evolution by a two-stage model. *Earth Planet. Sci. Lett.* 26, 207-221.
- Steiger R H, Jager E, 1977. Subcommittee on geochronology: convention on the use of decay constants in geo- and cosmochronology. *Earth Plan. Sci. Lett.* 36, 359-362.
- Torne M, Banda E, Garcia-Duenas V, Balanya J C, 1992. Mantle lithospheric bodies in the Alboran crustal Domain (Ronda peridotite, Betic Rif orogenic belt). *E. Plan. Sci. Lett.* 110, 163-171
- Torne M & Banda, E, 1992. Crustal thinning from the Betic Cordillera to the Alboran Sea. *Geo. Mar. Lett.* 12, 76-81
- Tubia J, Gil-Ibarguchi, J-I, 1991. Sequential development of the metamorphic aureole beneath the Ronda peridotites and its bearing on the tectonic evolution of the Betic Cordillera. *Tectonophysics* 279, 227-252.
- Tubia J M, Cuevas, J, 1986. High temperature emplacement of los Reales peridotite nappe (Betic Cordillera, Spain). *J. Struct. Geol.* 8(3-4), 473-482.
- Turner S P, Platt J P, George R M M, Kelley S P, Pearson D G, Nowell G M, 1999. Magmatism associated with orogenic collapse of the Betic-Alboran Domain, SE Spain. *J. of Petrol.* 40, 1011-1036.
- Vissers R L M, Platt J P, van der Wal D, 1995. Late orogenic extension of the Betic Cordillera and the Alboran Domain: A lithospheric view. *Tectonics* 14(4), 786-803.
- Yardley B W D, 1990. An introduction to metamorphic petrology. Longman Earth Science series, pp248.
- Zeck H P, Monie P, Viila I M, Hansen B T, 1992. Very high rates of cooling and uplift in the Alpine belt of the Betic Cordilleras, southern Spain. *Geology* 20, 79-82
- Zeck H P, Albat F, Hansen B T, Torres-Roldan R L, 1989. Alpine tourmaline-bearing leucogranites: intrusion age and petrogenesis, Betic Cordilleras, SE Spain. *N. Jb. Mineral.*

Mh., 11, 513-520.